Mapping totally-focused flaw signal variation introduced by interface curvature in ultrasonic array inspection

Roy Brown

Engineering Doctorate in Non-Destructive Evaluation

2019

Centre for Ultrasonic Engineering
Department of Electrical and Electronic Engineering
University of Strathclyde
United Kingdom

November 7, 2019

DECLARATION OF AUTHORSHIP

This thesis is the result of the author's original research. It has been composed by the author and has not been previously submitted for examination which has led to the award of a degree.

Signed:

Date:

ABSTRACT

This thesis documents the use of the Total Focusing Method (TFM) for performing ultrasonic C-scans of components with irregular and curved surfaces. Ultrasonic inspection depends on an understanding of the link between an ultrasonic indication and flaw size. Some existing methods at Rolls-Royce use target defects of a known size and metal path through flat surfaces to create a Distance Amplitude Curve (DAC) that can be used to accurately size flaws. This study investigated a DAC equivalent for surface-adaptive TFM techniques applied through non-planar surfaces. There was business interest in development of this technique, and also in its delivery by use of general purpose robotic manipulators.

Firstly, a robotic inspection process was developed, and a C-scan was conducted on an irregular titanium plate. cueART, software developed by the University of Strathclyde was adapted to create a TFM C-scan. Results were found to be comparable to an existing production inspection process.

A series of curved test pieces were manufactured and target Flat-Bottomed Hole (FBH) defects were added. BRAIN, software developed by Bristol university, was adapted and used with equipment at Rolls-Royce to conduct TFM C-scans. DAC curves were generated experimentally for a test inspection, showing convex radii from 10 to 40 mm led to a drop of 2 dB, and concave 10 dB. This was repeated at various depths to produce multiple DAC curves.

Modelling techniques for these experimental cases were developed, finding that a 2D finite element model, and 3D CIVA model followed a similar trend to the DAC. Modelling was used to extend results to produce a map of peak flaw signal through a curved surface. An experimental study of flat, rough surfaces showed that an Ra of 12 µm led to a 6.4 dB reduction in peak TFM signal, and 13.2 dB reduction in signal to noise ratio.

ACKNOWLEDGEMENTS

Prof. S. Gareth Pierce I would like to express my gratitude for the help of my academic supervisor Gareth. He has supported me at every stage of this project, and has helped develop my passions for research, technology, and doing things the right way. He is great at rallying people around a common cause, and created a research environment that was as productive as it was a pleasure in which to work.

CUE My project has been influenced by a great many researchers in CUE. The robotics experts, including Carmelo Mineo, Charles Macleod, Jonathan Riise, Rahul Summan and Maxim Morozov, helped me with all sorts of practical robotic concerns. I am also very grateful for help in matters related to use of TFM from Jerzy Dziewierz, Timothy Lardner and Jeff Dobson.

Rolls-Royce plc. I have been based in Derby for the latter three years of my project, and as such would like to thank my colleagues at the Elton Road NDE office for their continued support. I would like to particularly thank Ian Collison for supervising my project, David Wright for taking time to contextualise the work, and Tim Barden for his help in directing the course of the project. Additionally, fellow Rolls-Royce EngDs Rich Phillips, Naomi Shipway and Arnau Garriga-Casanovas were a great help.

RCNDE The Research Centre for Non-Destructive Evaluation has been a wonderful source of training and support, pooling expertise from across the UK to create a comprehensive education for the incredibly broad discipline of NDE. I would like to particularly thank Bristol University for their development of BRAIN phased array software, which was used extensively in this work.

Family and Friends I am grateful that my family and friends never fully abandoned me, even after I disappeared to Derby for so long. Special thanks must go to Euan and Lawrie, who drove some Nerf guns down from Scotland just for an ambush on Brook Street. This was the street of 'EngD HQ', a flat I shared with Rich who I'd like to thank again for being a great flatmate there in Derby. Thanks also must go to Gordan for being a wonderful flatmate in Glasgow towards the end of my research. Finally, thanks to Katharine for giving me stern looks and telling me to finish my thesis.

CONTENTS

LIST OF FIGURES

LIST OF TABLES

ABBREVIATIONS

API	Array Performance Indicator
CAD	Computer Aided Design
CAM	Computer-Aided Manufacturing
CCF	Curvature Correction Factor
CFRP	Carbon Fibre Reinforced Polymer
CIVA	named after "Shiva" [4] - commercially available NDE modelling software
CPU	Central Processing Unit
CUDA	Compute Unified Device Architecture
cueART	CUE Array Research Toolbox
CUE	Centre for Ultrasonic Engineering
DAC	Distance Amplitude Correction
DGS	Distance-Gain-Size
DOF	Degree Of Freedom
DSL	Diagnostic Sonar Limited phased array controller
FARO	a metrology company
FBH	Flat-Bottomed Hole
FE	Finite Element
FEM	Finite Element Method
FMC	Full-Matrix Capture
GPU	Graphics Processing Unit
GTD	Geometrical Theory of Diffraction
GUI	Graphical User Interface
HMI	Human Machine Interface
KRL	KUKA Robot Language

KUKA	Keller und Knappich Augsburg - a robotics company
LL	abbreviation for a Longitudinal-Longitudinal wave interaction
LIN	LINear motion mode for KUKA manipulator path definition
LTI	Linear Time Invariant
MATLAB	MATrix LABoratory
MMP	Multiple Metal Path
NDE	Non Destructive Evaluation
OPP	Offline Path Planning
PA	Phased Array
PAC	Phased Array Controller
PoR	Point of Refraction
PTP	Point To Point motion mode for KUKA manipulator path definition
RCNDE	Research Centre for NDE
RSI	Robotic-Sensor Interface
rx	receive or receiver
SDH	Side-Drilled Hole
SE	Single Element
SMP	Single Metal Path
SNR	Signal to Noise Ratio
SPL	SPLine motion mode for KUKA manipulator path definition
TCP	Tool Centre Point
TFM	Total Focusing Method
ToF	Time of Flight
tx	transmit or transmitter
UT	Ultrasonic Testing

SYMBOLS

A_{b}	attenuation due to beam spread
A_{flaw}	voltage amplitude
A_{rel}	relative amplitude difference between DAC voltage and flaw voltage
A_{s}	attenuation due to grain scattering in steel
A_{w}	attenuation due to absorption in water
B	fluid-solid boundary shape function
b_{d}	distance from TFM imaging point and closest bilinear interpolation point
b_{s}	spacing between bilinear interpolation points in TFM image
c	wave velocity in a medium
c_{l}	longitudinal wave velocity in medium
c_{i}	longitudinal wave velocity in incident medium
c_{r}	longitudinal wave velocity in refracting medium
c_{s}	shear wave velocity in medium
D	array element directivity
d_{FBH}	diameter of FBH used as reference
d_{flaw}	flaw diameter
d_{probe}	probe diameter
E	Young's modulus
f_{c}	wave centre frequency
f_{p}	pulse repetition frequency
f_{s}	sampling frequency
g	number of parallel transmissions from an ultrasonic array
l	length
l_{p}	array element pitch

l_r	resolution of a C-scan
n	number of entities
N_0	sound path length from transducer face to beginning of far field
n_el	number of elements in an ultrasonic array
n_epw	number of FEM elements per ultrasonic wavelength in a FEM model
n_s	number of samples in an A-scan acquisition
p	pressure
p_i	incident pressure
p_r	reflected pressure
p_t	transmitted pressure
P	point
r	radius or radial distance
R	reflection coefficient
R_a	average roughness of a surface
R_ll	reflection coefficient for longitudinal-longitudinal interaction
s	surface point spacing interval for TFM surface definition
S	correlation coefficient
t	time
T_a	acoustic-elastic transfer function subsystem
t_c	time taken to calculate a TFM image representation for use in a sensitivity map
T_ll	transmission coefficient for a longitudinal to longitudinal wave
T_lt	transmission coefficient for a longitudinal to transverse wave
t_Ptxrx	time taken for wave to pass from transmitter to TFM pixel and back to receiver
t_r	time taken to capture an A-scan or B-scan, based on ultrasonic range setting
T_sys	system transfer function

$\boldsymbol{u}$	particle displacement
V	voltage
v_{d}	data-related maximum scanning speed of an ultrasonic array mounted to a scanner
v_{p}	physical scanning speed of a probe mounted to a scanner
Z	acoustic impedance
α	attenuation coefficient
Γ_{a}	pose of robotic arm
Γ_{t}	pose of Cartesian scanning tank
θ_{i}	angle of incidence
θ_{crit}	critical angle of incidence
θ_{dl}	angle of refraction from longitudinal to longitudinal wave
θ_{dt}	angle of refraction for a longitudinal to transverse wave
θ_{rl}	angle of reflection for longitudinal to longitudinal wave
θ_{rt}	angle of reflection for longitudinal to transverse wave
λ	ultrasonic wavelength
λ_{B}	bulk modulus
μ	data transfer rate from phased array controller
ρ	density
τ_{step}	time step used for FEM model
τ_{cr}	critical time step used for FEM model
τ_{tsf}	time step stability factor for FEM model
τ_{w}	time step used in water zone of FEM model
τ_{st}	time step used in steel zone of FEM model

Chapter 1

INTRODUCTION

1.1 MOTIVATION

Jet engine components are subject to high temperatures and stresses. In this environment, a small crack or void can grow, eventually leading to part failure. Manufacturing processes at Rolls-Royce plc. are therefore strictly controlled in order to ensure no defects are introduced. Additionally, inspection is performed, at an intermediate stage or post-manufacture, to verify that these stringent processes have resulted in a defect-free component, or if defects are introduced, that they are below a critical threshold in size. This is particularly relevant for parts under heavy stress and temperature loading, such as fan blades and turbine discs.

Recently, in the October of 2016, there was an explosive reminder of the importance of disc inspection. In Chicago, a GE CF6-80 engine suffered an un-contained disc failure, leading to a jet fuel fire and ejection of disc fragments, one of which was found 890 metres from the aircraft [5]. The cause was an internal inclusion of foreign matter; or in other words, a defect introduced at the manufacturing stage which could have been detected prior to service, with improved Non Destructive Evaluation (NDE).

NDE gives a measure of component integrity without damaging the part in question. Visual, electrical, magnetic, thermographic and ultrasonic techniques are among those routinely deployed. For an inspector to decide that a component is safe to fly, there must be a well defined relationship between component geometry, any possible defects, and the results obtained from the inspection equipment. Introduction of a new technique requires proof that it is predictable, can be de-

ployed reliably, and has the performance to identify defects of the appropriate size.

Ultrasonic waves can penetrate deep into metals, scatter off of small voids, and subsequently be detected on their return. This makes them ideal for interrogating components of around 100 mm thickness for defects as small as 0.3 mm, for example, as long as the appropriate frequency is used. Ultrasonic NDE gives time-traces and images related to the pressure variation returned by the wave. It is the responsibility of the person qualified to ultrasonic level two or three [6] to ensure that flaw size can be inferred accurately from these results. This demands that the calibration of equipment, wave physical effects, inspection method, and operator interpretation are combined in a well understood procedure.

Consequentially, a company requires a very good reason to introduce a new technology into an established inspection procedure, as well as a supporting body of evidence to prove its worth. One such pressing reason is the desire to automatically inspect curved components. Inspection of curved components is more complicated than planar geometries, due to the added difficulty of compensating for the refraction induced by surface curvature.

It is standard procedure to machine flat sides into forged components prior to inspection, in order to ensure that the ultrasonic method gives predictable results. The extra material added at the design phase to enable this could be removed, if only inspection of curved forgings was proven to be predictable enough. Additionally, improved inspection through curved surfaces could increase the performance of in-service techniques. Potential benefits are therefore cost reduction at manufacture, and an increase in safe working lifespan.

For these reasons, the motivation of this thesis is to provide evidence that curved components can be automatically inspected with a predictable response, using ultrasonic techniques. It focuses specifically on two existing automated inspection techniques of interest to Rolls-Royce. Chapter 2 converts the innovations required into technical objectives for the thesis, with following chapters detailing the technical work carried out to reach these goals.

The work in this thesis centres around the fact that flaws inside a forging can take the form of a flattened void in the material. Inhomogeneous cooling leads to a void inside a cast billet, which takes on a flattened shape when forged and is aligned along the forging flow lines. In order to represent this sort of defect, a flat-bottomed hole (FBH) is used as a reference reflector.

In this case, a FBH is drilled with known diameter and location, in a test piece with a flat interface. The test piece is inspected, and results recorded. From this, inspection performance at different depths can be calculated. These results can then be used to plan the inspection of objects with flat sides. By taking into account probe position and edge interactions, a diagram can be created describing the ability to find flaws at particular points of a component volume. This is known as a coverage map.

The map is an essential tool to design forgings with minimal wastage, without compromising on safety. Advanced solutions have been developed for optimising the iteration process between forging design and inspection planning [7]. To execute these inspections, automated systems drive probes to the required locations. Experimental data is then fed back into the inspection planning system, to help validate and, if necessary, supplement the theoretical coverage map. This holistic approach has been proven to improve inspection efficiency, and is under continuous development at the time of writing. One current limitation of the approach is its inability to plan inspections for curved components.

Optimal results can be obtained by designing a probe specifically for a given curved surface. However, an automated inspection with multiple curved surfaces would require an impractical number of probe changes. Linear phased array probes are capable of adapting to arbitrary 2D surface curvatures, so provide a potential solution. This capability has been demonstrated in a research environment, and has recently been integrated into commercially available hardware [8]. It is a promising technology but needs to be well characterised before inspectors can have confidence in applying it to critical components.

A large number of variables are introduced by this change. These are explored in detail in chapter 2, but one example is the component geometry relative to the probe. Instead of using performance through a flat interface as a baseline for every probe position, the interface could be continuously changing, with a corresponding change in performance. This needs to be quantified and controlled for an effective solution. The interplay between automation, data capture, analysis and component design make it necessary to carefully consider the effects on each part of the process.

For development of phased array techniques, a technique called Full Matrix Capture (FMC) allows a re-focusable dataset to be obtained. This is attractive in many ways, the primary attraction being the ability to apply different focal laws in the post-processing stage to change many imaging parameters without the

costly and time consuming step of re-scanning a component. Imaging techniques that are not possible using classical beamforming methods are possible with FMC, primarily the Total Focusing Method (TFM).

Much work using TFM has been carried out at the University of Strathclyde and Bristol University in the last decade. This ultrasonic technique has not been widely adopted in industry, but where it has, it offers improvements for many applications, especially for obtaining signal through irregular surfaces [9]. Another contemporary research interest in the UK's Research Centre for NDE (RCNDE) is in automated inspection delivery using general-purpose robotic manipulators [10].

The overall aim of this thesis is to combine these technologies to move towards predictable curvature-corrected TFM automation processes. The next section aims to succinctly summarise the focus of this thesis.

1.2 THESIS PROBLEM SUMMARY

One example of a defect that form in forgings is porosity. During the casting process, dissolved gases in the liquid metal create bubbles in the metal as it cools. The flaw takes the shape of a spherical void, until the forging process is applied.

Forging is the act of shaping metal using compressive forces, often at high temperature. Material grains are flattened, and a pore-like defect is transformed into a disc-shaped defect.

Flow lines are created inside the forging, where the material is forced along contours of the forged shape. This strengthens the material preferentially in the direction of the flow lines.

These disk-shaped defects are often represented by flat-bottomed holes (FBH) for ultrasonic inspection purposes, as they have a similar top surface shape. The face of a flaw is most likely to be oriented facing towards the outer surface of the component, sitting along a forging flow line. This is a favourable orientation for detection via ultrasonic methods.

In this study, a defect size of 0.63 mm is used. Forgings can have much smaller flaws than this that still weaken the structural integrity of the component. In order to understand the full population of flaws present in the component, it is necessary to use statistical methods to predict the population of flaws that are

too small to detect. The number of flaws found within the detection limits, as well as their relative closeness to each other, are used to estimate the overall flaw population. If this poses a risk to the suitability of the component, then it is rejected. More accurate methods than the one used in this study can find flaws of 0.5 mm and below in forgings.

An illustration of the forging and inspection process is included in Fig. 1.2.1, which shows three different cross-sections of a forged part.

Firstly, the forging cross section is shown in blue. This is the shape of the forging immediately following the forging process. In this state, the part has a "black forged" surface, which is rough and must be removed.

Secondly, the forging is reduced to a rectilinear shape, shown in green. This step is included to enable inspection of the volume of the forging shown in yellow - the material that comprises the final part. Currently, the inspection process is only able to operate through a flat interface, hence the need for the rectilinear, green stage. If it were possible to inspect through a curved surface, the yellow final part cross section could be inspected directly.

If the intermediate green cross section could be removed from the figure below, a large amount of cross-sectional area could be saved, and therefore material savings would be realised.

The focus of this thesis is based around the integration of automated inspection delivery with TFM techniques. In Fig. 1.2.2, panels a)-f) illustrate key ideas by considering the inspection of a forging, shown as a cross-section.

In panel a), the rectilinear forging outline is shown in black (i). This represents the entire forging, shown here as a 2D cross section. Shown in green (ii) is an area within the cross section referred to here as a "Detectability Region" (DR). To clarify by example, this could represent the volume within the forging where a FBH of diameter 0.63 mm can be detected, with an amplitude of greater than -24 dB compared to a reference FBH defect in a calibration block. The shape of the DR is determined by the method; here using a single element probe (iii), scanned in straight lines (iv) across the flat faces of the forging. Changes to inspection parameters such as the angle, frequency, or diameter of the transducer all affect the DR.

Diagrams similar to this are produced as part of the forging design process in industry. Components are to be milled out from the forging shape after inspec-

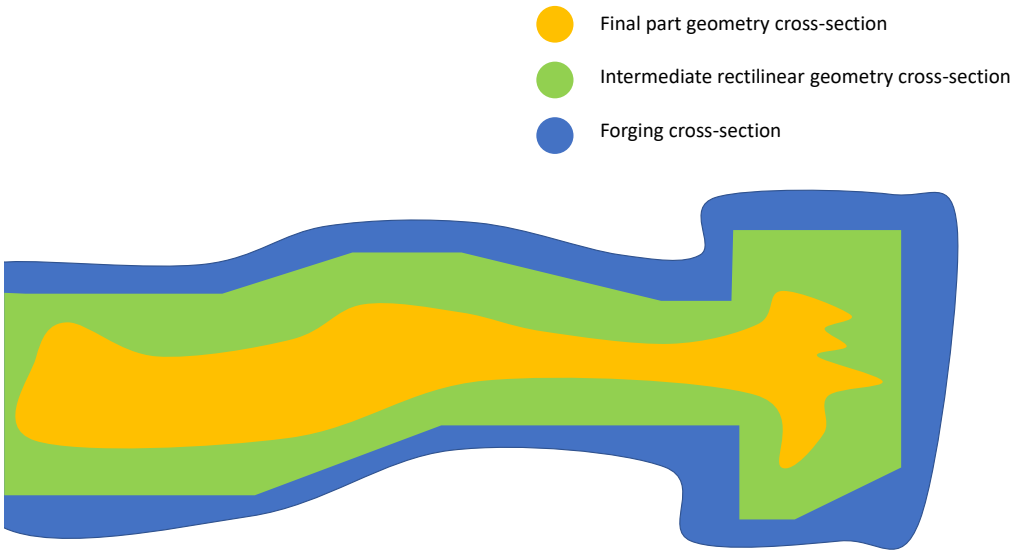

Figure 1.2.1: Illustration of different cross sectional geometries relating to stages of forging and inspection process. The original forging is shown in blue, which is machined down to the rectilinear stage shown in green. Finally, the component is milled and polished to its final form, shown in yellow.

tion. The design of the forging and the inspection must therefore be such that the extent of the final component sits within the DR. For a given design, the DR is predicted from the forging outline (i), scanned faces (iv), and ultrasonic inspection performance at the proposed probe positions. This is predicted from a combination of beam calculations and heuristics based on experimental data. Once a suitable candidate design is selected, experimental trials verify the DR.

Separate to this thesis, a design technique that performs more advanced modelling for single element transducers is under development. Using a more comprehensive beam model, this seeks to better define the DR, and could lead to improvements e.g. the enlarged DR (v) in panel b). A major benefit of this approach is that wastage of material, and experimental time could be reduced if the DR could be more confidently estimated.

Often, the final component shape uses only a fraction of the forging. Sometimes the final component has a curved shape, around which a curved initial forging envelope could be designed. This offers an excellent opportunity for reduction in material use (see panel e). However, existing approaches are limited to planning inspections for a rectilinear forging. The curved case is illustrated in panel c), where two elements of the inspection have changed. Firstly, a curved path of the

probe must be planned to maintain normality to the surface. Secondly, surface curvature has an effect on the DR (viii) due to beam steering and focusing.

TFM has been shown to compensate for surface curvature. It has been suggested that a technique employing surface-corrected TFM could deliver a more even response to flaws, resulting in a more even DR (see (ix) in panel d). In order to investigate this, it is first necessary to establish techniques to model and capture TFM data through curved surfaces. This thesis aims to demonstrate that the process in a) can be recreated using TFM and industrial robots. Further, it develops methods to explore the level of defect amplitude encountered in a DR under curved surfaces. These are referred to as sensitivity maps.

In a wider manufacturing context, closer integration of automated NDE with other manufacturing processes is desirable. The use of a general purpose robotic manipulator to enable the path-planning for the curved path of this inspection was explored for this reason. This thesis describes use of a flexible programming interface to plan probe paths for TFM inspections, and deliver an automated surface-corrected TFM C-scan for an irregular component.

This thesis works on these two technologies, and combines them to make progress towards developing an inspection planning system such as that shown in d).

A further motivation for developing such a system is when there is interplay between the path planning and inspection capability; illustrated in panel f). The larger size of the array requires a different standoff from the surface at different points in the scan. A robotic scan planning method can take account of the size of the probe to avoid collision with the component, and a TFM modelling method can determine the extent to which this affects the DR.

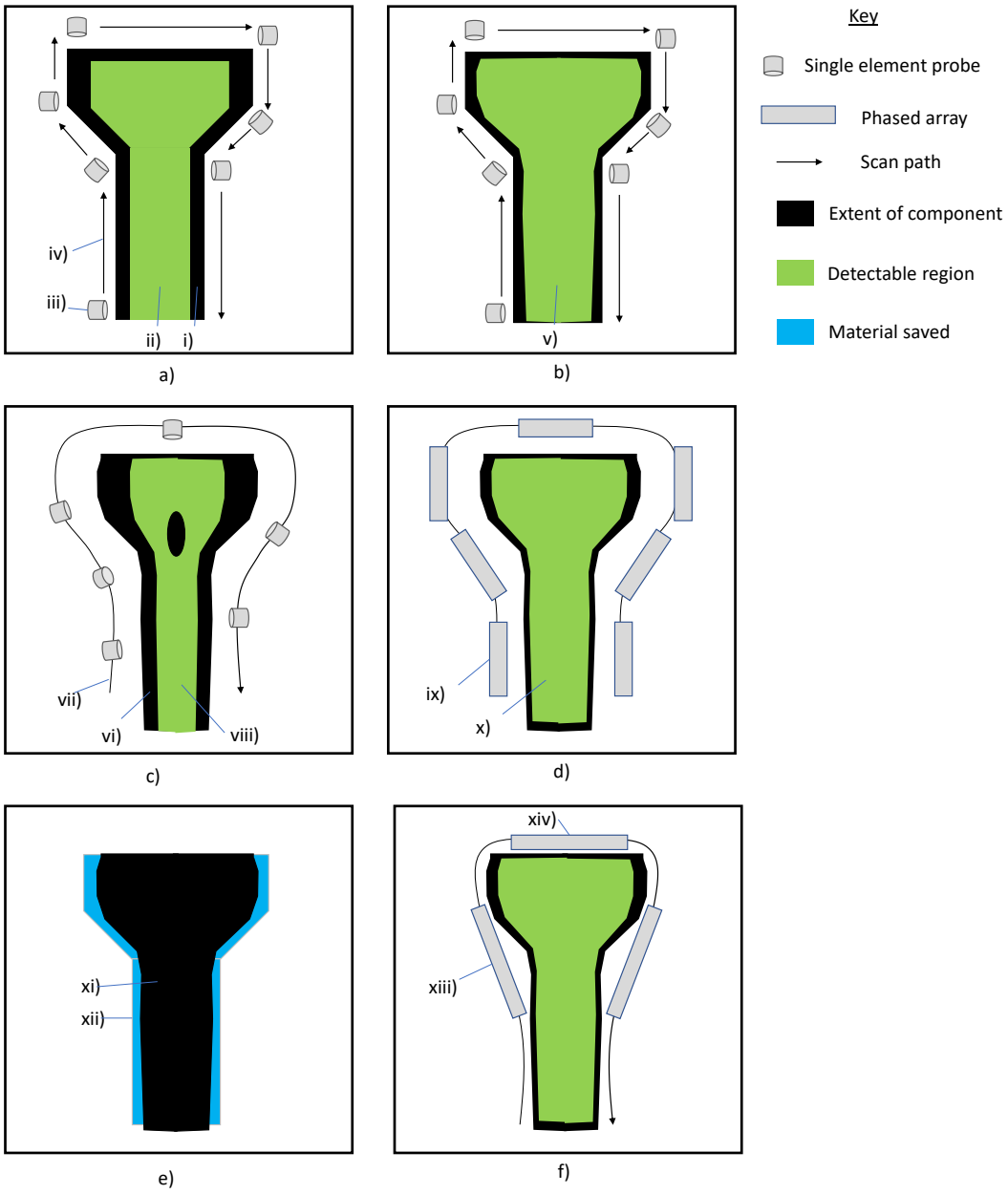

Figure 1.2.2: Illustration of main thesis problem through different approaches to inspection of a rectilinear or curved forging cross section.

1.3 THESIS OUTLINE

A literature review incorporating enabling technologies is presented in Chapter 2. The level of background included establishes the current state-of-the art, and also translates the business requirements (stated below) into the technical objectives that define chapter content. Background details above and beyond those required

to understand the main technical objectives of the thesis are included in relevant sections.

Chapter 3 describes the development of a robotic FMC scanning system for scanning an irregular plate. It demonstrates the application of TFM techniques for development of a C-scan on an industrially relevant sample, and shows how robotic manipulators can be used to automate the inspection delivery.

Chapter 4 details the construction of three different types of FMC models, and use of them to create TFM images. A 2D FE model is developed in PZ Flex, a 3D model is developed in CIVA, and a simplified MATLAB ray tracing coverage mapping model is proposed. Note that details of software versions are in Section A.2.

Chapter 5 documents the methodology used to capture experimental FMC results, and use of TFM for imaging. This includes the design of calibration blocks for inspection through curved surfaces, and techniques for performing and analysing TFM C-scans.

Chapter 6 presents experimental results from the calibration blocks detailed in Chapter 5, and compares these with models created using the modelling techniques described in Chapter 4. Signal strength of TFM through curved surfaces, and rough surfaces is quantified.

Chapter 7 summarises the thesis, evaluates progress against technical objectives, and discusses ideas of future applications.

1.4 SUMMARY OF THESIS BUSINESS REQUIREMENTS

Below are listed a summary of the main requirements of this project. These were developed after consultation with the stakeholders in the company, for whom the automated ultrasonic inspection of components is a day-to-day concern. These drive the technical approach, and lead to the formal technical objectives stated in Section 2.4.4.

1. DEMONSTRATE AUTOMATED CAPTURE OF TFM FOR COMPLEX PARTS USING GENERAL PURPOSE ROBOTIC MANIPULATOR

A flexible, automated, easily programmable system that can deliver TFM imaging of complex parts was sought. Key requirements included an easy to use human-machine interface (HMI), and the ability to automatically scan irregularly shaped components. The use of general purpose robotic manipulators was suggested, rather than bespoke ultrasonic scanning equipment.

2. INVESTIGATE THE ULTRASONIC INSPECTION OF CURVED FORGINGS USING TFM

Inspection of rough or curved forgings was highlighted as an area of interest by the business. Key requirements were to investigate the effect of curvature on ultrasonic techniques, and correct any changes in apparent flaw size. A particular interest was expressed in measuring the ability of a technique to maintain sensitivity through a given surface curvature.

3. USE OF TFM COVERAGE MAPS FOR INSPECTION OR COMPONENT DESIGN

To establish how knowledge of ultrasonic testing limitations can be used to design optimal scanning paths, and structures closest to final component shape that can retain inspectability.

These can be thought of as the business-level objectives for this project - progress to any one of the three would improve automation capability (1), understanding of advanced inspection techniques (2) and help develop new processes (3). The specific technical objectives of this thesis are derived from these business requirements, after first considering the technical state-of-the art in inspection technology described in the next chapter.

1.5 KEY CONTRIBUTIONS

The aim of this section is to identify and summarise the key findings and contributions from this thesis as succinctly as possible.

1.5.1 KUKA|PRC AND GRASSHOPPER FOR INSPECTION PLANNING AND EXECUTION

A process for offline path planning, executing robotic inspection, and data visualisation was created using these tools. This achieved similar results to previously known options, but offered a more open and cheaper approach.

1.5.2 MODELLING FMC IN PZFLEX AND CIVA FOLLOWED BY VISUALISATION IN BRAIN

Using these two commercial modelling packages was valuable to Rolls-Royce, as it allowed them to use readily available tools to perform FMC modelling. Integration of these results with BRAIN, the software also used for data acquisition, allowed a representative and intuitive comparison between modelled and experimental data.

1.5.3 PRODUCTION OF A TFM C-SCAN USING MANIPULATOR POSITIONAL DATA AND CUTFM

This method involved combination of TFM data generated from cuTFM, with robotic internal encoder positional data (X, Y, Z position and A, B, C tilt). This was applied to an irregular plate, to inspect disbonds in a titanium membrane. This was an industrially relevant inspection. The C-scan was used to show equivalence between results from this method and a C-scan process already used in production.

1.5.4 PRODUCTION OF A TFM C-SCAN USING CARTESIAN AXIS SCANNER POSITIONAL DATA AND BRAIN

This method involved the combination of FMC data captured using BRAIN with time-encoded data (X, Y) from a Cartesian axis scanner. MATLAB code was developed to run BRAIN on the captured data, gate the data, and present a C-scan. Further tools were developed in MATLAB to measure the peak signal, and

SNR from these TFM C-scans. This technique was applied to a set of purpose-made calibration blocks, of industrial relevance to Rolls-Royce.

1.5.5 QUANTIFICATION OF TFM PEAK SIGNAL AMPLITUDE USING CURVED CALIBRATION BLOCKS

Calibration blocks for inspection of flat-sided forgings are commonly used at Rolls-Royce. A set of blocks with the same material, targets and similar range of metal paths were produced; only with radially curved surfaces. The technique described in Section 1.5.4 was applied to these blocks. The influence of concave and convex curved surfaces on peak signal strength were compared to a flat block.

This thesis contributed experimental results, showing relative peak signal strength for centrally-located FBHs under surfaces with curvatures between 10-40 mm. Results from concave and convex curvatures were presented. All results used a 32 element, 10 MHz phased array probe.

This thesis also contributed experimental results from multiple metal paths, showing the relationship between flaw depth and relative signal for radial curvatures between 10-30 mm.

This thesis also contributed a comparison of results modelled using the techniques developed in Section 1.5.2 with the experimental results.

1.6 PUBLICATIONS ARISING FROM THIS THESIS

Two publications have been made from work in this thesis. The first was entitled "Automated full matrix capture for industrial processes." and was presented at QNDE 2014 [11]. The second, "Quantifying performance of ultrasonic immersion inspection using phased arrays for curvilinear disc forgings", was presented at QNDE 2016 [12].

Chapter 2

LITERATURE REVIEW AND TECHNICAL OBJECTIVES

2.1 SINGLE ELEMENT ULTRASONIC IMMERSION INSPECTION

This section describes the considerations that must be made, and the common terms used in single-element pulse-echo immersion inspection. This section is written to serve the dual purpose of introducing concepts common to both single element and phased array transducers, as well as to provide background for the existing case study processes. Single element techniques are used for existing processes. As equivalence is sought between existing techniques and new ones, this section helps explain the performance required from a replacement technique. Immersion mode is used for all simulated and experimental imaging in this thesis.

2.1.1 SINGLE ELEMENT ULTRASONIC TRANSDUCERS

Single-element (SE) ultrasonic transducers are used for both of the industrial cases under investigation for this project. One particular transducer type of interest is a disc-shaped planar transducer, (such as that shown in Fig. 2.1.1) with piezoelectric oscillation mode in the z-direction to produce a "piston-like" motion. The oscillation encountered at the front face is a function of the input

voltage, which is typically a negative rectangular pulse.

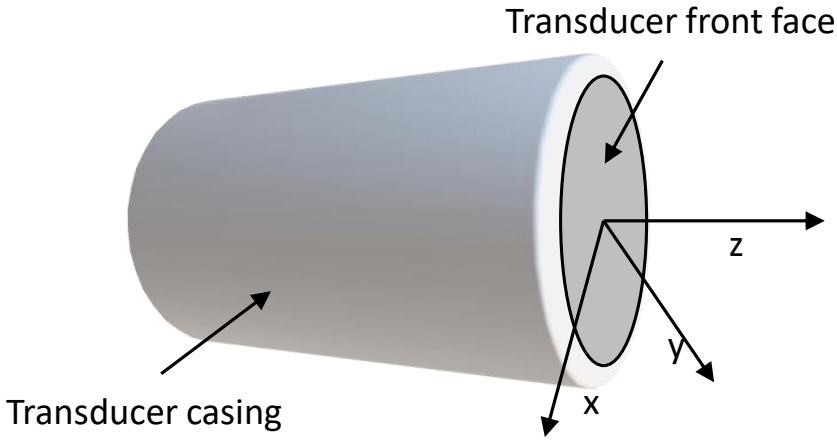

Figure 2.1.1: Depiction of single element transducer, as well as co-ordinate system defining the direciton of oscillation in the z-direction. This is a planar, unfocused transducer.

Consider an unfocused SE transducer placed in a non-viscous fluid such as water. In response to an electrical impulse, the element expands and contracts relative to the input voltage, and thus creates longitudinal waves emanating from the transducer face in the water. These waves propagate with a velocity according to the fluid properties, through the wave equation.

The wave equation describes particle displacement with time. For ultrasonic inspection it is useful to express this in terms of 2D pressure distribution [1, Ch. 1] $p(x, z, t)$ by considering the application of Newton's law to a small fluid element

$$-\nabla p = \rho \frac{\delta^2 \boldsymbol{u}}{\delta t^2} \tag{2.1}$$

and the relationship between pressure and displacement in an ideal compressible fluid

$$p = -\lambda_{\mathrm{B}} \nabla \cdot \boldsymbol{u} \tag{2.2}$$

satisfying the wave equation

$$\frac{\delta^2 p}{\delta x^2} + \frac{\delta^2 p}{\delta z^2} - \frac{1}{c_1^2} \frac{\delta^2 p}{\delta t^2} = 0 \tag{2.3}$$

where $\boldsymbol{u}$ is particle displacement, ρ is material density, λ_B is the bulk modulus of the fluid, and c_l is the longitudinal wave velocity.

Wave velocity is therefore linked to material properties, and is given by

$$c_\mathrm{l} = \sqrt{\frac{\lambda_\mathrm{b}}{\rho}}$$

which is valid for the longitudinal wave mode. Solids can additionally support shear waves, which propagate at approximately half the velocity. For an isotropic homogeneous material with Young's Modulus E, Poisson's ratio ν, and density ρ, the velocities for each mode are given by [13, Ch. 4]

$$c_\mathrm{l} = \left[\frac{E}{2\rho(1+\nu)}\right]^{1/2} \tag{2.4}$$

and

$$c_\mathrm{s} = \left[\frac{E(1-\nu)}{\rho(1+\nu)(1-2\nu)}\right]^{1/2} \tag{2.5}$$

where c_s is shear wave velocity.

For immersion inspection of defects $\leq 1\,\mathrm{mm}$ across, frequencies used range from 2.5 MHz to 20 MHz. For frequencies that are too low, small defects do not reflect enough energy for detection, however frequencies that are too high do not penetrate deeply enough. The probe diameter usually ranges from 10 to 50 mm across. A consequence of this is that the probe radiation pattern cannot be simplified to either an infinite plane wave (a valid approximation when $\lambda \ll d_\mathrm{probe}$) or a spherical wave (a valid approximation when $\lambda \gg d_\mathrm{probe}$), therefore the ultrasonic beam profile has to be well-understood for use in an inspection.

To address the non-uniformities in the beam profile, the near-field of the beam is defined based on transducer geometry. Within the near field, there is non-monotonic fluctuation of the beam strength along the central axis. The maximum amplitude of the transducer beam profile is known as the "N-point". Beyond this, the far-field consists of a smoother, monotonic drop in beam strength. For practical use, the N-point is determined from probe geometry, and can be further characterised by experimentally measuring the beam profile at a range of depths. An example of the near and far field pressure variation is shown in Fig. 2.1.2.

Note that this, and the beam profiles shown in this chapter, were modelled using the approach detailed in Schmerr [1].

The smoothly-varying, monotonic structure of the beam (shown to the right of the peak marked N-point in Fig. 2.1.2) can then be used for predicting the size of flaws situated at different depths, as discussed in Section 2.1.2.

Spherically-curved SE transducers make use of a curved front face to alter the beam profile. This focuses the beam at a certain depth, and also changes the position of the "N-point". A curved face increases sensitivity to small defects near the focal point, however energy diverges more rapidly with depth far beyond it.

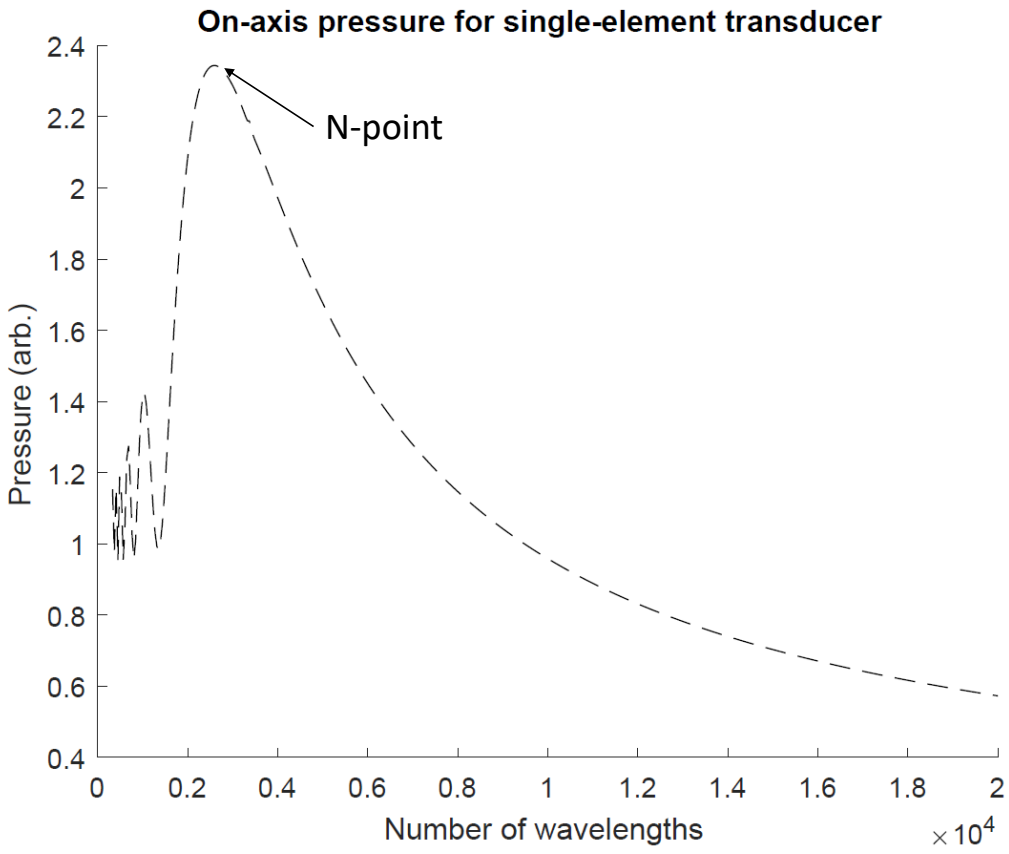

Figure 2.1.2: On-axis pressure profile for a single element transducer, with a diameter of 6 mm, in water, at a frequency of 10 MHz, and a focal length of 50.8 mm. Modelled using the function `on_axis_foc2D` from Schmerr [1], which uses the paraxial approximation to write the pressure field in terms of a Fresnel integral.

This section has described how a single element transducer transforms a voltage pulse into a useful beam of sound energy with predictable characteristics. The

next section discusses how this transducer can be used in the pulse-echo mode to size defects.

2.1.2 SINGLE ELEMENT PULSE-ECHO INSPECTION THROUGH FLAT INTERFACES

In situations where the interface between two media is large compared to the wavelength of the ultrasonic wave, diffraction effects can be ignored and the path of the energy can be approximated by a ray. Refraction in this case can be described by Snell's law,

$$\frac{\sin\theta_{\mathrm{i}}}{\sin\theta_{\mathrm{d}}} = \frac{c_{\mathrm{i}}}{c_{\mathrm{r}}}; \tag{2.6}$$

where θ_{i}, θ_{d} are the incident and refracted angles, whereas c_{i} and c_{r} are the wave velocities in the incident and refracted media.

Derived from the Huygens'-Fresnel principle, Fermat's principle of least time states that the path a ray takes between two points is that which takes least time to traverse, illustrated by considering multiple ray paths between two points as shown in Figure 2.1.3. This is useful for the situation where there are well-defined source points in the first medium, well defined targets in the second medium, but where the intersection point with the surface is not known.

Forward ray propagation could be used instead to find the path of the ray. The problem with this approach is that it cannot constrain the end point of the ray following refraction with the surface. The rays refracted into the surface could be interpolated, covering all points of interest. An issue with taking this approach compared to Fermat's principle is that the resulting interpolated range of ray values may not provide an even spacing, as the end points are not known prior to forward propagation. Use of Fermat's principle adds a small extra computational burden as it requires iteration of the refraction point, but has the benefit that the end points are known precisely. These end points can be pre-determined as the pixel locations to ensure an accurate ToF.

Another alternative to Fermat's principle is the application of an analytical solution for the ToF between P1 and P2 for a given surface. This was not considered for the work in this thesis, as to apply the approach generally would require a method to quickly compute analytical solutions for arbitrarily curved surfaces.

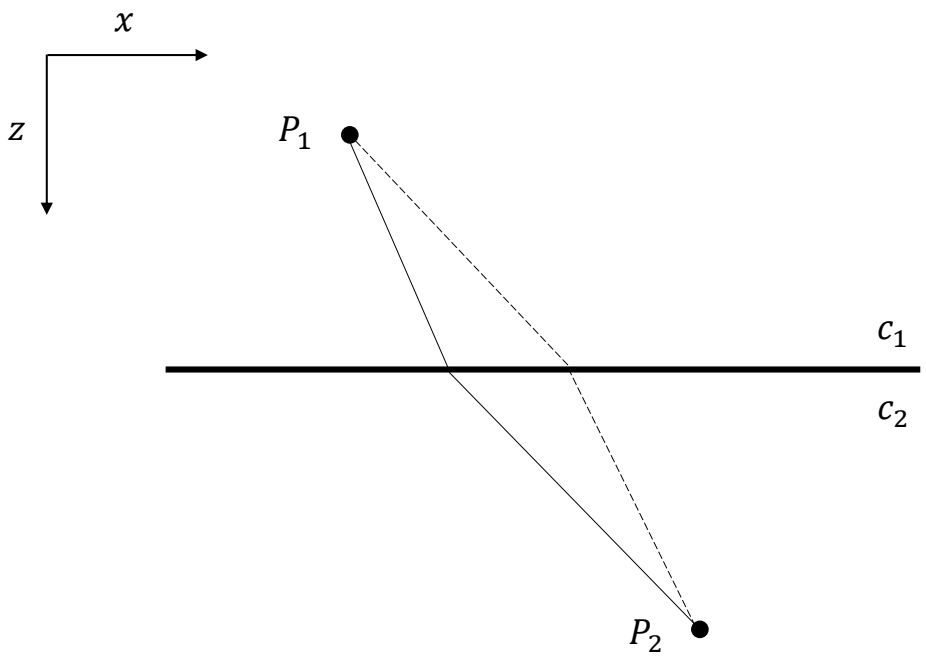

Figure 2.1.3: If $c_1 > c_2$ then ray takes the path of the dashed line, if $c_2 > c_1$ then ray takes the path of the continuous line. If P_1, P_2, c_1 and c_2 are known, then the true intersection point with the surface can be found by iterating through different interface points, and selecting the one that gives the lowest ToF.

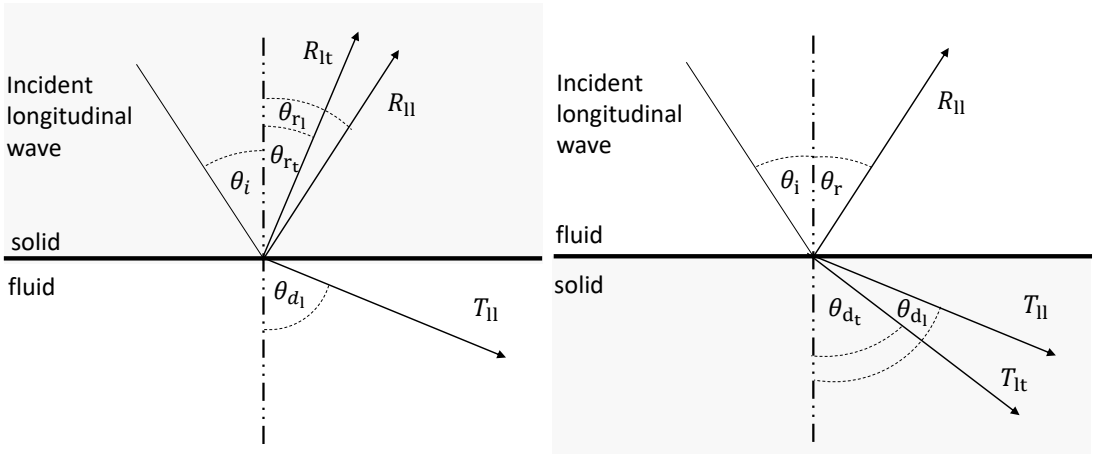

Figure 2.1.4: Mode conversions at a solid-fluid interface from incident longitudinal waves.

While this could result in faster surface compensation once the analytical solution is available, it was deemed too complex to automatically calculate these analytical solutions for measured surfaces during a scan. A fixed analytical solution would be more appropriate in an application where the surface is always the same shape.

Fermat's principle therefore provides the best trade-off between accuracy, computational burden, and complexity of implementation for calculating ToF through an arbitrarily curved surface.

This allows calculation of the angle at which a ray strikes an interface, which has an effect on the pressure amplitude of the wave. The amplitudes of the transmitted and reflected waves can be related by defining the reflection coefficient $R = p_\mathrm{r}/p_\mathrm{i}$ and the transmission coefficient $T = p_\mathrm{t}/p_\mathrm{i}$, where p_i, p_t and p_r are the incident, transmitted and reflected pressures respectively. Figure Fig. 2.1.4 show the wave modes that can be generated, and the associated coefficient required to calculate the pressure amplitude at each mode after the interaction. Coefficients are distinguished by subscripts such that R_ll is the reflection coefficient following a longitudinal-longitudinal interaction, and is dependent on θ_i, with a value given by Eq. (2.10). Transmitted and reflected angles are denoted as θ_dl meaning transmitted angle for incident longitudinal wave.

The acoustic impedance $Z = \rho c$ of the materials and θ_i can be used to calculate the coefficients, and predict the pressure difference of the wave before and after interaction with the interface. Energy is conserved when passing through the interface by taking the form of longitudinal, shear or surface waves in the second medium, with the proportion of energy in each mode determined by θ_i. The reflection and transmission coefficients for a longitudinal-longitudinal interaction through a fluid-solid boundary, R_ll and T_ll can be found by defining the abbreviation [2]

$$N = \left[\left(\frac{c_\mathrm{ss}}{c_\mathrm{ls}} \right)^2 \sin 2\theta_\mathrm{l} \sin 2\theta_\mathrm{s} + \cos^2 2\theta_\mathrm{s} + \frac{\rho_\mathrm{w} c_\mathrm{w}}{\rho_\mathrm{s} c_\mathrm{l}} \frac{\cos\theta_\mathrm{l}}{\cos\theta_\mathrm{w}} \right] \tag{2.7}$$

where c_ls and c_ss are the longitudinal and shear wave velocities in the solid, and c_w is wave velocity in the liquid, θ_l and θ_s are the longitudinal and shear wave angles in the solid, and θ_w is the wave angle in the liquid, and where ρ_w and ρ_s are the densities of the liquid and solid respectively.

The coefficients for the liquid-solid case (incident wave in liquid) are found to be

$$R = \frac{1}{N} \left[\left(\frac{c_\mathrm{ss}}{c_\mathrm{ls}} \right)^2 sin2\theta_\mathrm{l} \sin 2\theta_\mathrm{s} + \cos^2 \theta_\mathrm{s} - \frac{\rho_\mathrm{w} c_\mathrm{w}}{\rho_\mathrm{s} c_\mathrm{l}} \frac{\cos\theta_\mathrm{l}}{\cos\theta_\mathrm{w}} \right], \tag{2.8}$$

$$T_\mathrm{ll} = \frac{2}{N} \cos 2\theta_\mathrm{s}. \tag{2.9}$$

For the solid-liquid case (incident wave in solid),

$$R_{\mathrm{ll}} = \frac{1}{N}\left[\left(\frac{c_{\mathrm{ss}}}{c_{\mathrm{ls}}}\right)^2 \sin 2\theta_{\mathrm{l}} \sin 2\theta_{\mathrm{s}} - \cos^2 2\theta_{\mathrm{s}} + \frac{\rho_{\mathrm{w}} c_{\mathrm{w}}}{\rho_{\mathrm{s}} c_{\mathrm{l}}} \frac{\cos\theta_{\mathrm{l}}}{\cos\theta_{\mathrm{w}}}\right], \tag{2.10}$$

$$T_{\mathrm{ll}} = \frac{2}{N} \frac{\rho_{\mathrm{w}} c_{\mathrm{w}} \cos\theta_{\mathrm{l}} \cos 2\theta_{\mathrm{s}}}{\rho_{\mathrm{s}} c_{\mathrm{l}} \cos\theta_{\mathrm{w}}} \tag{2.11}$$

Depending on incident angle, a range of amplitudes of longitudinal and shear waves are produced in the second medium. These can be used to predict the alteration in signal amplitude for a pulse-echo ultrasonic inspection owing to the interface geometry, but only when surfaces are smooth and large compared to the incident wavelength - otherwise the reflection and refraction is not specular, and a more general scattered field is created. In this study, the problem is simplified to only take into account longitudinal-longitudinal (LL) interactions. Note that the imaging mode used is denoted by a string of letters based on the type of mode conversion at each stage. For example, a signal arising from a three-stage longitudinal-transverse-longitudinal interaction is denoted LTL.

A simple inspection setup is shown in Fig. 2.1.5. The dotted line shows the direction of wave propagation, following the path of interest for pulse-echo inspection, with various different interactions numbered from 1 to 5.

A pulsed voltage placed across a piezoelectric element causes it to deform in the z direction, producing a longitudinal wave in water at the transducer face (1). The wave propagates through the water until reaching the steel surface at point (2). At this point, waves are reflected and refracted, with alteration in wave amplitude given by T_{ll} and R_{ll}, where the transmitted longitudinal wave is of interest. If the interface is smooth, then the amplitude of the transmitted wave is described by Eq. (2.9). The wavefront propagates through the steel, and reaches the flaw at point (3). Multiple wave modes are produced as outlined in 2.1.8, but only the LL mode is considered here. The scattered portion of the energy propagates to point (4), then part of this energy is transmitted to point (5). At (5), the wave distorts the piezoelectric element and a voltage is produced.

By sampling this transducer voltage with time, the pressure history at the transducer face can be inferred. This is termed as an A-scan, and when combined with a knowledge of the part geometry and material properties, amplitude variations can be used to detect defects. The interpretation of an A-scan for immersion inspection is shown in 2.1.6. The A-scan records the initial pulse, the surface

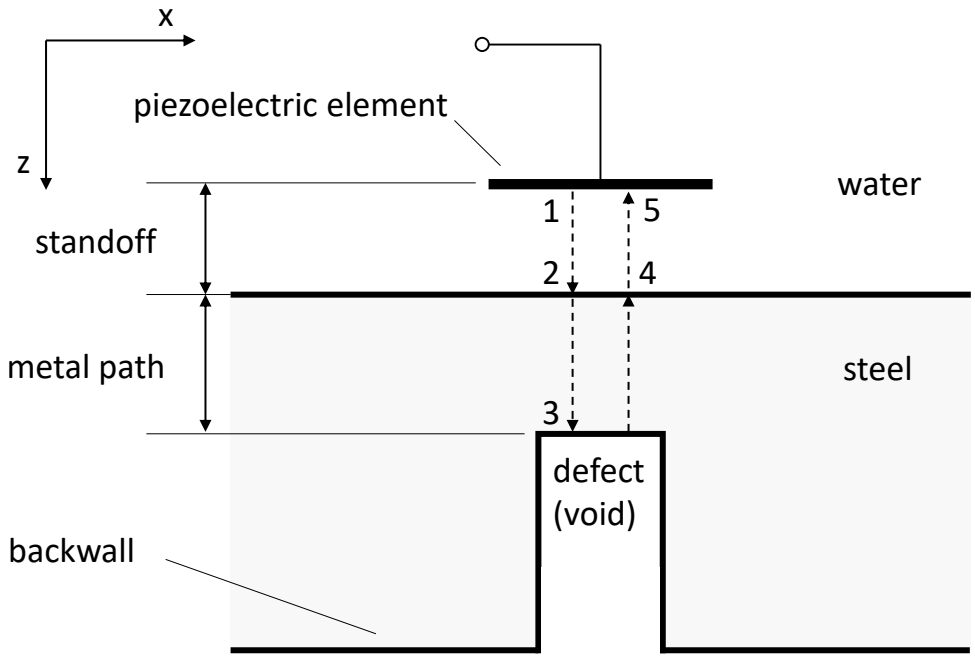

Figure 2.1.5: Diagram of single element pulse-echo immersion inspection

reflection, the defect reflection (if it exists), and the backwall reflection; shown at 1, 2, 3 and 4 respectively.

For the purposes of modelling an ultrasonic inspection system as a collection of Linear Time-Invariant (LTI) systems in the frequency domain, Schmerr [1] divides the steps of an inspection into discrete transfer functions. Even when not describing this particular modelling technique, it is a useful representation for understanding the inspection method.

The transfer function between the ideal negative square wave input and the oscillation produced at the probe face can be referred to as the system function T_{sys}, which can be extended to include the response of the pulser electronics and cable attached to the probe. Acoustic wave propagation, and any alteration to the bulk waves encountered is encapsulated in the acousto-elastic transfer function T_{a}. This study assumes that T_{sys} can always be reliably measured for a given inspection scenario. There is therefore no attempt made in this study to model T_{sys}. From this point forward, it is assumed that the effects of T_{sys} can be measured and accounted for, and stay constant for a given inspection e.g. the same

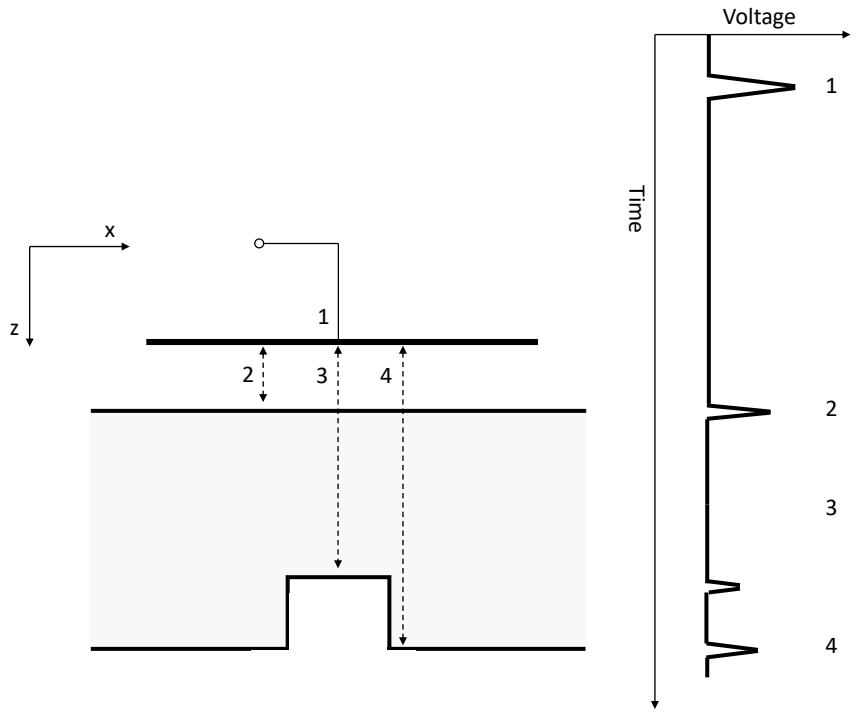

Figure 2.1.6: A-scan interpretation for immersion inspection. A diagram of the inspection setup is shown on the left, with the corresponding A-scan indications shown on the right.

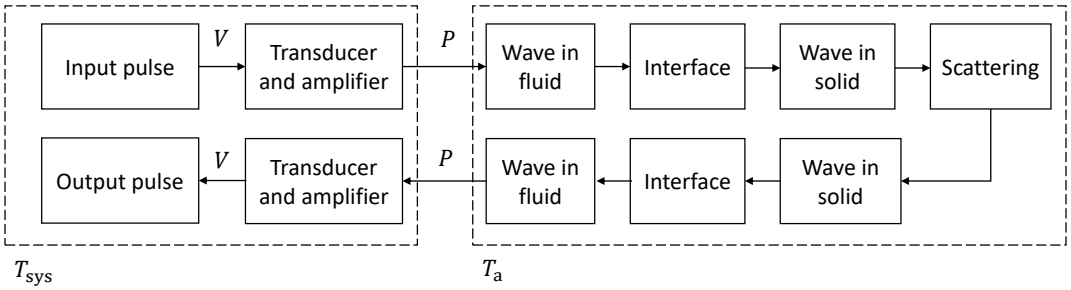

Figure 2.1.7: Systems diagram showing stages of pulse-echo inspection. Subsystems T_a and T_{sys} are shown. Letters V and P indicate voltage and pressure inputs respectively.

pulser setup is used when comparing results.

T_a can be decomposed into two separate parts: the beam part, and the scattering part.

Ray-like propagation is a high-frequency approximation, and assumes that the wave and field properties of the travelling energy can be ignored. This is valid for the frequencies used in ultrasonic NDE when analysing wave propagation through smoothly changing curved interfaces. For interaction with defects, the

dimensions involved are much closer to that of the wavelength, and therefore diffraction plays more of a part. Furthermore, defects have sharp edges from which new mode conversions can emanate.

Figure 2.1.8 shows the scattered field from a longitudinal plane wave perpendicularly striking a disc-shaped reflector. The incident wavefront is distorted, with transverse and longitudinal waves reflected from the defect, similar to reflection at a boundary. Additionally, Rayleigh waves are generated, travelling in both directions along the surface of the defect. These are converted at the edges to longitudinal and transverse waves known as edge waves.

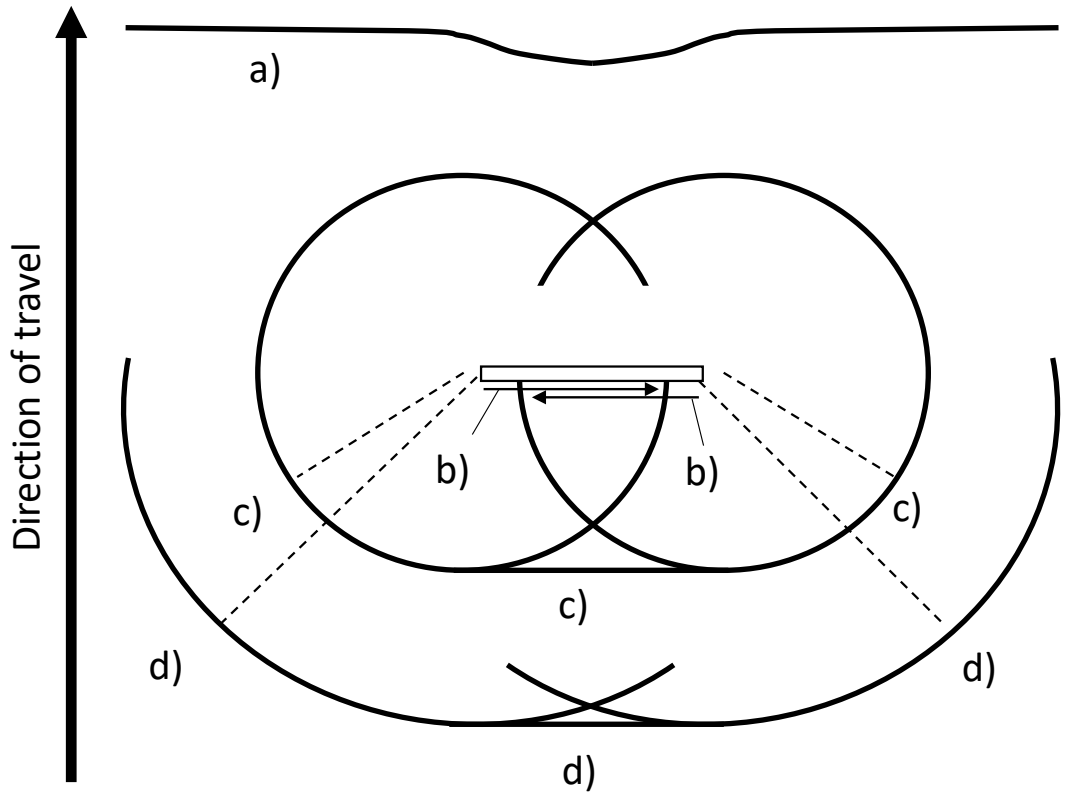

Figure 2.1.8: An L-wave travels from the bottom of the figure, and continues upward with a distortion in its wavefront a), after interacting with a disc-shaped reflector (indicated qualitatively in this diagram). Rayleigh waves b) are produced at the surface of the FBH and travel along the incident surface. Reflected T-waves c) and L-waves d) travel back towards the transducer. Adapted from [2].

The influence of λ on the scattered field from a disc-shaped reflector is illustrated in 2.1.9, where it can be seen that the directivity pattern of the reflected energy varies drastically from $d_{\text{flaw}} = 2\lambda$ to $d_{\text{flaw}} = \lambda/2$. For NDE methods of imaging that assume point reflectors, it is therefore important that f_{c} is chosen such that

$\lambda/2 > d_{\text{flaw}}$.

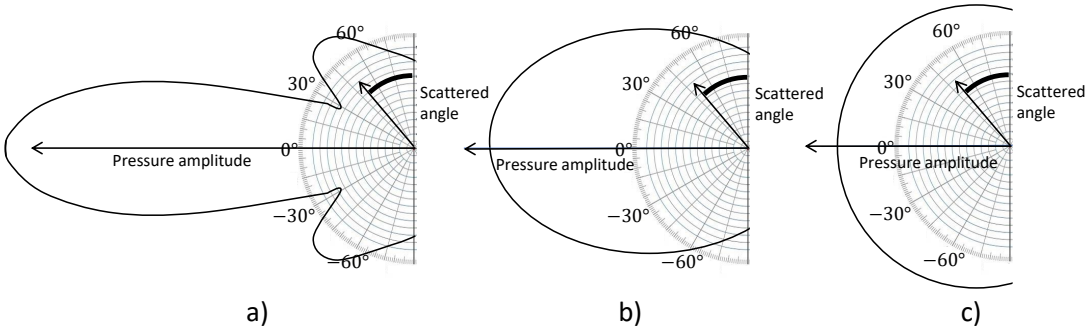

Figure 2.1.9: Change in longitudinal wave scattered field for a disc reflector of size a) 2λ, b) λ and c) $\lambda/2$. Adapted from [2]. The distribution of pressure amplitude with angle changes dramatically for disk reflectors between these two sizes. Predicting this is one of the challenges of modelling a disc-shaped reflector.

For immersion inspection through a flat interface, the beam can be calculated by performing ray-tracing to each point and considering attenuation effects, including the transmission coefficient. The modelled beam profile in steel, obtained by an unfocused SE transducer with a standoff in water of 203 mm, is shown in Fig. 2.1.10. The standoff distance in this case is chosen to be identical to the focus length of the focused probe for comparison purposes. Side lobes - regions of sensitivity off of the probe axis - can be seen. It is important that information from the side lobes does not adversely affect the ability to size flaws. The -6 dB region marks the limits of the main beam, for the purposes of determining ultrasonic coverage for the inspection technique under review.

The incident pressure is therefore determined by the transducer position, surface shape, and material properties. Assuming reciprocity for SE probes, the reception of energy follows the same beam pattern as for transmission of energy.

For small, circular flaws, with faces perpendicular to the direction of the sound beam, and assumed to have a reflectivity of unity, the scattered energy is proportional to the ratio between the flaw diameter and transducer diameter. In practise, the relationship between flaw signal and size is determined by the creation of a Distance Amplitude Correction (DAC) curve, to take account of any variations introduced by the material. Targets of a known size are drilled into calibration blocks representative of the component material properties. The DAC then allows the sensitivity of the practical pulse-echo inspection setup to be quantified at different material depths.

This is illustrated in Fig. 2.1.11. For a probe situated at $z = 0$ at the centre of

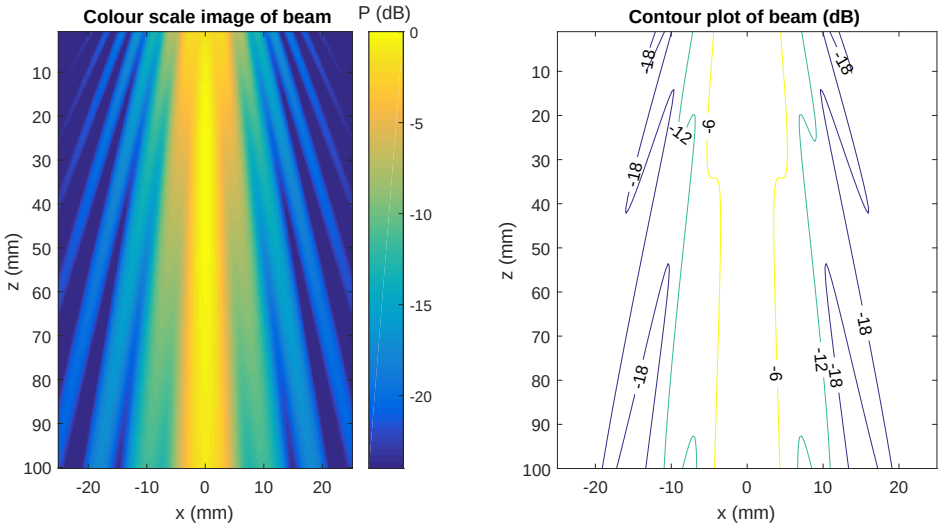

Figure 2.1.10: Beam profile for 10 MHz transducer in steel, with diameter of 12 mm and focal distance (in water) of 203.2 mm, where z = 0 shows the interface position. Beam profile simulated using `ls_2Dint` from Schmerr [1]. P is pressure amplitude of the beam, log normalised with reference to the maximum.

a calibration block shown on the top axis, a calibration peak signal is obtained with the amplitude of the solid black line on the bottom axes. Interpolating these calibration peak signals (usually with a third-order polynomial) results in the DAC curve. The curve can then be used to size defects, provided these defects are still significantly smaller than the -6 dB beam width at the required depth of the material. Sizing by this method assumes that the beam strength is even across the width of the defect.

In Fig. 2.1.11, the dotted line shows a response obtained from an unknown defect A_{flaw}, superimposed on the DAC production axis at the bottom. Assuming a constant value across the beam, reference sensitivity can then be used to evaluate the size of A_{flaw} using

$$A_{\text{rel}} = 40 \log \frac{d_{\text{flaw}}}{d_{\text{FBH}}} \tag{2.12}$$

giving

$$d_{\text{flaw}} = 10^{\frac{A_{\text{rel}}}{40}} d_{\text{FBH}} \tag{2.13}$$

where A_{rel} is the indication amplitude relative to the reference sensitivity line.

This assumes that the reflector is based in the far-field of the transducer, and acts

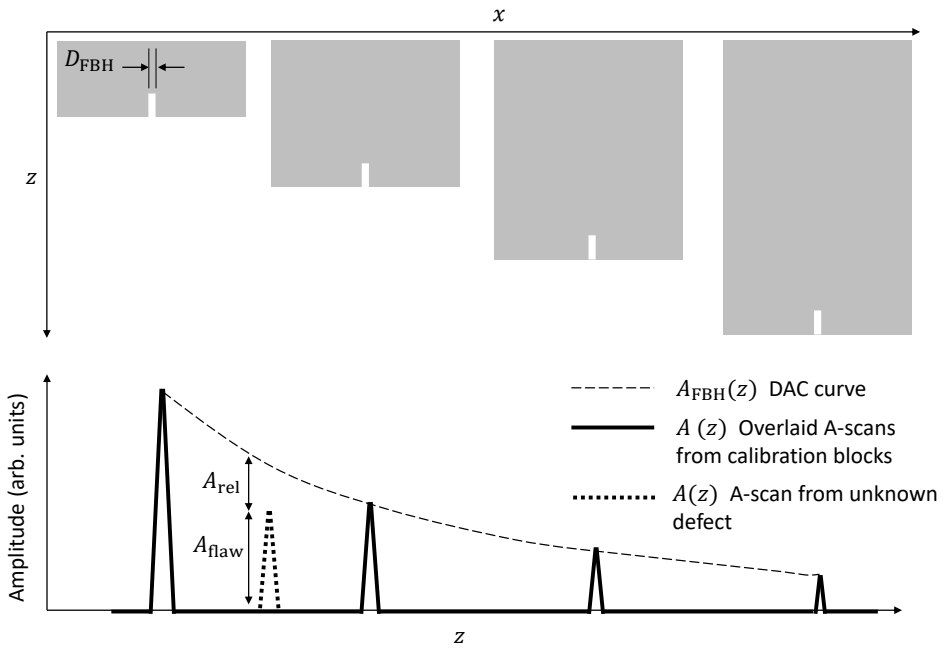

Figure 2.1.11: Production of a DAC curve using calibration blocks

as a secondary disc-shaped transducer. This expression can be used to predict signal variation with flaw size, but it is only applicable when the element used is much larger than the wavelength, when the distance between flaw and element is large compared to the element diameter, and if the wavelength is smaller than the defect. The formula for the FBH has been shown to be correct when $d >> \lambda$ [14].

DAC curves from test pieces with differently sized FBHs can be used to create distance-gain-size (DGS) curves [2], showing how much gain is required to bring the signal of a given flaw to the same level as a reference reflector. DGS curves have also been modelled for phased array testing [15].

For this example, the DAC curve in Fig. 2.1.11 can be normalised to its peak value, converting it to a DGS curve. With a 0.63 mm FBH as the baseline, a curve plotted using 1.27 mm FBHs would be expected to have approximately +12 dB offset from the baseline, whereas one with 0.31 mm FBHs would be shifted approximately -12 dB from the baseline. Often, flaws are described by their deviation from the baseline rather than their size, so one might hear reference to a "-10 dB indication" from a given experiment.

Sometimes many DGS curves are plotted, using series of blocks with differently sized FBHs, however it is common to use just one flaw at different depths to create a baseline DGS curve. To simplify this study, especially because it involves the

creation of blocks with multiple curvatures as well as depths, a single size of 0.63 mm only has been used for creation of DGS curves and their 2D counterparts, due to its common use in the industrial processes considered.

It should be noted that for values of $d_{\text{flaw}} \approx \lambda$, waves cannot diffract the same way around the FBH as a disc shaped target with the same diameter [16]. The size obtained from the DGS curve is therefore taken as the minimum of d_{flaw}.

Altering the gain can bring up the sensitivity to small defects, but the electronic and structural noise in the reading is also amplified. The signal to noise ratio (SNR) for a given defect size, can be thought of as the limiting factor when aiming for the best inspection sensitivity. To claim an inspection has sensitivity to a defect, the defect indication must be at least 4 dB above the noise level [17] for this case study.

Schmerr developed a sizing method [18] [19] that was more general for sizing FBHs in contact and immersion, not limited to sizing defects in the far field.

A more advanced method of sizing flaws is to find the far-field vector scattering parameter, which indirectly contains information about the flaw geometry [20]. This can be difficult to obtain using a single-element probe, so a simplified approach can be taken by using a best-fit representation of a defect - such as an ellipsoid - in conjunction with the Kirchoff approximation to develop an amplitude sizing method.

2.1.3 SINGLE ELEMENT PULSE-ECHO INSPECTION THROUGH CURVED INTERFACES

Fig. 2.1.11 shows that sensitivity to defects varies with depth. This is due to absorption and scattering within the material, as well as beam spread. For curved surfaces, there is an additional change to the sensitivity related to focusing and steering of the ultrasonic beam. Focusing and defocusing is illustrated in Fig. 2.1.12, where a convex interface defocuses the beam, and a concave interface focuses it. In order for Eq. (2.12) to remain accurate, the DGS must be updated to reflect this.

To determine the DGS for a curved surface experimentally, the process shown in Fig. 2.1.11 must be repeated for every curvature. For forgings with many different radii of curvature, this could result in an impractical number of test blocks and calibration routines.

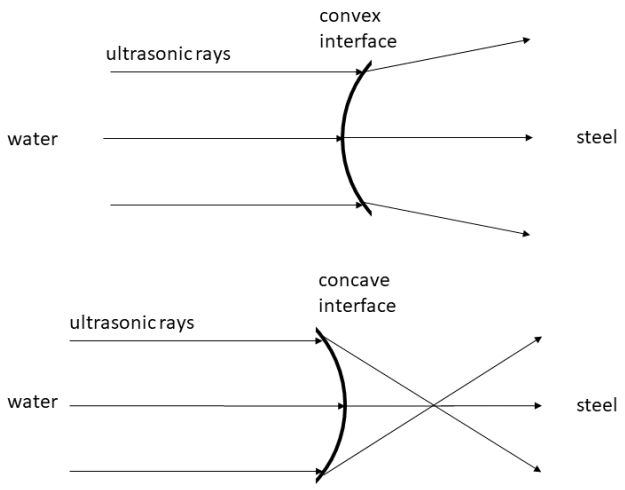

Figure 2.1.12: Travelling from water to steel, a beam consisting of parallel ultrasonic rays diverges following interaction with a convex surface (top), and converges with a concave surface (bottom). Focusing and de-focusing of the beam in this way affects reflections from flaws.

One method to overcome this practical problem is to model the attenuation due to curvature, and predict a curvature correction factor (CCF). An industrially relevant study comparing inspection of FBHs through curve d surfaces was carried out by Gray [21]. Gray modelled pulse-echo inspection through a curved surface for FBHs of 2 mm across at 5 MHz. Limited to only bulk wave propagation, specular reflection, and ignoring attenuation in water and steel, the model showed close agreement with experimental results for 38.4 mm radius of curvature. A modelled CCF was applied to a turbine disc of 25.4 mm radius, where the out-of-plane radius of 356 mm, was shown to give only a $\pm 1.2\,\mathrm{dB}$ difference to the CCF. This shows that modelling to predict variation in the DAC introduced by curvature for disc forgings has been practised for at least two decades. Note the small error introduced by out-of-plane curvature; in this thesis it is assumed that this is a small contributor, and therefore curvature is only considered in the imaging plane.

Improvement of the sensitivity to defects through curved surface can be achieved by using a curved transducer face with geometry matched to the interface, or a flexible transducer [22] [23]. This may be impractical for the automated scanning of a component with multiple radii of curvature, as it would require the use of many different probes, interchanged between scan stages.

The DAC curve produced by the process shown in Fig. 2.1.11 is actually based on the beam strength within the material. It is used with the assumptions that the beam shape around the central axis is the same at each probe position, and that the central axis of the beam is not steered at the interface. Beam strength varies laterally as well as longitudinally, but the lateral variation is simplified by including enough overlap between scan steps to treat the DAC curve as a 1D change within dB limits determined by the overlap. For curved surfaces, the first assumption is made invalid by the focusing and defocusing interface effects changing the beam shape. The second assumption is made invalid by any mean tilt of the surface relative to the probe, changing the beam direction below the interface.

Accurate sizing of flaws must therefore depend on the knowledge of a unique 2D beam profile at every flaw location. This thesis aims to provide an equivalent 2D DAC matrix, developed from a model-based approach, and shows how this can be applied to determine the optimal scan step and forging design for continuously curved shapes. This is different to just calculating the beam profile of the inspection method used, as it takes into account the imaging method used to produce the B-scan - it is referred to in this thesis as a flaw sensitivity map (FSM).

2.1.4 SCANNING AND IMAGING USING SINGLE ELEMENT PROBES

Using the aforementioned approach allows capture of useful A-scan data for a single position. To inspect the entire volume of a complex forging, the probe position must be scanned over well-defined regions, over which a series of A-scans is captured. In Fig. 2.1.13(a), probe positions 1-3 have a planar interface, so the same DAC can be used. In Fig. 2.1.13(b) all have varying interface curvatures, so for a continuous scan, the CCF needs to be updated in every position.

Rather than represent the data obtained from a scan across the flat face on Fig. 2.1.13 a) 1 by a series of A-scans, it is common practise to use a brightness scan (B-scan) representation. For a) in Fig. 2.1.14 the B-scan combines the A-scans by populating a line of pixels with a brightness determined by the amplitude at each point, and plots this at the beam centre locations as determined by the Δx.

Three regions are shown in Fig. 2.1.14, regions i, ii and iii. Scanning a curved part complicates the production of an accurate B-scan. Applying the same scanning

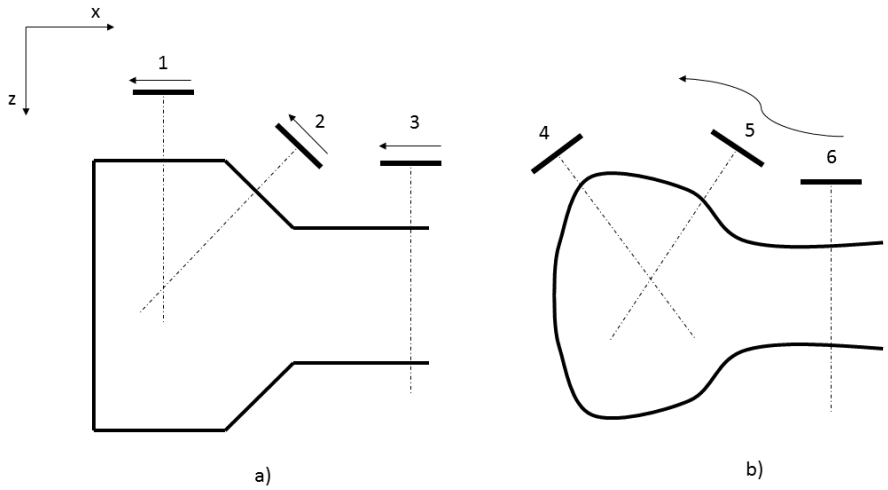

Figure 2.1.13: Multiple probe positions for a) rectilinear and b) curvilinear forgings

pattern from region i to region ii, comprising a fixed Δx and flat scan path, results in unevenly spread spaced beam centres at the part surface, and are also refracted at different angles through the surface. This does not insonify some areas of the B-scan region, and so would obtain poor coverage of region 2. By maintaining probe normality with the curved surface, the effects of refraction are reduced, and by varying Δx, better coverage is obtained for region iii. Note however that the relationship between the A-scan beam centres and the B-scan region is not as regular as in region 1, which will result in a lower spatial sampling frequency when interpolating onto the same regular grid.

The scan spacing for flat-sided components is typically determined by ensuring that the beam width overlsaps at a certain dB value. The case study processes are based on a rule that scan increments must be at one half of the diameter of the probe. For the example shown earlier in Fig. 2.1.10, this produces coverage as shown in Fig. 2.1.15, with 3 mm increments between scan steps. A 3 mm increment is chosen, as the probe minimum -6 dB beam width is 5 mm for Probe C (Table A.4), so this ensures scan steps overlap when the stand off is chosen so that the minimum beam width occurs at the entry point to the component.

A slice of the beam amplitude at a certain depth is referred to as the echodynamic, and shows the variation in sensitivity across the scan. The variation across the beam is only 1.5 dB, so this is factored into any sizing assumptions made using

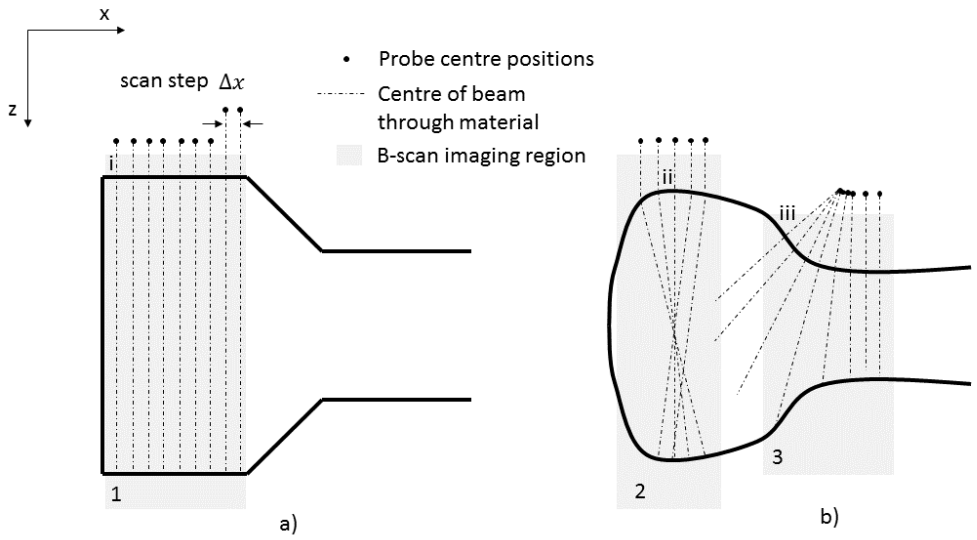

Figure 2.1.14: Demonstration of probe scanning across a) rectilinear, and b) curvilinear forgings, highlighting the additional considerations for creating a B-scan from a series of A-scan acquisitions through a curved surface.

the 3 mm scan step for this application. The variation across the scan could be reduced using a smaller scan step, however this increases scanning duration. The effect of the scan step can be thought of as raising the required gain on the DGS diagram by +1.5 dB, when assuming the worst case flaw position.

For a curved surface, the beam centres are not parallel, as depicted in Fig. 2.1.14 b). The sensitivity will be reduced as the gap between beam centres increases, decreasing the minimum echodynamic value. This means that a scanning system for components with complex geometries should have an adaptive step size. The step size should be chosen so that the coverage meets the required criteria (e.g. no more than 1.5 dB variation at a scan depth of 50 mm from the surface profile).

A B-scan is produced by stacking scanned A-scans together, and produces an image of the flaw showing spatial dimensions. A pixel grid is defined, and each pixel assumes the value of the A-scan closest to that pixel. A C-scan can be created by extracting particular properties from ("gating") each A-scan, and plotting it on a 2D grid of the relevant scan and index directions.

In disc scanning, a B-scan is produced when stacking A-scans circumferentially, and a D-scan is produced when stacking A-scans radially, as shown in Fig. 2.1.16.

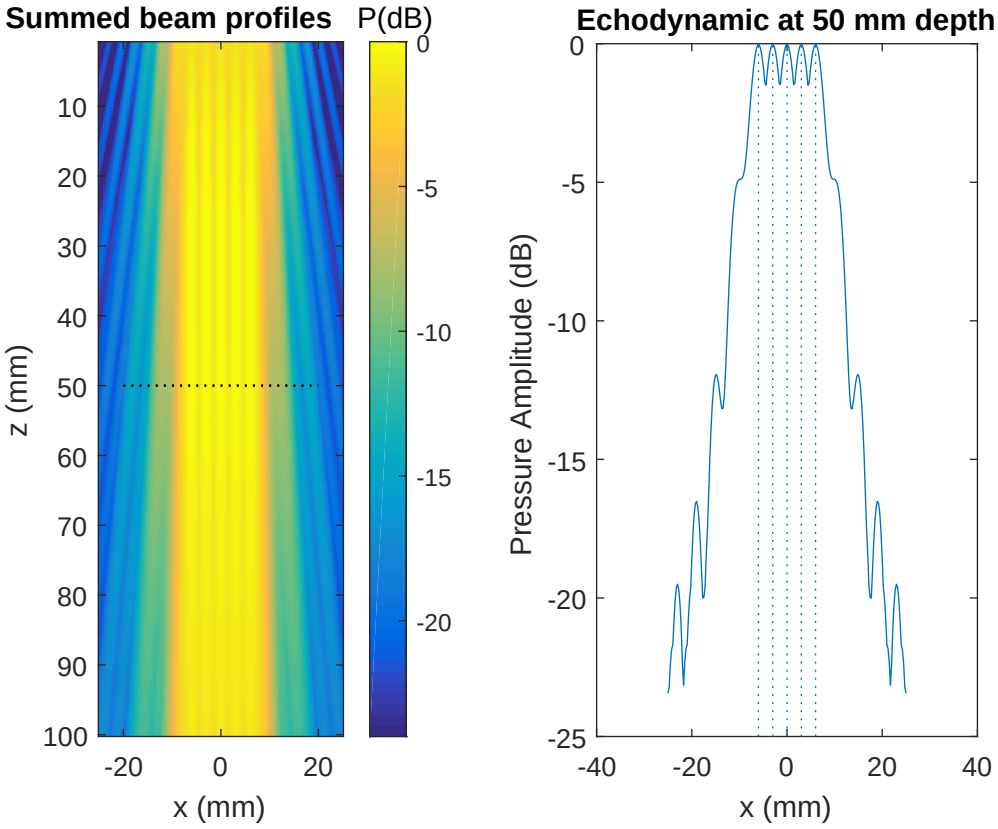

Figure 2.1.15: Coverage of flat-interfaced component using SE transducer in immersion. The summed beam profiles from the scan are shown on the left, and the echodynamic taken from 50 mm depth is shown on the right. The minimum scan amplitude is - 1.5 dB for this scan spacing, taken from the centre of the echodynamic curve. P is pressure amplitude of the beam, log normalised with reference to the maximum.

The 1000 gates technique [24] utilizes knowledge of the disc-cross section to aid automation of disc inspection. This works by applying a 2D gate to ultrasonic scan data as it is collected. In this way, each A-scan is gated for the full forging profile depth as it is collected. This innovation was a useful step forward, as without it, a fixed size time gate would trigger from thinning geometry, even when no flaw was present. Once data is correctly gated, a meaningful C-scan is produced by extracting the maximum A-scan amplitude from between the gate limits. This shows the flaw extent in the step direction, as well as the scan direction. Important features, such as the proximity of indications in a "cluster" can be evaluated.

Measurement of a calibration FBH is achieved by setting appropriate gates for the calibration block thickness, and then performing a C-scan. This will generally produce a C-scan with multiple pixel values, so the peak value is extracted from

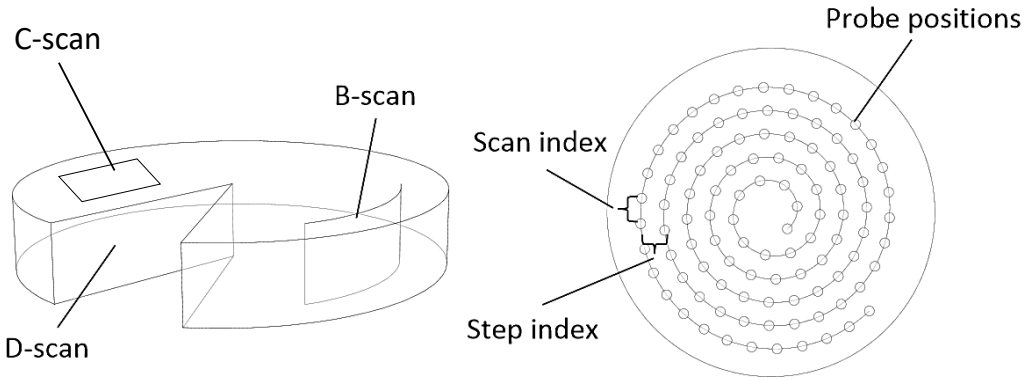

Figure 2.1.16: B-scan and D-scan definitions for a spiral disc scan

the flaw indication on the C-scan. The amplitude is then added to the appropriate part of the DAC curve.

The link between scanning and ultrasonic imaging has been shown in this section. Crucially, the peak value of a FBH depends on the successful production of a C-scan. Additionally, an automated scanning system must be able to follow component curvature with the probe normal to the surface. The ability to alter scan step size is also important. The next section introduces the use of automated scanning systems to implement these requirements.

2.2 ROBOTIC SCANNING SYSTEMS FOR ULTRASONIC NDE

Automated ultrasonic inspection systems often come in the form of application-specific scanning tanks. For example, the LS200 series by Scanmaster [25] is purpose built for the inspection of jet-engine discs, with integrated inspection software. This system can allow the import of CAD files, and the execution of complex automated scan paths.

Alternatively, general-purpose robotic manipulators can be used for automated NDE [10, 26–32]. The idea of using these, rather than bespoke inspection sys-

tems for NDE are manifold. Of particular interest is the increased flexibility these systems possess - for example, allowing re-configurable gantry systems for inspection of large composite parts [27]; or movement of the component instead of the scanner [33] to improve speed; or for the mounting of laser ultrasonic systems [34]. Integration with computer vision systems can enable complex handling operations [35], which could be used to link manufacutring processes with inspection.

Components that do not have accurate CAD files are difficult to scan by use of an ultrasonic system. A basic mode of operation is the "point-and-teach" mode, whereby an operator manually drives the robot to a selection of points on the surface of a part.

If the point-and-teach method were used for one of the applications considered in this thesis, the scanning of an uneven plate, the manual burden would quickly become unacceptably large.

Assuming an area of 0.5 m by 1 m, and a probe width of 0.05 m, ten passes of the probe would be required to cover the surface of the uneven plate. For each of these passes, the probe must be adjusted in terms of standoff and tilt at several points in order to follow the curves of the part.

Assume at least ten sampling points along each path are required for an acceptable result, and that the time taken for the operator to drive the robot into position and carefully angle the probe is around thirty seconds.

As no two plates are exactly alike, this process needs to be repeated for every component. Using this rough estimate as a lower bound, at least fifty minutes would be required to set up the scan for each plate. As scan time for each plate is currently an hour, any speed improvements would be marginal. Additionally, the process would place a large burden on the operator, and is likely to be error prone.

Instead, a more automatic approach is taken in this work. CAD geometry can be measured by using an appropriate metrology system, such as structured light projection [36]. This method can also be automated [37], providing a surface representation more quickly than the point-and-teach method. Movement of the probe across the surface must be applied in a carefully controlled pattern to create a C-scan giving appropriate coverage. Either a spiral pattern in the case of a rotationally symmetric part, otherwise a raster pattern. Any aberration in the scan steps must be controlled within the beam coverage requirements, as

demonstrated in Fig. 2.1.15.

Generation of the scan pattern is referred to as path-planning. Computer-aided machining (CAM) software can be used to generate the scan pattern, and translate it to a program written in the robots native control language. This is known as offline path planning (OPP) [38], and has been used to generate raster patterns for robotic scanning of curved components at the University of Strathclyde. Commercially available CAM software [28], and a custom-built MATLAB toolbox [10] have been applied to the NDE path-planning problem. This approach allows application of new techniques, for example the use of twin cooperative robots to perform through transmission ultrasound [39].

There is a middle-ground between purchasing expensive commercial software, and developing completely bespoke solutions. An architectural CAD program called Rhino (Rhinocerous 3D, Robert McNeel & Associates) can handle many common file formats, and can be extended through its scripting language. One such extension is the visual programming language Grasshopper (Grasshopper 3D, Robert McNeel & Associates) previously used for parametric geometry generation in architectural applications [40, 41]. The unique aspect of this approach is that the language consists of pre-programmed blocks, allowing the parametric generation and manipulation of CAD surfaces and paths. This native parametric capability allows for complex 3D transforms to be performed using a few building blocks of code.

The Association for Robotics in Architecture used Grasshopper to create KUKA|prc [42], an OPP program for architectural applications. This has the flexibility of a full programming language (Grasshopper), the compatibility of an established CAD program (Rhino), and many of the features of commercial path-planning software (KUKA|prc). Previous work in milling applications [43] shows that it can be used for similar applications to Mastercam (Mastercam CNC Software inc.), the OPP software used in Morozov [28].

Considering time and cost limitations of this EngD project, KUKA|prc was chosen as the most effective platform for development. This was used together with general purpose KUKA manipulators, with further details described in chapter 3. The underlying philosophy was to create a method to generate scan patterns based on UT limitations, as well as providing a platform to visualise UT results, in the same package.

In this section, the need for OPP has been explained in the context of the ultra-

sonic scanning requirements. The ultrasonic inspection requires that the toolpath is normal to surface, and that raster scan width can be adjusted based on modelled beam width at a given probe location. Furthermore, this toolpath should be created automatically, given an irregular surface input. It was argued that these requirements could be fullfilled by use of KUKA|prc. This can ensure optimal probe positioning for single element inspection of curved components.

With a scanning system in place that ensures the probe is in the optimal position, the next step is to optimise the probe for the application. Considering that the surface profile "seen" by the probe at any position is of variable curvature across the probe aperture, an adaptive solution is required. Phased array ultrasonic transducers can focus and maintain sensitivity through curved surface, so provide a potential improvement for a given scanning system. These are reviewed in the next section.

2.3 ULTRASONIC ARRAY TRANSDUCERS FOR INSPECTION OF CURVED SURFACES

2.3.1 TYPES OF PHASED ARRAY TRANSDUCER

Ultrasonic arrays consist of many small transducers, referred to as elements, which can be fired independently. A set of time delays can be applied to each element, and using the principles of geometric optics [44], synthesise a new summed wavefront.

Transducer arrays are most commonly implemented in 1D, 2D or annular element configurations. Linear 1D arrays consist of multiple elements with length much greater than their width - approximating ideal line-sources. These transducers can focus in an imaging plane directly below the probe - therefore they are suitable for focusing through surfaces with curvature primarily in this 2D imaging plane. Two-dimensional arrays can focus through a surface with curvature in both directions, whereas annular arrays are limited to altering depth of focus. Many other array configurations exist, designed for specific inspection geometries, or for enhanced characteristics such as noise suppression

The element layout for annular, linear and 2D matrix arrays is shown in Fig. 2.3.1.

SE transducers only have a single focal point for a given probe position, whereas phased arrays can focus anywhere in their imaging region.

For an annular array, delay laws can be applied to shift the focal point to multiple depths, thus ameliorating the tradeoff between focal length and peak sensitivity shown in Fig. 2.1.2. The resulting DAC produced would have a higher average signal, and therefore better sensitivity through depth versus a SE transducer. It cannot move the focal point laterally and cannot perform an electronic B-scan of surface profile.

For a linear array, focal laws can be applied to steer the beam inside the focal plane, as well as focus at depth. 2D matrix arrays allow beam steering and focusing in 3D, further improving signal, and granting ability to correct for curvature in two planes. Other options such as 1.5D arrays seek to achieve some of the out-of plane steering capability of a 2D array for less complexity [45].

Two different acquisition modes used with transducer arrays are phased array, and full-matrix capture (FMC).

Phased array inspection is the term used when elements are excited with a pattern of delays amongst them, and waves emanating from the elements propagate through the material in parallel. This creates a desired wavefront shape in the inspection material through superposition. For example, an appropriate delay pattern can result in a convergence of waves at a point in space and time, focusing the ultrasonic beam.

In contrast, FMC does not create a beam focus at acquisition time. Instead, elements are excited and waves propagated in series. For each single-element that is excited, the received signal at every array element is recorded. This data is saved, and is referred to as the full matrix. Similar focusing to phased array techniques can then be achieved by post-processing the full matrix, applying virtual delays corresponding to the physical delays used in phased array inspection. FMC techniques are discussed further in Section 2.3.3.

For a matrix array with a similar density of elements to that of a linear array, the computational hardware and software requirements to generate focal laws and process received signals increase dramatically. Additionally, matrix arrays are not widely used in industry at present. Linear arrays are however widely available, and commonly used. For this study, it is asserted the acquisition position can always be chosen to minimise out-of-plane curvature, and that out-of-plane curvature is minimal. For these reasons, a 1D linear array type is chosen for

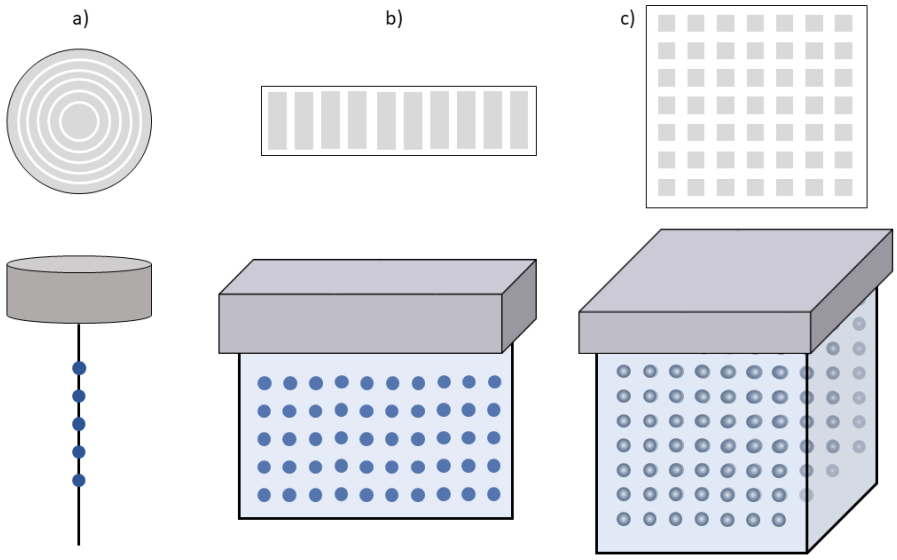

Figure 2.3.1: Diagram of element layout for three main types of array probe. Top row shows element layout, and bottom row shows possible focal point locations. Annular array with focal line shown in a), a 1D linear array with focal plane shown in b), where dots symbolise focal cylinders, and a 2D matrix array with focal volume is shown in c).

evaluation of curved surface inspection.

Arrays with flexible elements [46], or using a coupled conformable wedge [47] have been used to improve sensitivity through curved surfaces. These methods require component contact, either with the probe face, or the membrane wedge.

Deployment of contact techniques in high-speed automated scanning applications, such as those considered in these studies, may result in rapid wear. Laser ultrasonic FMC [48] offers a non-contact solution, however does not scan quickly enough for the proposed application.

The work in this thesis assumes that effect of curvature in the second plane of a component is negligible and therefore 1D arrays are applicable. A typical forging shown in Fig. 2.3.2 has an out-of-plane curvature of 150 mm; large compared to the 5 mm elevation of the array element. This will nevertheless have an effect, and future work should consider use of 2D matrix arrays, especially for forgings with a small inner diameter.

In the passive plane of a flat-faced linear array, there is a beam width with a natural focus determined by the width of the transducer. In this direction, the profile has a similar shape to Fig. 2.1.10. Some linear arrays have a face curved

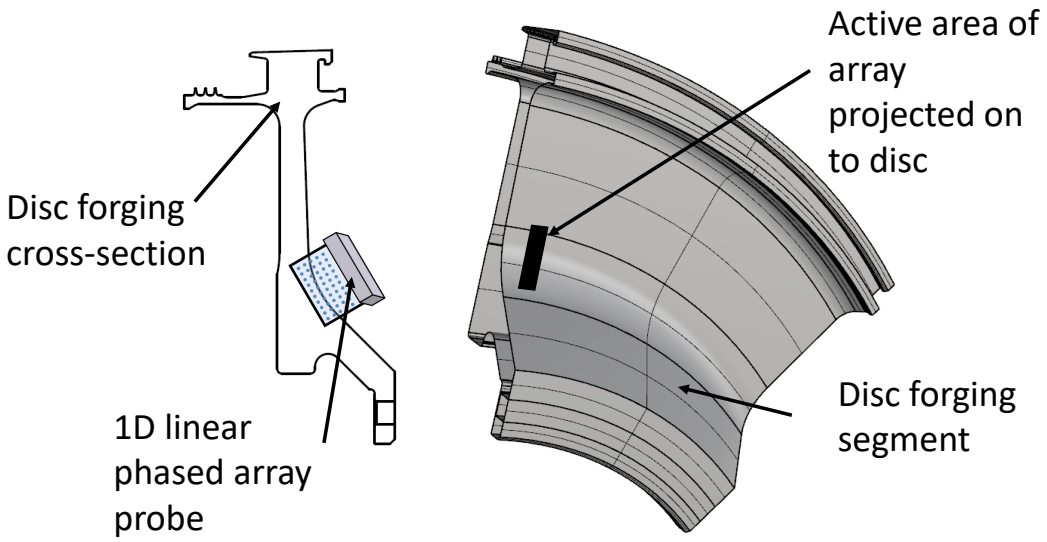

Figure 2.3.2: A typical forging profile. The phased array probe is shown in context, on the left in cross section next to the part cross section. On the right, the area projected from the front face of the array onto a disc forging is shown.

in the passive direction, which optimises this beam profile for a given depth. This study avoids introducing a fixed focus on the passive plane, to solely explore the effect of curvature on the active plane of the array. It should be noted that passive plane curvature could improve the sensitivity of the results gained in this study; depending on required depth of the application.

Business objective 2 demands that transducer efficacy through curved surfaces is quantified. In this thesis, a process is produced for a 1D array, which could be extended to other array configurations. The emphasis is on characterizing the performance of a given array through curved surfaces, not on optimizing an array design for a given application. For this reason, an array that was suitable for the task, but not perhaps optimal, was chosen. A 10 MHz, 32 element linear array was selected, and is characterised throughout the thesis. There are a number of reasons for this choice. Firstly, 10 MHz is the central frequency used in the SE inspection this work emulates. Secondly, 32 elements provides a large enough aperture for measuring a curved surface, but keeps the computational burden low. Thirdly, this type of probe was readily available at Rolls-Royce, and stakeholders were keen to test its performance.

2.3.2 LINEAR PHASED ARRAY IMMERSION INSPECTION

As waves propagate, a wavefront is created from multiple waves that are in phase at a particular point in time. It usually forms a complex shape, but is often represented by a simplification such as plane waves or cylindrical waves. Amplitude and pressure can vary at different points on the wavefront, only the phase is the same [2, Ch. 1].

According to the Huygen's-Fresnel principle [49], any point on a wavefront can be thought of as a new spherical wave source. This is demonstrated in Figure 2.3.3. Point sources at different locations, radiating simultaneously, produce spherically curved wavefronts. These sum to create a total wavefront, with a larger overall radius. Were the point sources arranged on a differently shaped curve, this total wavefront would change shape accordingly. The principle can therefore be used to reconstruct wavefront shapes emitted by an aribitrary radiating element. Note that it is the change in phase that determines the wavefront shape, so that introducing a time-delay between elements can emulate the effect of altering their position in space.

Phased arrays thus exploit Huygen's principle to produce arbitrarily shaped wavefronts, by programmatic application of time delays.

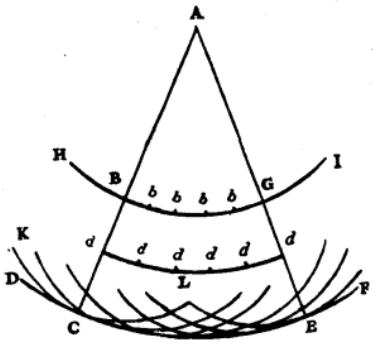

Figure 2.3.3: Point sources displaced in a curve, producing wavefronts which combine to re-create the curve of their origin. Taken from Huygens' notes [3].

An ideal array would have an infinite number of infinitesimally spaced elements, each able to independently generate an arbitrary waveform and receive reflected signals [50]. In reality, array elements have a finite size, which affects their ability to create completely arbitrary waveforms. An ideal element would produce a cylindrical wave, and thus give a circular directivity pattern. Manufacturing

limitations result in a finite width, creating a non-circular directivity pattern [51]. For example, a 0.3 mm wide element excited at 10 MHz gives the beam patterns shown in Fig. 2.3.4.

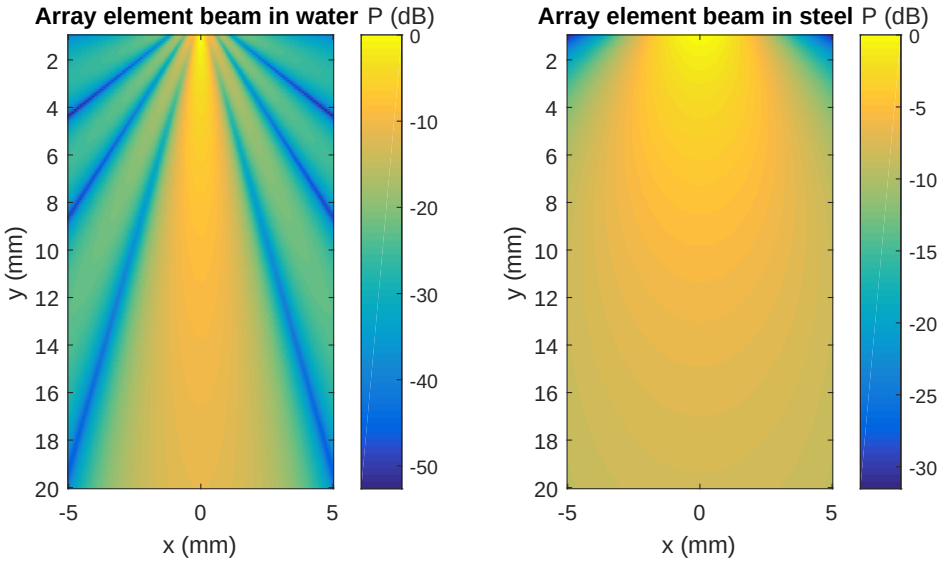

Figure 2.3.4: Beam profile for a single array element. Shown in water (left) and through a steel interface with a 10 mm standoff in water. Simulated using function `rs_2Dv` from [1], with an element width of 0.3 mm, a frequency of 10 MHz, and speed 1500 m/s for water, and 6000 m/s for steel. P is pressure amplitude of the beam, log normalised with reference to the maximum.

By applying a delay law to array elements, the focal point can be adjusted. In immersion inspection, the correct application of focal laws can create a beam focused at a particular point in the component. This process is known as beam-forming, with an idealized 2D example given in Fig. 2.3.5. The greatest ultrasonic intensity can be achieved at this point if the energy from each element arrives simultaneously. To achieve this, the distances travelled through the fluid and solid media, l_a and l_b can be used with the material velocities c_a and c_b to find the overall time-of-flight (ToF) from the equation.

$$l_\mathrm{a} = \sqrt{(x_\mathrm{I} - x_\mathrm{el})^2 + (z_\mathrm{I} - z_\mathrm{el})^2} \tag{2.14}$$

$$l_\mathrm{b} = \sqrt{(x_\mathrm{p} - x_\mathrm{I})^2 + (z_\mathrm{p} - z_\mathrm{I})^2} \tag{2.15}$$

$$\Delta t_\mathrm{n} = c_\mathrm{a} l_\mathrm{a} + c_\mathrm{b} l_\mathrm{b} \tag{2.16}$$

where t_n is the delay required for element n.

Refraction points are calculated by using a combination of Snell's law and Fermat's principle, as illustrated in Section 2.1.2 and Eq. (2.6). Assuming $c_{\mathrm{a}} < c_{\mathrm{b}}$, there is a larger difference between Δt_1, Δt_2 and Δt_3 for the curved interface case, resulting in a different delay law profile as shown in step 2.

Firing the elements with the delays calculated in step 2 creates an overall wavefront with the desired curvature. These wavefronts are shown at time t_1 to highlight their different profiles in water, and at t_2 to demonstrate that they converge similarly at the focal point in the test piece.

Note that the θ_{i}, are different for curved interfaces, reducing the energy transmitted to $P(x, z)$ by the amount given by Eq. (2.9).

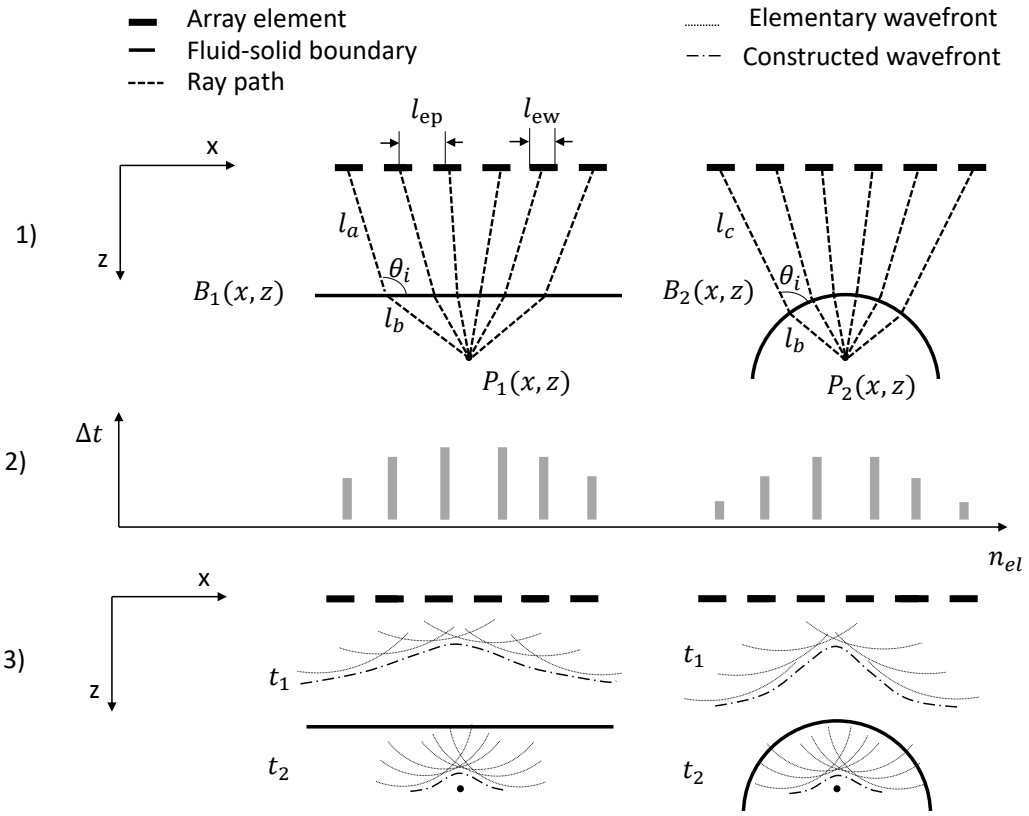

Figure 2.3.5: Phased array beamforming procedure for point focus through flat interface (left) and curved interface (right), where B is the shape function of the interface. In step 1, the distance between each element centre and the focal point is calculated. In step 2, the delay law is calculated, used in step 3 to generate a wavefront that will converage at the focal point.

An example of two array beam profiles, through a flat interface, is shown in Fig. 2.3.6. This is the same inspection problem as considered with SE probes in Fig. 2.1.10, using Probe B (see Table A.3), focused 7.5 mm below the interface.

Note that a focal point can be chosen at a given location $P(x, z)$ in the imaging plane, enabling an angle scan to be performed electronically. The existing inspection takes three passes with an SE probe to achieve coverage from ± 20 deg, therefore the array technique makes it possible to replace two physical scanning stages with electronic scans.

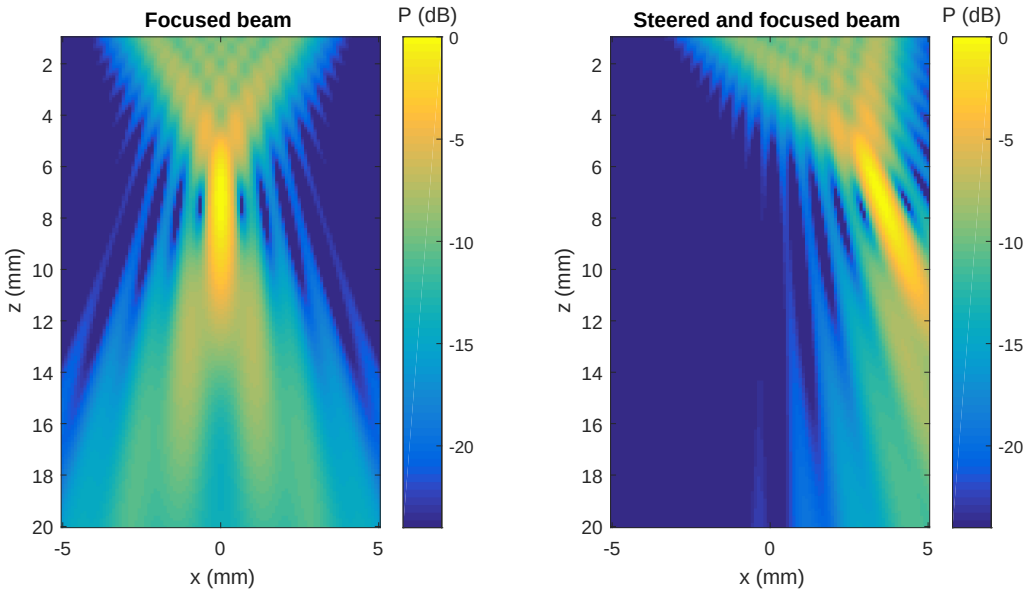

Figure 2.3.6: Beam profile obtained for a 32 element array, at 10 mm standoff to a steel interface, focused at 7.5 mm depth in the steel. A focused beam at 0 deg (left), and at 20 deg (right). P is pressure amplitude of the beam, log normalised with reference to the maximum.

The areas of increased sensitivity off of the central axis are called side lobes. The influence of side lobes can be suppressed by filtering out signals returned outside the known valid directivity range of the central lobe. Failure to do this can result in false-positives returned from features that do not intersect the central axis from the probe face.

Arrays introduce additional complexity to the scanning-positioning-curvature correction problem, and therefore add to the requirement for inspection modelling. Array elements can be modelled using finite elements, Huygen's models, or more advanced semi-analytical models (e.g. the commercial package CIVA) [52]. Finite element models provide the ability to model more complex geometries, but are more computationally intensive. Huygens models relies on the summation of point sources at the transducer face. An approach based on the Huygen's approach, but modified so that array elements are modelled as point sources with a given directivity is presented in Drinkwater [50]. This shows a method to im-

plement beam and point-spread-function modelling for different modes of array acquisition, especially applicable to a 2D simulation for an array inspection of small scatterers.

Beamforming has been used in the medical [53, 54] and NDT fields [55–57] to correct for the effects of unknown surface aberration when conducting pulse-echo ultrasonic methods. A point target situated in the test material is used to determine the effect of the interface, and then the delay law is updated to take these paths into account. In Chakroun [55], this is referred to as the time-reversal mirror approach. The benefit of this is that knowledge of the exact surface representation is not required a-priori. One drawback is that the inspection is only focused at a single point directly beneath the transducer, and another is that it requires the signal from the defect prior to time-reversal to be strong enough for detection. A defect with too weak a response to the inital pulse would not provide the necessary signals to set up the time-delays required to strengthen the signal.

This can be improved by using the reflection of the front surface in immersion to determine the focal laws. Conformable arrays have been shown to give good sensitivity to complex components [58]. The same principles can be applied to immersion inspection, using automated detection of the surface curvature and updating focal laws to compensate for the change in sound path length [59].

Similar to the case in Fig. 2.1.2, the focus at $P(x, z)$ comes at the expense of a reduced on-axis pressure deeper in the material. This can be balanced by firing a planar beam, however the benefit of increased sensitivity at the focal point is lost. Another technique, called the Total Focusing Method (TFM) moves $P(x, z)$ to every location in the desired B-scan image. This maximises the sensitivity of the beamforming technique throughout the depth and breadth of the imaging plane.

2.3.3 FULL-MATRIX CAPTURE ACQUISITION AND TOTAL FOCUSING METHOD

The ability of TFM to focus at every point in the imaging plane is an advantage for the proposed application in this study. It removes the variation in sensitivity through depth that occurs with a single focal point. Super-resolution algorithms such as MUSIC [60] can provide better performance in some scenarios, but perform less well when SNR $< 20\,\mathrm{dB}$ [61] and are not considered. TFM

outperforms all other beamforming algorithms [62], and has been shown in previous, industrially-applied work to improve signal sensitivity through irregular surfaces [9] [63]. It has also been implemented in off-the-shelf systems [8].

This makes it an excellent candidate for use in an automated scanning system for curved components. The primary concern from Rolls-Royce was the ability to ensure that it can be used as part of a controlled and understood inspection procedure. An example of such a procedure is that of automated rectilinear forging inspection described in Section 2.1.2. The most important aspect of this is the ability to link the amplitude of an indication - in this case a gated peak within an A-scan - to the likely size of a flaw. This relies on a good understanding of the on-axis pressure within the depth of the material, constructed using a DAC curve. This study sets out to produce something similar to a DAC curve for the TFM.

To perform TFM, the full-matrix capture (FMC) acquisition mode must be used. While PA inspection can be characterised in a similar fashion to SE techniques with equivalently focused beams, FMC has fundamentally different behaviour. The effects of probe characteristics when using FMC and TFM has been characterised [64], and FMC-specific calibration methods for probes have been proposed [65] [66]. Multiple skips can be incorporated into a TFM image, each with an associated sensitivity [67], with a different effect on different types of flaw [68]. In this thesis, only the direct path longitudinal TFM view is considered.

Producing an equivalent to the DAC curve requires careful consideration of the mechanisms behind the technique. In this section, TFM inspection is discussed, broken down into constituent process, and their likely effect on flaw sensitivity is discussed.

FMC produces an A-scan for every transmit-receive combination between elements in a given array. This data can then be used to re-create the results of any linearly beamformed A-scan, without requiring new data capture [62].

Fig. 2.3.7 illustrates the algorithm behind the total focusing method. Consider the three element array shown in the figure. FMC is performed by transmitting on element 1 and receiving on elements 1, 2 and 3. The top three A-scans on the right of the figure illustrate the expected response - the initial pulse is recorded, followed by a weaker reflection from the hole. The data is likewise recorded for transmits on element 2 and 3, together forming the $n_{\mathrm{el}}^2 = 9$ A-scans of the full matrix.

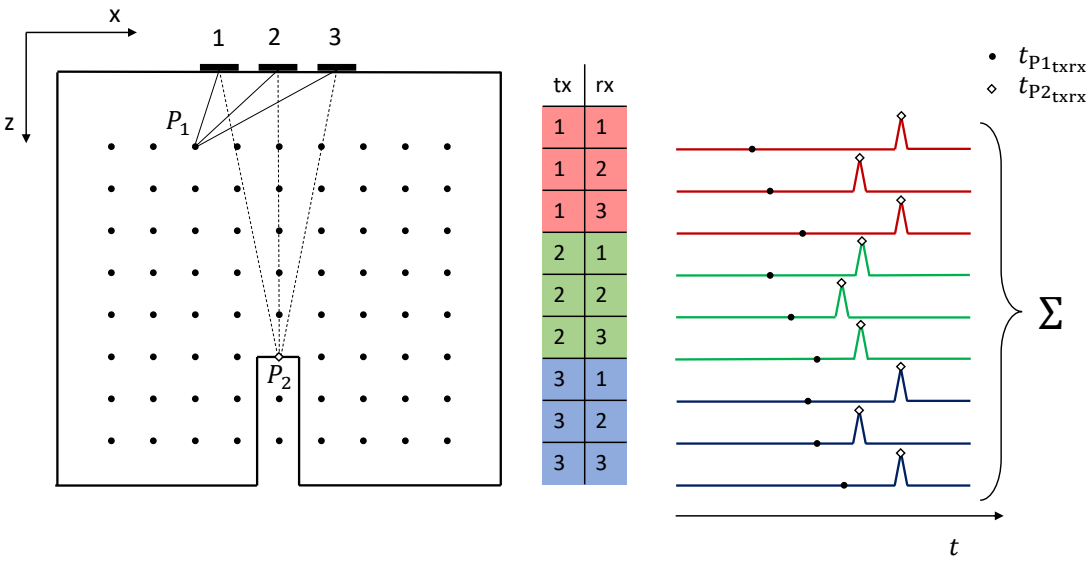

Figure 2.3.7: Illustration of TFM for contact ultrasonic inspection. Left shows a depiction of the test piece with pixel locations through the test piece volume. Right shows how the time-of-flight is used to calculate which part of each A-scan is relevant to the current pixel, by summing corresponding values of the n_{el}^2 A-scans.

For the TFM, a grid of pixels is assigned covering a planar region of the component to be inspected. The brightness of each is calculated in turn; take pixel P_1 for example. Its brightness is determined by the following steps. Firstly, the propagation distance between element 1 and P_1 is calculated, and then the return journey from P_1 to element 1 is added to this, giving the full pulse-echo return distance for tx = 1, rx = 1. Secondly, knowledge of the material velocity is used to convert this distance to a propagation time, from which the corresponding amplitude value can be found on the A-scan for tx = 1, rx = 1. The round dot on the top A-scan in Fig. 2.3.7 shows this corresponding time. Note that the amplitude of the A-scan here is zero.

Every contribution is calculated by working through the element combinations shown in the table in the centre of Fig. 2.3.7. The solid lines connecting the elements and P_1 show all possible propagation paths. For each path, the propagation time to and from P_1 is found, then used to extract the relevant amplitude from each A-scan. These times are shown as round dots on each A-scan - note that the timing differences are exaggerated for illustrative purposes.

All contributions are summed giving the brightness at P_1 - in this case zero. We might expect this, as there is no reflector at P_1. This process is repeated for every

pixel in the grid, building the TFM image.

The TFM image created by this process is an RF image. The peaks and troughs of this image make it difficult to determine the true value of the peak signal, and the location of the centre of the flaw. Both of these properties are considered in this thesis, so the TFM image undergoes rectification before it is used for further analysis. An example of a flaw image before and after rectification is shown in Fig. 2.3.8.

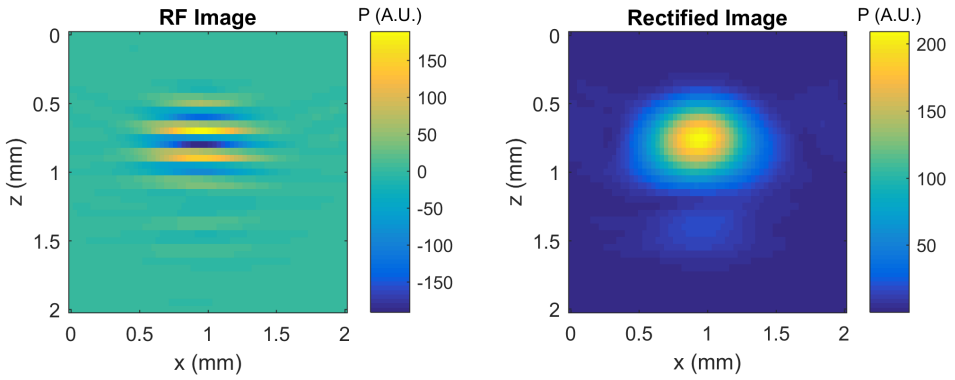

Figure 2.3.8: A TFM image before rectification (left), and after (right). The Hilbert transform is applied to each column of pixel values in the left image, and then the amplitude of the complex resulting values is used to find the pixel values for the image on the right. This image was produced using simulated flaw data supplied with BRAIN.

The RF image is produced by summing all A-scans from the FMC data. To obtain the rectified image, the Hilbert transform is applied to each column of pixels in the RF image. This creates a matrix of complex values, from which the amplitude is taken to obtain the rectified image. This process performs envelope detection along the columns of the RF image.

Consider pixel P_2. The corresponding propagation times are shown as white diamonds plotted on the A-scans. Summing these amplitudes results in a large brightness value - representing the location of the reflector in the TFM image. Note that the brightness of P_2, and therefore the accurate representation of the flaw peak magnitude, depend on an accurate value of t_{P2txrx}. The amplitude of a TFM image is an angular integration of the front surface reflectivity of the flaw [69]. Errors in t_{P2txrx} will result in a change in the TFM image amplitude, potentially causing issues with flaw sizing.

Time of flight errors occur when incorrect assumptions are made about the inspection geometry. An improved TFM image is obtained when this is better taken into account. Correction of the ToF has been used to improve TFM imaging in industrial applications, including through CFRP layers [70], anisotropic welds [71], and curved interfaces [63, 72, 73].

2.3.4 TFM INSPECTION THROUGH CURVED SURFACES

For TFM through dual-media, an accurate ToF depends on the method used to calculate the path of sound propagation through the two materials. The principle is the same as shown in Fig. 2.3.5 (1), where Fermat's principle is used to find the points of refraction (PoR).

Efficient methods of calculating a TFM image have been published by Dziewierz [74] and Zhang [73]. The procedure is the same as outlined in Section 2.3.3, except there is a different method for calculating the ToFs, to take new ray paths into account. If a surface has an unknown surface, it can be volumetrically imaged in 3D using TFM prior to subsurface inspection [75]. A summary of this process is as follows:

1. If surface is unknown, perform TFM in water to create image of surface
2. Define surface representation points; extract from initial TFM if necessary. These become a set of potential PoR.
3. Select a ToF interpolation point.
4. Iterate through potential PoR. For selected, calculate time for ray to travel: rx element -> potential PoR -> Tof point -> potential PoR -> tx element
5. Record minimum ToF, giving the PoR by Fermat's principle.
6. Repeat steps 3-5 for every element combination and interpolation point
7. Apply interpolation throughout imaging plane to give a ToF value for every pixel
8. Perform TFM, using the calculated ToF values

Performing TFM through dual-media requires careful selection of the interpolation spacings shown in Fig. 2.3.10 and Fig. 2.3.9. Zhang [73] presents a method for selecting the optimal surface point spacing interval s and grid interpolation

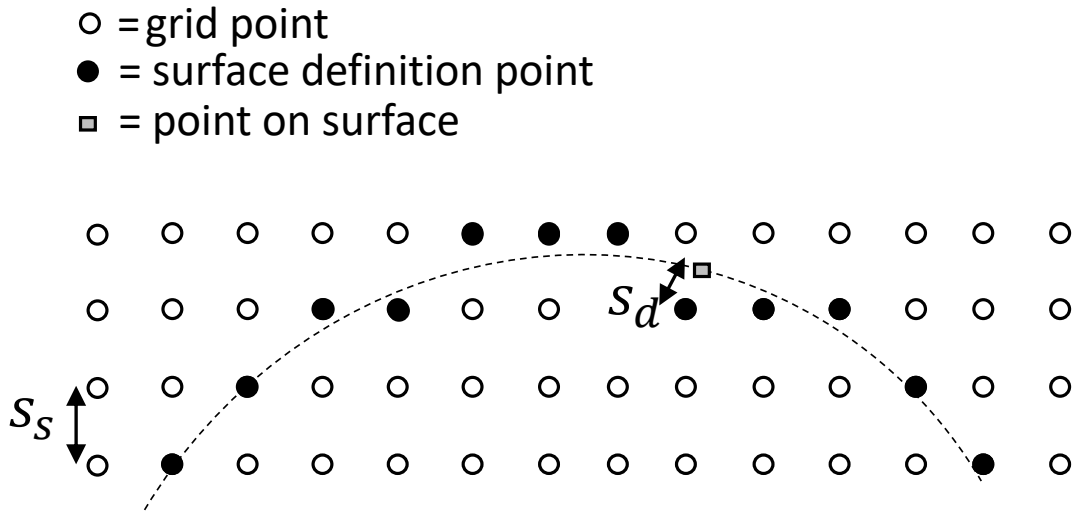

Figure 2.3.9: Surface definition points are extracted from the TFM image, and used as potential points of refraction. On a regular grid, the maximum error s_d is $\sqrt{2}s_\mathrm{s}$.

points within the component. For a given surface, in this case a convex 35 mm radial interface, it shows that an increase in surface discretization step size results in a decrease in the amplitude of a 2 mm SDH - for a fixed grid spacing of 3 mm the flaw amplitude decreases by 2 dB compared to the exact case.

This variation depends on the location of the flaw within the material, with flaws closer to the surface more adversely affected by time errors introduced by an undersampled surface. The bilinear interpolation of the second leg is shown to be important, with flaw signal changing by -1.3 dB, with targets closer to the surface again being most affected by the time error introduced.

It is shown that selection of a maximum allowable deviation, in this case -1 dB, can be used to calculate which s and p provide the most computationally efficient solution within the allowable amplitude deviation. Zhang states that this detailed error assessment only needs to be used once for a given array surface combination to find these optimal values of s and p. This paper highlights an important issue - the imaging algorithm itself introduces an error that is different depending on the surface shape for each array/surface combination, and for each of these combinations there is a range of error values throughout the imaging volume.

Additionally, this error distribution varies slightly even with identical array / surface combinations, as the interpolation error changes based on the exact origin position of the grid. This error is because of the distribution of errors across

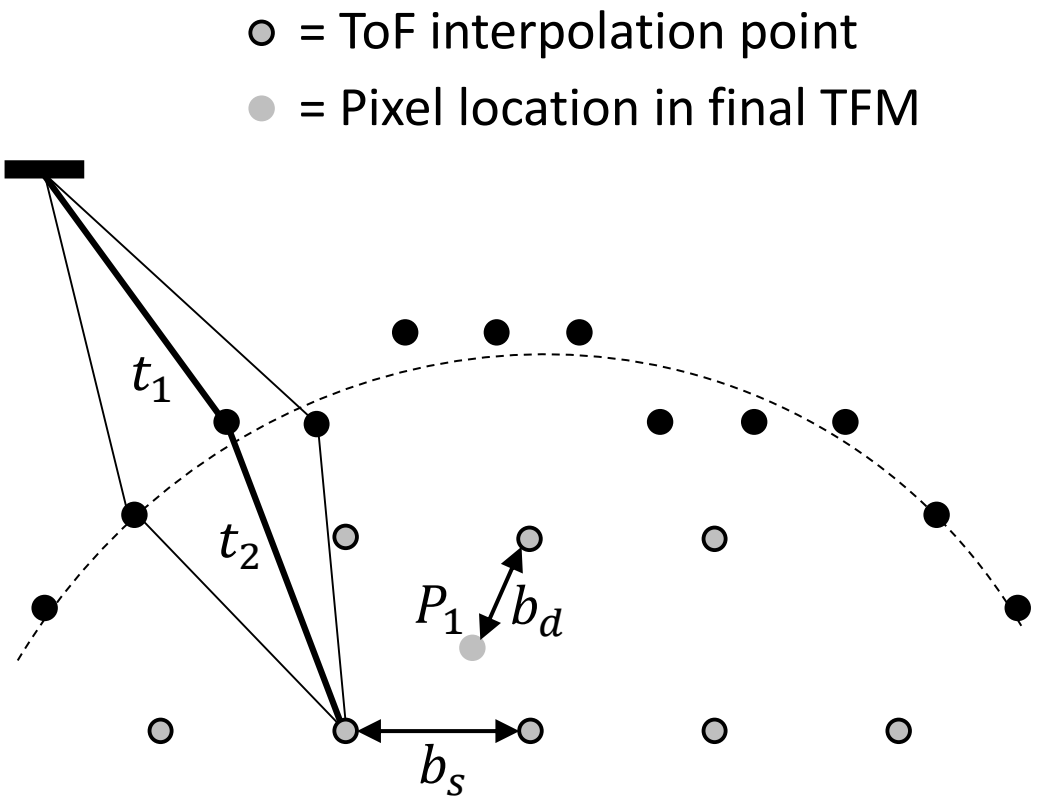

Figure 2.3.10: Time of flight interpolation points shown in the imaging plane within a component. Lines show path of rays between element and one ToF point; bold line shows quickest path. ToF at P_1 is calculated by interpolation between the surrounding four points.

a square introduced by bilinear interpolation. Potentially, this error could be reduced by combining multiple scanning frames, if the scan step is below the interpolation step. In the example from Zhang, a 5 mm step results in less than 1 dB imaging error.

The connection between s, p and scan step are of consequence for this study, as they must be specified to ensure a controlled inspection technique. Imaging noise introduced by the interpolation must be accounted for when quantifying the performance of a given inspection.

Inaccuracy in the surface measurement has a similar effect to under-sampling of the component surface. Timing errors are introduced in the ray paths used for the reconstruction of the TFM image, resulting in reduced summed amplitude from the flaw. Additionally, these timing errors will lead to a more spread-out flaw image. Considering Zhang's work on surface sampling, the results can

be used as a lower bound on the amplitude reduction expected from surface measurement inaccuracy for a curved surface. These results suggest that an amplitude reduction effect is introduced by surface measurement inaccuracies, with neglible reduction at a 1 mm accuracy, a 1 dB reduction at 2 mm accuracy, and 6 dB reduction at 3 mm accuracy. For inaccuracy in surface measurement that is less regular than the sampling error, the amplitude reduction effect is more pronounced, suggesting that an accuracy of 1 mm or better should be sought.

Another consideration when using TFM to measure surfaces, is that it is built on the assumption of point-like reflectors. The ability of TFM to image planar reflectors is poorer than its ability to measure point-like reflectors, and this gets worse the further the surface to measure is tilted from parallel to the face of the array.

Dziewierz explains these effects in his thesis [76]. The TFM algorithm can be thought of as summation of intersecting ellipses, describing points of equal ToF. These sum to a high contrast, and thus give good representation for a point reflector, however Dziewierz found that for planar reflectors, the intersection of ellipses was not as representative of the planar reflector as it was of the point reflector. This resulted in a mis-located image of the planar reflector, as well as strong side lobes.

Dziewierz proposes accumulating the signals from the FMC into a reflector parameter space similar to a Hough transform, and matching the FMC signals to those expected from an analytical geometric model. This was applied successfully to separate a TFM image of a point reflector from the backwall of a ball-bearing.

An approach like this, but applied for surface detection and correction of TFM images, could be used to improve the surface representation used for corrected TFM imaging.

2.3.5 COMPUTATIONAL CONSIDERATIONS FOR TFM

Implementations of the TFM algorithm on general-purpose graphical processing units (GPUs) have been a key enabling factor for the applied research activities in this thesis. The hardware of a GPU is different to the central processing unit (CPU) of a PC, containing many more cores which can perform calculations in parallel. The primary reason for this is to accelerate the ray-tracing calculations

required for rendering scenes in modern video games [77]. The power of parallel processing can be leveraged for other tasks, given the algorithm can be organised such that each parallel calculation result is independent of the others. Calculation of a TFM image is a problem that lends itself well to this sort of parallelisation; as each pixel value can be calculated independently of every other pixel. Studies have highlighted the use of GPUs for TFM as apposed to the use of the CPU [78–83]. Further reduction of the computational burden is possible by using a sparse-TFM algorithm [84]. The parallel processing capability of FPGAs has also been used to speed up TFM [85].

Consider the algorithm depicted in Fig. 2.3.11, describing the individual generation of a pixel value for a TFM image in a serially processed calculation. This is an un-optimised implementation of the TFM description given in Fig. 2.3.7. For a given tx-rx combination, a ToF is calculated, the amplitude extracted from the FMC, then added to the pixel total brightness, before repeating the process for the next tx-rx combination, until all contributions have been summed to create the final image. Note that this figure, and Fig. 2.3.12 are not based on a complete understanding of the implementation, but on discussions with the code creators of cueART, as well as reviewing the code of cueART and BRAIN. Code for BRAIN is available for inspection online at https://sourceforge.net/projects/bristol-brain, and is actively used and developed by the NDT lab at the University of Bristol. While this code is freely available, it is not open source. Code for CueART is not freely available, and is maintained by CUE at the University of Strathclyde.

Notice that the top subsystem, for iteratively determining the ToF value to and from the pixel, does not depend on any of the FMC data. The calculation of the ToF set ("set" referring to the ToF values for all tx-rx combinations) for each pixel can therefore be performed before loading any FMC data. Notice also that the ToF result for one pixel location does not require prior knowledge of any other ToF, therefore the ToF calculation can be held in parallel. This is depicted in the first subsystem of Fig. 2.3.12. The bottom subsystem in Fig. 2.3.11 shows the extraction of amplitude at the relevant ToF - a calculation independent of other pixel values. The algorithm in Fig. 2.3.12 exploits this by loading the relevant ToF set to each pixel individually, and performing this operation in parallel. Note that pre-calculation of the ToFs is only possible if the surface geometry is known in advance.

The architecture of NVidia graphics cards is particularly suited to the indexing of A-scans due to the low-latency of the shared on-chip memory. This allows

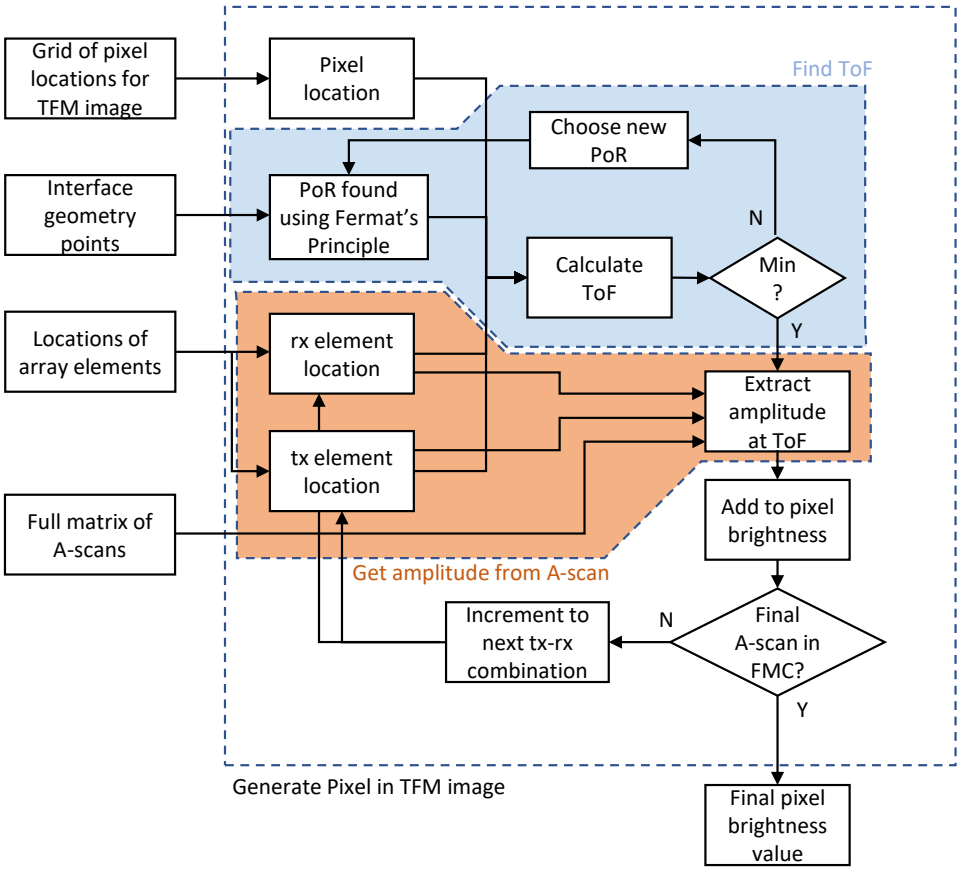

Figure 2.3.11: Simple algorithm for performing TFM on a single pixel. This is a high-level description of the process, based on the author's understanding of how cueART operates.

seperate threads access to the same data. In the context of TFM, this means that multiple independent calculations can access parts of the same A-scan simultaneously.

cueART, developed by the University of Strathclyde, and BRAIN, developed by Bristol University, both implement algorithms similar to Fig. 2.3.12 in ultrasonic array inspection software. The aim of figures 2.3.11 and 2.3.12 is to demonstrate how the TFM process can be made parallel on a high-level; and the consequences of this. Further implementation details are out of the scope of this thesis, however BRAIN source files are available for download [86].

Both of these software packages unlock the potential for TFM inspections to be used in practical situations - speeding up acquisition-imaging times by three orders of magnitude compared to CPU implementations, with typical speeds of 1 Hz for BRAIN, and up to 100 Hz for the latest cueART implementation [10].

As this project focuses on scanning systems, the need for fast TFM production was a high priority. As such, and in light of the benefits of GPU processing described in this section, a GPU-based solution was sought. Considering the lengthy development time required, and the existing software available, the decision was made to use both CueART and BRAIN for TFM imaging in this project. Existing software was extended to create the imaging tools used in this study. An added benefit was the integration with existing hardware at Rolls-Royce, creating workable new tools for industrial use, and applied to new inspection problems (such as gear teeth).

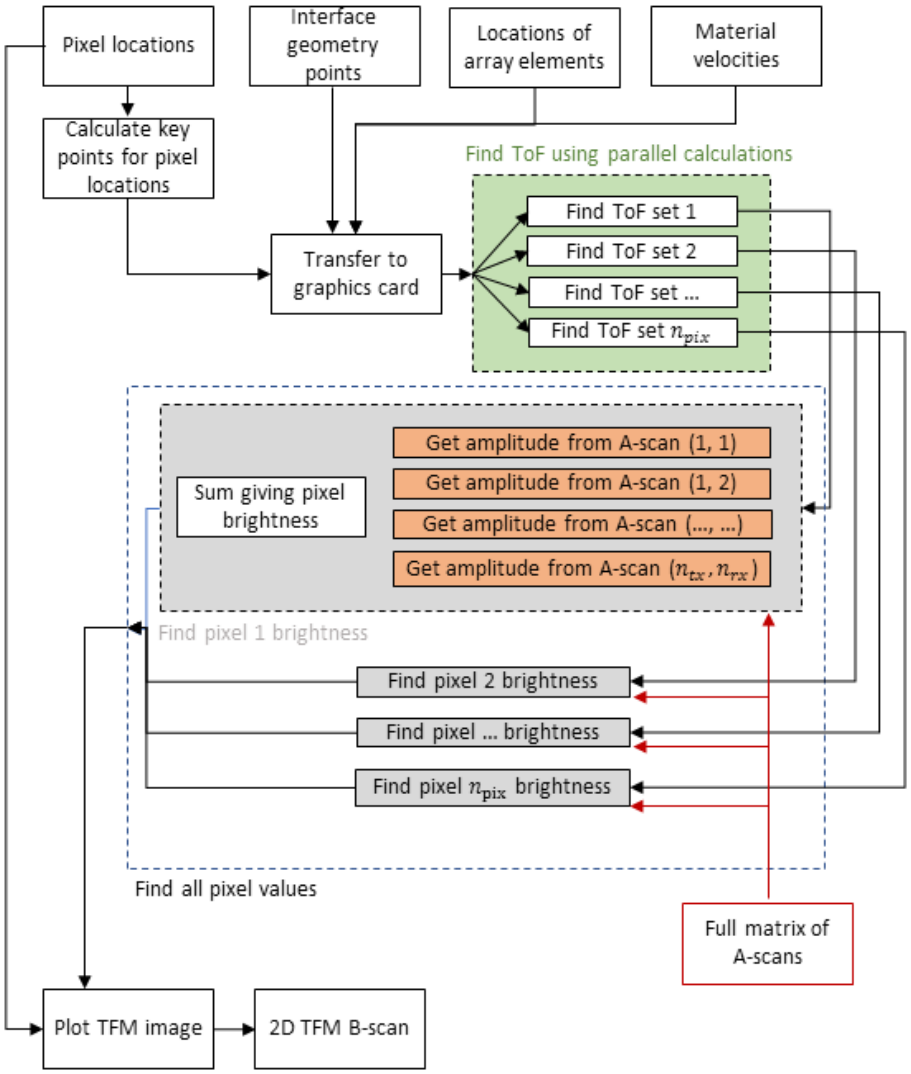

Figure 2.3.12: Efficient TFM algorithm. Uses GPU parallel processing capabilities to calculate ToF sets for each pixel, and then the amplitude of each pixel independently. This is a high-level description of the process, based on the author's understanding of how cueART operates.

2.3.6 FLAW SIZING USING TFM

Great care must be taken when sizing flaws using TFM; the assumptions made for the amplitude sizing technique used for single element probes do not apply for a linear array. The image produced in a TFM B-scan is closer to a measure of the reflectivity of the flaw across its surface; or in other words, describes how "point-like" the flaw appears at that pixel.

For amplitude-sizing using a single-element probe, the assumption is that if the transducer face is significantly larger than the flaw, then the proportion of energy reflected back is related to the size of the defect. This clearly does not apply to the array case, because the TFM algorithm (ideally) only selects the parts of the synthesised beam that fall on a given pixel - ignoring the rest. The beam does not therefore cover the whole of the flaw, so it cannot be said that the receiver obtains a full measure of the energy reflected from the defect. Owing to non-infinitesimal sized focal spots produced by TFM however, the received energy will not exactly be the reflectivity of the flaw at the pixel, but that integrated across the focal spot at the defect at that point.

Imaging measurement models [1] can be used to predict the image produced by a given flaw, and therefore accurately size it. This method, akin to modelling every flaw for sizing purposes, has not been taken due to the complexity of implementing an imaging measurement model within the timescale of this project. This should almost certainly be the approach taken by future work.

One method of quantifying array inspection capability is by using the API, as presented in Holmes [62]. This study showed the ability of a given array inspection to image a point scatter, with a lower API value indicating a better focusing ability at a given point in the volume. This work shows that when considering the TFM, the API extends beyond the bounds of the probe. For the contact inspection case considered, it is shown that the API contour map has a geometric similarity to drawing a locus through the triangle connecting array end points to the imaging point. This suggests potential for fast approximation of an API map for a given inspection. Of further interest to the application of scanning, the bounds of the array sensitivity are predicted beyond the lateral dimensions of the array, showing that scan step sizes could possibly be increased. Modelled results are compared with experimental results, showing the API at three different depths matches experimental measurements at three lateral locations (the flat interface means lateral law positioning can be experimentally measured simply

by displacing the probe. Equivalent work for mapping the sensitivity to FBHs through curved surfaces could take a similar approach to this work, albeit requiring use of a more complex model and more target reflectors to investigate the API variation to the same degree.

Three distinct methods for TFM flaw sizing were highlighted by Zhang [87], with validity based on flaw size compared to λ.

The amplitude method compares the peak amplitude of the flaw to a reference reflector, and size is inferred similarly to a SE inspection, as described in the previous section.

An S-matrix is a function that characterises the reflectivity of a flaw at all angles [88]. Given the incident and scattered angle, the amplitude change in the wave is calculated. For the purposes of ray-tracing, the flaw can be treated as a point reflector response, multiplied by the S-matrix. This can be measured experimentally, and therefore used for sizing.

Sizing directly from the image can be performed by using the -6 dB method at the edges; measuring the extent of the largest imaged dimension at an amplitude of greater than -6 dB from a reference signal. This is called "box-fitting".

The presence of noise affected the performance of sizing techniques. In the absence of noise, the S-matrix technique could size flaws from a minimum of 0.2λ, with 10% noise from 1.6λ. Box-fitting worked from 0.6λ in the absence of noise, and from 1.4λ at 10% noise.

The amplitude technique in Zhang was not selected, as that study did not want to make the assumption that the elements were in the equivalent far-field of the crack. This assumption can be made for this investigation - as the flaw width is limited to that of small FBHs compared to the inspection wavelength. Using the far field formula [13]

$$N_0 = \frac{D_{\text{probe}}^2 f}{4c} \tag{2.17}$$

the far field starts around 0.7 mm from the flaw. N_0 is distance to the start of the far field; D is the diameter of the probe; f is the central frequency of the probe, and c is the speed of sound in the propagation medium. This is within the near-surface-resolution zone currently removed from forgings during inspection, therefore does not represent a loss in coverage.

For these reasons, all three methods could be applied to the flaws in this study. The flaw size is similar to the ultrasound wavelength, therefore the noise level would determine the applicability of the S-matrix and box-fitting methods.

Noise can be produced by electrical and material sources, as encountered by SE inspection. Additional sources of error from TFM include the interpolation imaging parameters discussed in Section 2.3.4, which can result in a reduction of amplitude, and therefore must be taken into account when sizing flaws. Furthermore, the influence of variations in element sensitivity and firing delays can change the TFM image significantly [65] [64], and thus affect sizing performance. Other imaging parameters, such as the resolution; or algorithm used to create a surface representation, have an influence.

This study looks at the change in apparent size of a defect of 0.63 mm through different surface curvatures, at a single frequency. The aim is to identify the ability to maintain sensitivity through a curved surface. Sensitivity makes reference to the relative gain, determined by the DAC - therefore applies only to the amplitude technique.

This section has discussed inspection through curved surfaces using TFM in general. The chapter so far has covered different aspects of technology relating to a TFM-based curved surface scanning system. The next section discusses the specifics of the thesis question.

2.4 QUANTIFYING TFM SENSITIVITY TO FBHS THROUGH CURVED SURFACES FOR AUTOMATED SCANNING

This section takes the background described in previous sections, and applies it to the specific technical and business backdrop of this industrial project. The problem statement of the thesis is refined using terms introduced in previous sections. Two case studies of existing inspections are introduced, and areas where this project could result in technology transfer are highlighted. From these two case studies, common required activities are translated into research objectives. These objectives are clarified, and serve as the basis for the rest of the work through the thesis. The aim of the section is to bring together the state-of-the-art described previously, with specific multi-faceted industrial problems. To

ensure a cohesive narrative for this thesis, it is necessary to view the work in this broader context, especially by referring to the system-level diagrams shown in Fig. 2.4.1. This section justifies why the thesis can be roughly split into three activities, in pursuit of an overall goal.

2.4.1 INDUSTRIAL PROBLEM STATEMENT AND DISCUSSION

The NDE department at Rolls-Royce plc. is often asked by stakeholders in different fields, "can we inspect curved forgings?". This seems from the outset to be a reasonable request, as the process of machining the rectilinear stage adds complexity and consumes material. There is currently a very good reason for answering in the negative - there is not a well-validated standard technique to achieve this; one giving repeatable results and global component coverage. Further questions abound, such as "what limits of curvature can we inspect?", "how can we calibrate such a method?" and most importantly "how can we show its equivalence to what we have done before?".

This thesis sets out to partly answer these questions, bridging the gap between the academic research that has enabled inspection through curved surfaces, and the requirements of Rolls-Royce. Previously in this section, the fundamentals of sizing flaws using the amplitude method, combined with an experimentally determined DAC, were discussed for single-element UT. This is the key process that is currently used to determine whether the inspection process is controlled and quantified. Further on in this section, the newer technology of TFM was described along with its associated benefits for inspection through curved surfaces. Creating an analogue of the DAC method for TFM inspections is necesssary for its deployment in industry.

Repeating the DAC method described, but replacing the single element probe with a phased array, would give an idea as to how well TFM would work as a drop-in replacement for the inspection of rectilinear discs. It is the opinion of the author that the business case for this idea is weak. It would require replacement of all existing flaw detectors, and the re-approval of an existing process, for only a marginal improvement in inspection sensitivity, and the continuing necessity of pre-inspection machining. Crucially, this approach would not leverage the two main advantages of the TFM method - its ability to correct for curved surfaces, and its ability to image flaws in a 2D space below the probe. The performance

of these two properties would be un-quantified, therefore unusable.

A process to quantify these capabilities would necessarily be model based - there are simply too many permutations of interface curvatures and flaw positions to experimentally build a thorough DAC equivalent prior to every inspection. This may increase overall process complexity; but there are two main factors from the industrial context of this technology that make the idea economically feasible.

The first is that an NDE based forging design optimisation loop already exists. A designer creates a candidate forging design, and after running through in-house software, the ultrasonic coverage of the part is predicted. An existing model then uses an "origami approach" [7] [89] to determine the likely ray paths of single element ultrasonic probes. This relies on relatively simple beam properties, along with a set of heuristics developed with decades worth of NDE experience. The results from this thesis can therefore be used to refine performance of future versions of this existing software - there is no need for a completely new approach.

Secondly, increased cost and complexity of the NDE process could result in dramatic savings elsewhere. There has been a recent trend to substitute single element inspections with array inspections in order to increase inspection speed. This has been very successful, resulting in some inspections times, and therefore NDE cost, reduced by over an order of magnitude. Looking forward, however, it is the opinion of the author that the greatest industrial gains, in cost saving as well as performance, are yet to come.

Modelling and performing FMC-TFM processes is a computationally intensive task; however dramatic speed improvements, and optimised data-handling procedures are inevitably going to continue in coming years. Faster inspection and modelling means lower NDE operational costs; lower-cost computing power translates to lower NDE capital costs. Materials, on the other hand, are very unlikely to become significantly cheaper - certainly not at the rate of Moore's law. If it can be shown that curved surface inspection has the potential to reduce the volume of material used for the overall manufacture process, then a cost-benefit analysis can be made.

There is a direct link between the performance of the NDE process, and the material saving that can be realised. This thesis progresses methods to assess performance of the NDE process, in the context of wider work to link the performance of a given phased array system to the potential volume saving for forged parts. Additionally, the practicalities of performing a given modelling-inspection

process are discussed. Together, these results should help an executive evaluate the right time and place to deploy these techniques to deliver overall cost savings.

To understand the central argument of this thesis, it is important to consider not just the NDE technique used, but the context - optimisation of the manufacture process. Investigations into array inspection of curved surfaces and robotic scan planning are seemingly disparate tasks, unified under this common goal. It is argued that reliable quantification of the TFM process, with consideration to probe positions and surface features, has important consequences for overall inspection performance. A case is made for the continued development of this capability, and guidance is provided for the direction this should take. This thesis also argues that understanding the limitations of TFM through curved surfaces is useful for applications outside a manufacturing context.

One aim of the EngD project was for the improvement of two automated UT scanning processes, detailed below.

2.4.2 CASE STUDY: 3D TOOLPATH GENERATION AND INSPECTION OF WARPED PLATES

After diffusion bonding, but prior to a second expensive manufacturing step, a plate is ultrasonically inspected in an immersion tank. The front surface of each plate is warped in a unique and non-predetermined fashion, necessitating an adaptive process. This is achieved by the following steps:

1. Fix test piece in place to ensure baseline repeatability
2. Measure front wall amplitude at set sampling locations, and adjust for probe normality
3. Perform inspection, build C-scan from A-scans, interpolating probe positions between initial point measurement sample locations.
4. Check C-scan for contiguous regions that lack ultrasonic coverage (indicated by presence of membrane reflection)
5. If a lack of coverage is found, adjust the fixturing and re-scan the plate

A single element probe is used for this inspection, with a very narrow beam that is sensitive to misalignment. Even when step 4 shows sufficient signal, there are still deadzones on the part related to surface curvature. This highlights a possible

area for improvement with the application of phased array technology.

Steps 1 & 5 require significant manual intervention in the process. Employing skilled operators to repeatedly set up plates in a fixture does not effectively leverage modern automation technologies. Considering that there is a view to increase the level of automation in the inspection itself, it would be efficient to also consider the process as a whole. The use of a general system, such as a standard 6 DOF manufacturing robot, would lay the groundwork for a system that handles components as well as inspecting them.

The sampling locations used in step 2 are based on trial-and-error for a given plate type, typically spaced around 50 mm apart on regions expected to be mostly flat, and down to around 5 mm on regions with a large surface gradient. This sampling process could be one of the reasons for occasional loss of coverage. Time taken to measure the component geometry is another issue; taking 10 minutes from a 60 minute process. It was suggested that a structured-light metrology system could be used to create a point-cloud of the component geometry, followed by toolpath generation. This would potentially afford greater accuracy and speed to step 2.

The upgraded system would have the following (changes are **highlighted in bold**):

1. Fix test piece in place to ensure baseline repeatability
2. **Perform metrology on plate, mesh point cloud and calculate optimal toolpath**
3. **Perform inspection using robot. Build C-scan from TFM corrected B-scans, with probe position determined by toolpath and focal laws determined by measured surface shape at each point**
4. Check C-scan for contiguous regions that lack ultrasonic coverage (indicated by presence of membrane reflection)
5. If a lack of coverage is found, adjust the fixturing and re-scan the plate

The value of deploying this system in a production environment would depend on the extent of the increase in speed and coverage of the system, for particular candidate parts. In chapter 3, a prototype process is developed for a representative calibration plate, and recommendations are made for further development of an automated system. Other related robotic inspection activities are detailed to build an understanding of the processes used. Investigation into metrology-assisted robotic positioning, the primary focus of this topic, was abandoned due

to a change in requirements from the industrial partner.

A shift in focus towards model-assisted inspection planning for curved surfaces was desired; which is also relevant to the inspection process detailed above. Specifically, the relationship between surface curvature and the efficacy of TFM inspection was investigated - essentially focusing on steps 2 and 3 above. While this is still relevant for wavy plates, the application area was changed to look primarily at forged discs.

2.4.3 CASE STUDY: 2D TOOLPATH GENERATION AND DESIGN OPTIMISATION OF ROTATIONALLY SYMMETRIC FORGINGS

The difference between this process and the one outlined above is related to the shape of the part. A unique, undefined waviness was a side-effect of a manufacturing process for the plate, whereas each disc is machined to a pre-determined shape. To reflect this, the process is summarised below as a combination of design and inspection steps. For a given final disc shape:

1. Suggest candidate inspection geometry (rectilinear)
2. Use inspection planning software to determine expected coverage obtainable through single element inspection; considering access and insonification limitations
3. Forge billet into approximate disc shape
4. Machine disc to rectilinear form
5. Apply surface finishing to disc
6. Use flat-sided calibration blocks with 0.63 mm diameter FBHs drilled at different metal paths to build a DAC curve up to maximum thickness of disc
7. Apply DAC curve to pulser-receiver unit
8. Capture A-scans from disc in a circular pattern, building up a C-scan representation
9. Extract flaw regions by use of gating out known disc profile (1000 gates technique, [24] (see Section 2.1.4)

10. Use amplitude-based sizing method to quantify any flaws on C-scan

Replacing step 1 with a curvilinear profile was not supported by the existing inspection planning software, which also did not have the ability to predict coverage for array inspection. This highlighted the need to develop a technique to model the expected coverage obtained by a given array probe.

It was suggested that the complexity of steps 4 & 5 could be reduced by simply sandblasting the component following the initial forging step. This would require the ability to analyse coverage and plan the scanning of an uncontrolled shape. Part measurement and toolpath planning could be performed as in the previous case study, with the added requirement of modelling the UT coverage of the uncontrolled surface profile.

For a less complex inspection, steps 4 & 5 could be replaced by machining to a curvilinear form.

Step 6 is a crucial process to ensure that the response from calibration FBHs corresponds to expectations, allowing an accurate gain to be applied in the inspection process. The TFM equivalent is different in several ways. Firstly, the TFM image to be adjusted is a B-scan, rather than an A-scan, therefore adjustment of the result is required across the imaging plane, rather than just on the amplitude axis. Secondly, the introduction of curvature means the calibration blocks can only represent a subset of the possible probe position / surface shape combinations.

The largest portion of ultrasonic modelling and experimental work in this thesis sets out to provide a suitable replacement for this step. A body of evidence was built to help describe how a flaw signal varies with surface curvature for certain cases. This then allowed recommendations to made for further research into the effects involved, tools that can be used to quantify these effects, and future work to establish a well-understood and controlled replacement to step 6 in the process.

Step 7 is replicated on curved test pieces at different depths, as well as on a challenging curved and rough forged disc test piece.

The scanning at step 8 was not replicated in this study, however steps were made towards defining the optimal toolpath to use in 2D. The optimal arrangement for a single element probe scanning a rectilinear surface is fairly straightforward - align the probe face normal to the surface, and scan at a height where the N-point coincides with the surface. With a phased array on a curved surface, the optimal

angle of incidence and standoff can be different for every point at the surface. This dramatically increases the size of the problem, therefore in this study has been considered for a simplified case. It is assumed that the radius of the disc is much larger than the passive beam spread in the array imaging plane, therefore the problem can be sufficiently expressed in 2D.

Gating is applied to the TFM images, based on the near surface resolution limitations found in the example inspection. Curved gates are applied to B-scans when appropriate, and gates in the C-scan representation are used for flaw sizing and noise quantification. A simple user interface was created in MATLAB to accomplish this.

Stage 9 was replicated. The suitability of each sizing technique is determined by how well the size is preserved through different curvatures. It should be noted that this study is primarily concerned with the ability of the imaging technique to maintain ultrasonic sensitivity to flaws of a certain reference size (0.63 mm diameter). Comparing the ability to accurately size different flaw diameters is outside the scope of this thesis, however the techniques developed within can be used to determine the applicability of a certain sizing regime.

The modified, prototype process can therefore be summarised as:

1. Suggest candidate inspection geometry (curvilinear)
2. Use model of TFM image change through curved surfaces to predict flaw variation.
3. Evaluate whether influence of curvature still allows detection of flaws of a given size. If not, identify regions where curvature radius is too low, optimise, and feed back to stage 1
4. Forge billet into approximate disc shape
5. Machine disc to curvilinear form
6. Apply surface finishing to disc
7. Use radially curved calibration blocks, with 0.63 mm FBH drilled at different metal paths. Ensure that radii used encompass range of disc radii
8. Capture FMC frames from disc in a circular pattern, building up a C-scan representation. Ensure optimal array positioning is used normal to each curved surface on disc face.

9. Apply gates to B-scans to extract FBH peak values and plot C-scan. Apply gates to C-scan to extract peak values, other flaw-sizing metrics, and evaluate the overall measurement noise

10. Save FMC files relating to subregions where flaws are detected for future research by reprocessing. Delete unecessary FMC frames if there are storage limitations.

The majority of this thesis focuses on establishing steps 2, 7 and 9, mainly using purpose-built calibration blocks. Discussed in context, however, the results help show how progress has been made towards implementing the above progress, and what further steps need to be taken.

2.4.4 TECHNICAL RESEARCH OBJECTIVES

Chapter 2 has provided a review of the background and previous research work completed in the area of automated ultrasonic NDE. Following this, two existing industrial inspection processes were described. Potential improvements based on the existing process steps and the reviewed research were discussed, and areas for innovation were highlighted. The technical objectives listed below take these requirements, and explicitly state the areas of research and innovation that comprise the work undertaken in this EngD.

OBJECTIVE 1. DEMONSTRATE A ROBOTIC FMC SCANNING SYSTEM ON A WAVY PLATE

Demonstration of a general system able to generate toolpaths on complex geometries is a beneficial step for both industrial problems. Considering that the wavy plate varies in 3D versus the approximately 2D disc profile, it was decided that a demonstration of automated FMC on the plate would cover both cases. A standard KUKA manipulator was used in conjunction with the Grasshopper parametric geometry add-on to the CAD program Rhino. This allowed the creation of a process whereby an NDT operator without specific robot programming experience could create and run a complex toolpath, as well as superimpose TFM B-scan slices on the CAD of the part produced. This is discussed in chapter 3.

OBJECTIVE 2. QUANTIFY EFFECT OF SURFACE CURVATURE ON TFM INSPECTION

Modelling of FMC inspection through radially curved surfaces was chosen as accurate test pieces could be created with the desired curvature. Furthermore, many curves on example disc profiles are radial in nature. FMC was chosen compared to other acquisition modes, as it allows the image obtained from any linear beamforming operation to be generated from the modelled data.

The well-defined surface profiles were used to evaluate performance of TFM algorithms that rely on the frontwall to calculate the focal laws. FBHs were investigated, as these most closely resembled the sorts of flaws (small elliptical disbonds and cracks) likely to be found in both inspection processes. Most work in the literature benchmarks array performance using side-drilled holes (SDH) as target reflectors, so using a FBH is both closer to the business requirements and more novel.

Performance is quantified in terms of the ability of sizing techniques to reproduce a predictable measurement of flaw diameter. Features such as the peak brightness and the geometric spread of the imaged flaw are discussed. Validity and applicability of modelling techniques are determined in the context of the desired application.

OBJECTIVE 3. DEMONSTRATE APPLICATION TO NEW FORGING INSPECTION TECHNIQUE

This final objective aimed to demonstrate the application of TFM performance quantification to the inspection planning of new forging. In order to realise this, some steps were taken to summarise the change in flaw peak signal throughout the volume of a part with a curved interface. This was embodied as a sensitivity map, with modelled sensitivity maps included in chapter 6.

The key aim was to show that use of modelled results, together with a single calibration measurement of the target defect, could be used to predict the relative change in flaw representation at any point within the volume.

2.4.5 CONTEXT FOR AUTOMATION INSPECTION SYSTEM

One way to contextualize the work in this thesis is to consider the system concept shown in Fig. 2.4.1. This incorporates the required functionality of the two case studies discussed in Section 2.4.4. The bold links represent optimisation processes. Link 1 represents the UT coverage based design loop, and link 2 represents the relationship between robotic path planning and UT coverage.

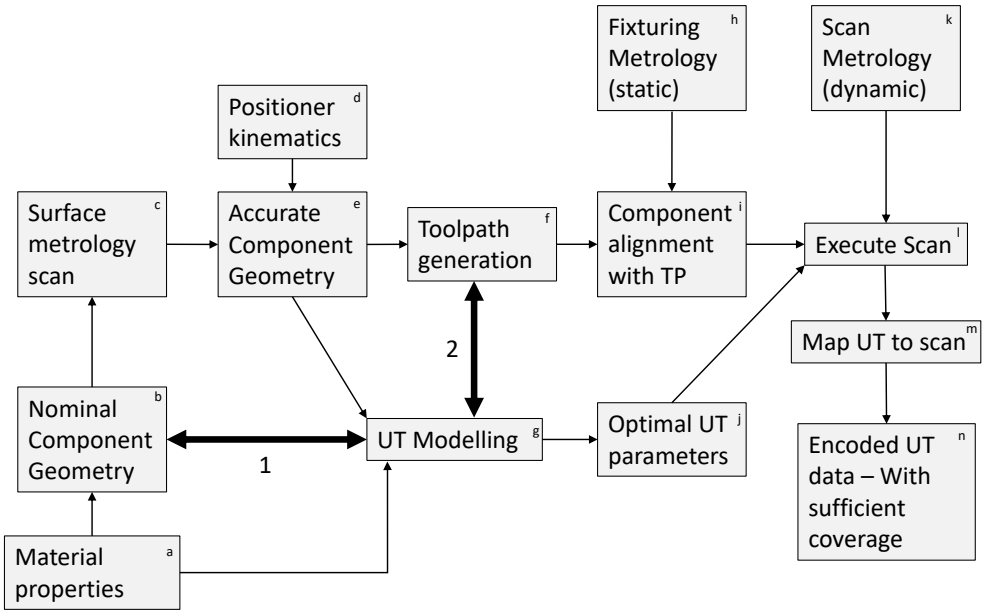

Figure 2.4.1: System concept for an automated inspection system where nominal inspectable geometry is a controlled variable, and inspected geometry is an uncontrolled variable within a tolerance region of waviness.

2.5 SUMMARY

In this section, fundamentals of ultrasonic wave behaviour were outlined. Shown was the link between material properties, wavefront pressure, and speed of propagation. Also discussed were Huygen's principle and the variation in pressure amplitude as a wave propagates through a material.

Behaviour was described where a wave hits a smooth boundary with dimensions much larger than its wavelength, and how the amplitudes of the reflected and refracted wave modes are affected. The change in amplitude versus angle of incidence and material properties of the media are shown to affect the relevant coefficients, and an example of the effects at a flat water-steel interface are shown. This has an effect on the wave amplitude, which is fundamental to understanding the change in flaw sensitivity for ultrasonic inspection of curved surfaces.

Wave and defect interactions were discussed, showing how the ray approximation does not take into account the effects of diffraction. A disc-shaped flaw is considered, and the relationship between wavelength and directivity of the scattered field is demonstrated. This was relevant to the FBH shape considered in the study, and showed that ray-based solutions alone may not be suitable for predicting flaw response.

The practicalities of single-element ultrasonic immersion inspection are covered in Section 2.1. Existing processes were described, alongside candidate replacements. Emphasis was placed on characterisation of a transducer beam, finding a region of predictable variation, and ultimately using this to then size defects. An example beam profile through a planar water-steel interface was shown, using typical inspection parameters to demonstrate this. The concept of creating a DAC based on experimental measurements was explained; showing the basis currently used for Rolls-Royce for controlling ultrasonic inspection of rectilinear forgings.

As scanning of the component is closely tied to performance of the inspection, Section 2.1.4 discussed the link between probe position and obtaining satisfactory ultrasonic coverage for a given scan. The relationship between beam width in an immersion inspection, and the scan step required, was demonstrated for a planar scan in Fig. 2.1.15. It was suggested that curved surfaces require the probe to be oriented normal to the surface at every scan location, and also need a positioning system with a variable scan step. This showed the need for a method of automated control that can perform advanced path-planning, such as that developed in chapter 3.

Each probe position in a curve-following scan is faced with a curved interface. Methods to adjust inspection sensitivity for curvature using SE inspection were discussed in Section 2.1.3, notably the use of a curvature correction factor (CCF) to adjust defect size representation. It was explained that this is similar to updating the DAC for every surface curvature encountered by an inspection. The

case was made for using phased array technology instead of applying a CCF to a SE technique, as many components have continuously changing curvature, and phased arrays have been shown to maintain sensitivity through irregular surfaces.

Use of array transducers, applied to immersion inspection was discussed in Section 2.3.

A linear array was chosen, after comparing different types in Section 2.3.1. Curvature in the passive plane was deemed negligible. For the study, two different types of linear array were used. Each was an immersion probe, with a centre frequency of 10 MHz. Probe A had 128 elements while probe B had 32 elements. Details of these probes are provided in Table A.2 and Table A.3.

A focus on PA immersion inspection in Section 2.3.2 was included to show how a linear array probe can perform in the same flat-sided inspection scenario as the SE probe in Section 2.1. Differences such as electronic scanning, a movable focal point, and a steerable beam were discussed. A simulated beam profile for the 10 MHz array in steel was included, showing performance through a flat interface. Beamforming was introduced as a concept, and specifically the previous use of beamforming to improve sensitivity through curved surfaces was discussed. It was shown that an array can achieve maximum sensitivity at a focal point in the material through an interface. It was suggested that moving the focal point to every location within the material would give the best overall sensitivity - TFM.

The TFM was described in Section 2.3.3. It was selected as it has been shown to outperform other beamforming algorithms, and has previously been applied in an industrial context. The aim of this thesis is to provide an equivalent to the DAC curve used for SE inspection, but applied to TFM. Full-Matrix Capture (FMC) acquisition was described. An emphasis was placed on how an error in the calculated time-of-flight (ToF) values used to index the FMC A-scans can affect a TFM image in Fig. 2.3.7.

Application of the TFM to curved surface inspection was outlined in Section 2.3.4. The process of calculating the ToF values and creating images was explained. The effects of ToF surface representation and end points were discussed in the context of errors. This showed that errors can be introduced, and quantified, for the surface-corrected TFM process, based on chosen ToF interpolation values. Computational factors were discussed, and the innovations behind high-speed implementations of TFM were explained. BRAIN and cueART were introduced as two specific implementations of TFM inspection software. Flaw-sizing methods

in TFM were covered, including amplitude sizing, scattering matrix methods, and image size methods. A justification was given for use of amplitude sizing in this study.

In Section 2.4, the industrial context was established, making reference to the preceding technical detail in the chapter. Two existing industrial processes were examined. Areas where increased automation, and integrated TFM scanning technology would deliver an improvement were identified. Potential new processes were suggested. From each, key innovations were translated into technical objectives, and described in Section 2.4.4. The technical objectives made clear the research aims of this thesis. Furthermore, Section 2.4 as a whole showed how these link to academic background discussed in the rest of chapter 2 and the business needs for two case studies.

This chapter detailed the theoretical and industrial background necessary to contextualise the technical objectives in this thesis. Progress towards these research objectives is detailed in the following chapters.

Chapter 3

DEVELOPMENT OF ROBOTIC SYSTEMS FOR FMC SCANNING OF AN IRREGULAR PLATE

This chapter details work done towards the creation of an automated ultrasonic NDE solution for the scanning of wavy plates. More specifically, the problem of inspecting a diffusion bonded membrane held between two forged, irregular plates, using a general-purpose robotic manipulator is examined. The primary aim of this section is to cover all activities related to robotics and metrology undertaken as part of the EngD.

The main aim of this work was to create a tool for the automated TFM inspection of components that are nominally planar, but with an uncontrolled, irregular deviation introduced during manufacture. Rolls-Royce were keen to demonstrate that a system using a robot arm and phased array could achieve equivalent performance to an existing technique. Ultimately, a tooltip scanning velocity of around 100 mm/s was desired.

Note that the automated scanning techniques presented here could be applied to both industrial case study processes, but this chapter focuses on case study 2. The steps of the original ultrasonic inspection, as well as the suggested updated inspection, were outlined in Section 2.4.2. This was adequate to establish two areas of research covered in this chapter:

- Perform surface metrology on plate, mesh point cloud and calculate optimal toolpath.

- Perform inspection using robot. Build C-scan from TFM corrected B-scans, with probe position determined by toolpath and focal laws determined by measured surface shape at each point.

Practical work towards these goals is detailed in this chapter. A logical starting point is a detailed description of the original inspection process.

3.1 BACKGROUND AND GOALS FOR IMPROVING AUTOMATED SCANNING OF AN IRREGULAR PLATE.

3.1.1 DETAILS OF ORIGINAL AUTOMATED INSPECTION

The geometry of the test plate is as shown in Fig. 3.1.1. Inspection of the diffusion bond between the membrane and the two plates is necessary. Included in the test plate are holes in the membrane; these are the targets used to prove that the NDT technique is working correctly. The material is forged titanium (Ti-6-4).

The test plate is approximately 1000 mm long, 500 mm wide, and thickness ranges from 100 mm to 5 mm along its length.

At the start of every shift in the NDE section of the factory, the test plate is scanned, and the C-scan is examined to ensure that every hole on the membrane can be accurately detected. If not, the system is recalibrated. If every hole can be seen, then the system is said to be calibrated for plates of similar geometry.

An initial scan is conducted using a single element transducer, sampling the front surface distance at predetermined points. This maps out the surface profile unique to each part. Sampling point density is 400 per square metre at flatter regions, and 10000 per square metre at the most highly curved regions. The probe must be physically moved to each point and take a ToF measurement to build up the surface profile. Probe tilt angles are also adjusted to calculate required orientation for peak signal, and therefore maximal normality. This takes around 6 minutes.

The second scan then interpolates between these points, rastering across the plate and producing a C-scan. The probe is focused on the membrane, which is 1 mm

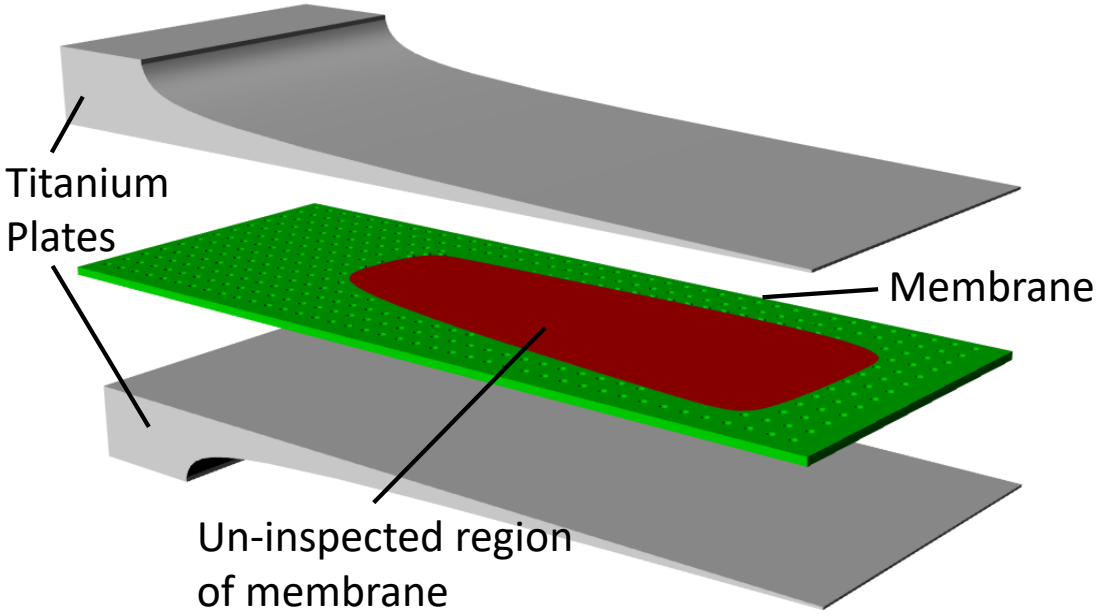

Figure 3.1.1: Internal structure of diffusion-bonded titanium test plate, showing membrane, inspection region and holes representing disbonds

thick. Consequently, any misalignment between the probe and the surface normal results in a loss of coverage - in other words, the inspection is very sensitive to any positional inaccuracy. Parts of a successful C-scan using this method are shown in Fig. 3.1.2.

A 20 MHz, 6 mm SE transducer, with a fixed focus of 40 mm in water is used. A purpose built 5-axis ultrasonic immersion scanning system is used to drive the probe across the plates. Software on the system is proprietary, and maintained by the company who owns the tank.

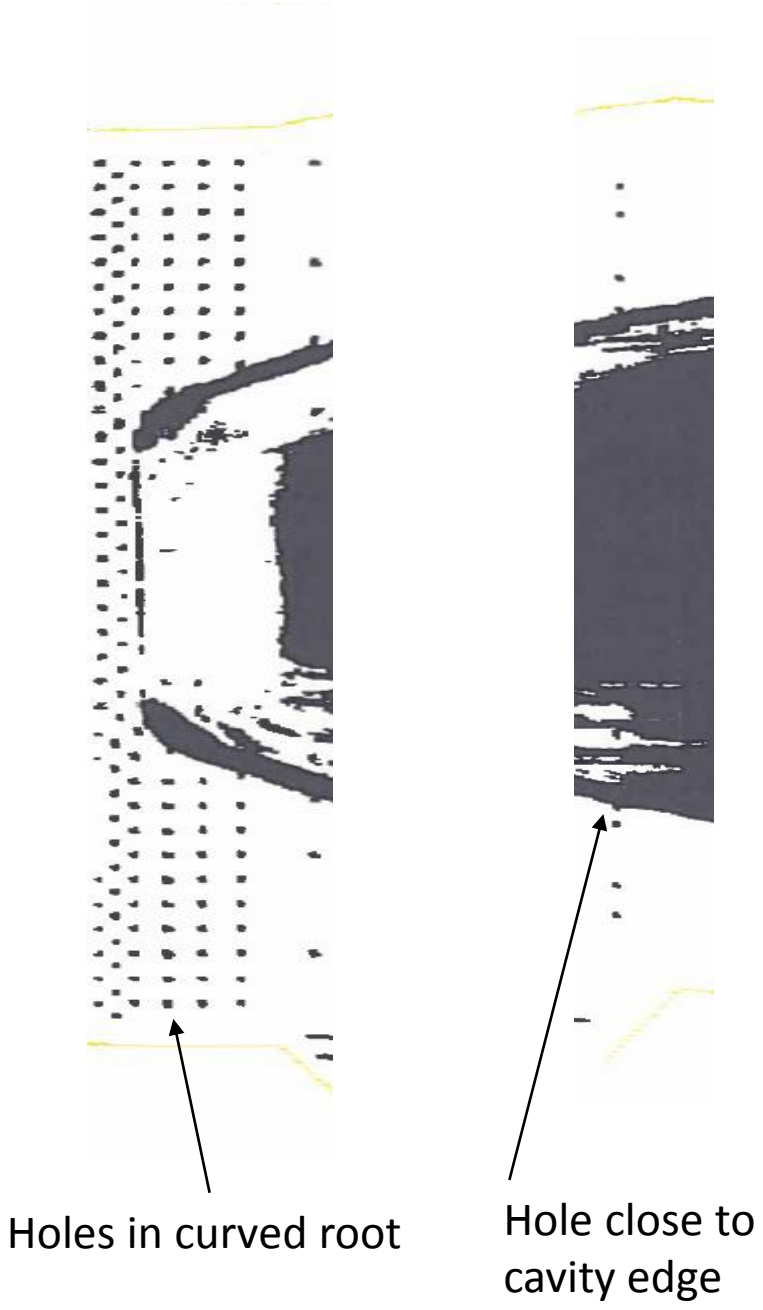

Figure 3.1.2: Parts of C-scan generated from SE process described in Section 3.1.1.

3.1.2 HIGHLIGHTED AREAS FOR IMPROVEMENT

It was suggested that phased array ultrasound could help speed up the production of a C-scan for this inspection. Rather than scanning the SE probe at 0.5 mm

raster step intervals; the ability of a phased array to conduct an electronic B-scan gave an opportunity to scan a wider aperture with each raster pass. Previous work by Rolls-Royce showed that a similar inspection problem could be speeded up by a factor of four [90].

Further to this improvement to instantaneous scan velocity, improvement was sought regarding the surface measurement technique. Instead of driving the probe to each location and sampling the ultrasonic ToF from the front surface, an optical metrology technique was suggested, removing the need for an initial ultrasonic process. Previous work on a structured-light approach to speed up the surface metrology of composite panel measurement showed the feasibility of the approach [37].

Ultrasonic coverage gaps were frequently encountered in regions of pronounced curvature, especially near the root region. Whilst automatic adjustment of probe scan paths optimised probe normality across the scan, there were nevertheless losses in coverage of the membrane. This occurred either due to inaccurate curve-following due to under-sampling in the initial ToF measurement process, or due to the effects of curvature on the fixed focus of the SE probe. The fixed focus was optimal for measurement in flatter regions of the plate, but the effects discussed in Section 2.1.3 steered and defocused the beam where curvature was too high. Considering the ability of PA probes to correct for curvature-induced aberrations, as discussed in Section 2.3, it was suggested that use of PA could improve coverage of the membrane across irregular surfaces.

Much work has been conducted by the University of Strathclyde on the subject of automated inspection [10, 28–31]. KUKA manipulators have been used to demonstrate the feasibility of flexible, automated NDT delivery. It was suggested a KUKA manipulator for implementation of an upgraded automatic PA scanning solution would be a useful platform for this work.

CAM software is used to generate milling patterns for complex shapes. This has been used to generate scan paths for NDT inspection of components with complex shapes. One problem with this approach is the expense of CAM software - it includes a number of features not necessarily required for creating an NDT scan path. Further, re-purposing software for NDT may lead to confusion for operators that are not machining specialists.

A custom MATLAB toolbox for robot control was separately under development during the course of this EngD [10, 32]. This approach afforded a user-interface

tailored for an NDT engineer. Whereas this was low-cost using readily available software (MATLAB), it was a labour-intensive task to create the toolbox, and the decision was made not to replicate this ongoing work. A third option presented itself in the form of RhinoCAD paired with the parametric Grasshopper extension. This software enabled a graphical programming approach, combined with simulation of robot kinematics and production of the code needed to execute an offline toolpath. For these reasons, it was suggested that this program could be used as the basis from which to develop a robotic NDE OPP and visualisation tool.

Another key reason for use of RhinoCAD was its ability to interpret point clouds, such as those produced by surface metrology methods. The ability to simulate the upgraded process, using RhinoCAD as the central platform connecting metrology, path-planning, and data visualisation, underpins the philosophy behind the integration work carried out in this chapter. In other words, the CAD program and its extensibility help realise the system concept introduced in Fig. 2.4.1. The process was developed as a prototype, and as such could not operate with the level of speed or integration required of a production process, but helped demonstrate that these technologies can be connected to produce an automated NDE solution.

Areas of improvement detailed by this section determine the work undertaken for this chapter. These activities are:

- Use surface metrology to build representation of surface component
- Create offline-path planning scan program using Grasshopper
- Integrate metrology, scan planning and data visualisation into one platform
- Investigate ability to create TFM C-scan equivalent to original method
- Predict speed improvement for phased array scanning using TFM

and are discussed in the next section, which details the automated inspection process that was developed.

3.2 DEVELOPMENT OF A ROBOTIC FMC SCANNING PROCESS FOR AN IRREGULAR PLATE

3.2.1 ULTRASONIC DATA CAPTURE

To obtain TFM images, it was necessary to use an FMC-enabled phased array controller. A 64-channel Diagnostic Sonar FIToolbox controller [91] was used. This was chosen for two primary reasons. The first was speed; it had 64 channels and a data throughput of 1600 MB/s, upgradeable to 3200 MB/s. This was far in advance of other phased array controllers compared at the time, such as the Zetec Dynaray at 20 MB/s [92], or the Advanced OEM PAC at 160 MB/s [93]. Another key feature was the open and adaptable nature of the design [94]. This allowed integration of external encoding systems. Further, it allowed direct access to the FMC data, enabling researchers to build Strathclyde's cueART software into a custom LabVIEW program. A system such as the M2M Gekko [95] has TFM hard-coded into the on-board FPGA, giving fast TFM performance, but access to the raw FMC data is limited to 50 MB/s, therefore this was not suitable for the fast, automated collection of raw FMC data ultimately required by the industrial application.

cueART was used for data capture. It is a set of tools that can be used to perform fast and efficient TFM, as described by Dziewierz [79]. In addition to performing TFM, it also handled and controlled the acquisition of FMC data, and enabled data to be encoded by means of an external source.

To produce accurate TFM images, code developed for a previous study into the inspection of irregular weld caps was adapted [9]. This used a surface interpolation method that was optimised for small deviations from a nominally flat surface - similar to the geometry of the plate at any one probe position.

The following process was undertaken to produce an image. Firstly, a TFM image of the surface of the component in water was created, as shown in Fig. 3.2.1. The Hilbert transform was applied to the TFM surface image to provide rectification.

A threshold of -6 dB was used to extract points from the image, and then these points were interpolated to approximate the front surface, as shown in Fig. 3.2.2. This was necessary, as the technique used to calculate the ToF for all pixel loca-

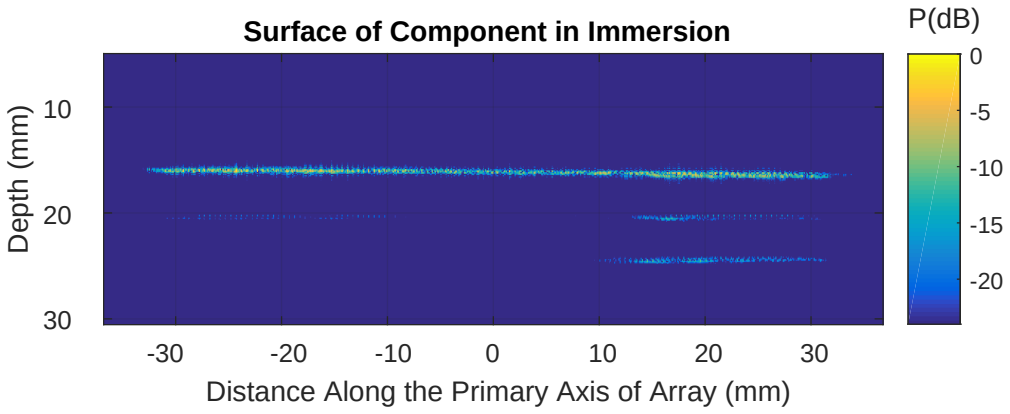

Figure 3.2.1: Example TFM image obtained from front wall of plate, used to obtain surface points. Flaws and the backwall of the part are not clearly visible in this initial image. The resolution of this image is lower than the later TFM flaw image, and the distance to each pixel is used to calculate ToF assuming waves propagate at the speed of sound in water.

tions required a continuous function describing the surface profile.

The points extracted and shown in Fig. 3.2.2 have a quantization error related to the pixel size of 0.1 mm. This could be improved using interpolation between pixel locations to provide a more accurate set of points for curve-fitting. Furthermore, the fitted curve appears to be over-fitted, and this likely introduced some errors into the final TFM image. These issues were considered for improvement, however later in this work different software was adopted for the production of TFM images (BRAIN). It was found that the performance of this process worked well enough to obtain flaw images from the test plate under examination, and this was deemed acceptable for reaching the goal of demonstrating a TFM C-scan produced by a robotic system.

By applying the updated ToF, the TFM was then improved as shown in Fig. 3.2.3. This allowed imaging of the flaws in the membrane, and provided visibility of the back wall.

By gating away the front and backwall reflection, the peak flaw signal was obtained from B-scans similar to the one shown in Fig. 3.2.3 and used to construct the C-scans; shown in Section 3.3. These were created by plotting the probe location associated with the B-scan. The internal encoders of the robot were used to determine the X and Y position of pixels included in the C-scan.

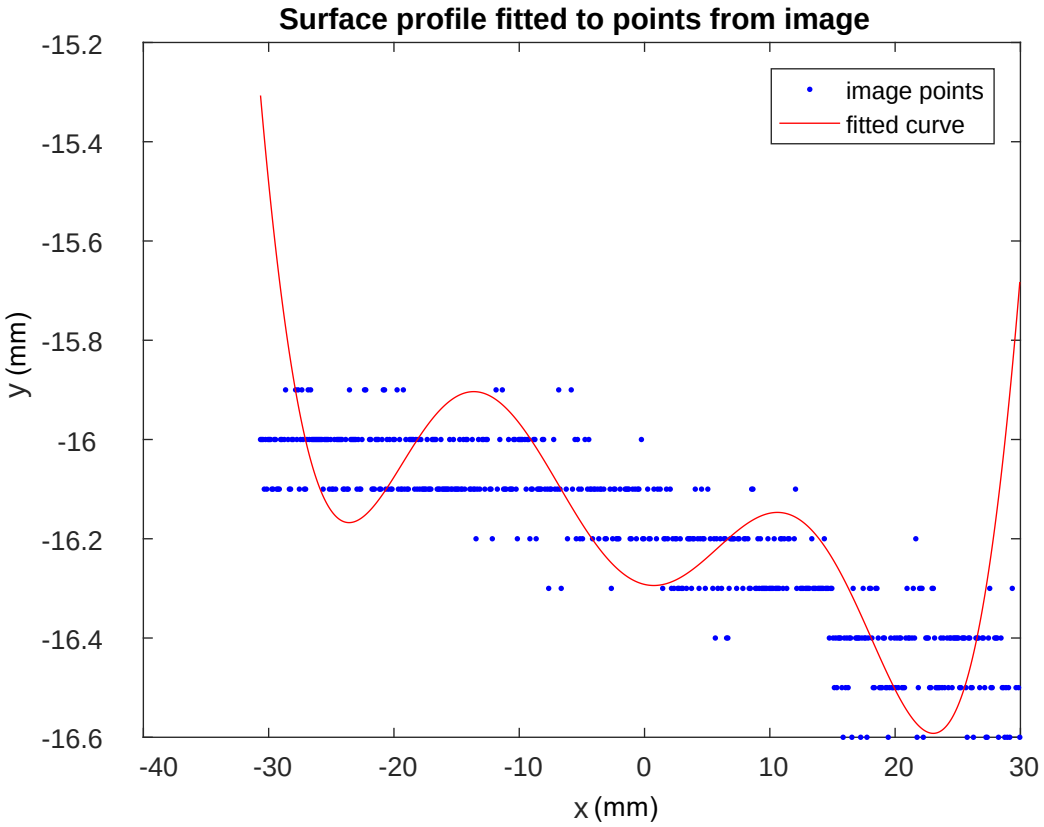

Figure 3.2.2: Surface representation from pixels extracted from Fig. 3.2.1 that exceed the threshold of -6 dB. The polynomial fit is shown in red, which is then used to update the ToF values for production of an adjusted TFM image. The quantisation seen is from the coarse resolution of the initial image. Note that the polynomial is over-fitted.

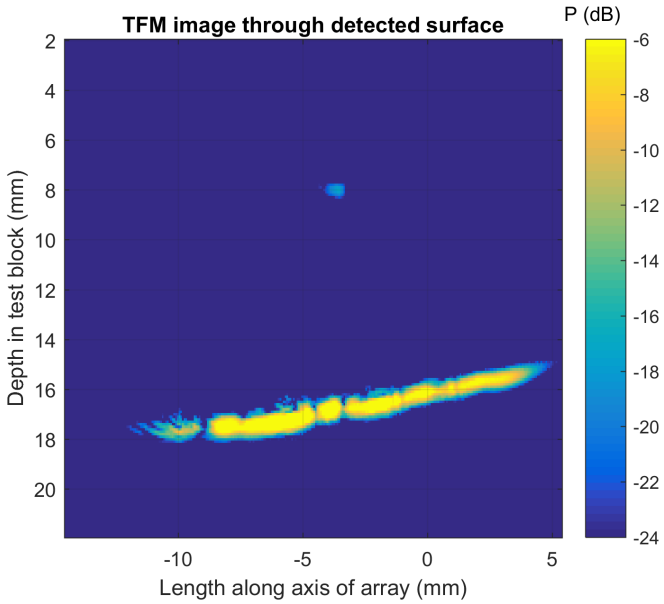

Figure 3.2.3: Example corrected TFM image created using cueART, created by updating ToF values to those expected from an interface extracted from surface TFM image such ts the one shown in Fig. 3.2.2. Once the fitted surface is used to update the ToF values in the image, the flaw and backwall can be seen below the surface.

3.2.2 SURFACE METROLOGY AND HIGH-VOLUME METROLOGY TO SUPPORT NDE ACTIVITY

It was stated in Section 3.1.1 that the inspection is sensitive to probe position. While phased arrays can compensate for surface variation, it was thought wise to improve the accuracy and precision of a robotic scanning system as much as is feasible. Accurate representation of the component allows volumetric mapping of NDE data to components [96], however it has been shown [97] that overlapping TFM images can be used to compensate for robotic positioning inaccuracy.

This ensured the adaptive capabilities of an array were used to correct for irregularities in the component surface, rather than correcting for errors in probe position.

Two types of metrology system can be used to improve accuracy of a robotic scan.

The first type is that for surface representation. These systems measure the surface shape of a component. Giving an accurate surface geometry for the component then allows a curve-following probe path to be developed that maintains normality to the component surface. A method of surface metrology is deployed using ultrasonic ToF, as described in Section 3.1. Ultrasonic ToF can build up an accurate representation of a component surface, however the method currently deployed relies upon sparsely spaced point measurements. The relatively sparse point-measurements of the component that are obtained may under sample the surface, compared to a more advanced surface measurement. An example of this used for robot path planning is detailed in a study by Guo [98].

The second type is the use of an external, high-volume metrology system to track the scan path of the robot in real time, and correct for any deviation from the ideal raster pattern. Positional errors during a robotic scan path can arise due to backlash or inaccurate robot kinematics.

Robot kinematics can sometimes differ from the model of the kinematics stored by the controller. When a robot is installed, "mastering" must be performed, where the technician manually jogs the angle of joints to a pre-set position using a mastering tool. Once the robot is mastered, the kinematic model should be accurate.

Errors can occur in this process, and even if the process is carried out correctly, there is inherent manufacturing variation between different robots of the same type, including link length or flexibility.

Over the lifetime of operation of the robot, collisions with the end effector can lead to joints becoming misaligned, and cause the mastering of the robot to fail. The kinematics of the robot have diverged from the kinematics stored by the controller, and therefore the accuracy of the robot cannot be guaranteed. Absolute accuracy is very important for critical component inspection purposes, as the entire path of the robotic motion must be trusted. One option is to use an external metrology system as a measurement reference.

While a scan path produced from a surface metrology process will be accurate in the part co-ordinate system, if that part co-ordinate system is not well-aligned with the robot co-ordinate system, the absolute accuracy of the probe position will be wrong. This is otherwise known as linking the TCP co-ordinate system with the base co-ordinate system, and is discussed in Section 3.2.4. With an incorrect representation of the co-ordinate system, this could lead to probe scanning at an angle other than normal-to-surface; potentially reducing the signal.

Only surface metrology was considered in this work, however work assessing the accuracy of robotic scanning using external metrology systems is closely related, and could improve the performance of techniques described here [29].

3.2.3 SURFACE METROLOGY OF WAVY PLATE

To measure the plate, a FARO arm coordinate measuring machine [99] was used. Using precise encoders at each joint, together with a laser line probe at the tool tip, this equipment translated operator movements at the tip into a point cloud representing the component geometry.

Lines along the surface profile were recorded, by calculating the distance between the transmitted laser light and the surface reflections. Together, these produced the point cloud shown in Fig. 3.2.4 a). Verisurf software was used to create a mesh from these points, with a specified minimum distance between mesh nodes of 1 mm. This was much denser than the 50 mm sampling frequency used in the original UT spot measurement technique. In total, 2 million points were recorded in the point cloud.

It should be noted that the laser scanning process was carried out manually, and took a long time (2 hours). A quicker solution would be to automate a Leica T-scan, or a photogrammetry system, something which has been explored at the University of Strathclyde for the application of composite panel measurement [37].

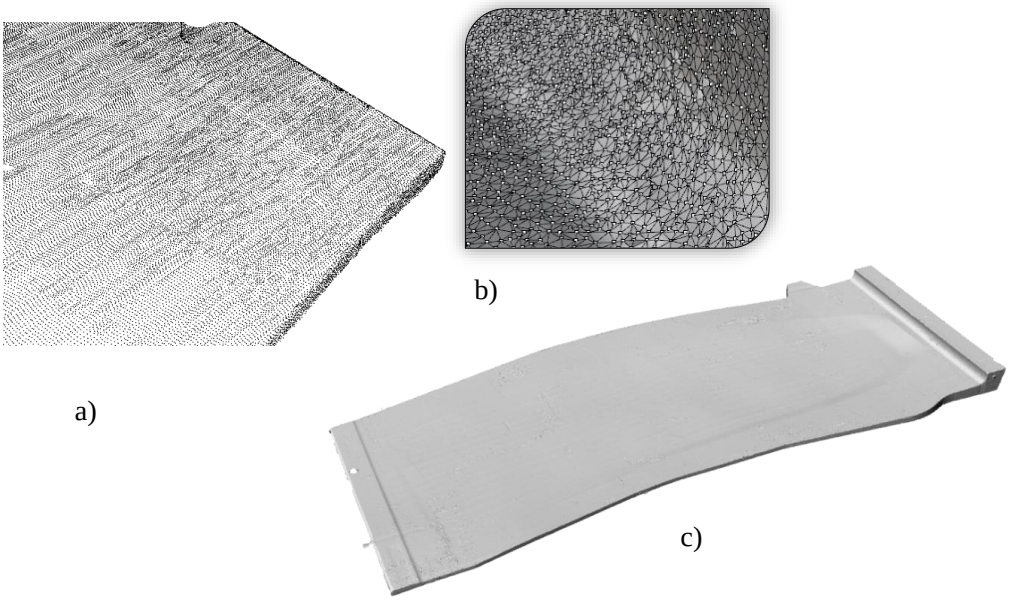

Figure 3.2.4: Digitised plate geometry. Point cloud (a) created by FARO arm. Surface representation obtained by meshing points near curved root region (b). Overall component geometry is then accurately represented, with maximum node spacing of 1 mm (c)

For the purposes of this chapter, however, the surface profile is said to be representative of the type of data that could be obtained in a metrology process, and is used to develop the automated NDE technique.

3.2.4 ROBOTIC MANIPULATOR TERMINOLOGY AND BACKGROUND

The definition of a robot is given in the Oxford English Dictionary as: "A machine capable of carrying out a complex series of actions automatically, especially one programmable by a computer" [100]. By this definition, the original scanning tank used for this process classifies as a robot. To be more specific, it is a Cartesian robot with a 2-degree of freedom articulated wrist [101]. For clarity, this robot is referred to here as the "tank".

Degree-of-freedom (DOF) refers to the number of either linear or angular joint displacement variables that are required to fully describe the state of the system. For example, the position of the probe on the tank is fully described by the X, Y and Z values of the linear stages that make up the Cartesian scanner, and the orientation is determined by θ_1 and θ_2, the tilt angles of the wrist. The

combination of position and orientation is referred to as robot "pose", and in this case, pose for the tank Γ_t can be written as $\Gamma_t(X, Y, Z, \theta_1, \theta_2)$.

Calculating Γ_t for a given $X, Y, Z, \theta_1, \theta_2$ is a straightforward case of applying each translation and rotation to the probe. This is known as the forward kinematic problem. For NDE, we would like to specify the required pose (i.e. at a particular position, with orientation normal to the surface), and calculate the values of $(X, Y, Z, \theta_1, \theta_2)$ required to attain this. This is known as the inverse kinematics (IK) problem

Both the forward kinematics and the inverse kinematics of a robotic system can be solved by co-ordinate transforms. The inverse kinematics problem is generally more computationally intensive, and also presents further problems; there could be more than one set of displacement variables that obtain the required pose solution, or there could be none.

An NDT scan set to follow a surface at a specified standoff consists of many different poses, joined together into a scan path. If there are no continuous path solutions, a scan path can be broken into two. This is undesirable however, as it adds to the overall scanning time.

The tank calculates a new scan path for each plate. However, it does not do so completely from scratch. Rather, it uses a pre-programmed path to drive the probe to points on the plate spaced approximately 50 mm apart. The pre-programmed path is based on a nominally planar plate geometry. The probe stops at each point and adjusts θ_1 and θ_2 until the maximum frontwall reflection is received by the probe. These values are saved and then used to update the pose required at each location, and in turn, the inverse kinematics are used to determine the joint displacement variables. The final inspection scan then uses this new path to maintain probe normality, and therefore ultrasonic coverage, across the part.

This process is tailored to the specific component in question. One motivation of this study is to deploy a more general-purpose manipulator to create a more general solution to ultrasonic scanning of complex components. Benefits of this approach centre around the opportunities afforded by the platform. Manufacturing processes and component handling could be performed by the same type of robot used for inspection. Increasingly, more advanced pick-and-place, obstacle avoidance, path correction, and collaborative human-robot-interaction abilities are incorporated into these systems. This move therefore helps to demonstrate

that NDE can be further embedded into high-value automated manufacturing processes.

One type of widely used, general purpose manipulator is an articulated, six-axis serial revolute joint manipulator. These have been used for many other industrial applications [102], and there is ongoing research onto their applications in NDE [10, 28, 30, 31]. In this study, this type of robot will be referred to as the "robotic arm", or "arm" to distinguish it from the robotic tank.

For the tank, the probe pose can be transformed in the fashions shown from a)-c) in Fig. 3.2.5, while for the arm, pose can be transformed in the fashions shown in a)-d) due to the extra degree of freedom.

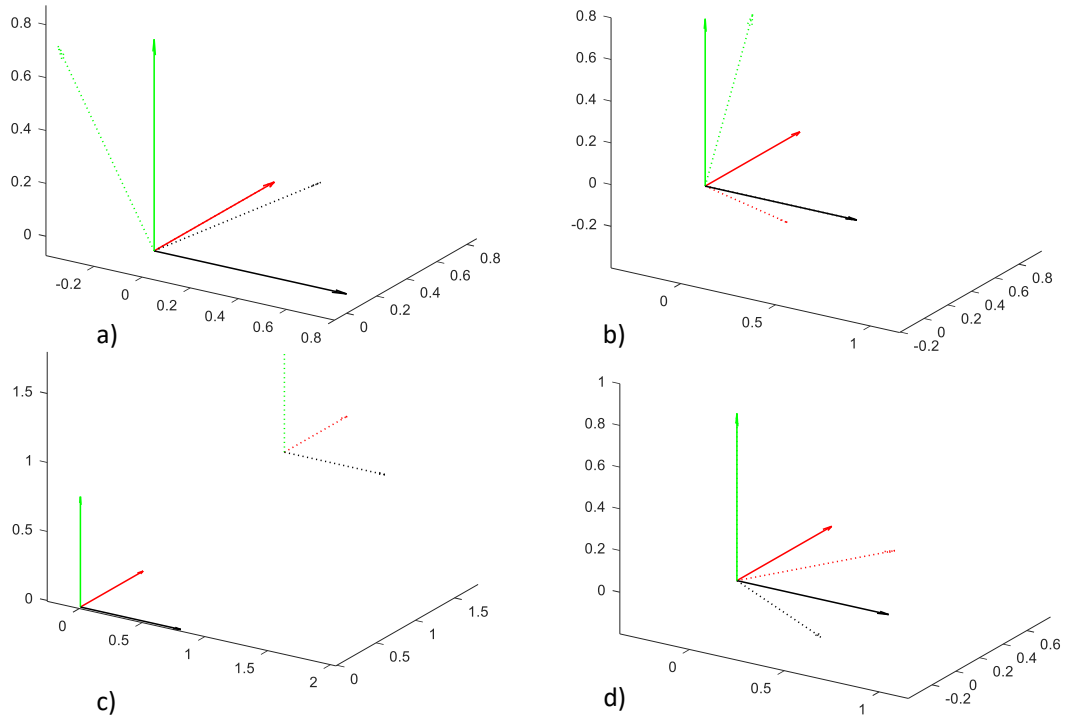

Figure 3.2.5: Rotation and translation of co-ordinate systems performed by robot. Probe face orientation relative to co-ords is shown at origin of c). X rotation shown in a), b) shows Y rotation, c) shows translation and d) shows Z rotation. z-axis is green, y-axis is red, and x-axis is black. Original co-ordinate system shown in solid lines, and transformed shown in dotted lines.

Pose for the arm is expressed as $\Gamma_a(\theta_1, \theta_2, \theta_3, \theta_4, \theta_5, \theta_6)$, where θ_x is the angular displacement of axis x. These axes are shown in Fig. 3.2.6.

Pose is entirely determined by the cumulative rotation of axes 1-6, and transla-

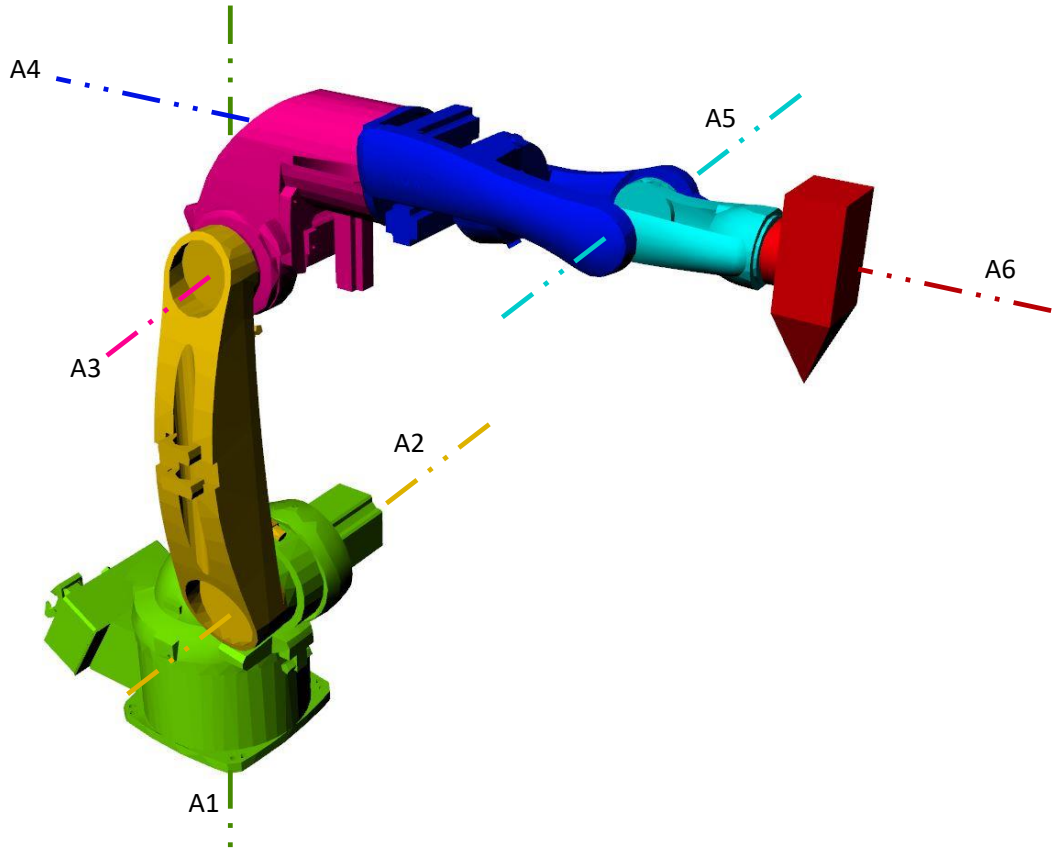

Figure 3.2.6: Robot arm revolute axes. Axis number A_x corresponds to angular displacement variable θ_x.

tion of the links between these axes. In order to follow a straight line, the robot must rotate its axes at different speeds in parallel. The result is a more complex IK calculation, which can result in singularity (as shown later in Fig. 3.2.11). The robot is controlled by a KUKA robot controller, which automatically calculates the inverse kinematics required to drive the end effector to a specified pose. KUKA Robotic Language (KRL) is used to specify a series of motions for the robot to execute, and the controller translates this into different speeds to rotate axes 1-6.

To ensure accurate motion control of the probe, it is necessary to ensure the co-ordinate systems of the robot, the part, and of any other systems are aligned. These are shown in Fig. 3.2.8. The transform between a) and b) is based on the robots kinematics, measured by the internal encoder system. Knowledge of c) depends on the geometry of the NDE tool. In this illustration, it is a small phased array on the end of a rod. The TCP is defined by use of a spike to define a point in space, and having the user carefully drive the TCP to and from this

point from different directions. The TCP coordinate system is then calculated from the robots kinematics. To define d), the robot was driven to the origin and along the desired x and y axes, and again the kinematics were used to define its position in space. This process is illustrated in Fig. 3.2.7. The KUKA system then automatically calculated an error in the TCP configuration. Riise discusses an improved technique for finding the TCP of a phased array in [103].

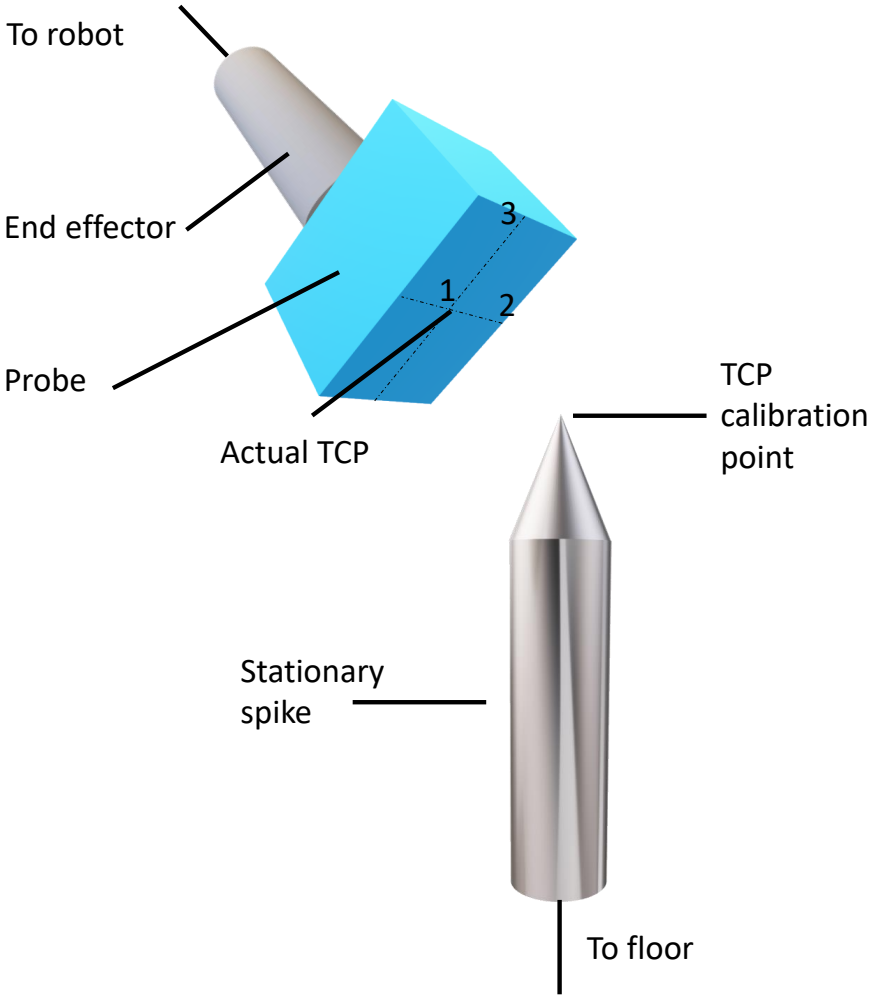

Figure 3.2.7: Illustration of TCP calibration procedure. Robot is driven to point 1 from four different directions. Then, probe is drive to point 2 to define the x-axis of the plane of the probe face, then point 3 to define the y-axis of the probe face.

An alternative method to define the position of a)-d) is to use an external metrology system, to define a global coordinate system. The benefit of this is that any errors in the robot kinematics, or dynamic behaviour, do not propagate into an NDE encoding error. A laser tracker could be used for this purpose, essentially tracking c) and d) and correcting the position of the robot. Use of metrology

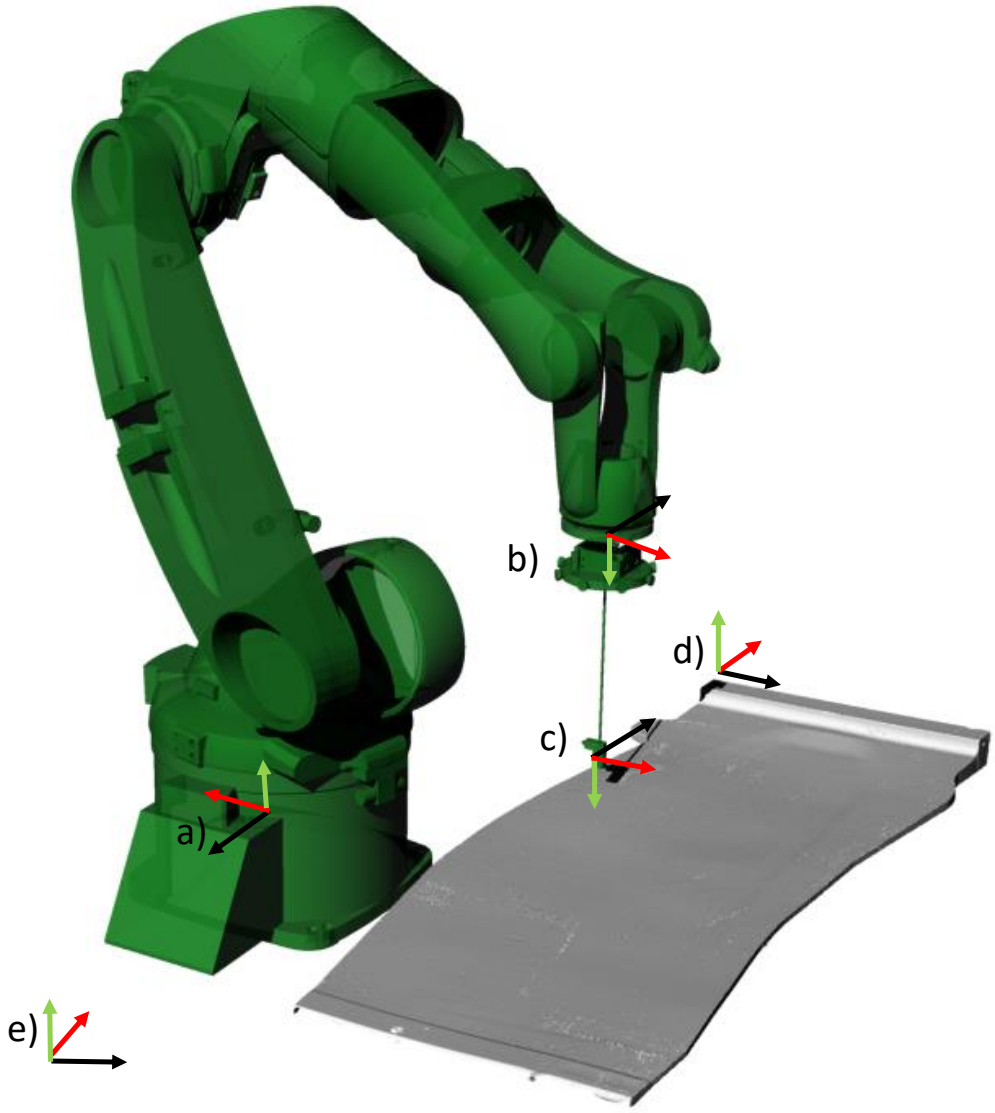

Figure 3.2.8: Coordinate systems used for robotic NDE Scan: a) robot base, b) robot flange, c) tool centre point (TCP), d) part origin and e) world co-ordinate system

.

systems to perform path-correction such as this is an ongoing research interest at the University of Strathclyde [29] and elsewhere.

The arm shown in Fig. 3.2.6 and in Fig. 3.2.9 is a KUKA KR5 HW-2; with a maximum payload of 5 kg, a hollow wrist to allow cable routing, and reach of up to 1423 mm. It was used in conjunction with a KUKA KRC-2 robot controller, which used KRL to execute motion commands.

Different movement types are shown in Fig. 3.2.10. Point-to-Point (PTP) motion

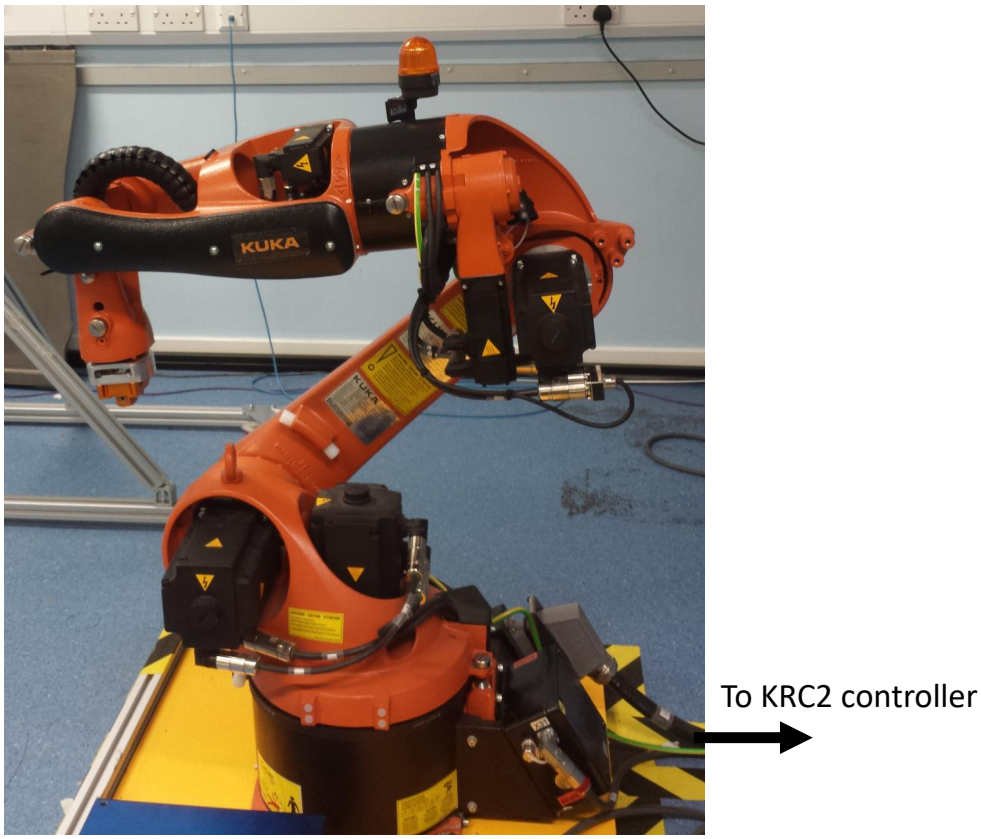

Figure 3.2.9: KUKA robot arm used in study.

drives the TCP to each point in the fastest possible path. This path is determined by the kinematics of the robot itself, and is not defined by the user. This is useful for when speed and position are important, but the path taken by the TCP is not important; such as at the beginning or end of a robotic scan. In order to accurately follow a path, it is necessary to use either linear (LIN) or spline (SPL) commands. Spline curves have the advantage that they can more closely follow a given path, however it is more complex to split up a measured CAD surface into practical spline curves. One problem is that overfitting can lead to unstable behaviour.

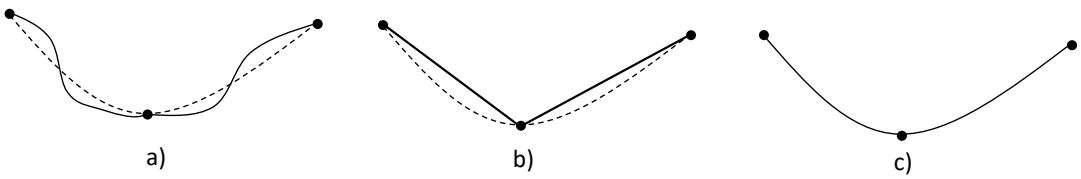

Figure 3.2.10: Robot motion types: a) Point-to-point (PTP), b) Linear (LIN) and c) Spline (SPL).

While it was possible to program the robot procedurally for simple and regular shapes by writing motion commands directly in KRL, this approach was impractical for irregular parts. This is because each small section of the path would have to be manually reprogrammed each time. Offline path planning techniques can be used, using CAD of the part to automatically generate the code required to follow a given scan path. The next section describes the development of an OPP method for this inspection.

3.2.5 OFFLINE PATH PLANNING USING GRASSHOPPER PARAMETRIC CAD

The component geometry shown in Fig. 3.2.4 was imported into RhinoCAD. Grasshopper and KUKA|prc were used to develop an application for NDE scanning of parts. This section highlights and explains some of its key features.

KUKA|prc allows simulation of the robot kinematics for a desired path. This ensures that the path does not produce a singularity, or any collisions, in the course of the inspection. It is useful to be able to predict the occurrence of kinematic singularity, as this restricts the workspace in which it is possible to perform the NDE scan. KUKA|prc allows the user to set the relative location of the component and the robot such that singularity is never reached.

An example of singularity simulation is shown in Fig. 3.2.11, where the robot follows a small curved path from left to right. The required movement of the tool tip from a) to b) is rather small, but this in turn requires a significant change in configuration in the axes of the robot. Axis 4 is highlighted by KUKA|prc to show that in order to follow the desired path, the axis would have to go through singularity. Note that in c) the robot has to again rotate axis 4 beyond its limit to follow the path.

This shows how the kinematic preview can help locate the component in the correct position prior to scanning. To solve the issue in Fig. 3.2.11, the component should be moved further from the base of the robot.

KUKA|prc allows the user to approximate an ideal curve with a combination of motion commands for the robot. Motion can either be point-to-point (PTP), linear (LIN) or spline (SPL). PTP motion was chosen for probe positioning prior to pulsing the transducer, and once the capture is finished, as it is the fastest. SPL and LIN motion was used where it was important to maintain orientation of

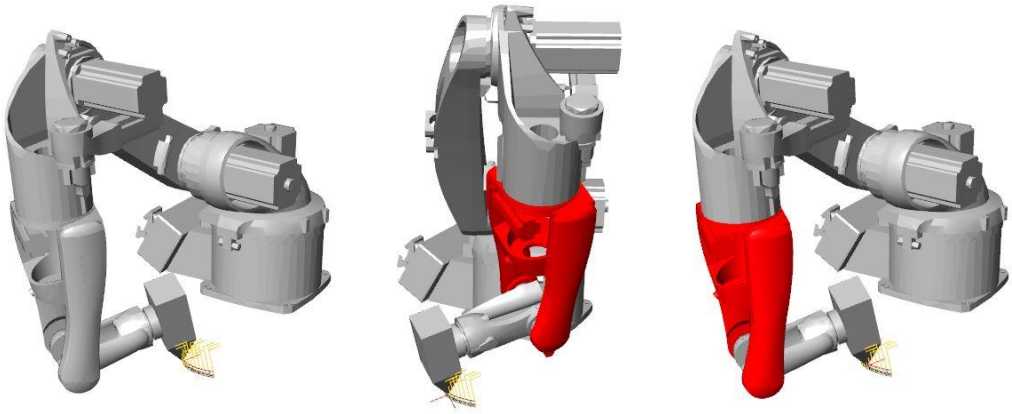

Figure 3.2.11: Example of KUKA|prc highlighting a singularity on a proposed robotic scan path. Tool moves in small increments along curved path, with a) a non-singularity configuration, followed by b) a singularity on axis 4, which would require very sudden repositioning c) for a very small TCP movement.

the probe, as these modes constrain the orientation of the probe, unlike the PTP mode. An example SPL scan path across the component is shown in Fig. 3.2.12, and the code to generate is shown in Fig. 3.2.13, which includes a custom-made "UT immersion toolpath" module.

The red surface shown in Fig. 3.2.12 is a Non-uniform rational B-spline (NURBS) surface [104] fitted to the mesh generated in Fig. 3.2.4. This created a smoother representation of the surface, helping to provide a more continuous target for the projected points that were used to create the toolpath.

For scanning using a rotationally-symmetric probe, assuming the beam was axially symmetric, it was inconsequential to rotate the probe while scanning took place. This was not the case for the 1D phased array probe used, therefore the toolpath was designed to maintain orientation of the array probe. Diagram Fig. 3.2.14 shows an example path drawn around the plate by the user. This was then converted into a probe inspection path by the process illustrated in Fig. 3.2.15. This shows the probe tilting to accommodate local surface curvature.

Firstly, the curves drawn by the user on a plane from the top-down view were taken to be the desired path of the probe if it were traversing a perfectly flat plate. These curves were split into a number of points, which were then projected

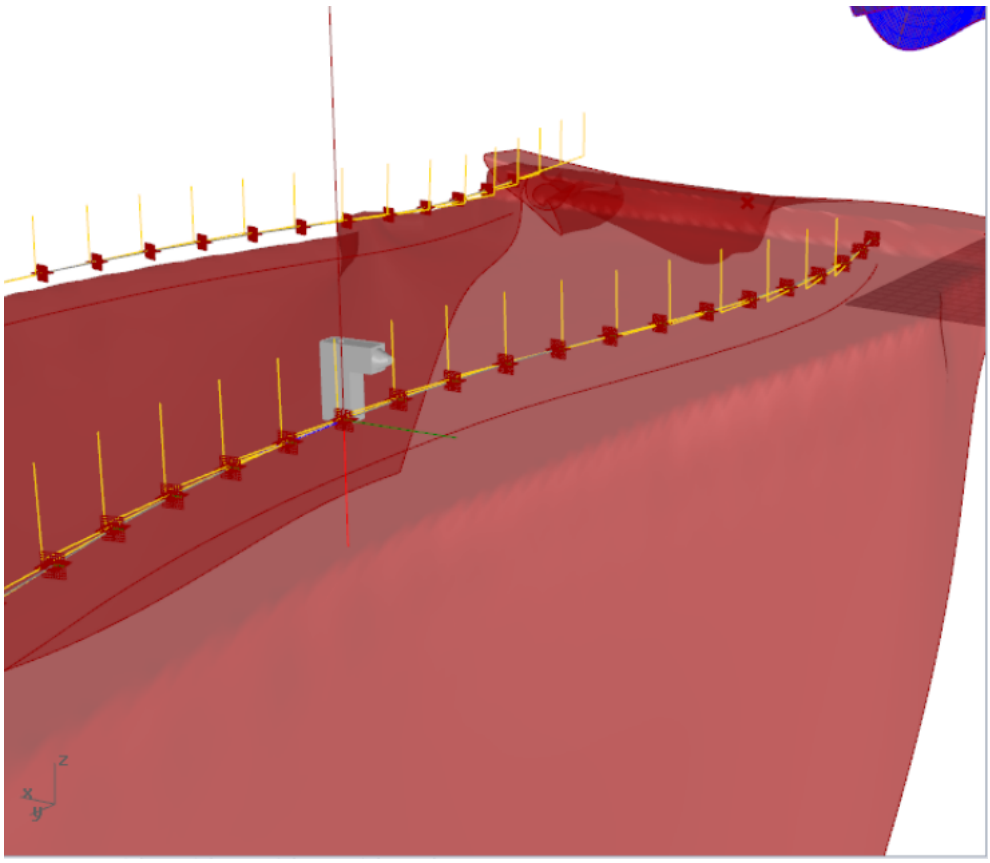

Figure 3.2.12: Single spline pass showing probe positions across plate in Rhino viewer window.

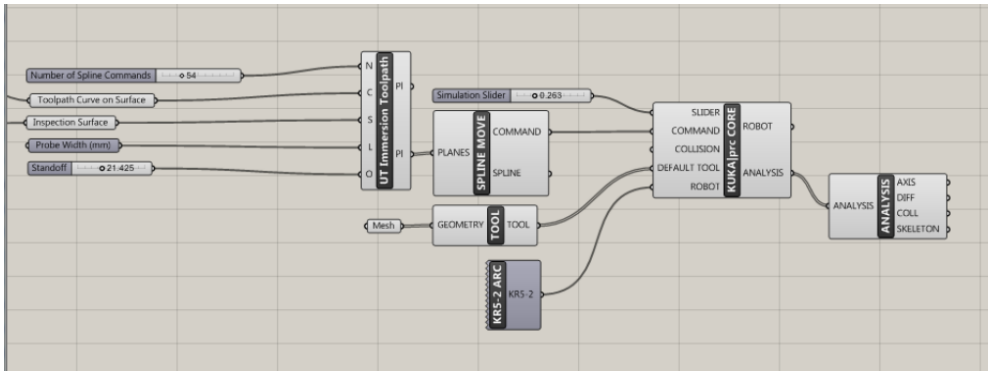

Figure 3.2.13: Grasshopper modules used to process the input of desired toolpath curve, and inspection surface using "UT Immersion Toolpath" module.

vertically, through the component. In this way, the intersection points with the component were found, which could then be used to calculate the average surface normal over the relevant area of the scan. These points were then transposed vertically, to provide the required standoff for the immersion inspection.

It was assumed that the mean geometry of the plate did not differ significantly

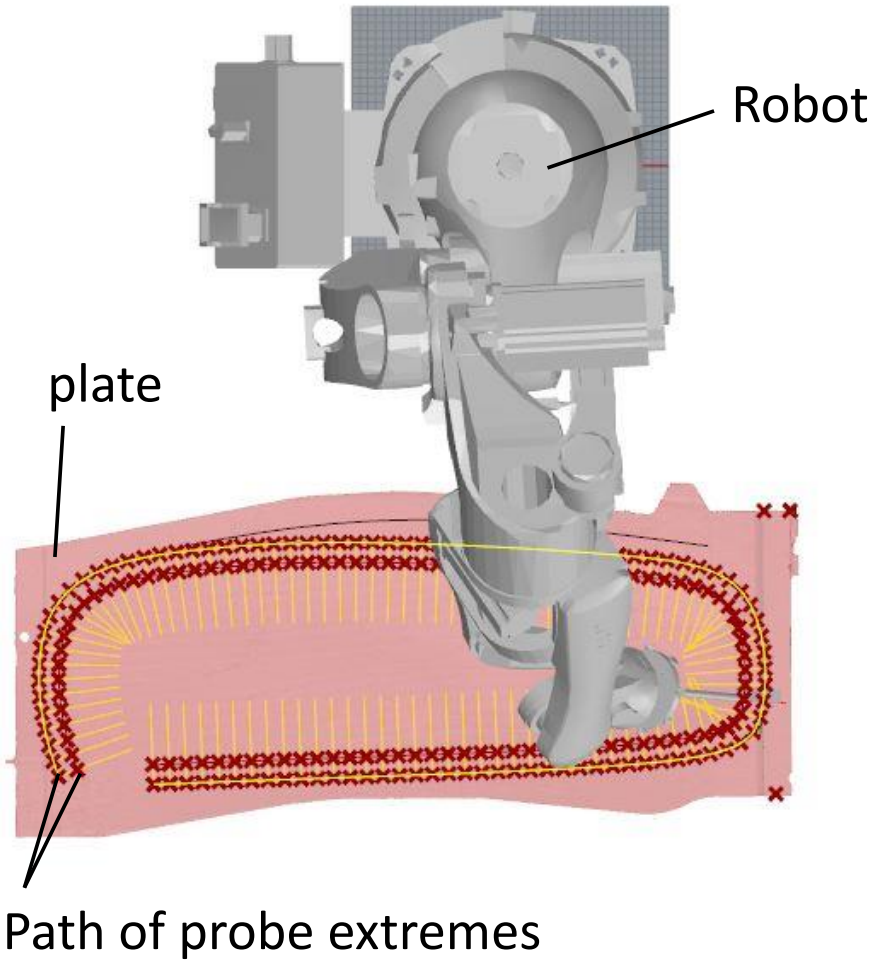

Figure 3.2.14: Example scan path, using intersection between probe edge paths and component to determine probe tilt angle (top view).

from a plane surface, and that a projection of the scan path from a plane onto the component would not result in large differences in scan path geometry. Were the component spherical, for example, this assumption would have to be revisited, as the projection from the desired path to the path calculated using intersection points may be large. This approach was therefore limited to surfaces deviating slightly from planar geometry. Segment width was increased for clarity in Fig. 3.2.15, but was more typically chosen at 1 mm intervals. Rather than just use the edge points of the array to calculate the surface normal, the average distance from each array element was also used to build a more robust curve-following method; however the principle remained the same.

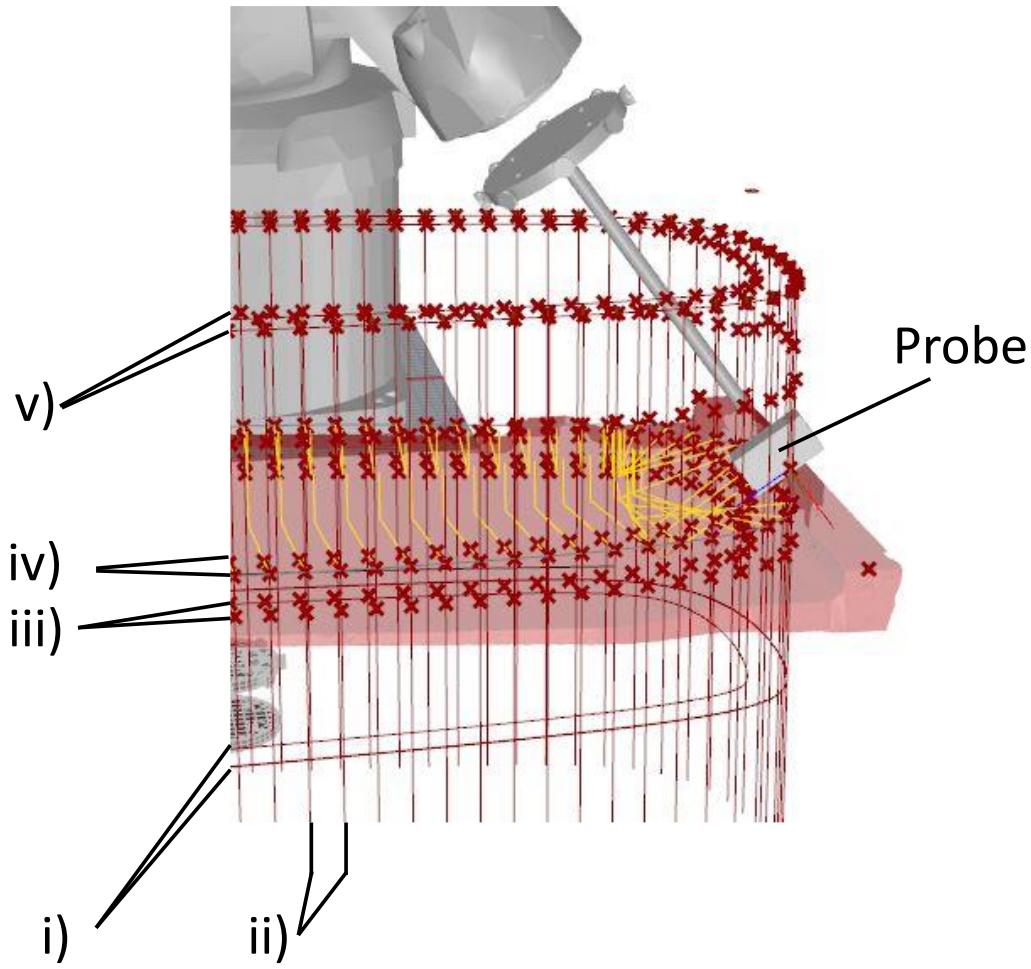

Figure 3.2.15: Using Grasshopper to maintain probe normality. i) path for probe to follow is specified by user, ii) path is divided and projected through part, iii) intersection points are calculated, iv) standoff is added to change probe position. v) shows extent of projection.

Following calculation of the points, the robot positions were then simulated across the entirety of the scan. Once there were found to be no cases of singularity or collision, the scan was said to be valid for execution. KUKA|prc automatically saved KUKA Robot Language (KRL) in an output file, which was then used with the robot control unit to execute the scan.

3.2.6 VISUALIZATION OF NDE DATA

Further to path-planning calculations, Grasshopper provides opportunities for data visualisation. A Grasshopper module was created to display TFM B-scan information at the relevant point where the robot captured data from the scan.

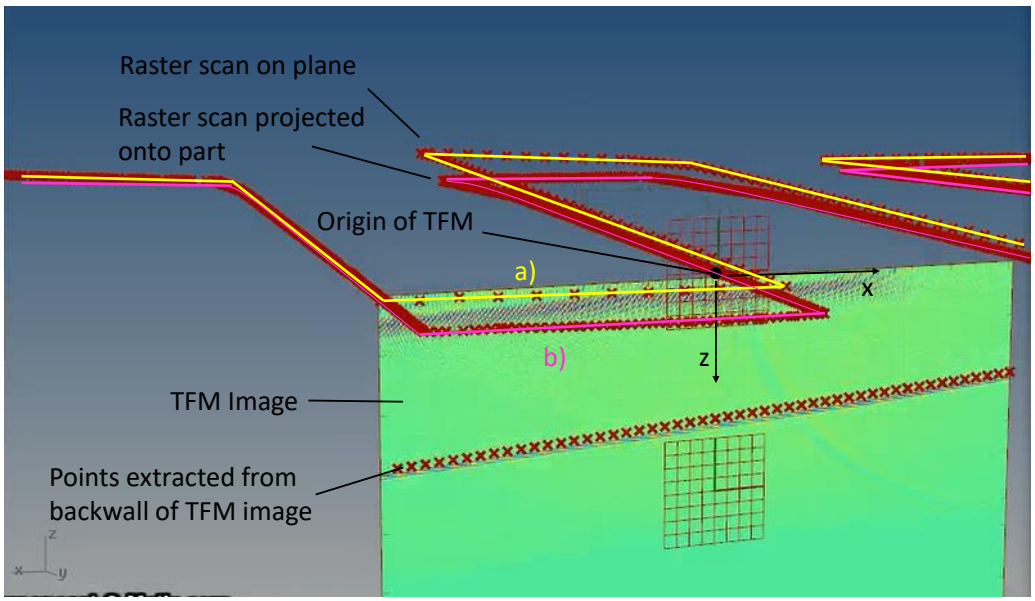

Figure 3.2.16: TFM B-scan projected onto scan path using Grasshopper.

In Fig. 3.2.16, a TFM B-scan is shown superimposed at the relevant scan position. The speed of ultrasonic data acquisition was not controlled or entirely regular, so the position of the robot was saved every time an acquisition was made. These positions are shown by a). Point series b) in Fig. 3.2.16 are the positions on the plane just above the component surface that were used to generate the scan path. Note the path of the raster pattern on the plane diverges from the curve-following path on the extremities of the plate.

The module developed allowed the user to scroll through different scan positions and examine the TFM image captured at that location. Further, a method to extract the backwall geometry was created, which thresholds the image within a certain gated region, and converts the results into point objects in the Rhino interface.

This section has described the key features developed in Grasshopper to support the robotic scanning of this project. The next section discusses the integration between the robot and the FMC enabled UT system.

3.2.7 HUMAN-MACHINE INTERFACE

The HMI developed in the course of this work was produced for the purposes of this research only, and therefore is limited in terms of its completeness. While it does not provide a complete solution for everyday use by an NDE technician, it does have some useful elements to assist with offline path planning for a robotic inspection.

The strategy for HMI development was to use as many of the built-in features of Grasshopper and KUKA|prc as possible to create an easy to use interface to aid offline path-planning for inspections.

As Grasshopper is a graphically-based programming language, the user interface is incorporated into the logic of the code. Inputs include sliders, input blocks which relate to CAD components, and processing blocks including the program logic. When combined together, these are called Grasshopper definition files. In Fig. 3.2.17, the definition file is shown on the right hand side, changes to which cause an instant update in the CAD window shown on the left.

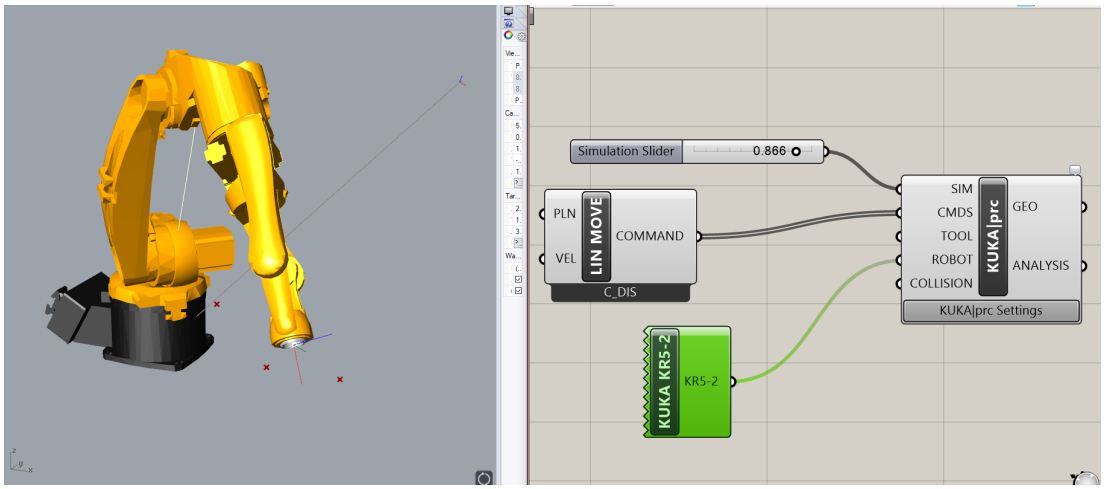

Figure 3.2.17: Split-screen workflow. On the left, the CAD window shows the position of the robot at a particular step in the simulation, which is controlled by the simulation slider shown in the right hand side. The right hand side is the Grasshopper definition file, and contains the user inputs, as well as logic of the OPP program.

An example path-planning problem is shown here as a demonstration. The aim is to import a set of points that have been extracted from an image processed in MATLAB, fit these points to a plane above the CAD component, project these points onto the component, and then program the robot to follow a curved path through these points.

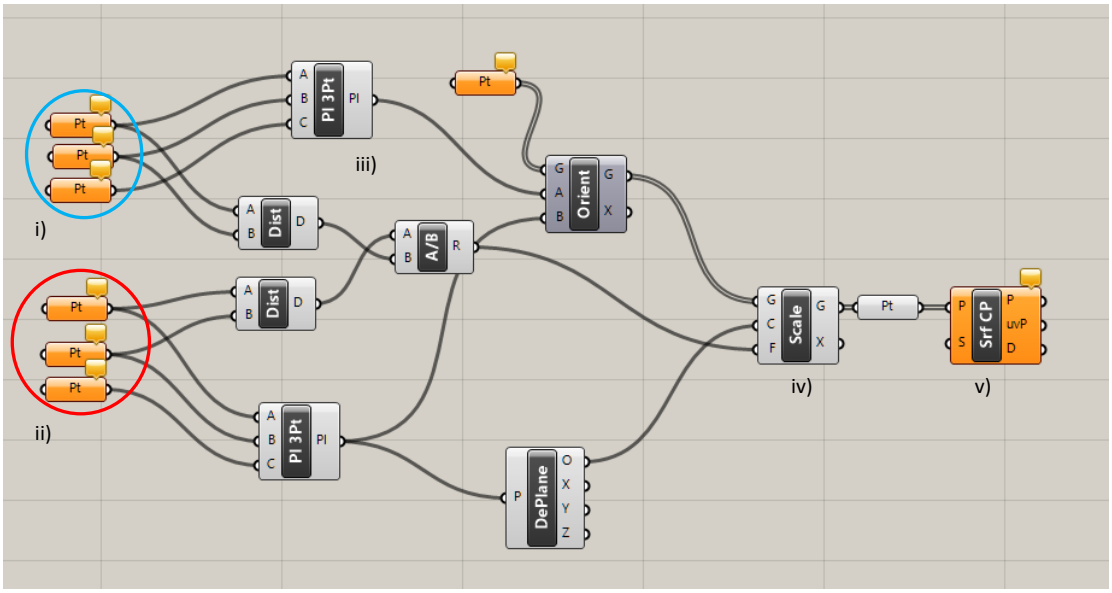

Figure 3.2.18: Grasshopper definition snippet. Point inputs in i) and ii) show the user that references must be selected for i) the CAD part, and ii) an image processed to show where flaws are expected. A plane is defined from these points in iii), and then used to scale the image to fit over the part in iv). The closest point from the projected image to the surface is calculated using v), and this projects points onto the CAD model surface.

Firstly, the points are imported from MATLAB. In order to scale them, the definition in Fig. 3.2.18 is used. The user must select three points in the CAD window defining the extent of the containing rectangle for the three points, and another three points in the CAD window defining the boundary of the CAD part. These points are converted to planes, and the relative distance between the points is used to scale the arrangement of points. The planes are used to re-orient the imported points onto the projection plane directly above the part. Finally, the closest point from the projection plane to the surface of the part is calculated using the built-in Grasshopper block shown in iv), and a set of points are then added to the part surface.

Next, the projection plane is oriented above the CAD surface relative to a plane, defining zero stand off. This is accomplished by the user drawing two curves on a flat area of the part (or otherwise producing two curves in the desired standoff plane). The definition for this is shown in Fig. 3.2.19, and the resulting image seen in the CAD window is shown in Fig. 3.2.20.

Next, the inspection surface defined (surface where the inspection is at zero stand-

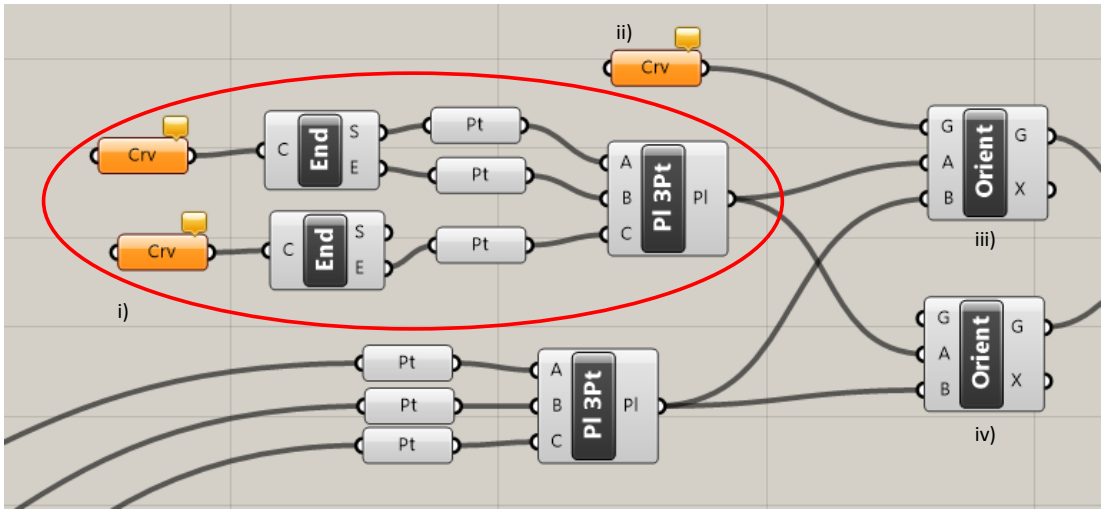

Figure 3.2.19: Two curves are drawn by the user to select perpendicular sides on the part for orientation of the projection plane at i). A curve is then added in the CAD window and linked to ii), and these are both oriented on the projection plane iii) and iv).

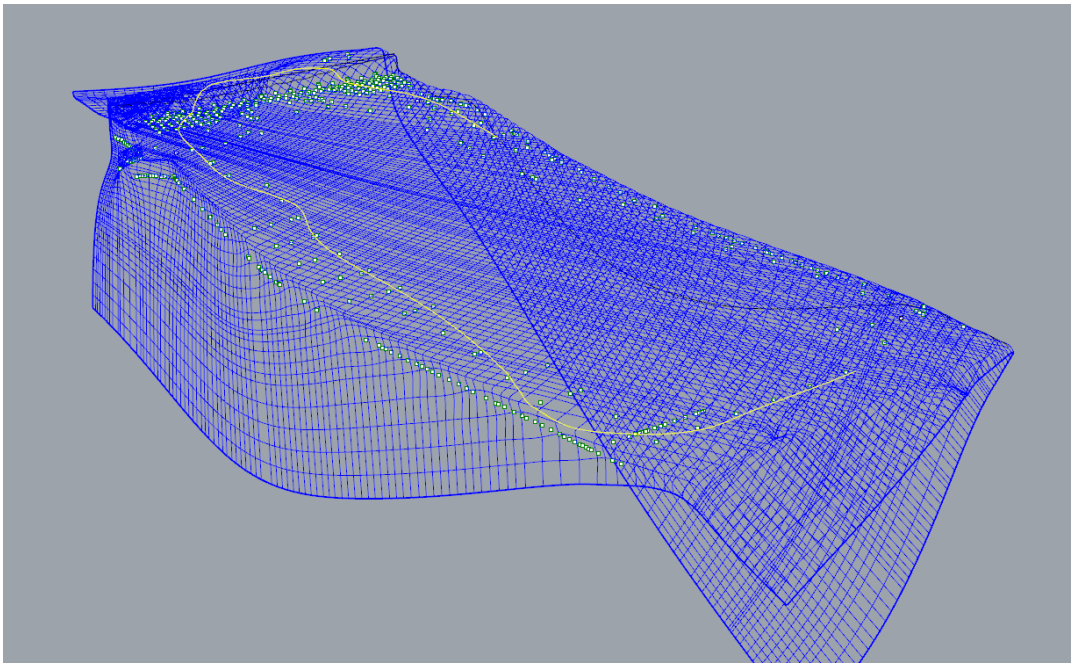

Figure 3.2.20: Curve shown in yellow is drawn through points projected from a plane onto the uneven surface of the plate. Later steps convert this curve into a series of planes, and translate the curve away from the surface to account for probe standoff, from which the robot scan path can be calculated.

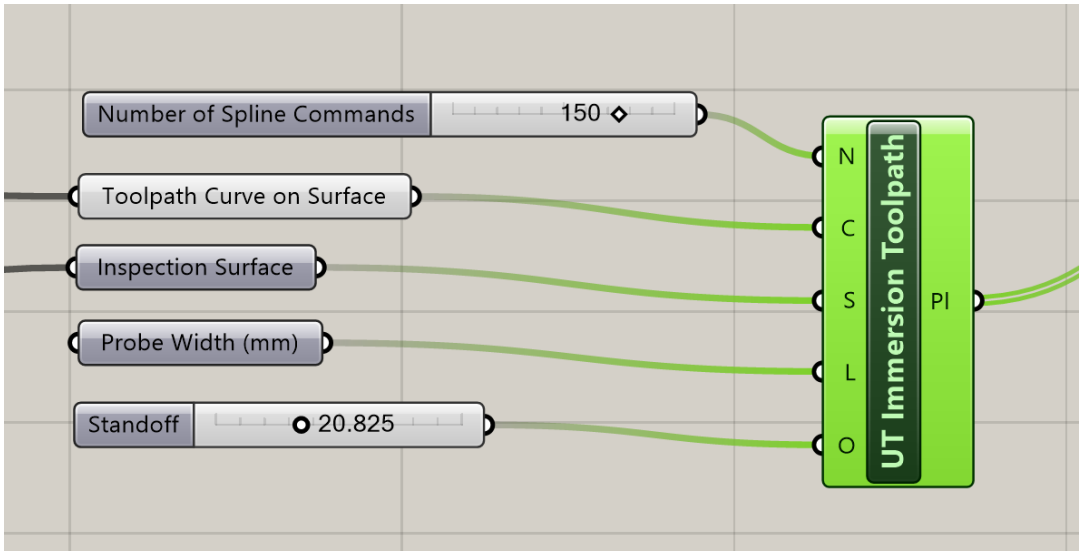

Figure 3.2.21: The "UT Immersion Toolpath" block contains the core of the path generation code. This splits the toolpath that has been defined by the user into a number of commands defined by the slider at the top. This then uses the inspection surface, probe width and standoff to create a list of planes to define probe positions for the scan.

off), and the toolpath curve drawn in the CAD window, is converted into a series of planes defining the probe position required for the scan. Other inputs include the number of spline commands to use, which determines how many "spline" commands are called by the KUKA robot. High values can increase the simulation time for previewing the robotic scan, whereas low values can result in a poor approximation of the desired toolpath curve. Probe width and standoff are included. Different probe widths result in different step sizes between raster scans if raster mode is enabled. In this case, raster mode is not used, so only the standoff has an effect. This alters the z-distance from the TCP to the surface point. The definition implementing this is shown in Fig. 3.2.21

The UT immersion toolpath module converts these inputs into a set of planes, which describe the position and orientation of the probe sufficiently for input into the KUKA|prc components.

The final part of the interface is shown in Fig. 3.2.22. Spline movements were converted to commands using the SPL MOVE block. Following this, the robot can be visualised following the chosen toolpath by use of the simulation progress slider. Tool geometry was defined according to CAD of the probe and mount. The user must select the "Geo" input block to link this. The final input is the robot, in this case a KUKA KR5. In order to select a different robot, the user

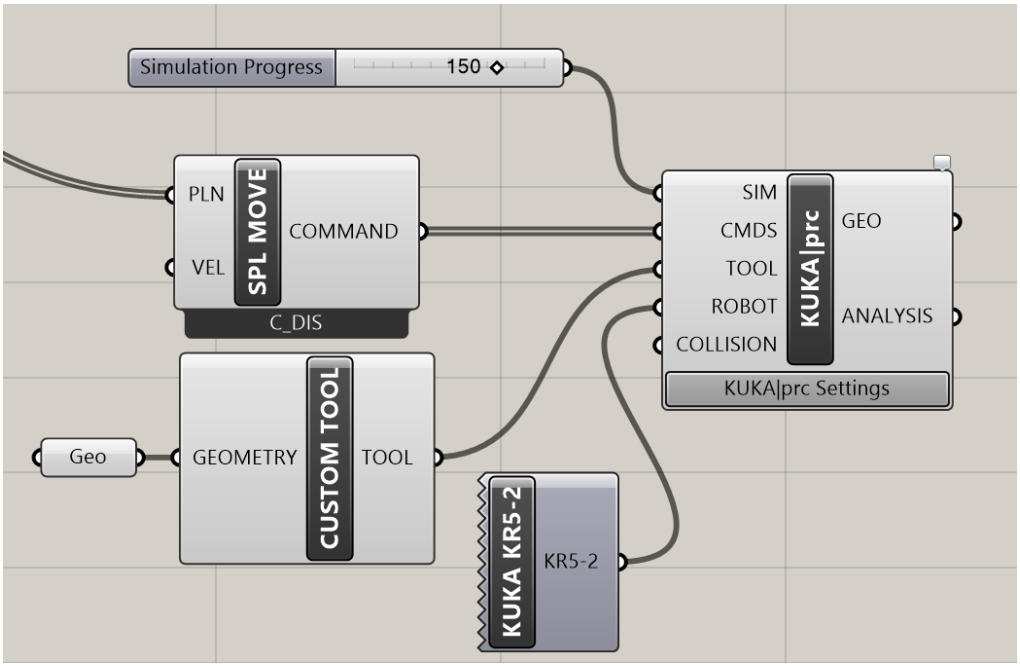

Figure 3.2.22: The connection between the NDE input interface and the core KUKA|prc block. The simulation process slider updates the robot position in the connected CAD window. The SPL MOVE block converts the planes output by the previous process into spline commands for the robot to execute. The CUSTOM TOOL block allows the UT probe and mount assembly to be factored into the inverse kinematics of the robot. The KUKA KR5-2 block contains data about the particular model of robot used, including the length of links and the orientation of rotational joints.

can drag out the KR5 block and replace it with another robot.

Using the KUKA|prc core block on the right hand side, the code for the robot was generated. This was then transferred to the robot controller for execution.

3.2.8 REVIEW OF HMI DESIGN

Peter Zhang [105] states that there are six main design principles to consider for a HMI. As this HMI borrows the functionality of Grasshopper to accomplish a lot of the tasks attempted by the user, the whole experience of using Grasshopper together with the Rhino CAD window is included as part of the HMI for the purposes of review. The principles discussed by Zhang are listed below, alongside related analysis for the solution presented here.

The structure principle "The design should organise the interface purposefully, in meaningful ways that are apparent and recognisable to users."

- The grasshopper language gives quick visual feedback, and allows concepts to follow a natural flowchart structure
- Interconnections between blocks can quickly start to look confusing. This is lessened by colour highlighting for active blocks, but can ultimately lead to a tangled appearance. By consolidating complex code into blocks, and ensuring connections cross as infrequently as possible, a confusing appearance can be avoided.
- Inspection of individual code components can be difficult for an observer that does not have access to the CAD model to interactively probe the effects of changing the code block.

The simplicity principle "The design should make commonly performed tasks easy to do, communicating clearly and simply in the user's own language"

- For a user familiar with CAD, a series of well-labelled input points, together with the integrated CAD window, allows an efficient workflow.
- As the grasshopper code is not separate from the user input interface, it would be easy for a user to break the logic of the program by accident.

The visibility principle "All needed options and materials for a given task should be visible, without distracting the user with extraneous or redundant information"

- Modularised blocks, such as the UT Immmersion block example given in Fig. 3.2.21 can be constructed so that only necessary input options are displayed.
- Selection of datum points from the Rhino CAD window does not follow this practise, as all the unrelated CAD drawing tools are visible during this step.

The feedback principle "The design should keep users informed of actions or interpretations, changes to its state or condition, and errors or exceptions that are relevant to the user through clear, concise familiar and unambiguous language"

- Changes in state are well communicated by the instant update of the CAD model.
- This can cause problems for very large CAD files, where the update takes a long time to process. Instant update can be turned off, but this then impacts

the HMI feedback principle, making it harder to immediately understand the effects of an input change.

- While the instant feedback from the CAD model can be used to spot errors, this is contingent on the operator spotting the error. More work would be required to address specific safety concerns that are not highlighted as collisions or kinematic singularities.
- Errors are communicated clearly in Grasshopper. An error turns a component block orange, as well as downstream blocks, making it clear to see how the error impacts the process.
- Error messages used for this project were restricted to default; meaning that problems were sometimes expressed in an abstract way relating to vectors and points, rather than NDE terminology. This could be improved by writing exceptions that capture this information.

The tolerance principle "The design should be flexible and tolerant, reducing the cost of mistakes by allowing undoing and redoing, while preventing errors where possible by tolerating varied inputs and sequences and by interpreting all reasonable actions"

- As the HMI is built on top of Grasshopper, undoing and redoing is possible.
- This HMI does not have an ability to interpret varied sequences and inputs, and would require further development of the inputs to achieve this.

The reuse principle "The HMI design should reuse internal and external components and behaviours"

- Use of KUKA|prc means that a different robot can be substituted in a Grasshopper definition file to execute an identical toolpath. This will use updated kinematics and allow the operator to determine any changes that must be made to the offline programming of the robot.

In addition to these design considerations, the impact of the HMI on safety should be considered. Collision detection built in to KUKA|prc made it possible to plan paths that did not collide with the edge of the scanning tank. This was particularly important for the start and end of the scan, where it was observed that PTP motion posed a risk of collision. LIN motion was used instead to counter this.

The biggest safety concern with this offline planning approach was the alignment

of the part with the planned path. An alignment error could lead to unexpected motion of the end effector. This could be improved with an external metrology system monitoring the position of the robot.

The following conclusions about the HMI design for this project have been drawn.

KUKA|prc is an excellent tool that handles the offline path-planning of KUKA robots. Grasshopper is very flexible, can be intuitive to use, and enables instant feedback in the Rhino CAD window.

The simple HMI in this study allowed the probe to follow a scan path defined in a 2D plane, projected onto a part with a complex, curved surface, and maintain normal orientation to the surface. It enabled quick prototyping of the scan path, by changing the standoff of the probe, complexity of the path, and the shape of the path on the 2D plane.

This approach gave quick feedback on the suitability of the scan path in terms of collisions and singularities. This helped enable experimental tool path design for the work in this thesis.

The HMI developed was used in a flexible Grasshopper definition file format, rather than a locked-down user interface. This means it does not guarantee safe and robust use by a user unfamiliar with Grasshopper. The primary reason for this is the combination of code logic with user input inherent to the graphical programming approach. This presents the opportunity for a user to accidentally change code logic during input. Use of the Human-UI for Grasshopper [106] can prevent this.

The HMI developed did however afford sufficient feedback, opportunity for reuse, and simplicity to allow an NDE operator to conduct offline path planning for a robotic inspection.

The HMI was not developed further for this work as it was not an industrial priority for the overall aims of this study. Furthermore, an advanced solution for path planning was developed using a custom MATLAB toolbox during the course of this research [10], which offers a more complete solution for NDE path planning problems.

3.2.9 CODE VERIFICATION

Formal verification of the path planning code was not performed. In order to ensure safety, each path used was first executed in T1 mode, which drastically limits the tool tip speed. This also requires the operator to hold down a button and a dead-man's switch.

During development, a flat surface was first used as a simple geometry input. A raster pattern was planned using the software, and then executed using the robot. This approach was used to check the safety and functionality of that path. At this stage, the start and end of the run were changed from point-to-point motion to linear for safety reasons - collision with the scanning tank was seen to be a risk, due to the uncontrolled intermediate path of the robot between points.

Different geometries were tested as CAD inputs. It was clear that more heavily warped geometries could not be handled by the approach. This is because the approach projected a path from a flat plane to the surface of the part. The main consequence of this was that raster patterns would not maintain an even spacing, eventually leading to lack of part coverage. This was tested by the operator inspecting the CAD window.

More formal verification would be required for using the path planning in automatic mode without a first reduced-speed trial run in T1 mode. In order to implement robust verification of the code for safety-critical applications, it would be necessary to develop a set of unit-tests, system tests and user tests. This approach could also help handle more general complex geometries.

One such test could involve that the average scan-step spacing does not exceed a certain amount scanning over a set of common shapes. This information could be combined with simulated ultrasonic data to ensure that the approach delivers the required coverage.

3.2.10 REVIEW OF LIMITATIONS OF RHINOCAD AND GRASSHOPPER

RhinoCAD is a 3D modelling package, most often used by architects. It is not as engineering-oriented as other often used CAD software, such as Solidworks. Due to this, it is less intuitive for engineers to create and manipulate geometry in a controlled fashion. Part of the reason for this is the increased flexibility of Rhino,

and the focus on art over an optimised engineering workflow.

This is a disadvantage for the purposes of setting up a useful NDE inspection platform, as there are many opportunities for users to lose control of the process. As Rhino is scriptable, it is possible to encode and enforce a process for the user to follow, however this presents extra work for the developer compared to using a more engineering-oriented CAD package.

Furthermore, as Rhino is very general, its ability to conduct NDE visualisation is limited and relies upon custom scripting. For example, the image shown in Fig. 3.2.16 is carried out by loading an image file based on position of the probe in the scan path preview of the robot. This creates a short but noticeable delay (≈ 0.5 s), which would cause problems for an everyday user. Compared to a purpose-built solution, with integrated and optimised visualisation such as in Mineo's work [10], this is far slower and more awkward. The speed problems are also true for the inverse kinematic calculations, and preview scans - time taken to calculate robotic position sometimes runs into around 30 seconds. This is due to the combination of Rhino tasks, Grasshopper tasks, and the way that they are integrated. While this level of delay is acceptable for occasional research use, it falls short of the usability required by an NDE operator.

The visual programming approach adopted by Grasshopper is advantageous in that it exposes the workings of some processes in a digestible flow-chart style format. This apparent strength becomes a weakness fairly quickly as the complexity of a project progresses. Software developers require modularity and testability for any large project, and this seems to be difficult to realise using Grasshopper as a development platform. While modularity is possible by creating composite flowchart blocks, the complexity of some of the graphical code implementations was hard to keep under control.

To combat this in part, Ironpython can be used to script individual blocks in Grasshopper. This allows piecemeal application of good programming practise, however it is hard to see how well-maintained codebase could be managed in Grasshopper. Finding or creating a non-standard development approach would be an additional cost of implementing this method.

The overall issue with this approach is that it is a stop-gap between fully customised research-grade software as developed by Mineo [10], and commercial grade robotics control software.

Bearing this in mind, the combination of Rhino and Grasshopper provides a good

solution when the complexity scan path is relatively low, only a few scans require to be conducted, and where operators posses skills with the software itself in addition to NDE experience.

3.2.11 ROBOTIC C-SCAN USING TFM

A C-scan was obtained of the calibration plate, using the original single-element method. Care was taken to select a C-scan where coverage was as good as possible. This was then used to pinpoint the defect locations on the measured part geometry.

Firstly, the image from the scanner was thresholded to isolate the flaws, using the histogram to achieve maximum contrast. Next, the centroids were extracted by using the `regionprops` command with `centroid` switch in MATLAB.

These centroid locations were then projected onto the surface representing the part. Some of the resulting locations are shown in Fig. 3.2.23. It should be noted that the centroid locations projected from the thick root region are not accurately located in Fig. 3.2.23, and were not considered in the scans that were conducted.

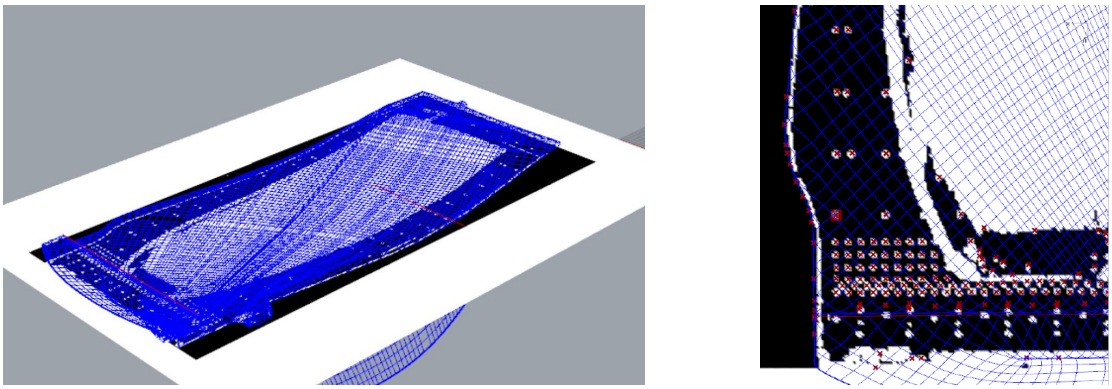

Figure 3.2.23: a) some of the points projected from image obtained from original flaw scanner onto component , b) giving locations on the surface of the component to include in the new planned path of the robot to ensure that calibration flaw targets are covered.

Owing to the large file size of each FMC frame acquired, two sub-areas were chosen for scanning rather than the whole part. These are shown in Fig. 3.2.24, and comprise of a small raster scan, as well as a continuous curved line. These paths were chosen to take into account the gradually changing curve of the planar surface, as well as the edge of the cavity region; both of which can limit imaging

capability in the original inspection. The scan aimed to cover many of the points shown in Fig. 3.2.23.

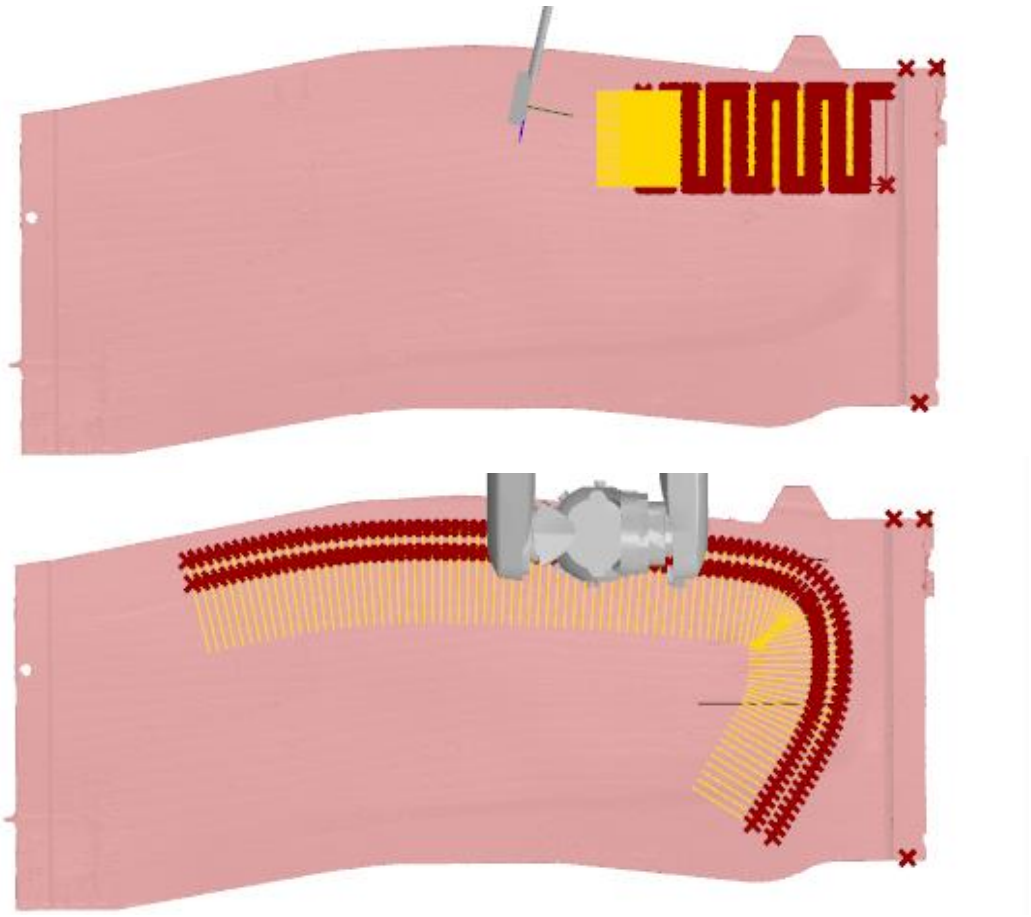

Figure 3.2.24: Sub-areas chosen for robotic FMC scans of plate. A raster scan (top) and a curved line scan (bottom) were conducted.

Rather than use an external metrology system for encoding, the co-ordinate system of the part and robot were linked, and the robot encoders were used. In order to achieve this, it was necessary to drive the robot to three datum points, shown in Fig. 3.2.26.

The KRC requires the user to drive the robot to coincide with these points on the component, using an end effector with a precisely known length. The spike of the end effector was carefully driven to the three corners, prior to the immersion tank being filled. This allowed the co-ordinate systems of the TCP and the base plane of the component to be linked. The accuracy of this relationship determined the error between the representation of the scan pattern determined in OPP, and the

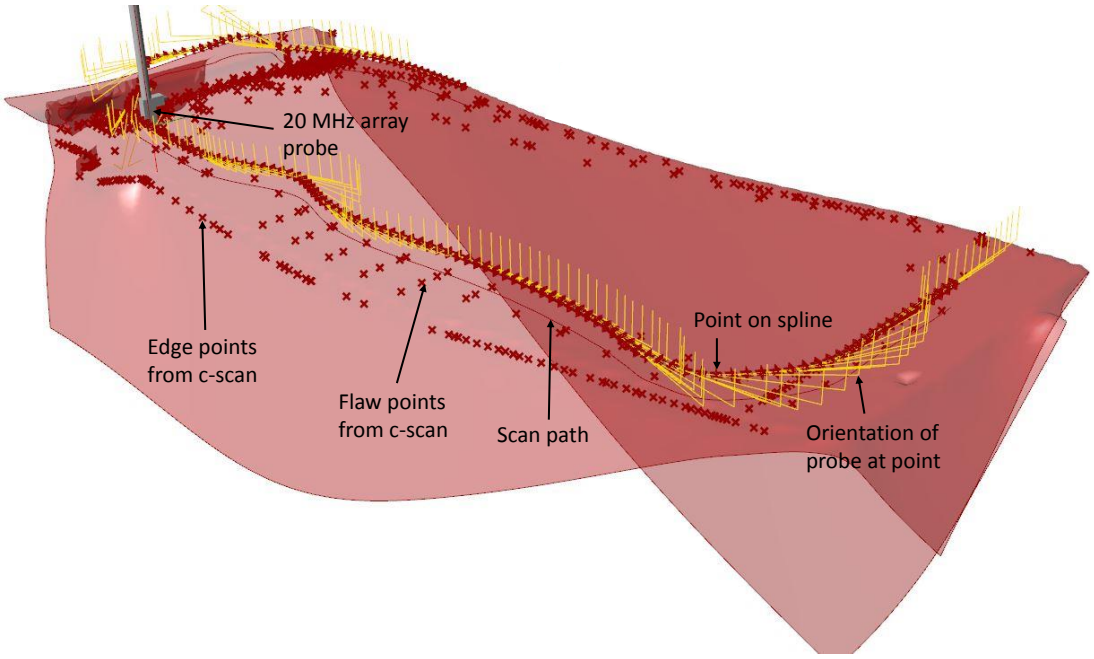

Figure 3.2.25: Curved spline scan through known probe locations, using Probe A.

Figure 3.2.26: Datum points chosen on part to establish scan reference axes.

relative position between the scan pattern and component in immersion.

While laser-tracking was not carried out at the time that the scan paths were developed for this, the deviation from nominal surface standoff was measured using a ruler at the opposite side of plate from DP3 in the x-direction, after the probe was attached. This was measured to be approximately 1 mm for the scan. It was therefore assumed that the absolute error between the scan pattern and the plate was around 1 mm over the scan area. This was deemed acceptable for the purposes of this demonstration system. Further experimental work is required to determine whether or not this sort of error would be acceptable in production.

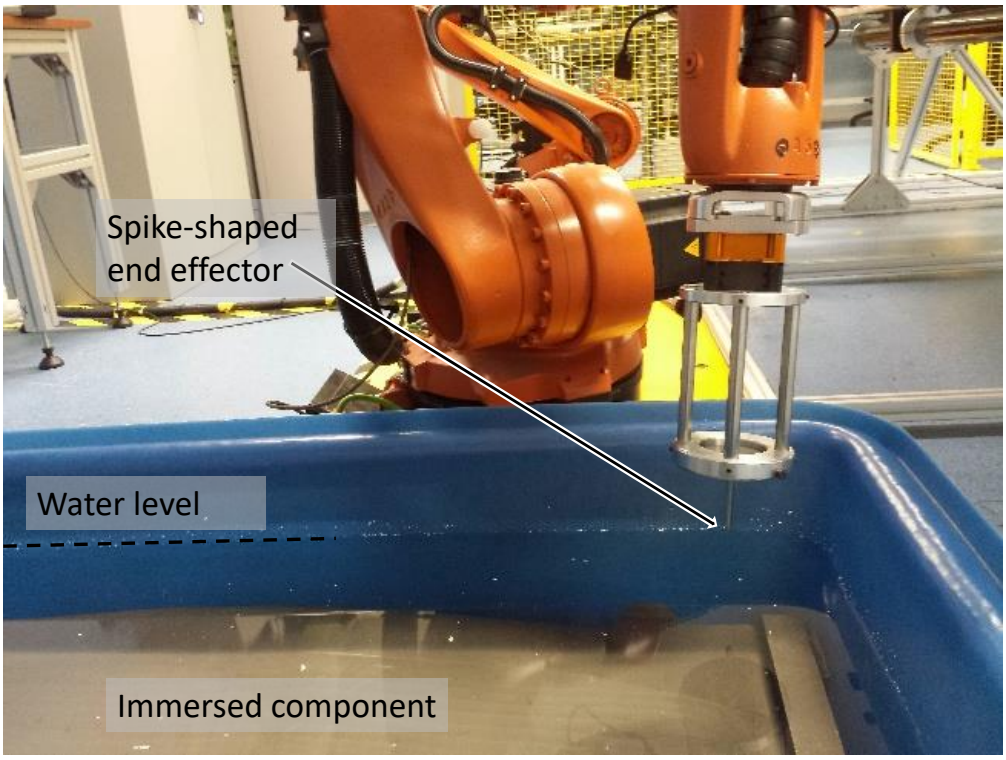

Figure 3.2.27: Robot is driven to datum points on component, connecting the co-ordinate system of the robot with that of the component.

The effect of the overall positional error on the signal returned from FBHs would indicate the suitability of the technique for industry. The aim at this stage of the work was to incorporate an external metrology system to improve upon this absolute error, however this was not completed before the goals of the EngD were altered.

Note that KUKA also produce a high accuracy (HA) edition of the KR5 positioners which where not used here. Use of the HA series would give better absolute accuracy.

3.3 RESULTS AND DISCUSSION

3.3.1 ULTRASONIC DATA

A 10 MHz immersion probe (probe A, detailed in Table A.2) was used to scan across the plate. This probe was used for all experimental work in this chapter. A standoff of 15 mm was used, and FMC acquisitions were performed at 0.5 mm

intervals along the scanning direction. The result is shown in Fig. 3.3.3.

The raster pattern shown in Fig. 3.2.24 was converted to KRL code and executed on the robot arm. The error between the ideal programmed path, and the path recorded by the internal encoders of the robot is shown in Fig. 3.3.1. The contribution of individual axes is shown in Fig. 3.3.2.

The ideal robot positions were linearly interpolated into an ideal surface, which was compared with the recorded position to find the error at each sampling point. Note that some of the recorded data was not available, which is missing on the top end of the y-axis in Fig. 3.3.1.

It was found that the path recorded by the encoders had mean error of 0.0064 mm, with a maximum error of 0.0384 mm and a minimum of -0.0310 mm. The magnitude of the error varied randomly throughout the scan path, however there was a clear change in mean error polarity when changing direction in the y-axis. This can be seen in the top-left, and bottom-right plot in Fig. 3.3.2 as a periodic shifting of error mean with sample number. A larger mean error is shown when the robot is scanning in the -y direction.

This error could be due to imperfect mastering of the robot, or due to backlash or other degraded robotic kinematics giving rise to this hysteresis-like effect.

The effect of this would be to change the standoff of the probe by up to 0.07 mm. Using pre-calculated focal laws, this could result in an amplitude reduction of the flaw signal. However, as the measured surface mode was used for this work, a larger error would be required to alter the signal amplitude. A window of $\pm$ 2 mm was used to detect the surface, so the error here does not have a significant effect.

This scan was conducted at a very slow scan speed (1 mm/s), therefore these errors represent the minimum practical error to be expected using this method. The aim from industry was to maintain a scanning speed of at least 100 mm/s, so this was much slower than was desired.

The results here only record the relative error between the robot encoders and the ideal scan path. The absolute accuracy of the scan was not measured. Later research using this robot [29] showed that the maximum positioning inaccuracy was found to be around 1 mm, and path inaccuracy at maximum velocity was 4.5 mm. A similar NDT scan in [29] resulted in a path inaccuracy of 0.35 mm, with a repeatability of 0.05 mm.

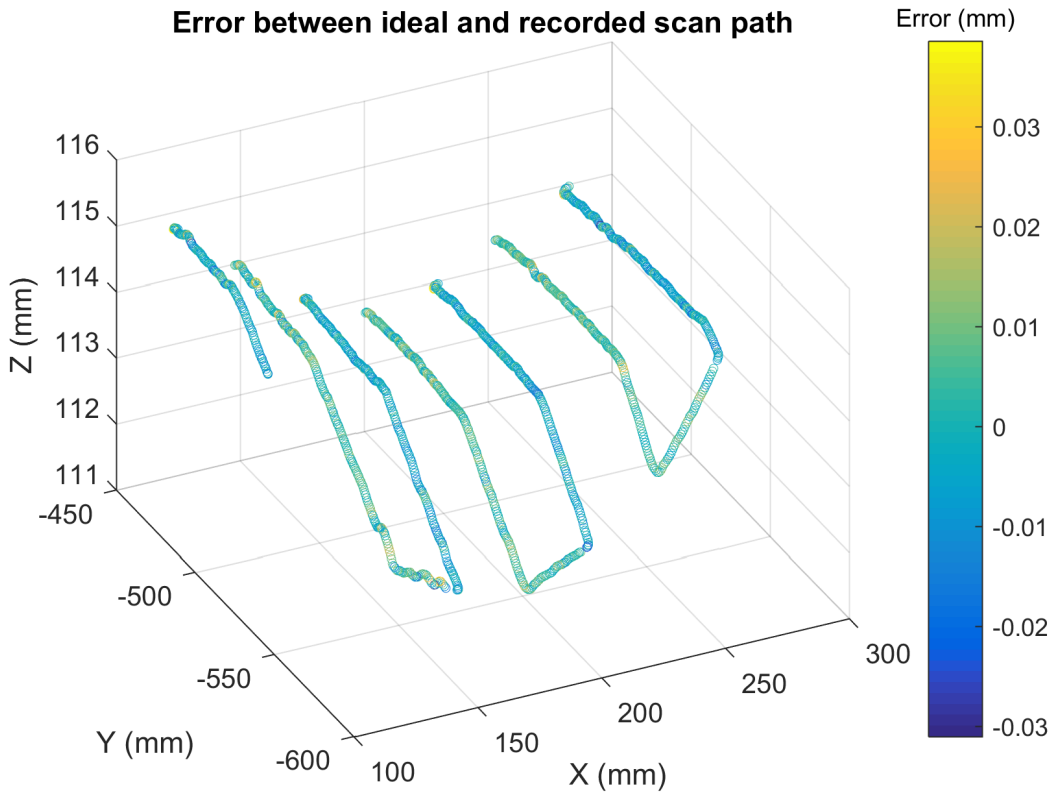

Figure 3.3.1: Detailed plot of robot positions during scan. Total error magnitude between the ideal path and the encoder-recorded path is shown by the colour. Note that some recorded values are not available, visible as gaps in the raster pattern at the top end of the y-axis.

The captured data was plotted using the recorded position of the probe at the scan location. Note that Fig. 3.3.3 shows the results projected onto a flat plane, giving rise to the apparent mismatch between raster passes. Relative location is compared to the original C-scan in Fig. 3.3.4.

The peak signals obtained from the scan locations have an average peak value of -28.2 dB compared to the signal from the front surface; which is 25.6 dB above the average noise of -53.79 dB.

These results show that the combination of robot arm and phased array probe can be used to image the calibration flaws in the membrane. The TFM technique was found to be suitable for this application, and robotic positional errors did not lead to a failure in obtaining a clear C-scan image of the target defects.

This demonstrated that this experimental technique could achieve similar results to an existing process at the company, building confidence in the method, and

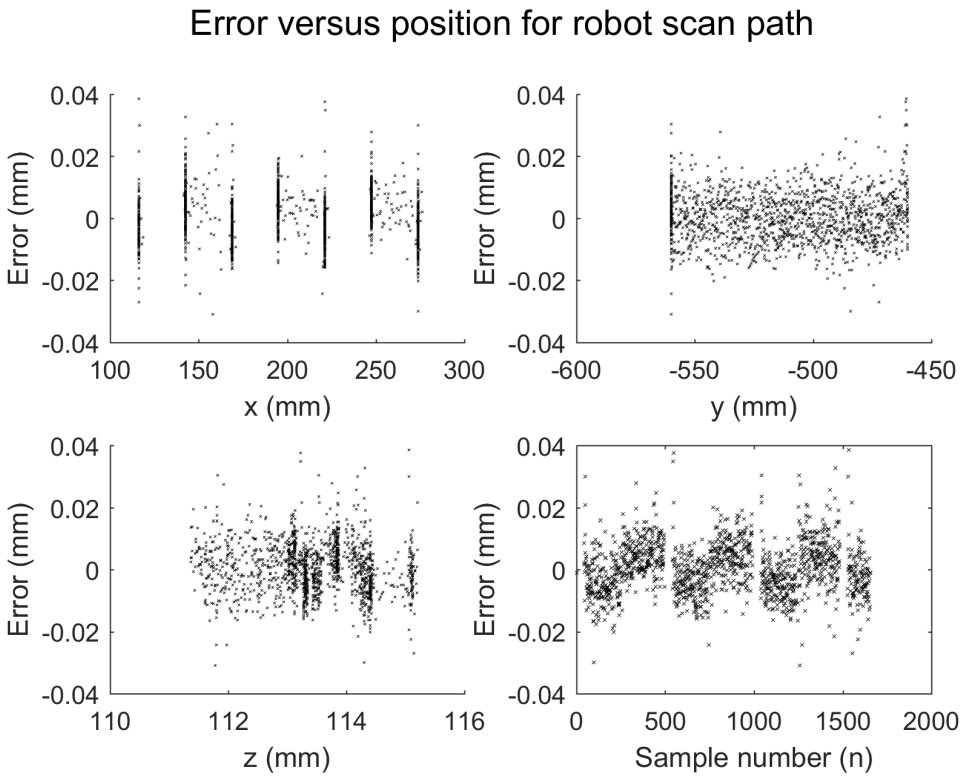

Figure 3.3.2: Errors between ideal and recorded robot positions during scan, shown per axis. Top-left shows error against robot x position, top-right shows error against y-position, bottom-left shows error against z-position, and bottom right shows the error against recorded sample number from the robot scan path

strengthening the business case for TFM-based C-scanning. One aspect of interest to industry related to the business case of FMC-TFM C-scanning is the speed to cover a specified area.

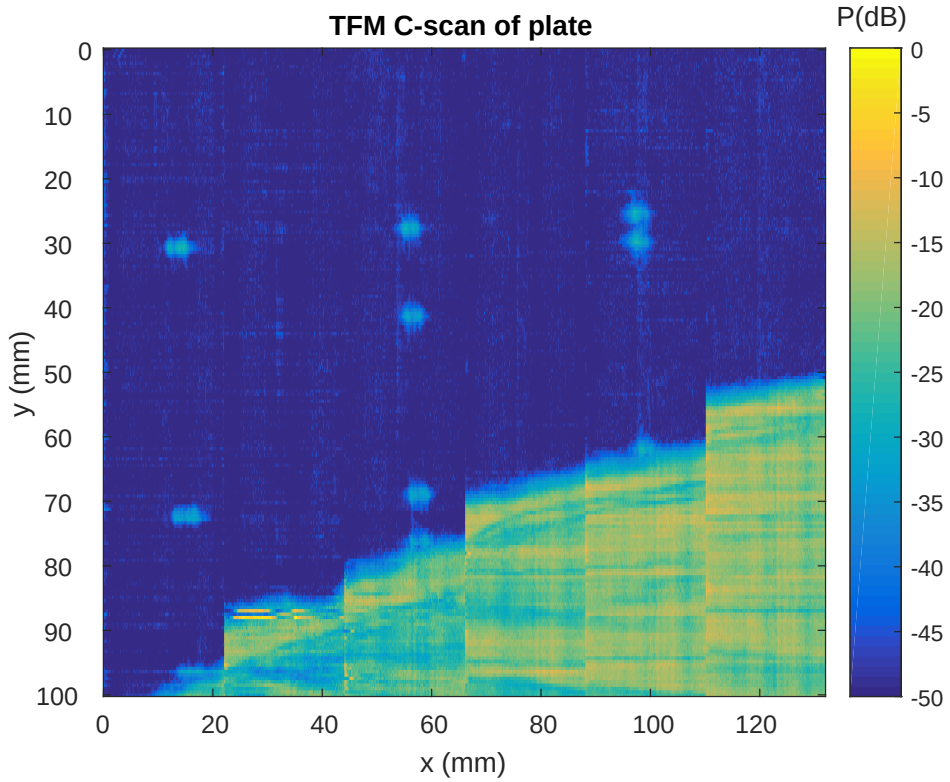

Figure 3.3.3: TFM C-scan of plate. Calibration flaw targets can be seen in the locations predicted by the scan using the original method. The striped structure appears as the C-scan was imaged by stacking lines from B-scans that are equally sized in the y-direction for each vertical pass, which is a slightly inaccurate approximation due to probe tilt. A more accurate method would use probe tilt to vary the thickness of each stacked line.

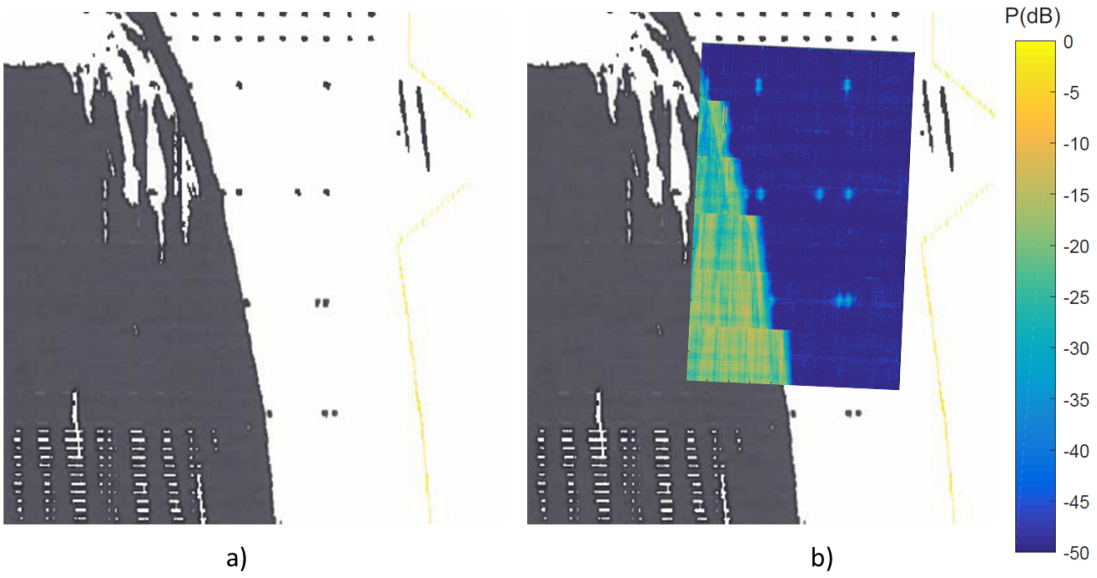

Figure 3.3.4: TFM C-scan superimposed on original C-scan of plate. In a) the scan using the original process is shown, and in b) the TFM process is shown. The same arrangement of calibration defects can be seen, which builds confidence in the new method.

3.3.2 SCANNING SPEED

The acquisition speed of the DSL phased array controller was first tested by use of a 128 element probe together with a 45 µs range chosen for this application. The total time taken from capturing the FMC to saving to disk was 1.5 seconds.

The rate of saving FMC data was the main limiting factor, at 40 MB/s. This was due to the long time it took to save files to disk using the interface developed for the experimental scanning system.

For the C-scan shown here, the scanning rate was approximately an order of magnitude slower than the existing single element scan used in industry.

This was not representative of the best performance of the DSL system however, and the system and approach has since been deployed with a data transfer rate of 1.6 GB/s [27].

To calculate the maximum scanning speed, first consider that there is a physical limit to the speed a phased array inspection can be carried out. For FMC, the scan speed must not be such that the displacement change between elements is significant; around a 1/4 of the length of an element. A spacing between elements that is too large renders the TFM assumptions used to reconstruct the image invalid; as the wavefronts would not combine accurately were they pulsed simultaneously. In this example, the elements were 8 mm long, whereas the resolution of the scan was set at 0.5 mm. This meant that the resolution requirement was the limiting factor (as it is less than 1/4 of the array element length).

The pulse repetition frequency f_{p} for an ultrasonic inspection is set based on how long it takes the initial wave to attenuate to a level that does not interfere with the measurement. One method is to set it as the period taken for the ultrasonic reverberations to attenuate to at most 10% of the initial value of the pulse, for a given element. For this experiment, it was found that setting $f_{\mathrm{p}} = \frac{1}{3t_{\mathrm{r}}}$, where t_{r} was the captured range of the A-scan, achieved this criteria.

"Ghosting" occurs when these repeat echoes interfere with the signal of interest from the scan. Even though TFM averages out these ghosting echoes, signal degradation still occurs, and it is best avoided by altering the PRF as stated above.

For a faster frame capture time t_{f}, coded excitation could be used. This has

been shown to provide a good SNR with parallel transmission of elements in EMATs [107] to reduce voltage. The principle can be applied to ultrasonic arrays, reducing the time of $t_f = nt_a/g$ where g is the number of parallel transmissions. This method of coded excitation causes artefacts when applied to ultrasonic imaging, however coded excitation without these artefacts is supported in the DSL FIToolbox.

A further reduction in t_f could be achieved by sparse techniques [108] which seek to obtain a similar TFM image with fewer elements.

Probes with 32, 64 and 128 elements were tested with cueART, using imaging for a planar interface. In Table 3.1, it might be expected that the time would scale proportionally to $n|el|^2$, however the constant time required to transfer data on and off the GPU (75 μs) disproportionately effects the time per from when 32 elements are used. Again assuming that the elements are equally spaced, the 64 element array would give the quickest TFM processing time for a given scan area.

Table 3.1: TFM processing times

n	size per frame (MB)	TFM time per frame (ms)
128	42.2	780
64	10.5	185
32	2.64	100

3.3.3 THEORETICAL SCANNING SPEED FOR A FMC-TFM C-SCAN

The scanning speed used in this study was slow (around 1 mm/s), due to problems with the practical setup during scan execution. The fastest possible speed obtainable using a FMC-TFM method is an important part of a business case for using this technology, and is explored here.

Included in this section is an illustrative calculation that purposely does not include the time taken to perform the TFM image processing. This decision was made as there was not enough data to extrapolate a representative relationship between element number and TFM processing time in a way that was applicable to curved surfaces in general. The simplified calculation does however demonstrate the relationship between scan speed parameters, and their effect on overall

scan time.

As a simplification, the TFM processing rate is assumed to be the minimum possible - only the 75 ms taken to transfer the data to the GPU is considered. This result therefore shows a lower bound for the generation of a C-scan, and demonstrates the trade off between the burden of data processing introduced by using more elements, versus the increased rate of area coverage.

Consider that the A-scan range is set to cover standoff l_{w} in water with speed c_{w} and l_{s} in steel with speed c_{s}, giving

$$t_{\mathrm{r}} = 2(\frac{l_{\mathrm{w}}}{c_{\mathrm{w}}} + \frac{l_{\mathrm{s}}}{c_{\mathrm{s}}}) \tag{3.1}$$

The time limit to physically acquire a frame t_{p} is

$$t_{\mathrm{p}} = n_{\mathrm{m}} n_{\mathrm{el}} (1/f_{\mathrm{prf}}) \tag{3.2}$$

where n_{m} is the number of multiplex cycles, n_{el} is the number of elements used and f_{prf} is the PRF, where in this example $f_{\mathrm{prf}} = \frac{1}{3t_{\mathrm{r}}}$.

The scanning rate could also be limited by the data transfer rate. The time taken to transfer a frame can be found by first considering the number of bits per frame

$$n_{\mathrm{b}} = f_{\mathrm{s}} n_{\mathrm{el}}^2 t_{\mathrm{r}} b_{\mathrm{d}} \tag{3.3}$$

where f_{s} is the sampling frequency, and b_{d} is the bit depth of the A-scan.

The data rate in bits per second can be found as

$$R_{\mathrm{b}} = (1024 \times 8) \times 1024 \times 1024 \times R_{\mathrm{G}} \tag{3.4}$$

where R_{G} is the data transfer rate in GB/s. The total time taken for a frame to be captured, transferred, and focused is therefore

$$t_{\mathrm{d}} = t_{\mathrm{gpu}} + \frac{n_{\mathrm{b}}}{R_{\mathrm{b}}} \tag{3.5}$$

where t_{gpu} is the fixed time delay for the TFM data to be transferred to the GPU.

The number of frames to capture in one square meter is

$$n_{\mathrm{f}} = \frac{1}{l_{\mathrm{r}}} \frac{1}{w_{\mathrm{array}}} \tag{3.6}$$

where l_{r} is the spacing between frames, and w_{array} is the width of the active region of a 1D linear array probe.

For this example, different values of n_{el} and R_{G} were chosen, to investigate the effect these parameters have on overall scan time. The largest of t_{p} and t_{d} was taken for each calculation, and multiplied by n_{f} to find the total time to scan one square metre t_{total}

In Fig. 3.3.5, the relationship between t_{p}, t_{d} and R_{G} is explored, with t_{total} shown in minutes. For low element numbers, t_{total} is very high. This is because w_{array} is low, therefore n_{f} is higher, and t_{gpu} is a time penalty incurred on every frame capture. t_{total} quickly drops as the higher rate of area coverage given by the wider probe comes into play. A minimum time is reached for each trace; this point is where the benefit of a higher rate of area coverage falls away, and the time penalty of processing n_{el} dominates, as it scales with n_{el}^2.

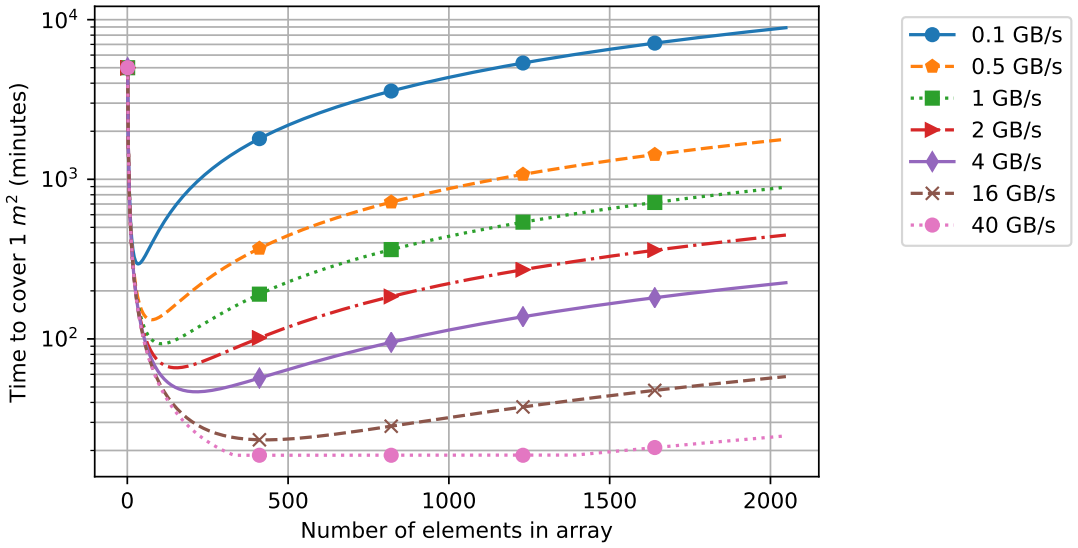

Figure 3.3.5: Time taken to scan one square metre, versus element number, for a selection of different data transfer rates. The 40 GB/s data rate hits the physical scan time limit, whereas the other values are dominated by the trade-off between an increase in t_{d} due to element count, and a decrease in n_{f} required due to increased array probe width.

For $R_{\mathrm{G}} = 40$ GB/s, t_{total} is at a minimum for many different element counts.

Table 3.2: Values used for variables to generate Fig. 3.3.5

t_r (μs)	46.7
l_r (mm)	0.5
f_s (MHz)	100
b_d (number)	12
w_el (mm)	0.5
t_gpu (ms)	75
n_m (number)	2

Table 3.3: For a selection of different data transfer rates, this table shows: minimum scan time for one squared metre, number of elements to use to achieve the minimum scan time, and tooltip velocity at this minimum,

R_G (GB/s)	t_total (minutes)	n_el	tool velocity (m/s)
0.1	295	33	0.2054
0.5	132	76	0.1993
1	94	107	0.1988
2	66	152	0.1993
4	47	214	0.1988
16	24	429	0.1942
40	19	462	0.2278

For this range of values, $t_\mathrm{p} > t_\mathrm{d}$ so that the data transfer rate does not cause a bottleneck.

The turn around points seen in Fig. 3.3.5 represent optimal scanning times, and element numbers. These are given in Table 3.3, along with the tool tip velocity required of the robot at that point.

Note that these results represent the lower bound for the time to produce a C-scan only if the distance travelled during the acquisition of a frame is small enough that the constituent A-scans of the FMC remain coherent. It was assumed for this calculation that l_r was sufficiently below this distance.

The key finding from this exercise exploring scanning speeds is that there is an optimal array size that should be chosen based on the data rate limitations of a scanner. While this simplified approach ignored the time taken for a TFM

algorithm to execute, it is expected that the TFM processing time increases with n_{el}^2, therefore a similar relationship between element number and scanning time is expected.

This means that for planning TFM C-scans on an industrial level, the data transfer rate versus element count of the array used should be used to perform an optimisation similar to this, but including either interpolated data from a set of timed TFM experiments, or using an accurate model of the TFM processing time relationship versus element number for a given surface.

3.4 SUMMARY OF DEVELOPMENT OF ROBOTIC INSPECTION SYSTEM FOR SCANNING OF IRREGULAR PLATE.

This chapter detailed the geometry of the test piece; an irregular plate with a thin membrane sandwiched between two forged layers, with small circular disbonds. It was then shown that the existing process for inspecting this component could be replaced with a robotic arm phased array system.

The chapter then described the automation of C-scan inspection applied to the titanium test plate. Features of the original tank, and the proposed robot arm were discussed in Section 3.2.4. Kinematics simulations and surface metrology integration were introduced as problems for deployment of a robotic arm.

Use of an offline path planning system was suggested as a solution for these issues. Development of an OPP system for ultrasonic immersion inspection was detailed in Section 3.2.5. KUKA|prc was used, as it is very cost-effective compared to purpose-made CAD/CAM packages. It was found to also offer the advantage of easy HMI creation due to its use of graphical programming. A technique to visualise B-scan images at particular points in a recorded scan was also developed.

This OPP approach was used to create code for the robotic inspection. In Section 3.2.11, the flaw locations were found using the original C-scan, and transferred to the measured representation. Scan paths were created through selected areas containing flaws. The key features of the simulated scan plan were highlighted, as well as the datum point used for aligning the co-ordinate system of the robot to that of the part. A photograph of the robot next to the part immersed in water was also shown in Fig. 3.2.27.

Results following the scans were discussed in Section 3.3.1. Path accuracy between the ideal and measured robot scan path were quantified using data measured by the encoders of the robot. The path error had an average of 0.0241 mm, and peaked at 0.3 mm in the corners. It was noted that this error was insignificant compared to the error introduced by differences in establishing the basis of the part co-ordinate system using the spike method. It was noted however that this error would likely increase with scan speed, and therefore should be considered for planning high-speed scans; perhaps by use of feedback from laser-tracking systems.

A C-scan of the plate was produced, and compared to the original C-scan in Fig. 3.3.4. All flaws in the original C-scan were reproduced in the TFM C-scan, and had an average signal value of -28.2 dB on a background of -53.8 dB. This showed that the automated process to create a TFM C-scan could be used to detect a selection of flaws that were detected using the original technique.

Finally, speed issues were considered in Section 3.3.2. An approach was developed to show how different factors of the inspection affected speed of FMC acquisition. It was found that there is an optimal number of array elements to use for a given data transfer rate in order to achieve the maximum rate of area coverage.

This chapter demonstrated an innovative method for using KUKA|Prc to conduct NDE inspections; however the robotic approach itself was limited in its scientific novelty. The value of the work to the research community is that is provides a cheaper option for creation of robotic NDE inspections than by using a repurposed CAD-CAM package, such as MasterCAM, or a purpose-made turnkey solution such as the GE Hydrastar robotic inspection system [109]. Furthermore, it opens up future work to collaboration with a community of engineers and designers that use Grasshopper, rather than relying upon commercially sensitive and platform-specific knowledge . These alternatives are a good investment for production processes, but for open and flexible research grade work on robotic NDE, the approach presented here offers an alternative.

It is anticipated that issues related to speed of transferring files, and processing TFM images, which are inherently tied to computing power, will be alleviated as general purpose computing resources become more powerful over time. Furthermore, implementation of the TFM algorithm on inherently parallel systems such as FPGA results in much faster operation. This is likely to become more common as the technique becomes more mainstream, and is the method used by the Gekko system [95], for example.

TFM was used in this chapter to focus through a surface that was slightly irregular. This was a useful result for demonstrating the applicability of the technology to components with near-planar geometry, but did not quantify the performance of TFM through interfaces of defined curvature in general. Rather than continue to develop the automated system, the focus of the project shifted to mapping the performance of TFM through surfaces of known curvature.

Chapter 4

MODELLING TFM INSPECTION OF FLAT-BOTTOMED HOLES THROUGH CURVED INTERFACES

Previously, Chapter 3 showed an application for adaptive TFM scanning, and that an existing automated process can be replaced. This helped Rolls-Royce reach a key technology demonstration milestone, and built confidence in the feasibility of automated TFM processes. It did not however quantitatively evaluate just how the degree of surface curvature affects TFM performance.

Calibration blocks were developed for this purpose, but creation of a calibration block for every single instance of flaw location and surface curvature was not a feasible endeavour. Further, considering that Rolls-Royce currently employ a model-based optimisation system for single element inspection [7, 89], there was a strong case for developing a modelling technique to predict TFM peak signal.

This chapter therefore details how FMC inspection of curved surface components was modelled. Multiple modelling approaches are considered, followed by the development of FE models using PZ Flex, semi-analytical models using CIVA, and a purpose-built ray tracing model in MATLAB.

4.1 ULTRASONIC MODELLING METHODS

4.1.1 EFFECTS LEADING TO SIGNAL REDUCTION OF TFM DUE TO CURVATURE

In order to evaluate which ultrasonic modelling techniques were suitable for this study, it was necessary to consider the effects that would likely lead to a reduction of flaw signal strength when using surface-corrected TFM. These can be summarised as the following:

Finite width cylindrical waves - in the passive dimension of a 1D array, there is a non-uniform beam profile, which results in sensitivity variation to a defect in the focusing plane. The 2D approximation used in TFM assumes that the elements can be thought of as infinite line sources, whereas they actually have a finite length in the out-of-plane dimension. This can be thought of as a 3D effect, related to probe geometry.

Increased average angle of refraction - at a fluid-solid boundary, the energy of the transmitted wave is related to the angle of incidence. A more oblique angle of incidence results in reduced transmitted energy. For higher degrees of curvature, more of the rays hit at a larger angle, and thus have a lower transmission coefficient than the flat case. In the extreme case, this results in an angle of incidence greater than the critical angle, resulting in total reflection. Energy that takes this route does not contribute to the final TFM image, no matter what ToF correction is applied.

Increased ray path attenuation - as curvature increases, the distance a ray travels through each material is altered. As cylindrical waves are used, the intensity is inversely proportional to the distance travelled. Material attenuation is also likely to play a part.

Scattering behaviour of a FBH - a FBH may not act as a point-like reflector, depending on probe frequency. A flat-bottomed hole extends into the passive plane of the inspection, and has edges near the direction of ray incidence. Diffraction effects are more likely as frequency increases (consider the radiation patterns that were shown in Fig. 2.1.9). The scattering from a FBH is likely to require a 3D model, as it is not a uniform effect across the incident field (unlike a deep side-drilled hole, for example).

A suitable modelling technique must be able to take into account these effects. Furthermore, it must be applicable to the range of geometries likely to be investigated in the inspection problem.

4.1.2 COMPONENT GEOMETRY TO BE MODELLED

Rolls-Royce were interested in modelling forged components in general. To act as a starting point, a candidate disc forging was chosen, and the curvatures of the final geometry were measured in Rhino. The majority of curvatures fell in the range of 10-50 mm. Tighter 2 mm radii were present at corners, but these were not considered.

Calibration blocks for inspection of rectilinear forms exist up to 100 mm thickness. This study only considered depths of up to 50 mm, which nevertheless covers most cases of interest. Modelling techniques were chosen to be applicable to these depths. This limit was imposed due to the budgetary constraints on test block manufacture.

Owing to the existing use of calibration blocks with standard 0.64 mm diameter FBH targets, this was chosen as the target for this study. Further, the ability to model the 32-element 10 MHz linear phased array probe selected for this study was deemed industrially relevant.

Probe standoff was chosen to be 10 mm maximum separation from the surface. Holding the array closer to the surface ensured more energy transferred to the material - however multiple reverberations from the frontwall were introduced, and had to be gated out of the final image. This was also deemed a realistic distance that could be maintained safely by automatic scanning processes at high speed.

It was necessary to develop a modelling technique suitable for simulation of FMC inspection for flaws present throughout the volume of the geometry shown in Fig. 4.1.1. The stepped blocks to be modelled had the same geometry as the new calibration blocks that were developed for this study; so that modelling results could be verified by the experimental approach taken in chapter 5. Note that for the geometry shown above, reflections from FBHs with the largest metal path of 47.5 mm arrived later than the front surface reflections from the 10 mm stand off. The frontwall signal was removed by gating, and was not found to interfere with the signal from the FBH at this depth

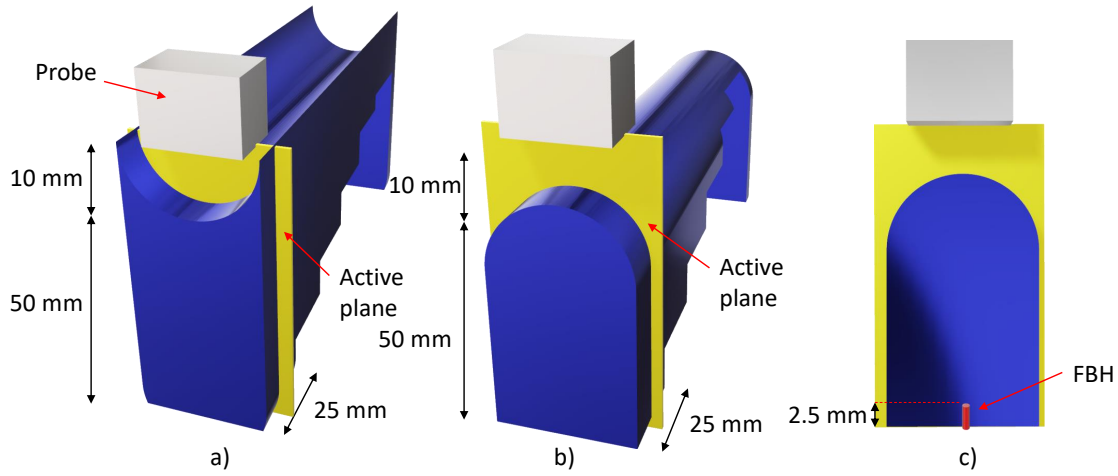

Figure 4.1.1: Geometry of deepest case of a) the concave model, and b), c) the convex model. Units are shown in mm.

Suitability of a given approach was judged based on its ability to model the effects and geometry outline here, as well as the practicability of executing the model on a standard desktop computer.

4.2 DEVELOPMENT OF A FINITE ELEMENT MODEL FOR CURVED SURFACES

4.2.1 AIMS OF FINITE ELEMENT MODELLING

The first approach taken was to create a 2D finite element model to simulate the inspection scenario outlined in Section 4.1. One benefit of using a finite element model was that it made the fewest assumptions about the inspection process; only relying upon the geometry of the probe and material properties to calculate the propagation of pressure waves. Further, it allowed general geometries to be modelled (such as rough surfaces) which could not be feasibly implemented deterministically using a semi-analytical ray-tracing solutions.

This activity was driven by a desire to use commercially-available modelling software to generate FMC data in the form of ordered A-scans. Production of a TFM image similar to that obtained through experimental methods was a key aim. In order to retain the link between simulated and experimental data, data in the same format obtained experimentally was required. To achieve this, PZ

flex pressure-time traces were reformatted to be compatible with BRAIN [86].

PZ Flex (2017 PZFlex, LLC) is a finite element software, with the ability to efficiently solve transient stress problems [110, 111]. Finite element modelling splits up the structure of a component into a mesh, onto which material properties are assigned. Elements are connected by nodes, at which simultaneous equations are solved to transfer stress and displacement through the structure. Interpolation of these piecewise solutions through the inspection volume can represent realistic field properties for ultrasonic wave propagation. Care has to be taken to ensure that the spatial and temporal discretisation of the model is such that it delivers sufficient accuracy, while still retaining reasonable execution times.

4.2.2 DEVELOPMENT OF FINITE ELEMENT MODEL FOR CURVED COMPONENTS

A general connectivity mesh is composed of irregularly shaped triangular elements that closely follow the geometry of a part, whereas a structured mesh is composed of regular rectangular elements that approximate part geometry. A structured mesh is orders of magnitude more efficient for calculating wave propagation than a general connectivity mesh, but it results in a less accurate approximation of curved geometry. For wave propagation, a structured mesh of rectangular elements was used for far improved run times (between 100 and 1000 times faster) than using a general connectivity mesh.

The model is split into computational zones, each with a relevant timestep τ_{step} chosen to be slightly below the time taken for the fastest wave mode to traverse a single element in the zone, referred to as τ_{cr}. In an explicitly-solved FE model such as this, it is critical that the state of the model is solved before the wave propagates to the next element. Owing to this, the ratio $\tau_{\text{step}}/\tau_{\text{cr}} = \tau_{\text{tsf}}$ is of importance. Known as the timestep stability factor, lower values result in higher computational stability, and higher values result in lower computational burden.

The choice of mesh element size had an impact on the accuracy and speed of the model. The two areas of importance for this work were the shape of the solid-fluid boundary (front surface) of the inspection, and the flaw. It was assumed that the front surface was radially curved, and that the flat bottomed hole could be represented as a flat-sided notch. This meant that mesh inaccuracy was not present for the idealised 2D FBH - as it was rectangular, but for the curved interface it was possible that the approximation of geometry could introduce

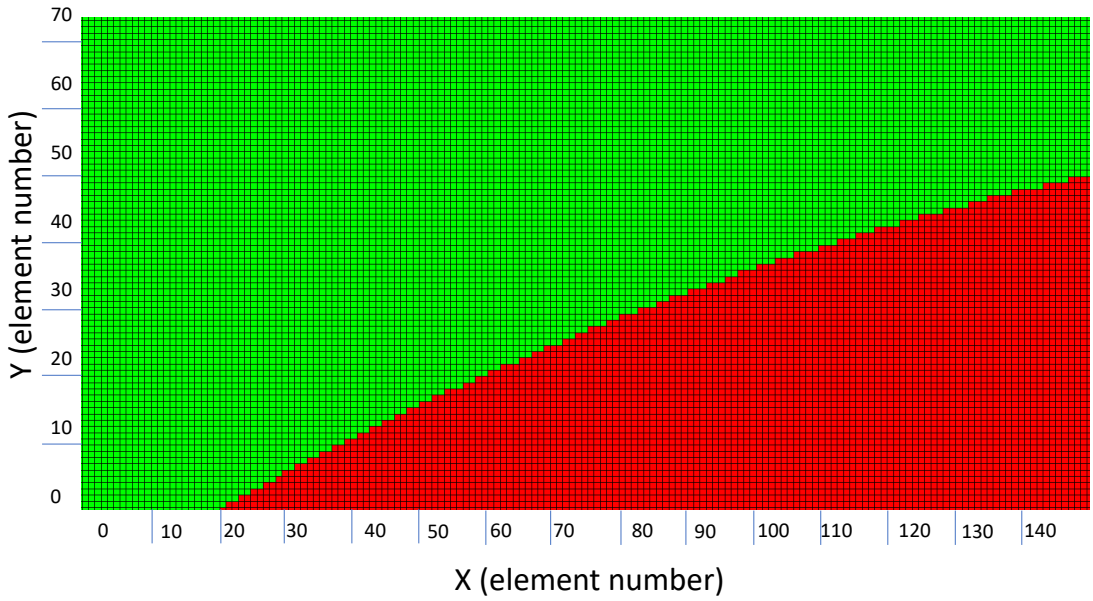

Figure 4.2.1: Magnified view of regular structured mesh representation used for modelling 10 mm convex curved surface.

additional scattering. This mesh scattering may have a similar effect to that of roughness on the surface of a component, and potentially introduce noise in the TFM image.

In addition to the accuracy of component geometry, the mesh size determines the degree to which the wave is spatially discretised. A minimum of between 6 to 10 elements per wavelengths is generally recommended, but higher densities result in increased accuracy [112]; for example, a density of 15 has been used before for FMC FE [111]. If the mesh density is too low, the wave is not sampled accurately enough to retain amplitude and phase information. Note that the TFM relies upon summing phase information, so low mesh density can result in noise shown in a TFM image.

Numerical dispersion occurs due to successive approximations made when sampling the propagation of a wave through time. As the model is split into elements, each one of these models the distribution of the pressure field with slight inaccuracy. These errors accumulate, and result in non-physical behaviour of a finite element model. This can result in phase and amplitude errors, with higher frequencies most affected. In order to reduce the effect of numerical dispersion in this work, the ultrasonic propagation path length was kept below 100λ where λ is the smallest wavelength for which each region was meshed.

4.2.3 MODEL INPUTS AND EXECUTION

The model was split into a separate script for each element transmit. Each script applied pressure to a line of nodes at the top of the model, with length equal to that of an array element. The resulting cylindrical wave propagated in the model, and the pressure at all other element locations was recorded, producing n_{el} A-scans describing the received signal at the element locations.

Each element transmit was modelled in turn, eventually producing n_{el}^2 A-scans. This gave the full-matrix of ultrasonic data. Table 4.1 shows the input parameters used for the model.

Mesh type	Standard partition
Spatial discretisation zones	1
No. elements per wavelength, n_{epw}	25
Temporal discretisation zones	2
$\tau_{\mathrm{w}}/\tau_{\mathrm{st}}$	3
τ_{tsf}	0.95

Table 4.1: Calculation input parameters

A MATLAB script was written to convert model simulation data into the format required for reconstruction in BRAIN. The required parameters are shown in Table 4.2

`time_data`	Simulated A-scans (n_{el}^2 A-scans, each n_{s} long)
`tx`	tx element used for each `time_data` A-scan
`rx`	rx element used for each `time_data` A-scan
`time`	actual times for sampling intervals
`ph_velocity`	sound velocity in inspection material
`array`	probe element locations

Table 4.2: Inspection input parameters required for BRAIN

Imaging of the FMC data was performed using the immersion focusing feature of BRAIN, using the "measure" option to automatically detect the surface.

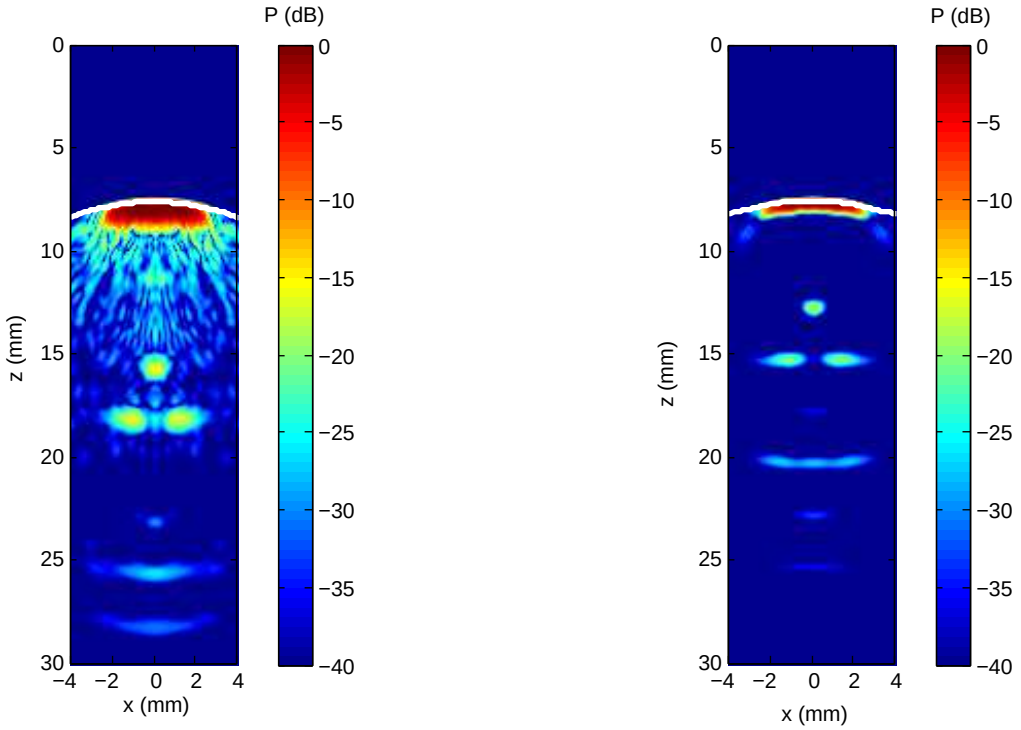

Figure 4.2.2: FE simulated FMC data, plotted using curvature-corrected TFM mode in BRAIN, for geometry described in Fig. 4.1.1. Comparison of TFM images using $n_{\text{epw}} = 15$ (left) and $n_{\text{epw}} = 30$ (right). Note the mesh scattering artefacts shown when n_{epw} is too low. The colour scale represents decibel drop from the peak value in the image.

4.2.4 OPTIMISATION OF FE MODEL

The mesh density of a finite element simulation can impact the quality of image obtained from the TFM, due to numerical dispersion and mesh scattering from the geometrical approximations in the model. To balance speed and accuracy requirements, it was necessary to assess the optimal number of elements per wavelength n_{epw}, as too low a value was found to result in imaging artefacts such as in Figure 4.2.2.

4.2.5 FINDING OPTIMAL NUMBER OF MESH ELEMENTS FOR MODEL

A Python [113] program was developed for batch control and analysis of the simulation data. It determined the mesh box size, calculated the required geometry, called PZ Flex to create the mesh, and then plotted results from multiple ex-

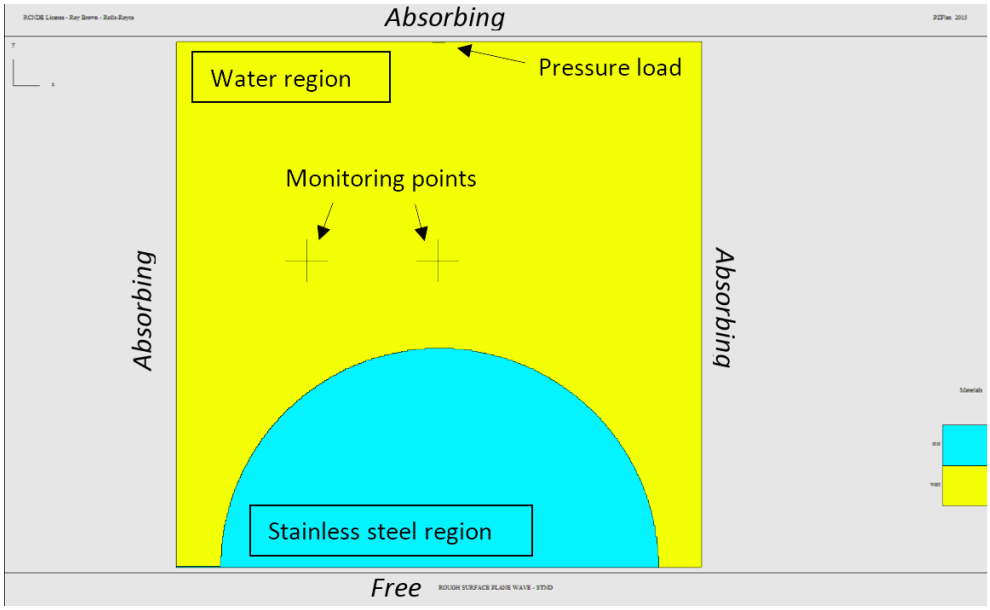

Figure 4.2.3: Annotated screen shot of model shown in PZFlex user interface. Material regions, and boundary conditions of the miniature model used for convergence analysis. Radius of the block $r = 1\,\text{mm}$ and standoff of the probe is 1.5 mm. Boundary conditions were either absorbing, or freely oscillating.

periments as super-imposed A-scans. Firstly, to find guidelines for the minimum acceptable n_{epw} value that could be used without causing scattering related to spatial discretisation, a miniature model was created with variable n_{epw}.

A single array element source was applied at the centre of the model, with the signal recorded at the monitoring locations. The incident pulse was 10 MHz, and radius of curvature of 1 mm. This geometry was chosen as the smallest representation of any non-rough surface interface. The wave propagation path $<< 100\lambda$ ensured negligible effect from numerical dispersion.

The second frontwall reflection was identified in the A-scans, with the signal shape compared for values of $n_{\text{epw}} = 15$ to $n_{\text{epw}} = 100$. A comparison of these is shown in Fig. 4.2.4.

The windowed signal shown in Fig. 4.2.5 was used to determine the ability of each mesh density to reproduce the reflection; by comparison for using the highest mesh density of $n_{\text{epw}} = 100$ using the correlation coefficient S_{ij}

$$S_{ij} = C_{ij}/\sqrt{C_{ii} * C_{jj}} \tag{4.1}$$

where C_{ij} is the covariance between the A-scan and the reference A-scan, C_{ii} is

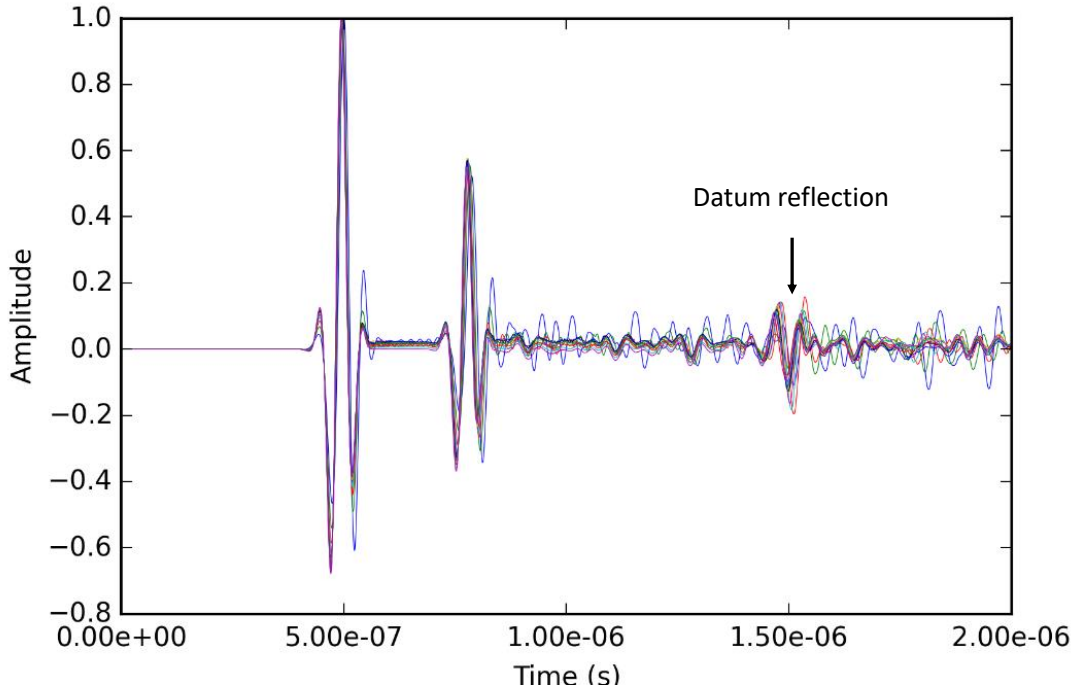

Figure 4.2.4: Superimposed A-scans for $n_{\text{epw}} = 15$ to $n_{\text{epw}} = 100$. Backwall reflection is taken as the datum point.

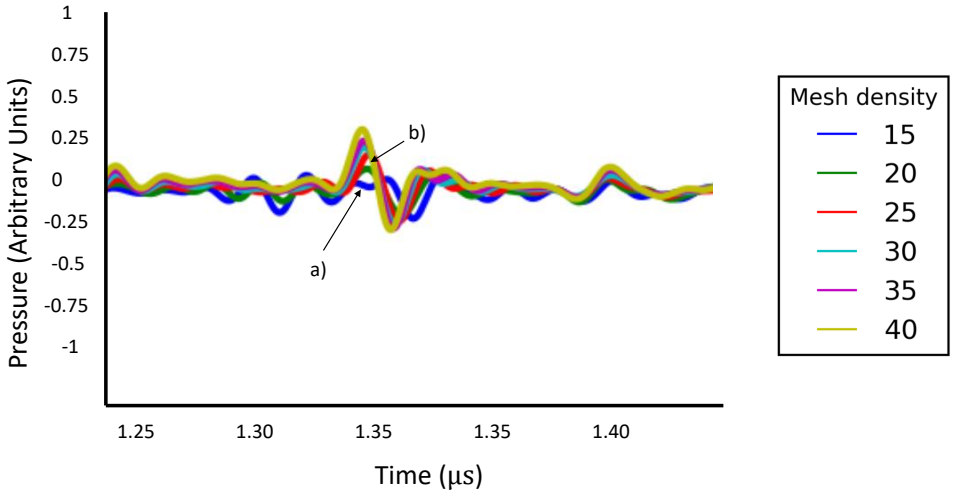

Figure 4.2.5: A window of an A-scan taken to show the differences in the reflection shape for different mesh densities. For a) a density of 15, or b) a density of 20, the reflection amplitude is noticeably reduced.

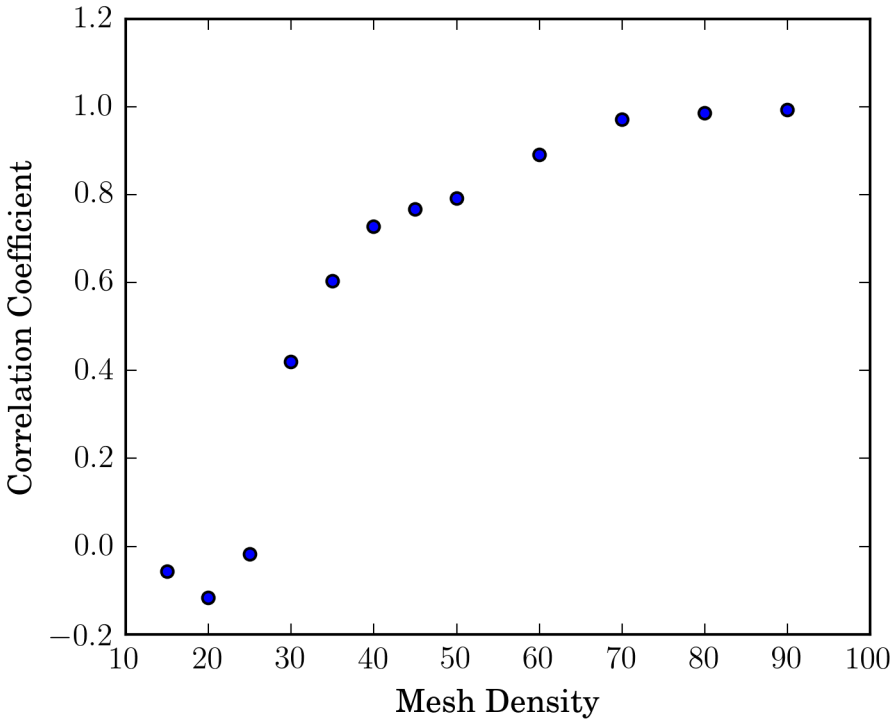

Figure 4.2.6: Correlation coefficient of backwall peak versus mesh density for windowed A-scan signal shown in Fig. 4.2.5.

the variance of the A-scan, and C_{jj} is the variance of the reference A-scan.

Plotting Sij against n_{epw} in Figure 4.2.6, values where $n_{\text{epw}} > 35$ give $Sij > 0.5$, indicating that these mesh densities are an optimal tradeoff between speed and accuracy for this interface geometry.

From 4.2.6, setting $n_{\text{epw}} > 35$ predicts a faithful reproduction of a curved interface where r $>$ 1 mm. This was used to generate the image on the right hand side of 4.2.2. However, this took 3 hours per array element to generate on the system used for this study (specifications are given in Table A.5). For the series of convex blocks studied, the smallest radius was 10 mm, therefore a model was produced to investigate whether this could be reduced further and retain similar correlation with a $n_{\text{epw}} = 100$ model.

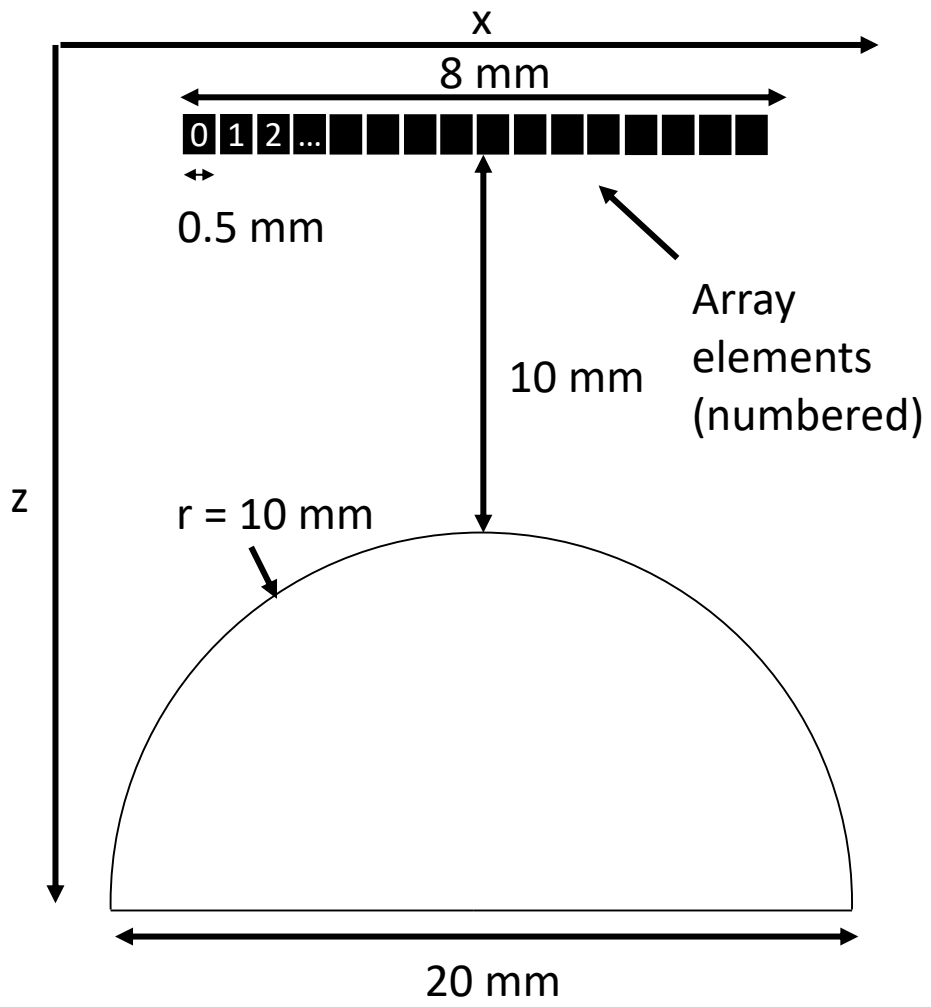

Figure 4.2.7: Model setup for full-size convergence analysis. 16 different element positions were used, representing a phased array. Element 0 was pulsed, and wave reflections were recorded at all 16 positions. The signal from the backwall was extracted for each element. This was then correlated with the same signal at a mesh density of $n_{\text{epw}} = 100$ to get the correlation coefficient.

4.2.6 FINDING NUMBER OF ELEMENTS PER WAVELENGTH TO USE FOR SMALLEST CONVEX BLOCK IN STUDY

Another model was created, this time with the full size geometry of the inspection scenario to model in FMC, shown in Fig. 4.2.7. A single element was pulsed, and A-scan traces were recorded for all elements. The element at the extremity of the array was chosen to maximise the effect of shear waves propagating in the steel region, as these have a smaller wavelength than longitudinal waves, and hence their accuracy degenerates first.

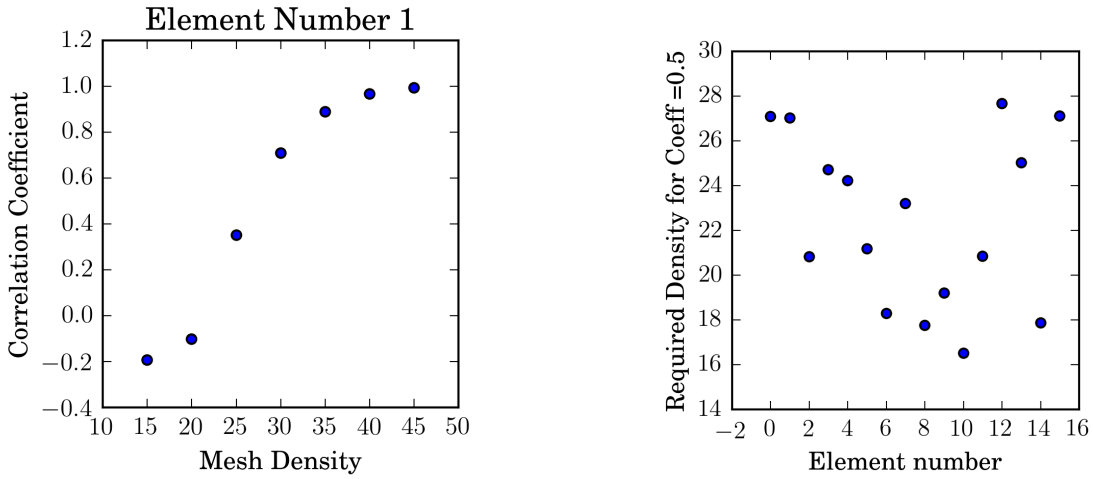

Figure 4.2.8: Correlation coefficient (vs. $n_{\text{epw}} = 100$)) for each element was calculated for different mesh densities; an example result is shown on the left for element 1. This was repeated for each element, and the mesh density required to achieve $S \geq 0.5$ was recorded, with results shown on the right.

The mesh density was varied, and plots of S for each element were produced, similar to Figure 4.2.6. The value of n_{epw} corresponding to $S = 0.5$ was extracted by linear interpolation of these plots, with the corresponding element sizes shown in 4.2.8 b).

Fig. 4.2.8 shows that for this particular inspection scenario, $n_{\text{epw}} > 28$ should be sufficient to achieve the desired correlation coefficient for each level.

4.2.7 REDUCING TOTAL RUNNING TIME OF MODEL

Firstly, the visualisation of the simulation was skipped in the calculation cycle. Secondly, τ_{tsf} was increased from 0.8 to 0.95 to reduce the total number of time steps. Finally, the model was split into two computational zones. The rectangular region of water above the apex of the curved interface was set with the time step in water one third of that in steel, as all wave propagation through the water interface occurs at a rate of approximately four times slower. This reduced the total number of computational steps in the model, without increasing risk of instability.

After these steps were taken, the run time was reduced from 3 hours per array element to 15 minutes. The strength of the FBH was found to be $\pm$ 0.4 dB of that from using $n_{\text{epw}} = 100$, therefore this model configuration was deemed sufficient

to estimate the strength of a FBH through an interface with curvature r $>$ 10 mm.

The approach taken in this section resulted in a 2D FMC model, which could be used to produce simulated TFM images in BRAIN. Furthermore, the development of a program to generate and run models of arbitrary geometry was a useful tool for simulation of arbitrary and rough surface geometries. The ability to accurately represent a rough surface was a key advantage of the FE model versus other approaches.

Three major limitations existed from the 2D FE model described here. Firstly, the flaw was approximated as a notch, therefore the difference in scattering behaviour results in a different TFM image intensity from a FBH. Secondly, due to the limit on numerical dispersion of around 100λ before computational instability, the depth of the flaw was limited to around 10 mm. This did not cover the full range of interest (2.5-50 mm) required for forging inspection. Finally, even though the model run time was optimised from 3 hours per array element to 15 minutes; this was still seen as prohibitive to the industrial application, considering the aim was to routinely generate a map of flaw response at different locations, through different surface interfaces.

To simulate 3D effects, and improve the speed of model execution, use of CIVA 3D was considered.

4.3 USE OF CIVA 3D TO CREATE SENSITIVITY MAPS FROM TFM IMAGES

The inspection software CIVA [114] was used to generate 3D models of the inspection problem.

The CIVA beam model applies electromagnetic wave theory described by Deschamps [115] applied to elastodynamic waves. CIVA assumes pencil-like wave propagation; this is another way of saying that rays are accompanied by paraxial rays which diverge as the principle ray propagates through the media. The region contained within the pencil allows efficient integration for interactions - maintaining the best of a ray-tracing approach with a full integral approach.

Assumptions in the beam model are:

- Transducer radiates into medium in thickness mode only
- No cross talk among elements in array
- No secondary diffraction from radiation of the curved surface
- All source points radiate with the same velocity
- Different energy paths are determined by Snell's law
- Energy associated with each path is quantified according to matrix calculations, with vectorial nature determined by Christoffel's equations to calculate the variation of the velocity of wavefronts in anisotropic media with the wavefront normal direction.
- Wave associated with pencil has plane wave properties, weighted by changes in energy. For example, a spherical wave is weighted by a $1/r$ decreasing factor.
- Assumes that no radius of curvature is shorter than the wavelength in the coupling medium.
- Active element must have a stand off of at least one wavelength in the coupling medium.
- Radiation field in the coupling medium is calculated using the Rayleigh integral.
- Accuracy number in CIVA refers to number of contributions used for the calculation and scales with length of the array, f_c and f_s.

CIVA uses a hybrid between Kirchoff modelling and geometrical theory of diffraction (GTD). Kirchoff is useful for measuring the echoes from specular reflections; but is less accurate for observation directions far from the specular one. GTD is not valid for specular observations, but is effective for prediction of edge diffractions in most configurations.

The model was set up to achieve the geometry described in Section 4.1.2. The number of modes considered was five; which was found to be the minimum number required to generate a TFM image. This corresponds to the legs of the inspection

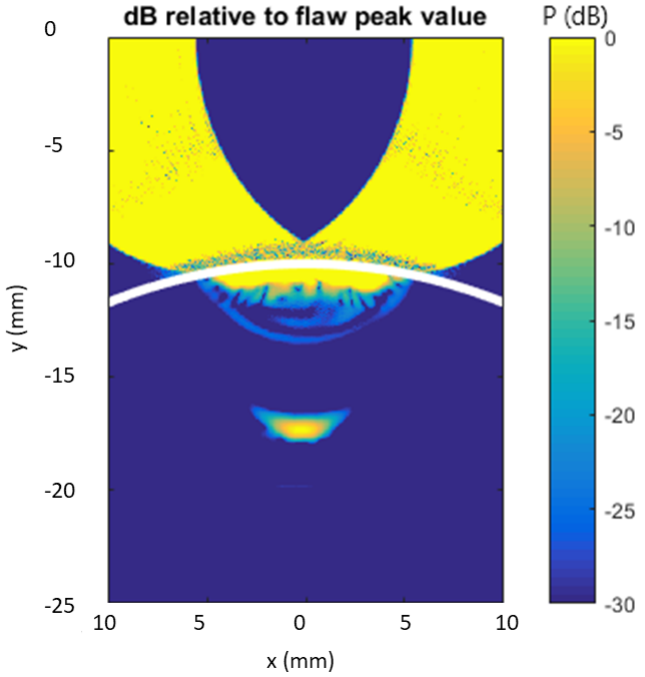

Figure 4.3.1: Example TFM B-scan of a FBH simulated using CIVA, using nominal surface profile (shown in white) for focusing the data.

path, as shown in Fig. 2.1.5, which can be summarised as probe-interface-flaw-interface-probe. This parameter was minimised to reduce simulation time. The "accuracy" setting in CIVA was set to 3, after running a batch of simulations with accuracy number set from 1-10, and observing that peak flaw signal from a 10 mm convex curved radius block changed by $< 1\%$ for values of 3 and above versus 10. CIVA includes an option for inclusion of interface reflections; this was selected to allow use of the surface detection TFM technique in BRAIN.

The CIVA model allowed faster execution, and therefore it was used to build up a map of flaw sensitivity. Individual TFM images similar to that shown in Fig. 4.3.1 were created for each flaw location. Each of these required execution of a separate FMC model in CIVA, followed by data export. Data was then restructured into BRAIN format, and used as an input to the TFM B-scan function. It is possible to reconstruct the detected surface in CIVA [116], however BRAIN was used to keep the method consistent between modelled and experimental data.

This made the creation of sensitivity maps more feasible, with an example shown in Fig. 4.3.3. These were created by taking the peak signal from a TFM image of the flaw oriented at different locations in the part volume, and then plotting the relative peak signal strength of each flaw in 2D. This process is shown in

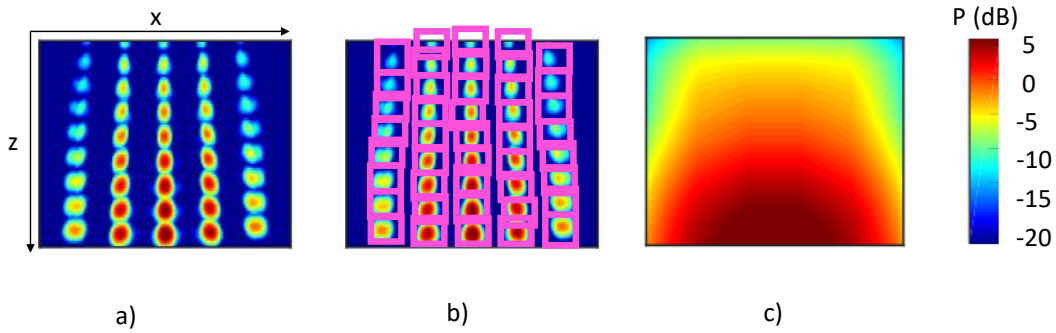

Figure 4.3.2: Steps taken to produce a sensitivity map. First in a), representative TFM flaw images are created for each flaw location. For each, the peak flaw value is gated, with peak value taken from the boxed region in b). Finally in c), the peak value at each location is interpolated in 2D to create a representation of peak flaw signal variation within the inspected volume.

Fig. 4.3.2.

While CIVA modelling was a less computationally intense solution than the finite element model, it was still limited by the time taken to calculate a result. More crucially for the work flow of the modelling approach, at the time of writing, CIVA had not implemented a technique to automatically transfer FMC data out of the program for further analysis. This meant that a laborious process was required to manually extract each individual result using the GUI before post-processing.

Next, a third, more simplified was used to create sensitivity maps.

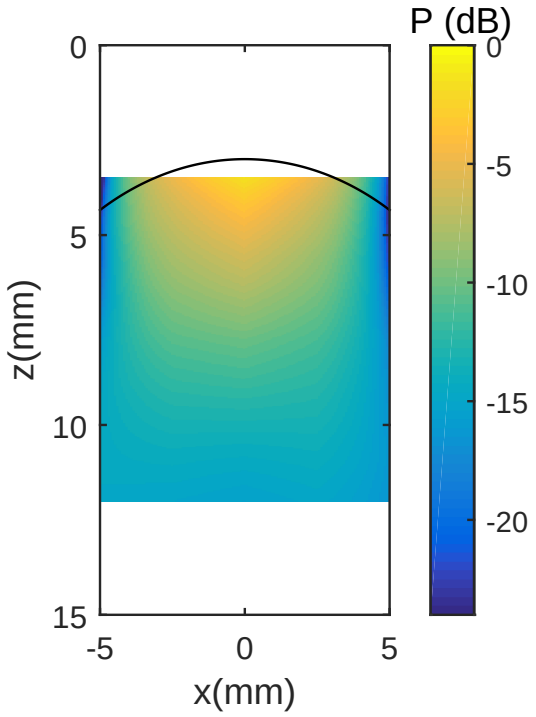

Figure 4.3.3: Example of a sensitivity map produced using CIVA. This was created by creating 45 separate TFM images similar to Fig. 4.3.1. Flaw spacings were 2.5 mm in this example. Peak signal was taken and interpolated in 2D to give 0.1 mm between values. Decibel scale is set relative to highest flaw signal in specimen.

4.4 SEMI-ANALYTICAL MATLAB MODEL TO CREATE SENSITIVITY MAP

This section describes the development of a ray-tracing based model in MATLAB. The aim was to create a model that was as simple as possible, yet still incorporated the key mechanisms influencing the variation in flaw sensitivity through the part volume.

4.4.1 MODEL SPECIFICATION AND LIMITS

Rather than model the image of a flaw produced during an inspection, as was the aim using the CIVA and PZ Flex approach, this purpose made model only considered the reduction in amplitude of plane waves passing through the volume of the part. The idea was to provide a 2D DAC profile for a given component surface geometry, which could then be used in conjunction with a measured flaw signal to predict signal strength elsewhere in the component. As a set of flat calibration blocks with target FBHs are already defined, and frequently used for immersion inspection at Rolls-Royce, the idea would be to model only the influence of the non-planar geometry, rather than the entire inspection. Output of the model was a sensitivity map based on geometry, similar to that shown in Fig. 4.3.3, rather than a TFM image.

The model of sensitivity variation was limited to a 2D approximation of the array behaviour in the active plane.

This model is based on that described by Zhang [87], developed from principles in Schmerr [117]. These techniques apply the ToF and amplitude values calculated by ray-tracing to Fourier-transformed input signals, then apply the inverse Fourier transform to create A-scans for each element combination.

There are four key differences with this model. Firstly, the A-scans are not calculated - therefore there is no need to apply Fourier transforms. Secondly, scattering is not taken into account; rays are assumed to reflect omni-directionally from targets. Another way of expressing this is to say the scattering matrix is fixed at unity. Thirdly, rather than model a single point (the flaw position), the produced image places an omni-directional scatterer with unity scattering matrix at every pixel position in the map. Finally, the inspection process of FMC, followed by TFM is not modelled. Instead, the sensitivity is calculated directly

by summing the contribution of rays from each tx-rx element combination, at each pixel in the sensitivity map.

4.4.2 MODEL DETAILS

Flaw locations are determined inside the model, and then Fermat's principle is used to determine the ray paths. An analytical description of the surface interface is used together with MATLAB's `fminsearch()` to find the PoR corresponding to the minimum ToF. A number of pixels n_{pix} is chosen, which creates an $n_{\text{pix}} \times n_{\text{pix}}$ sized grid. Typically in this thesis a value of $n_{\text{pix}} = 100$ and $n_{\text{el}} = 32$ were used for sensitivity maps; however a cut-down version is shown in Fig. 4.4.1 to allow visualisation. This uses an optional mode developed to show the ray paths, helping visualise the effect of different surface geometries.

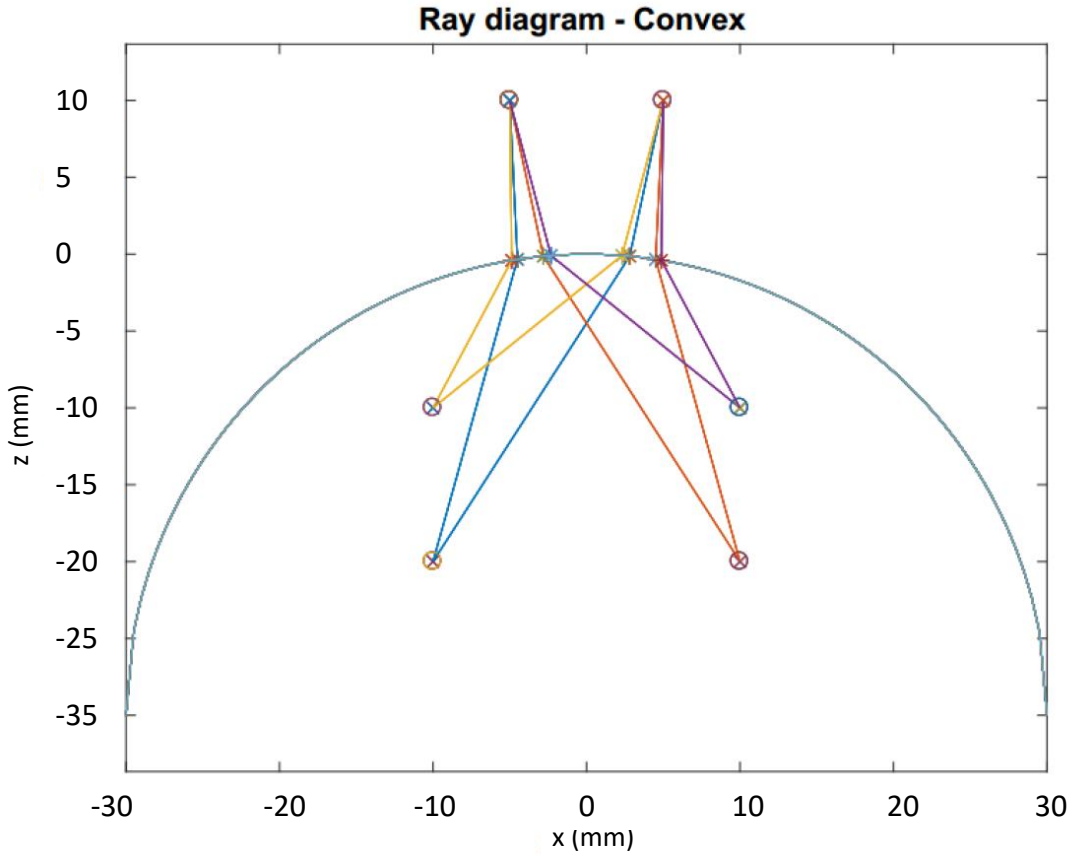

Figure 4.4.1: Plot of ray paths calculated through a water-steel convex interface when $n_{\text{pix}} = 2$, and $n_{\text{el}} = 2$.

For a sensitivity map with m pixels on the z-axis and n on the x-axis, the sensi-

tivity at pixel P_{mn} is calculated according to

$$P_{mn} = \sum_{i=1}^{n_{\mathrm{el}}} \sum_{j=1}^{n_{\mathrm{el}}} D(\phi_i) D(\phi_j) T(\theta_i) T(\theta_j) A_{\mathrm{w}}(a_i, b_j) A_{\mathrm{s}}(b_i, a_j) A_{\mathrm{b}}(a_i, b_i, a_j, b_j) \quad (4.2)$$

where i denotes transmitting element, j receiving element, $a_{\mathrm{i}}, b_{\mathrm{j}}, a_{\mathrm{j}}, b_{\mathrm{i}}$ relate to the paths labelled in Fig. 4.4.2, $D(\phi_i)$ and $D(\phi_j)$ are the element directivity calculated on tx and rx respectively, $T(\theta_i)$ and $T(\theta_j)$ are the transmission coefficents on entry and exit of the interface respectively, A_{w} is the attenuation due to absorption in water, A_{s} is attenuation due to grain scattering in steel, and A_{b} is the attenuation due to 2D cylindrical beam spread.

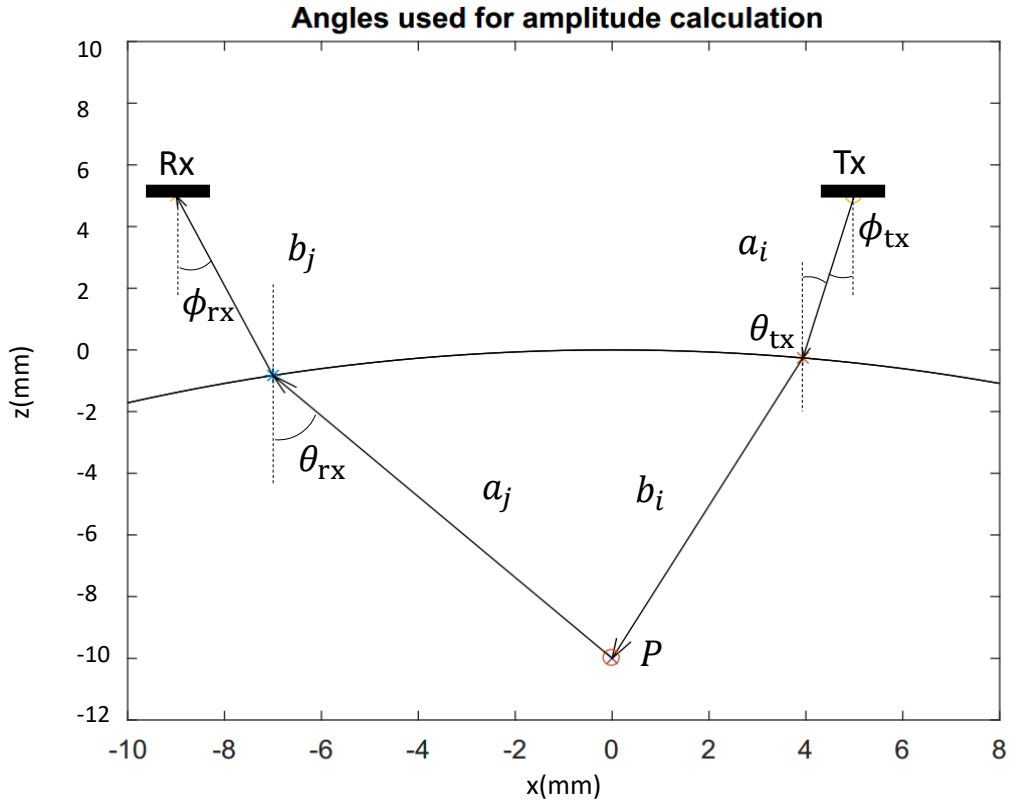

Figure 4.4.2: Example ray path from transmitting element, to imaging point P, to receiving element. Element directivity is related to ϕ, whereas transmission coefficient is a function of θ. Lengths a_{i} to b_{j} are used to calculate ToF.

Note that

$$D(\phi) = \frac{\sin(\frac{l_\mathrm{p}\pi}{\lambda}\sin(\phi))}{\frac{l_\mathrm{p}\pi}{\lambda}\sin(\phi)}, \tag{4.3}$$

where l_p is the array element pitch. The transmission coefficient is given by

$$T(\theta) = \frac{2\rho_1 c_1 \cos\theta}{\rho_2 c_2 cos\theta + \rho_1 c_1 (1 - \frac{c_2^2}{c_1^2}\sin^2\theta)} \tag{4.4}$$

where N is as defined in Eq. (2.7), ρ is material density, and c is the speed of sound in the material; with numbers 1 and 2 referring to water and steel properties respectively in the tx case, and with the opposite association in the rx case. Note that this is the longitudinal-longitudinal case, therefore treats the steel as an equivalent fluid.

Attenuation by absorption of water at 10 MHz is given [118] by

$$\begin{aligned} \alpha_\mathrm{w} &= 25.3 \times 10^{-15} f^2 \\ A_\mathrm{w} &= \exp(-\alpha(f) l) \\ \therefore A_\mathrm{w} &= \exp(-2.53(a_\mathrm{i} + b_\mathrm{j})), \end{aligned}$$

a value of $\alpha_\mathrm{s} = 4.94$ for FV535 steel was used to give

$$A_\mathrm{s} = \exp(-4.94(b_\mathrm{i} + a_\mathrm{j})),$$

and finally, the attenuation due to beam-spreading was taken into account by assuming 2D wave propagation to give

$$A_\mathrm{b} = \frac{1}{\sqrt{a_\mathrm{i} + b_\mathrm{i} + a_\mathrm{j} + b_\mathrm{j}}}.$$

4.4.3 EXAMPLE MODEL RESULTS

Running the above model with the inputs shown in Table 4.3 produced the output shown in Fig. 4.4.3. Note that these sensitivity maps are normalised to the

maximum signal in each plot, therefore they show the different distributions of signal strength given by different interfaces, rather than a comparison between them.

Table 4.3: Input parameters for Fig. 4.4.3

n_{pix}	n_{el}	s (mm)	standoff
100	32	0.5	10

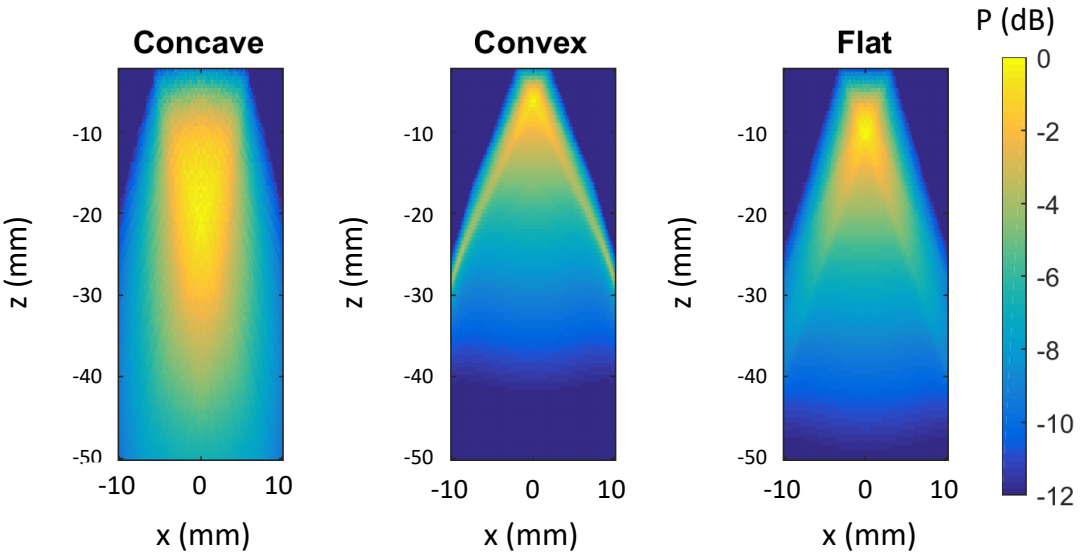

Figure 4.4.3: Example of sensitivity maps produced for convex, concave and flat interfaces. Note that radius of curvature of convex and concave interfaces is 30 mm. Colour bar shows dB values of pressure, relative to the highest value in each map.

4.5 SUMMARY

In this section, three different modelling approaches were considered, applied to the same problem. Reasons for observed differences in peak flaw sensitivity through curved surfaces were outlined in Section 4.1. These were thought of as the difference between the physical behaviour pre-supposed by the back-propagation used to create the TFM image, and the actual behaviour of the waves deployed during FMC. Finite width cylindrical waves, increased average angle of refraction and increased ray path attenuation were thought to be prime contributors

to sensitivity change. The geometry of the problem was defined, limiting the investigation to circular convex or concave curvatures, in the range of 10-40 mm radius. Depth was considered up to 50 mm in the material. These values were chosen based on the most commonly encountered geometries for disc inspection. The 10 MHz, 32 element probe selected for this study was used throughout.

The first model developed was a 2D finite element model using PZ Flex. Two mesh size studies were performed, using a Python based batch-controller developed for this purpose. The first showed that for features of 1 mm radius, the centrally modelled A-scan would have a correlation coefficient of greater than 0.5 compared to a gold-standard mesh density of $n_{\text{epw}} = 100$ for any $n_{\text{epw}} > 35$. Secondly, as part of a drive to reduce model run time, a similar study found that for the reflection from a FBH through a curve of 10 mm radius could be accurately reproduced with $n_{\text{epw}} = 28$, and that a greater mesh density was required to accurately match the response at more oblique elements of the array. Steps to improve the run time of the model from 3 hours to 15 minutes were detailed, and TFM images were produced showing an example of the B-scan representation that could be obtained from the model.

Use of PZ Flex allowed the modelling of a selection of flaw locations, however the computational burden of generating an entire map of results was deemed to large to be practical for creation of sensitivity maps. Furthermore, the limitation of a 2D model was considered to be a weakness in the approach. For these reasons, a 3D FMC model was developed using CIVA, as detailed in Section 4.3. The modelling assumptions of CIVA are discussed, and an example TFM image from a FBH model is shown. Furthermore, owing to the speed of the CIVA model (approximately 10 times faster than the PZ Flex model for the same problem), sensitivity maps were produced, with an example shown of the peak sensitivity map predicted from a 10 mm convex radius test piece.

Gathering results from the CIVA model required laborious manual intervention, and furthermore it was thought that the full-scale model may be an unnecessarily complex approach. A simplified ray-tracing model, considering only the angle of refraction, and attenuation effects outlined in Section 4.1.1 was produced. This had the added benefit of producing sensitivity maps in a fully-automated fashion, and providing faster execution than the CIVA model. The algorithm of the model, similar to the process used for creating TFM images, was described in Section 4.4, with example sensitivity map results for flat, convex and concave curvatures shown in Section 4.4.3.

In Table 4.4, the key differences between each approach are summarised. t_c refers to the typical time each approach took to simulate a representation of the peak signal from a TFM image, for the inspection problem considered here.

Table 4.4: Comparison of modelling approaches

name	t_c (s)	processing	dimensions
FEM	10800	automatic	2D
CIVA	30	manual	3D
MATLAB	0.005	automatic	2D

Following the demonstration of surface-corrected TFM detailed in chapter 3, this section detailed the development of tools to quantify the expected performance of TFM through surfaces of defined curvature. In order to validate these approaches, a set of experimental measurements were taken, through a process described in the next chapter.

Chapter 5

EXTRACTION OF FLAT-BOTTOMED HOLE RESPONSE THROUGH CURVED INTERFACES USING TFM C-SCANS

5.1 AIM

This chapter describes the method used to quantify the peak signal, API and SNR obtainable for TFM C-scan measurements of FBHs through radially curved surfaces.

Use of C-scans was preferred over B-scans, as this removed the possibility of reduced signal response resulting from the B-scan imaging plane not intersecting the centre of the defect. A technique for creating the C-scan, storing associated data, and extracting quantitative information was developed. This chapter aims to ensure that the method behind gathering the experimental results is clear, before they are compared to modelling results in Chapter 6.

5.2 TEST PIECES

Owing to the expense of creating accurate artificial defects, the number of test cases was not equal to that of the number of models used to create one sensitivity map in Section 4.4 for example. Instead, cases were chosen to show the key changes in flaw sensitivity for different curvatures, metal paths and flaw offsets.

A set of single-metal-path (SMP) test blocks were created; each with a centrally located and an offset defect as shown in 5.2.1. Blocks were produced with radii of 10, 15, 20, 25, 30, 35 and 40 mm. Each of these had a wire-cut surface profile, with a mean measured surface roughness value of $R_a = 0.8\,\mu m$. The details of these are shown in Table 5.1.

The dimensions of the test blocks in Table 5.2 and Table 5.1 were measured, to check that the wire-cutting process resulted in the desired dimensions. The metal path lengths of the blocks were measured using electronic calipers (specification given in Table A.1), and are included in the MPm column (standing for metal path as measured).

The radius for each test block was checked using image processing. Firstly, a flat side of the test block was scanned at 600 dpi using a flatbed scanner. This was used in order to obtain an image of the block without lens distortion. Images for each test block were binarised using the Fast Marching Method [119], and then the edge was extracted using a Sobel filter [120].

A circle was fitted through the edge points using a least-squares method described by Pratt [121] to obtain radius in terms of pixel size. Using the known pixel size of 0.042 mm a measurement was obtained for the radius. Measured radius is included in the tables as Rm, standing for radius as measured. MPn and Rn stand for metal path nominal, and radius nominal respectively.

A set of multi-metal-path (MMP) blocks were created to show how the flaw signal would vary with depth for different curvatures. Blocks were produced with radii of 10, 15 and 20 mm, with metal paths of 2.5, 7.5, 17.5, 27.5, 37.5 and 47.5 mm. Additionally, a flat block with the same metal paths was produced to provide a reference. The MMP blocks are pictured in Fig. 5.2.2, with geometry details listed in Table 5.2. FBHs with a 0.63 mm diameter and a depth of 2.5 mm were used as the target defect for all SMP, MMP and rough-surfaced blocks in this study.

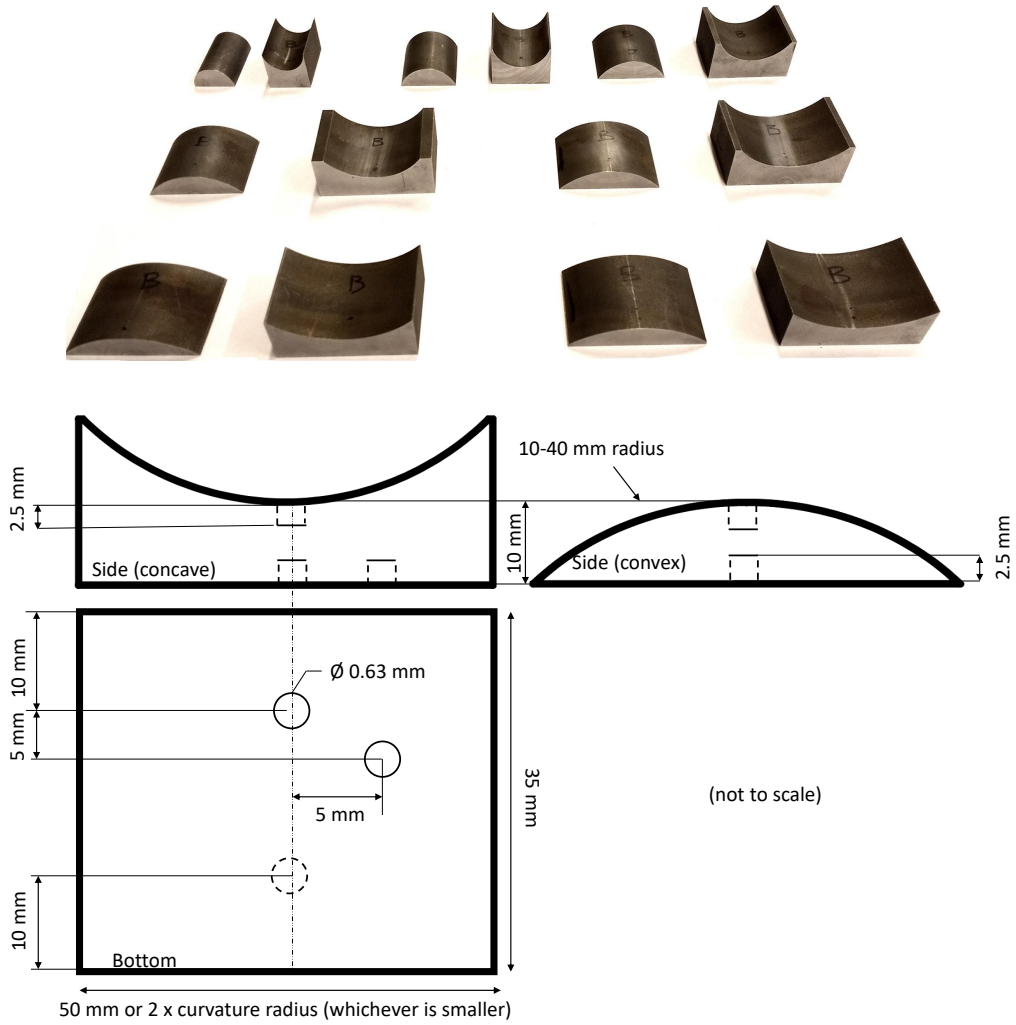

Figure 5.2.1: Diagram of single-metal path (SMP) block series. The blocks are made from FV-535, a high chromium martensitic stainless steel (12% CrMoV grade)

SMP and MMP blocks were both wire-cut out of a billet of FV-535, a high chromium martensitic stainless steel (12% CrMoV grade) designed to reduce high-temperature creep [122]. This is the same material as is used for disc forging inspection calibration blocks, so was chosen to make the results as industrially relevant as possible. The forged disc was made of a fine-grained steel, assumed to be isotropic and heterogeneous. The rough surfaced test piece was an existing calibration block for profile measurement systems, constructed of carbon steel.

Finally, a disc forging was used as a practical example of a challenging inspection scenario. The curvature and roughness of the surface were two features not present in the SMP and MMP test blocks. Three 50 thou (1.27 mm) diameter

Table 5.1: SMP Block Series Dimensions

ID	Surface Shape	Rn (mm)	Rm (mm)	MP (mm)	Hole Position
SV10C075	Convex	10	10.4	10.09	Central
SC10C075	Concave	10	9.85	10.04	Central
SV15C075	Convex	15	15.0	10.06	Central
SC15C075	Concave	15	14.6	10.06	Central
SV20C075	Convex	20	20.3	10.09	Central
SC20C075	Concave	20	19.0	10.03	Central
SV25C075	Convex	25	24.9	10.02	Central
SC25C075	Concave	25	25.1	10.18	Central
SV30C075	Convex	30	30.1	10.04	Central
SC30C075	Concave	30	30.3	10.02	Central
SV35C075	Convex	35	35.2	10.1	Central
SC35C075	Concave	35	35.4	10.07	Central
SV40C075	Convex	40	40.3	10.1	Central
SC40C075	Concave	40	39.2	9.81	Central

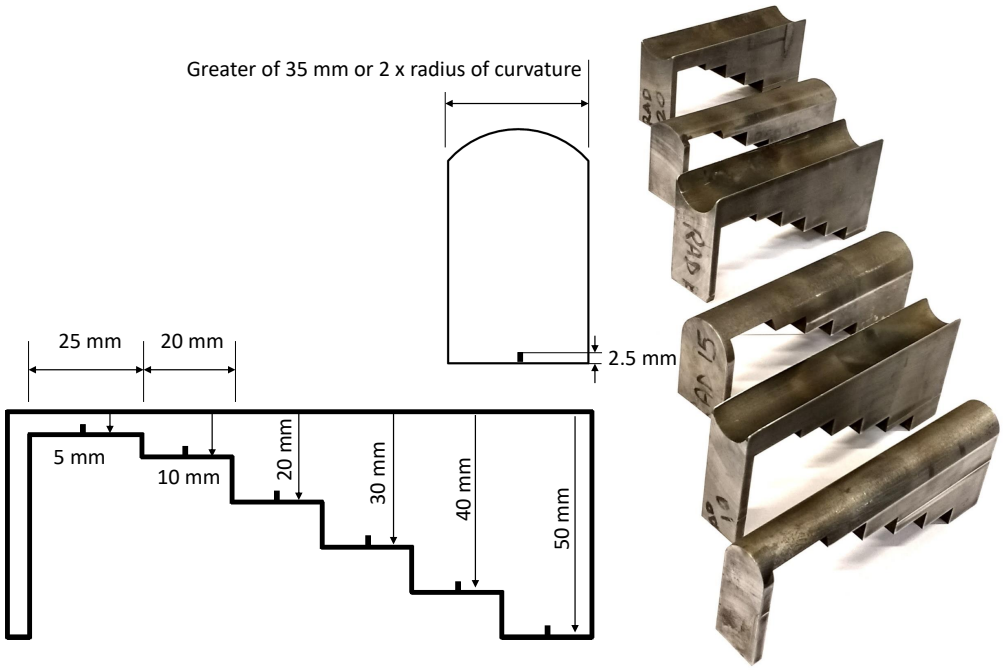

Figure 5.2.2: Diagram of multi-metal path (MMP) block series

holes were drilled into the back surface to act as example targets.

Figure 5.2.3: Photograph of black forged disc. Diameter is roughly 300 mm.

Table 5.2: MMP Block Series Dimensions

ID	Surface Shape	Rn (mm)	Rm (mm)	MPn (mm)	MPm (mm)
MV10C025	Convex	10	10.0	2.5	2.4
MC10C025	Concave	10	10.8	2.5	2.4
MV10C075	Convex	10	10.0	7.5	7.3
MC10C075	Concave	10	10.8	7.5	7.8
MV10C175	Convex	10	10.0	17.5	17.4
MC10C175	Concave	10	10.8	17.5	17.7
MV10C275	Convex	10	10.0	27.5	27.7
MC10C275	Concave	10	10.8	27.5	27.7
MV10C375	Convex	10	10.0	37.5	37.4
MC10C375	Concave	10	10.8	37.5	37.6
MV10C475	Convex	10	10.0	47.5	47.4
MC10C475	Concave	10	10.8	47.5	47.6
MV15C025	Convex	15	15.4	2.5	2.3
MC15C025	Concave	15	15.8	2.5	2.7
MV15C075	Convex	15	15.4	7.5	7.5
MC15C075	Concave	15	15.8	7.5	7.7
MV15C175	Convex	15	15.4	17.5	17.4
MC15C175	Concave	15	15.8	17.5	17.8
MV15C275	Convex	15	15.4	27.5	27.5
MC15C275	Concave	15	15.8	27.5	27.6
MV15C375	Convex	15	15.4	37.5	37.4
MC15C375	Concave	15	15.8	37.5	37.5
MV15C475	Convex	15	15.4	47.5	47.4
MC15C475	Concave	15	15.8	47.5	47.6
MV20C025	Convex	20	19.2	2.5	2.3
MC20C025	Concave	20	20.0	2.5	2.4
MV20C075	Convex	20	19.2	7.5	7.27
MC20C075	Concave	20	20.0	7.5	7.4
MV20C175	Convex	20	19.2	17.5	17.5
MC20C175	Concave	20	20.0	17.5	17.5
MV20C275	Convex	20	19.2	27.5	27.4
MC20C275	Concave	20	20.0	27.5	27.6
MV20C375	Convex	20	19.2	37.5	37.5
MC20C375	Concave	20	20.0	37.5	37.5
MV20C475	Convex	20	19.2	47.5	47.5
MC20C475	Concave	20	20.0	47.5	47.5
MF00C025	Flat	none	none	2.5	2.44
MF00C075	Flat	none	none	7.5	7.47
MF00C175	Flat	none	none	17.5	17.35
MF00C275	Flat	none	none	27.5	27.56
MF00C375	Flat	none	none	37.5	37.48
MF00C475	Flat	none	none	47.5	47.55

5.3 NDE EQUIPMENT

The equipment used is detailed in Table 5.3. The phased array controller was chosen for its ability to capture FMC data, and its availability at Rolls-Royce. BRAIN was chosen to acquire the FMC images, as it provided a flexible interface for performing TFM during experimentation. The Lenovo Y70 was chosen because the graphics card enabled the use of CUDA acceleration when performing TFM imaging.

Table 5.3: Equipment used for acquisition and processing

Phased array controller	Peak NDT Micropulse 5A
Phased array probe	10 MHz linear array (Probe B, specification in Table A.3)
Positioning system	Winspect NDT Cartesian 3-axis scanning system
Computer	Lenovo Y70 with Nvidia GTX 870M 4 GB graphics card
Software (data acquisition and imaging)	BRAIN MATLAB Toolbox
Software (data processing)	MATLAB

The encoders for the Cartesian axis scanner tank were not linked to the acquisition laptop, therefore time-encoding had to be used to create C-scans. Details of this process are outlined further in the next section. The Cartesian axis scanner was used with an immersion tank. In addition to X, Y and Z axis translation, it also had two degrees of freedom that could be manually adjusted to alter probe tilt. The tank was filled with water the day prior to scanning, to allow water temperature to reach room temperature, and to allow air bubbles to dissipate. For all scans conducted, surfaces of the probe and test pieces had air bubbles removed using a brush.

To fine-tune the orientation of each test piece prior to scan, an adjustment plate was created. This had four adjustable legs (with only three actually used in each scan), and a ridge along its length. The purpose of this was to allow alignment

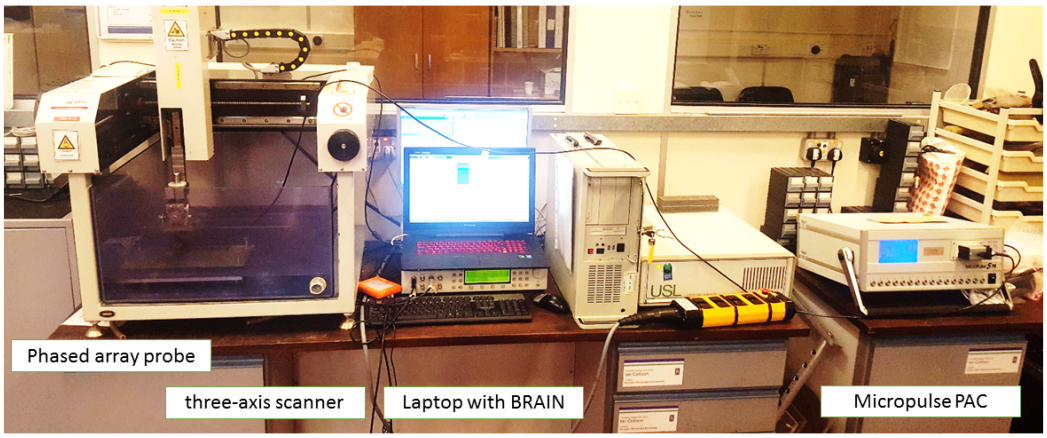

Figure 5.3.1: Photograph of equipment used, including scanner and phased array controller.

between the scanning plane of the probe in the x, y and z rotation directions. Although this was re-adjusted between tank refills, markings were made on the interior of the tank to minimise the re-adjustment required.

5.4 TEST PIECE POSITIONING

Position of the test block relative to the probe front face, and alignment of the scanning plane to the base plane were adjustable. The following procedure was developed to minimise position errors, using the A-scan display in BRAIN, which synthesised three A-scan signals from the 1st, 2nd and 3rd thirds of the array.

Firstly, the adjustment plate (shown in Fig. 5.4.1) was located in the same position in the tank each time it was set up. Then the probe tilt was normalised with respect to the surface of the plate. This was achieved by tilting in the active plane until time of flight of the three element groups was equal, and in the passive plane where the mean signal amplitude was highest for these three groups.

Once the probe was normal to the plate, the scanning directions of the Cartesian axis scanner had to be aligned with the plate. This was achieved by adjusting the rotation and tilt angles in the following fashion (refer to Fig. 5.4.2) for each step. The highest amplitude obtained by positioning the probe over the edge on

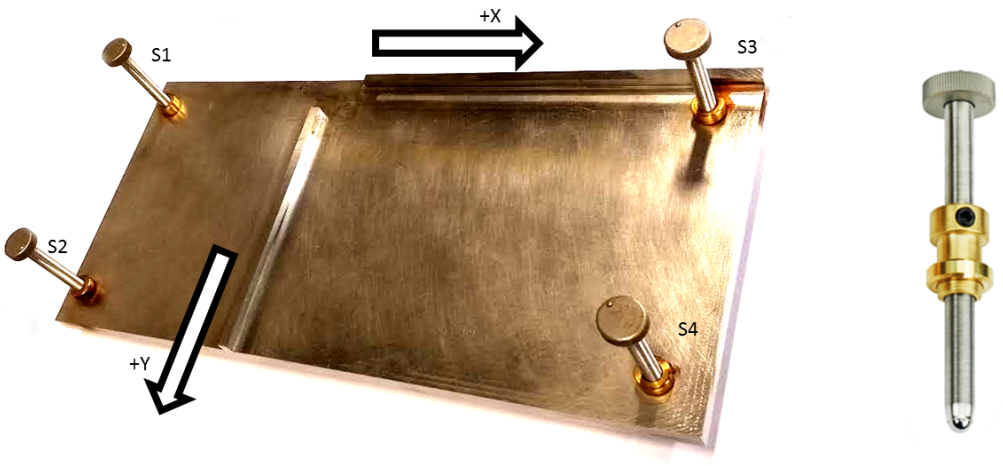

Figure 5.4.1: Photo of plate used for test pieces alignment, and adjustment screw example.

the y-axis was noted, and then the probe was scanned along this ridge. If a drop in amplitude was observed, the plate was rotated around S_1 and the process was repeated until the peak amplitude did not vary more than $\pm 10\%$. Next, tilt of the plate was adjusted by noting the time of flight to the surface at P_3, and ensuring this was equal to P_4.

The probe normality was then fine-tuned to find the centre line of the curvature of the test piece. The straight edge of the piece was aligned with the x-axis, and the centre line was found by adjusting tilt in the active plane until a symmetrical response was received from the A-scan groupings across the probe.

The process for measuring this is shown in Fig. 5.4.3). Diagram a) shows the test piece located in the test tank, underneath the array.

In order to align the scanning axis with the centre of curvature of the test piece, the following process was used. The array was split into three different element groupings. All elements in the first array grouping, shown in red, were fired simultaneously. This gave an A-scan describing the path shown in red in a). A zoomed in window from this A-scan is shown in b). This process was repeated for the other two groupings.

This produced three separate A-scans, with details of the peak signals shown in b). Using this display, the scanner was carefully positioned so that the red

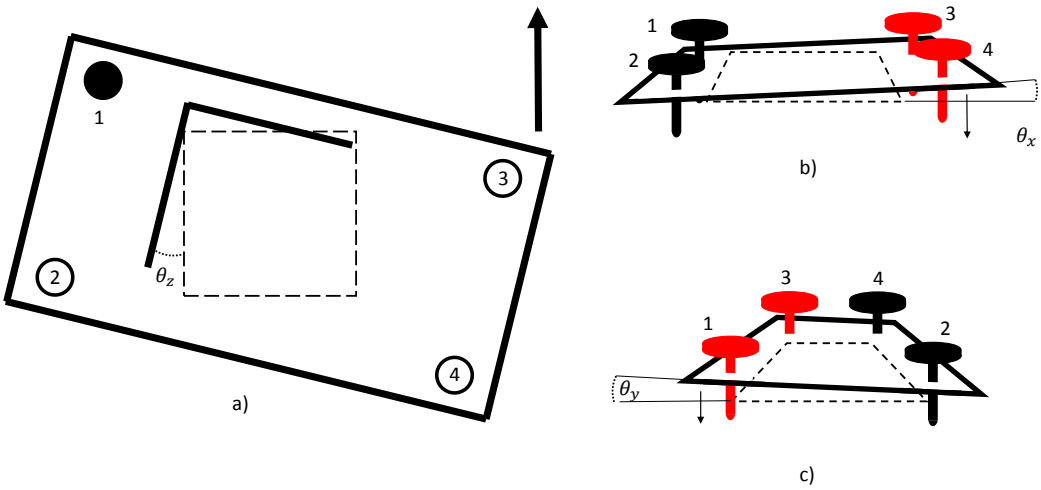

Figure 5.4.2: Angular adjustment of plate using screws, in a) plate is rotated around screw 1, b) screws 3 and 4 are used to adjust θ_x and c) screws 1 and 3 are used to adjust θ_y.

and blue A-scan peaks were superimposed, in order to ensure that the probe was exactly above the centre point of the surface curvature. This method was repeated prior to each scan conducted for this study.

Differences can be seen in the shape of the peaks of the red and blue A-scans. This was encountered during each alignment, and was thought to be caused by a difference in delay time among elements within the element groups. The position of the peaks of the red and green A-scans were used to determine whether the probe was in a central position. These peaks kept a similar form throughout different scans, and so were used as the most consistent reference available from the signal. The observed difference in the reference peak shape may have resulted in a slight misalignment, however any remaining misalignment in the scan setup was compensated for by the surface-measuring TFM mode used.

For tighter curvatures, such as where r = 10 mm the raw FMC A-scan display could be used together with the cursor, to determine the central location in the x direction. Stand off was set to 10 mm by driving the z-axis until the central frontwall reflection from the test piece was 13.48 µs.

Central position in the y-direction was found by driving the probe to the extremes of the test piece, noting the encoder value at the -6 dB edge drop point, and using the nominal location of the hole from the CAD drawings. Scans were conducted

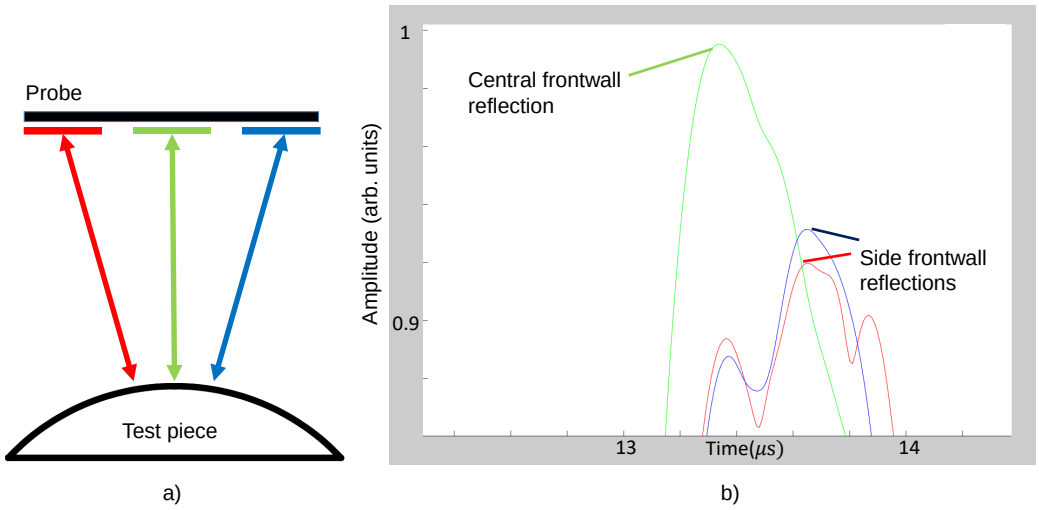

Figure 5.4.3: a) probe position relative to test piece, showing path of ultrasonic energy when probe is centered b) Zoomed in detail of A-scan peaks produced from this configuration, used to help ensure probe centrality. The positioner was moved until the red and blue peaks were aligned.

across a 10 mm region, aligned with the centre line of the curvature of the test piece. From this point onwards, C-scan production was performed in only the y-direction.

For pieces with FBH reflection clearly visible in the initial B-scan, probe position was centred at the location with the highest reflection amplitude. BRAIN's immersion TFM function was used, with the surface detecting "measure" option selected; which initially performed single-media TFM in water, extrapolated surface points, then performed dual-media TFM using the measured surface. Upper and lower bounds were set at 8 and 12 mm.

Probe standoff of 10 mm was chosen to ensure that the probe casing would not interfere with the curvature of the concave 10 mm block, ensuring that the acquisition parameters remained the same between each test piece.

5.5 ARRAY CALIBRATION

The array probe was calibrated by taking an FMC measurement from a flat, polished surface in water. The instrument delay, relative element timing error

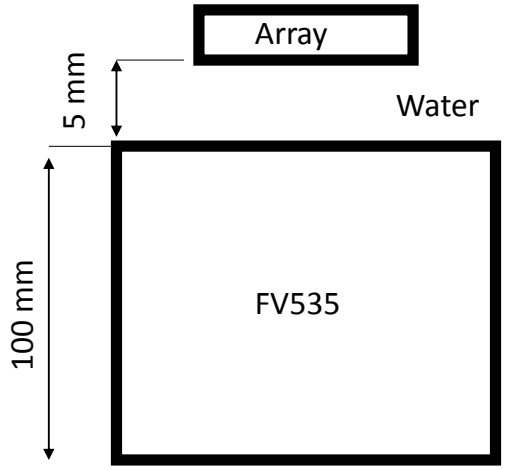

Figure 5.5.1: Experimental setup for measuring variation between array elements

and sensitivity were measured following the recommendations made in Duxbury's work [65] on phased array calibration for FMC processes.

FMC data was acquired in immersion using the setup shown in Fig. 5.5.1. A-scans were extracted using the same element for transmission and reception, with multiple front wall reflections shown. Sensitivity was measured by taking the peak values of the first reflection for all 32 A-scans and comparing their amplitudes to the mean amplitude value, shown in Fig. 5.5.3.

An example A-scan is shown in Fig. 5.5.2, with gates shown. The first gate was used to determine the amplitude of the initial frontwall reflection. The reflection times were taken at 5% amplitude from the first and second reflections, and the period of reflection between the front of the probe and frontwall of the calibration block were calculated. This was then subtracted from the first reflection time to give the overall instrument delay. By subtracting this from each element, the relative time delay for each element was as shown in Fig. 5.5.4.

The greatest timing error was 15 ns, corresponding to a path error of 0.02 mm from the water to the surface.

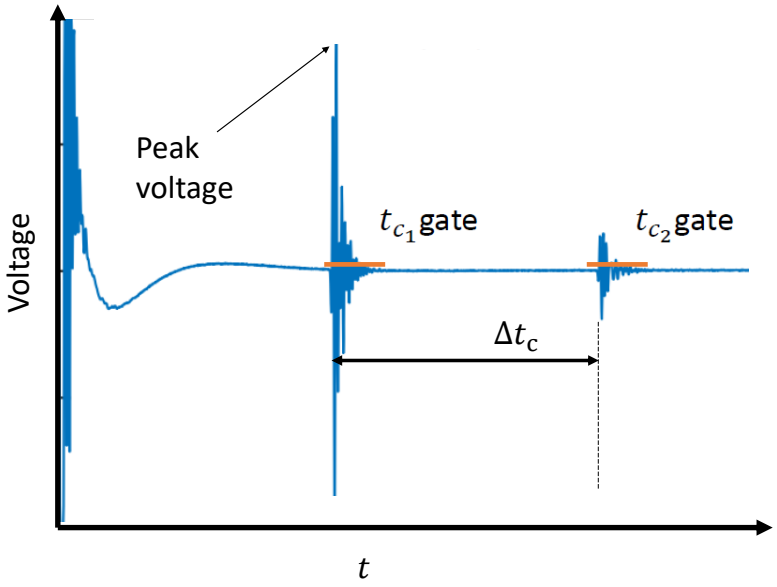

Figure 5.5.2: Example A-scan with gates used for measuring peak amplitude and element delay times. The time difference Δt_c is found by subtracting the times when the two reflections cross 5% of the maximum amplitude detected in each gate. This is then compared with t_c to find the system delay for each element.

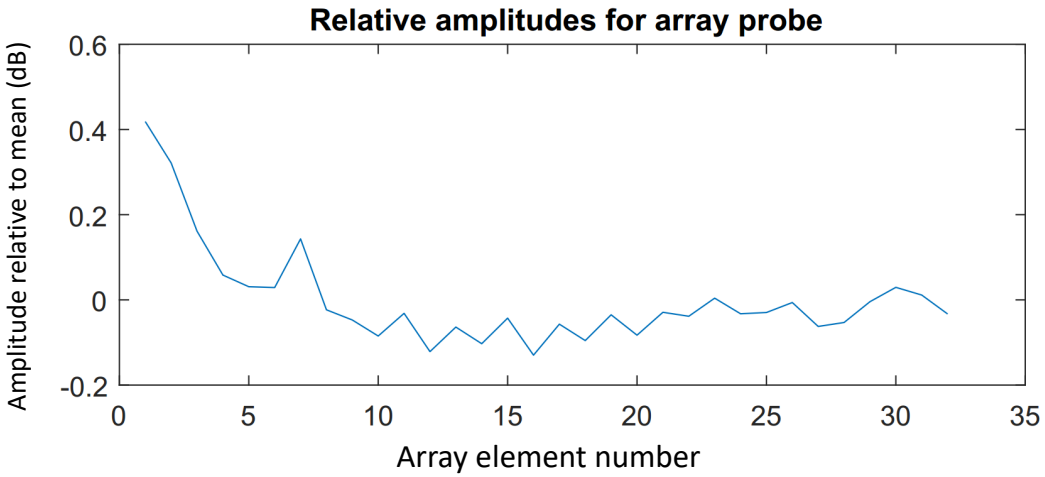

Figure 5.5.3: Relative sensitivities as measured by peak amplitude signal from planar reflector.

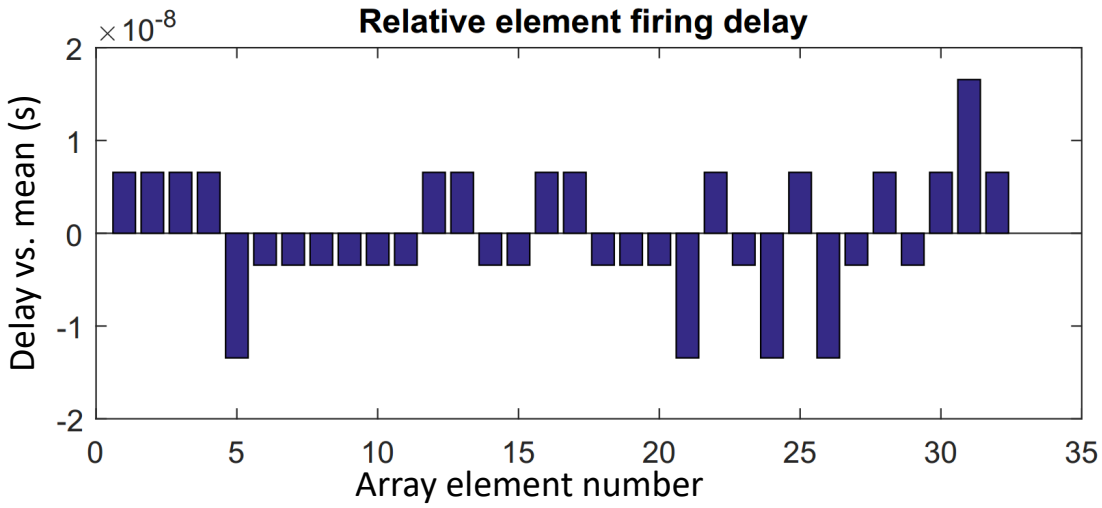

Figure 5.5.4: Relative timing delays of array elements, as measured using the method shown in Fig. 5.5.2.

5.6 DATA ACQUISITION

BRAIN was modified to save every FMC frame as soon as it was acquired, and also keep track of the time taken for each acquisition - a different value every time, usually between 1-2 seconds. The speed of the scanner was fixed at 0.05 mm/s, so that by using the time recorded in MATLAB and the known scanner velocity, the position of a given FM could be accurately determined. The gated values were then extracted, and interpolated to a grid at a resolution of 0.1 mm to construct the C-scan. As long as the maximum acquisition time between FMCs was less than two seconds, then this was sufficient to encode position in 0.1 mm/s steps.

The total time to capture and transfer FMC frames was found to be irregular, as shown in Fig. 5.6.1. While the PRF was set to 1 kHz, the bottleneck for speed was the time taken for the interface between the version of BRAIN and the PAC used to save the FMC frame. BRAIN was adapted by the author to save FMC frames in MATLAB. The implementation of this MATLAB code was not optimised for real-time execution, which led to these irregular delays in the saving process.

This delay was deemed acceptable for the limited scope of work carried out for this study. A more robust solution would need to be developed to enable faster operation for industry use.

Acquisition of an FMC frame was performed using the BRAIN settings outlined in

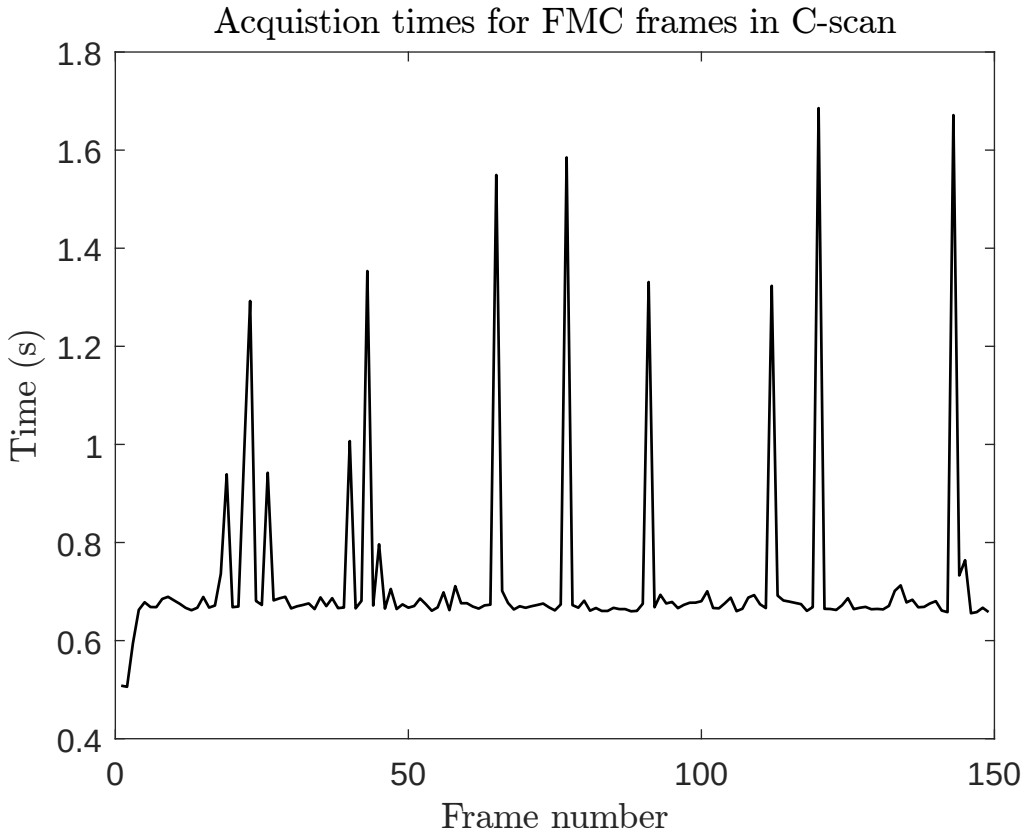

Figure 5.6.1: Time taken to acquire and save each FMC frame using BRAIN and a Peak NDT Micropulse for a typical C-scan. The irregularity of the times was due to the unstable nature of the modifications made to the BRAIN code.

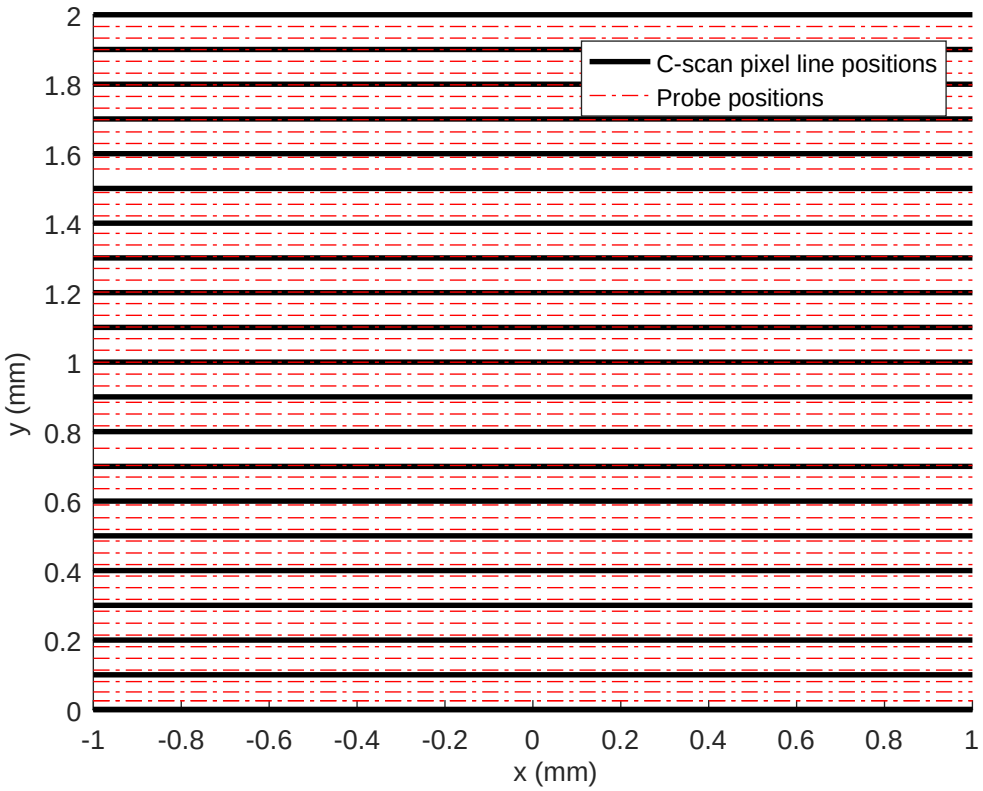

Figure 5.6.2: An excerpt from a C-scan, with ultrasonic data removed and pixel centre lines shown instead. C-scan probe positions are shown in red, and positions where TFM B-scans were interpolated to incorporate the data from the red lines are shown in black.

Table 5.4: BRAIN settings

Material velocity	$5850\,\mathrm{ms}^{-1}$
Acquisition mode	FMC
Sample frequency	100 MHz
Pulse voltage	100 V
Pulse width	50 ns
Time points	3000
Sample bits	16
Gain	40 dB
Filter number	4
Maximum PRF	1 kHz
Averages	1

Table 5.4. The position of the FBH was found using the TFM display, showing an indication when roughly above the centre of the hole (producing a B-scan similar to that shown in Fig. 5.7.1). The value on the y-axis encoder corresponding to this B-scan was set as the start point for the C-scan.

A script was written in MATLAB to extend the functionality of BRAIN to include time-encoded C-scan probe position recording. Lines plotted in Fig. 5.6.2 show the positions of the probe at the times where a frame was captured, alongside the positions that were used for calculation of a C-scan. The red lines are irregularly spaced owing to the irregular period of time the modified BRAIN code took to acquire and save each frame. Black lines show the sampling lines used to create the final C-scan image; the values at these lines were interpolated from the values obtained following focusing the TFM B-scans corresponding to each red line. The C-scanning speed (0.5 mm/s) was chosen to ensure that at least two samples were used for each interpolated value (e.g. there are at least two red lines corresponding to each black line).

A repeatability study was conducted, showing that scans of the same convex test block would produce a peak signal of within 1 dB. This variation was thought to have been caused by slight alignment differences between each scan.

Table 5.5: `cscan_info` saved variables

`path`	location FMC file folder for acquisition
`first_FMC_file`	first FMC in user-selected region of interest
`last_FMC_file`	last FMC in user-selected region of interest
`flaw_position)`	flaw position relative to centre point of test piece
`flaw_diameter (mm)`	diameter of FBH
`scan_speed (mm/s)`	speed of C-scan in x direction
`probe_position`	probe position relative to centre point of test piece
`radius`	known surface shape of test piece used
`repeat_number`	records how many times this scan has taken place

5.7 TFM IMAGING AND QUANTIFICATION

After capturing a set of FMC frames, the data collection was verified by running a MATLAB script called `initial_cscan` giving a `cscan_info` data file. The user could select the region of interest on the generated C-scan, and the acquisition information was saved in `cscan_info` in its most minimal form. This helped reduce the number of files considered for future analyses. `cscan_info` contained only the necessary information to reconstruct the C-scan, not including any of the data derived in the initial analysis. The saved parameters are shown in Table 5.5.

By following the path provided in a loaded `cscan_info` file, the `cscan_analysis` script then accessed the appropriate experimentally acquired FMs, and applied the user-input focal law and gating to each frame. A B-scan, along with other quantities was saved in the result file. `cscan_result` contained everything in `cscan_info`, plus the C-scan image, the imaging options used, and all of the TFM B-scans used to generate the result. Multiple `cscan_result` files were generated for each `scan_info` file when comparing different methods of TFM.

The key variables shown in tables 5.5 and 5.6 were generated using the following process.

Table 5.6: `cscan_result` saved variables

`cscan_info`	information related to the acquistiion of FMC data for this run
`surface_type`	TFM mode using known or measured surface
`surface_detect_limits`	Max and min z surface detection limits in z direction
`interface_gate_length`	Size of interface gate in z (mm)
`flaw_gate_length`	Size of flaw gate in z (mm)
`cscan_pixel_size`	Interpolated square pixel size of C-scan (mm)
`cscan_image`	Full C-scan image produced from all TFMs
`gated_cscan_signal_image`	Signal sub-region selected by user
`gated_cscan_noise_image`	Noise sub-region selected by user
`tfm_data`	All TFMs used in production of C-scan
`cscan_API`	Array performance index calculated using C-scan-signal and noise sub regions
`cscan_SNR`	SNR calculated using C-scan subregions
`cscan_peak`	Maximum pixel value from C-scan signal subregion
`tfm_surface_interpolation`	s value from Fig. 2.3.9
`tfm_bilinear_interpolation`	p value from Fig. 2.3.10

A scan of 10 mm in the x-direction was carried out over each hole, with corresponding FMC files and acquisition time values saved. These FMC frames, together with their positions, constituted the base data from each reflector. Using this data, a single hole could be imaged in a number of different ways. One relevant example was the use of different B-scan surface representation techniques in constructing a C-scan. In Fig. 5.7.1, two B-scans using different imaging modes are shown on the left, with the maximum amplitude gate result shown on the right.

The cyan lines represent the gate boundaries within the material, and the red lines show the upper and lower bounds of the surface detection algorithm where deployed. Indicated in white is the surface used to calculate time delays used for the TFM image. This shows an example of the difference in extracted amplitude from the B-scan was obtained using different TFM settings on the same FMC data. The measured surface algorithm would introduce imaging noise into the C-scan. Note that this example was purposely chosen to show the algorithm break down - selection of a smaller span in the x direction reduced this sort of imaging noise.

The line plots on the right hand side of Fig. 5.7.1 show the maximum amplitude at the x location in the gate. The main difference between the measured surface and the known surface B-scans is the noise produced by the inaccurate surface measurement in the bottom TFM image. This occurs due to the limitations of TFM when it comes to imaging surfaces at an oblique angle. The surface detected by this method, shown in white, is clealy not representative. This can be overcome by restricting the surface detection region to be closer to the centre of the x-axis. This effect is more pronounced for tight surface radii.

A C-scan is formed by stacking many of these B-scans together and creating a hole indication. Position for each maximum line was extracted and plotted at the nearest grid position shown in Fig. 5.6.2,

The C-scan was constructed by plotting the maximum value pixel line at the grid position determined closest to the actual probe position on acquisition (closest black line in Fig. 5.6.2 corresponding to the red line describing probe position).

For each of these C-scans, a noise and signal region was selected, as shown in Section 5.7. The noise region was used to determine the average background level in the part, for the specific imaging technique used. From the signal image, the maximum recorded value is taken as the peak signal from a given hole. The

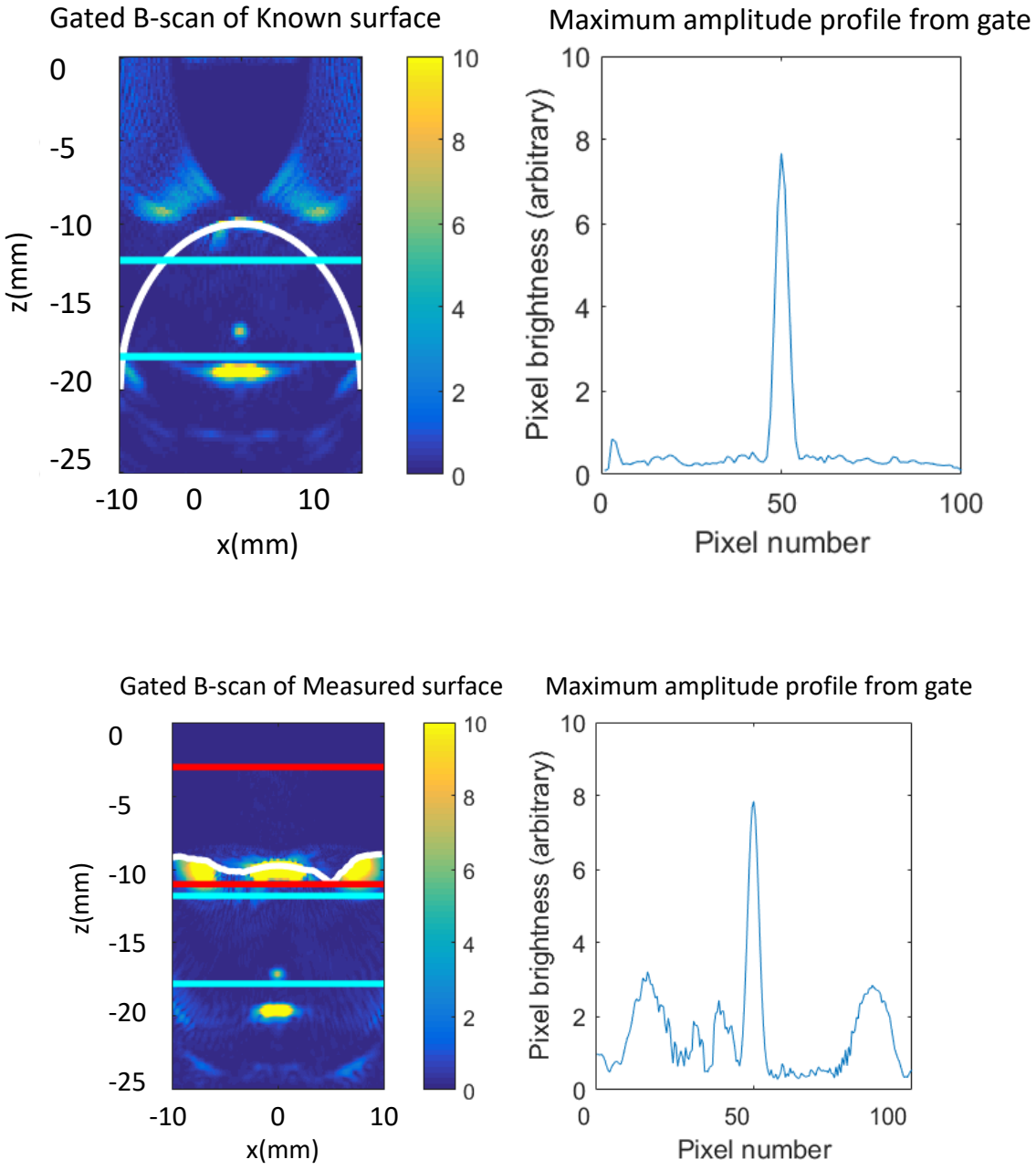

Figure 5.7.1: Brightest B-scans in a scanning run for a 25 mm convex curved block, imaged using (top) known surface and (bottom) detected surface. Surface geometry used for TFM production is shown in white in both. Greater noise is shown for the measured surface, although this can be removed by limitation of the surface representation.)

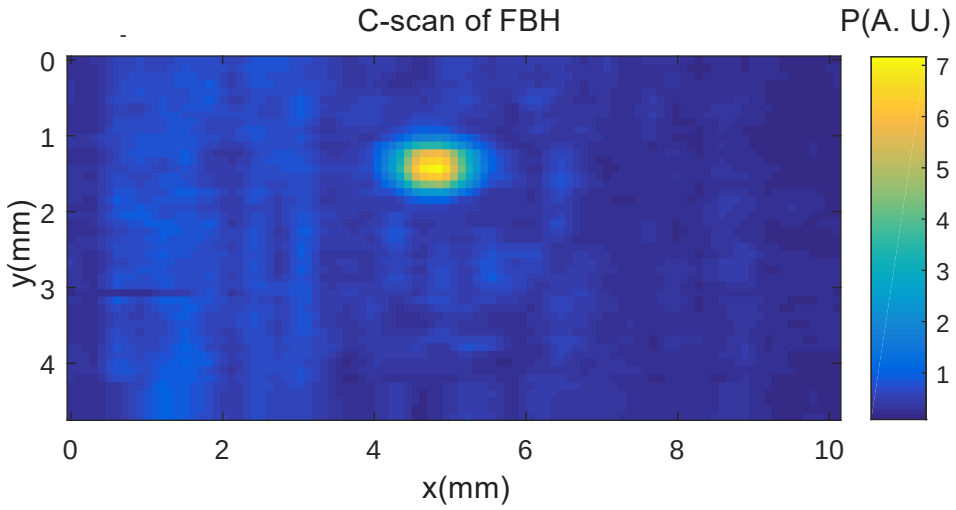

Figure 5.7.2: C-scan image using positions interpolated to a 0.1 mm grid. C-scans like this one were used for all FBH measurements in the next chapter. C-scans were used instead of B-scans due to the difficulty of positioning the probe over the centre of the flaw using the latter method.

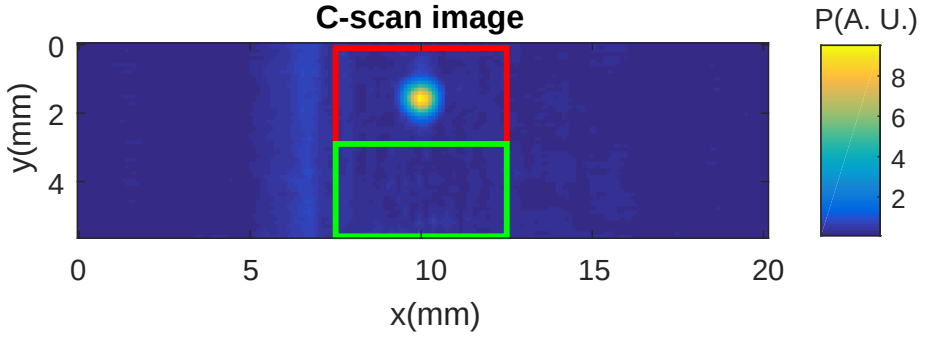

Figure 5.7.3: C-scan image showing regions used for signal analysis. Region extracted for signal image shown in red, and region extracted for noise image shown in green.

C-scan-API is calculated by taking the -6 dB area of the hole and using the API equation [62]:

$$Q_{\mathrm{A}} = \frac{A_{-6\,\mathrm{dB}}}{\lambda^2} \tag{5.1}$$

where Q_{A} is the API, and λ is the wavelength in the test piece. The 2D SNR is calculated by

$$Q_{\mathrm{S}} = 20 \log_{10}\left(\frac{A_p}{A_n}\right) \tag{5.2}$$

where A_{p} is the peak amplitude from the signal sub-image, and A_{n} is the mean amplitude from the noise sub-image.

The process described in this method section was repeated to capture each data point shown in Chapter 6. It is important to understand that each quantified relative peak or SNR value depended on a combination of the test piece geometry, imaging mode used, and method used to quantify the given image. This is summarised in Fig. 5.7.6, where every input or process can be thought of as a variable affecting the final C-scan or B-scan result.

Finally, to quantify the relative drop in peak signal, every group of FBH C-scans was compared to a reference measurement. Unless otherwise specified, the results in the following chapter used the peak signal from hole MF00C075 - a centrally located hole at 7.5 mm metal path below the flat-surfaced MMP block.

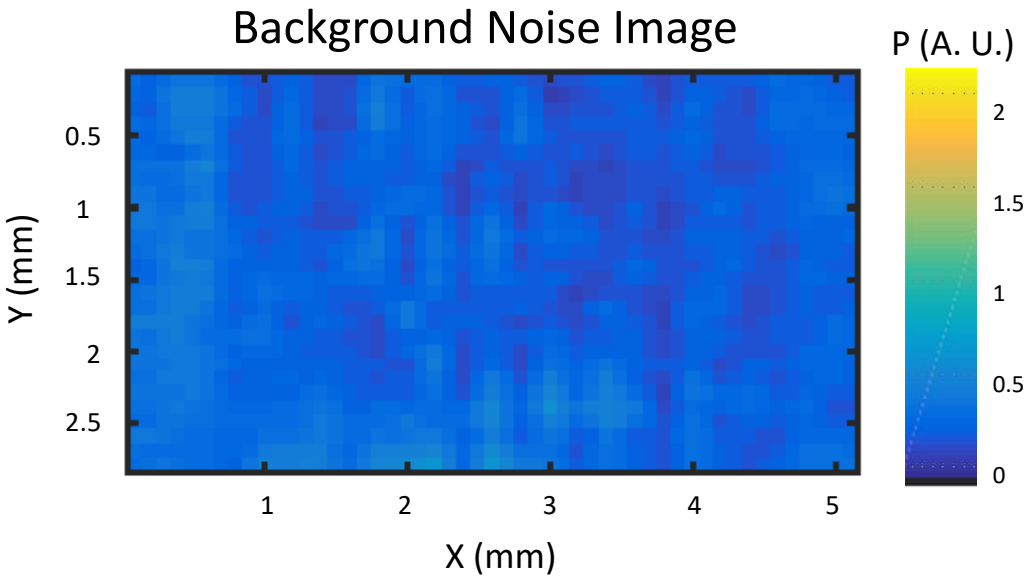

Figure 5.7.4: C-scan sub-image showing sampled noise region.

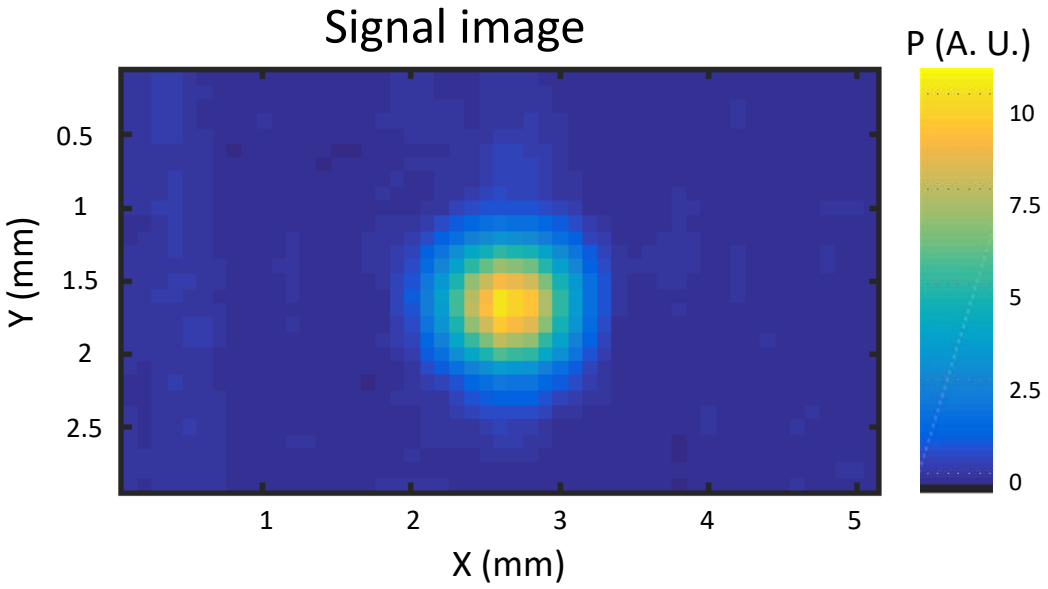

Figure 5.7.5: C-scan sub-image showing flaw imaging region.

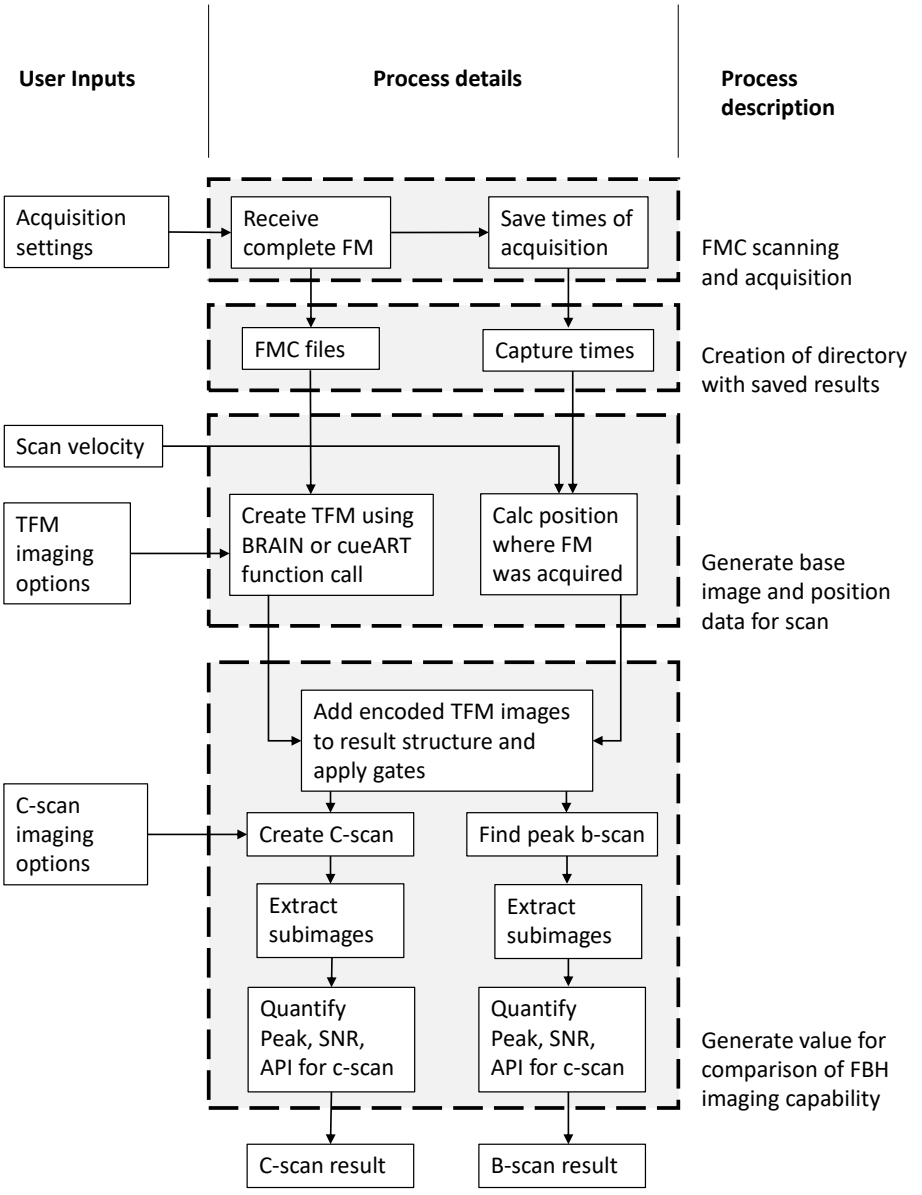

Figure 5.7.6: Flowchart describing data visualisation and quantification process used for each result.

5.8 SUMMARY

This chapter introduced the purpose-made test pieces used in this research, and their link to the geometry of the ultimately desired application - inspection of a black-forged disc. Their design was linked to the sensitivity mapping approach introduced in Chapter 4, with hole positioning chosen to validate the predicted signal at key parts of the material volume, for key curvature values. Chapter 3 considered the applicability of the corrected TFM technique on a case-by-case basis, the case in question being an irregular plate. In contrast, this chapter introduced purpose made test blocks to validate sensitivity maps which could then be used to predict inspection response at the design stage.

The equipment used for data capture was described. This differed from the integrated robotic scanning system used in Chapter 3, but allowed similar performance to be obtained for very simple scan paths. The advantage of this approach was that it used the existing equipment at Rolls-Royce.

Alignment and calibration of the array probe was detailed in this chapter. Each scan was conducted under the same conditions, with the same equipment and the same test piece alignment, so that all differences between measurements were solely related to the difference in test piece surface geometry.

As gated C-scans and B-scans were used as the basis for all results in this study, the process used to develop these was explicitly described. Use of C-scans was said to be necessary, owing to the difficulty of obtaining a repeatable result from a FBH using a 1D array; as opposed to obtaining the signal from a SDH, for which a single B-scan was deemed sufficient. A key step was to remove the positional irregularity introduced by the time-encoded approach of saving B-scans to create the C-scan.

Following capture, the method of organising and evaluating the data was discussed. This was important for both record-keeping, managing complexity of the results, and creating the plots necessary for validation in Chapter 6.

This chapter showed a technique for recording and extracting key information from C-scans of FBHs using BRAIN software to perform corrected TFM. The next chapter uses these results to show key relationships found between blocks of different surface geometries, how these relate to the models developed in Chapter 4, and discusses their significance.

Chapter 6

COMPARISON OF MODELLED VERSUS EXPERIMENTAL TFM IMAGES THROUGH CURVED SURFACES

This thesis has reviewed literature relating to TFM, and identified surface corrected TFM as a potential method for inspecting curved parts. Previous work in chapter 3 showed that TFM could be used as part of an automated, curve following process, and produce comparable C-scans of an aerospace component with an irregular surface.

To quantify the effect of radius of curvature and metal path on peak flaw amplitude, modelling techniques were developed in chapter 4. These were implemented using PZFlex (2D FE), CIVA 3D, and ray-tracing in MATLAB. A series of test blocks were developed, and a procedure for producing TFM C-scans of FBHs was developed in chapter 5.

This chapter presents the results of modelling and experimental measurements, undertaken to understand the effect of curvature and metal path on flaw signal amplitude using TFM. The method described in chapter 5 was used to produce the results shown here. Throughout, TFM is used to refer to the technique whereby surface of the part is measured, followed by TFM correction, as described in the previous chapter. All results use the same array as referred to throughout this thesis: a 32 element, 10 MHz linear array.

Note that data from the offset holes described in the previous data, as well as directly from the rough disc sample were not included. There was not enough time to fully process this data to the required standard. Some indications were hard to find, especially for tight radii, as they were below the background noise level. A spot-check value of a 30 mm concave block predicted a 7.9 dB drop compared to the centrally-located FBH, which can be compared to the 6 dB drop shown in the model in Fig. 6.3.11. More processing work is required to fully match up these experimental results with the modelling predictions.

6.1 SINGLE METAL PATH BLOCK RESULTS

All results in this section were obtained using the single metal path (SMP) block geometries, as described in Table 5.1. A 10 mm standoff was used for all results.

In Fig. 6.1.1 and Fig. 6.1.5 relative peak signal strength from TFM images measured through different interface curvatures is shown. It should be noted that the results for the 10 mm data point included in Fig. 6.1.5 used a standoff of ≈ 11 mm owing to geometry interference of the probe (the probe was too wide to position at a 10 mm standoff for such a tight concave radii). Error bars for $\pm$ 1 decibel were included, to incorporate the results repeating the process in Section 5.6.

Residuals, together with linear regression, were used to help quantitatively evaluate the performance of each modelling technique. Residuals were calculated using the formula

$$R = O - P \tag{6.1}$$

where R is the residual, O is the observed (experimental) value, and P is the predicted (modelled value). Linear regression was performed, with the Root Mean Squared Error (RMSE), the gradient, and the mean residual recorded for comparison purposes. RMSE was defined as

$$RMSE = \sqrt{(P - O)^2} \tag{6.2}$$

where P is the predicted value, and O is the observed value.

Results from the convex single metal path blocks are shown in Fig. 6.1.1. Agreement within 3 dB is found for the 3D CIVA and 2D FE results, with the 3D

model predicting a slightly lower signal for all blocks. These models agree with the experimental results for larger radii, but start to diverge at lower radii of curvature. The 2D raytracing results do not agree with the experimental observations, overestimating the peak signal at higher radii and underestimating it at lower radii. Residual plots are shown in Figs. 6.1.2 to 6.1.4.

The mean residual was lowest for the 2D FE model, which in general gave the best match to the observed values. The 2D FE has the lowest RMSE, and the gradient closest to zero; however it is very similar to the gradient in the CIVA results. While the RMSE and gradient are similar for the CIVA and FE results, the mean residual is roughly twice as much for the CIVA values, under predicting the relative signal for most measurements. Both these methods performed better than the MATLAB approach, which had a large RSME and steep gradient in comparison. While the FE and CIVA results under predicted on each result, the MATLAB approach dramatically under, then over predicted the result.

Residuals in the MATLAB model are likely due to too many simplifications. As the model does not include the TFM surface measuring process, it is predicated on a surface detection step observing a perfectly radial, or perfectly flat surface. This could account for the dramatic difference predicted by the model, if one considers that the surface extraction step introduces distortions in the surface used for the second focusing step, even for flat surfaces.

This could have the effect of lowering the absolute value of the flat reference signal, and therefore reducing the relative amplitude of those values seen above 0 dB for radii from 20-40 mm.

Another simplification that could be causing an increase in absolute amplitude across the board for the MATLAB model is the directivity of the reflection from the flaw, which is assumed to be a perfect omni-directional scatterer. In reality, the reflection would have a less even directivity pattern, resulting in a reduction in the energy received from wider angles of the array. Were these effects included, it is thought that a reduction in relative amplitude at larger radii would bring the results of the MATLAB model closer to those of the other two models.

Shortfalls of the CIVA and 2D FE models are likely to come from different places, although they have the same ultimate outcome regarding the effect on the signal.

For the CIVA model, it was noted that the TFM surface-extraction images obtained a surface with very limited width compared to the 2D FE or experimental results (e.g. only 5 mm of the surface rather than the whole 10 mm). It is thought

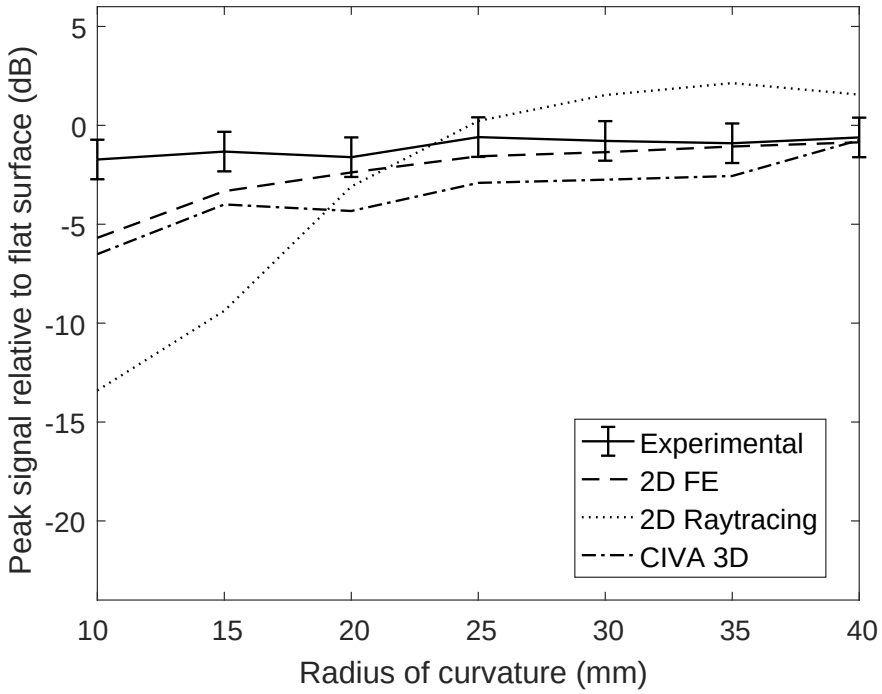

Figure 6.1.1: Relative peak signal values versus a flat interface for centrally-located FBHs imaged through different convex surfaces, with probe at 10 mm stand off.

that this is due to some of the semi-analytical approximations used with the CIVA software; specifically to do with optional surface refraction and reflection. This suggests that the surface imaging, with the settings used, did not reproduce large enough portions of the surface to be used for the surface correction step.

Another possible source of error is differences between the way reflection and refraction was calculated through a curved surface, and a flat surface. The lack of inclusion of reflections from the backwall and omission of shear and surface wave mode conversions were other configuration choices that may have contributed to errors.

The major approximation of the 2D model was the lack of a third dimension, and accompanying natural focusing effect. Inclusion of this may have raised the signal at tighter radii compared to the results that were obtained from the purely 2D approximation.

For all simulated results, detailed approximation of array effects were not considered, such as crosstalk between elements, and this may have contributed to the errors.

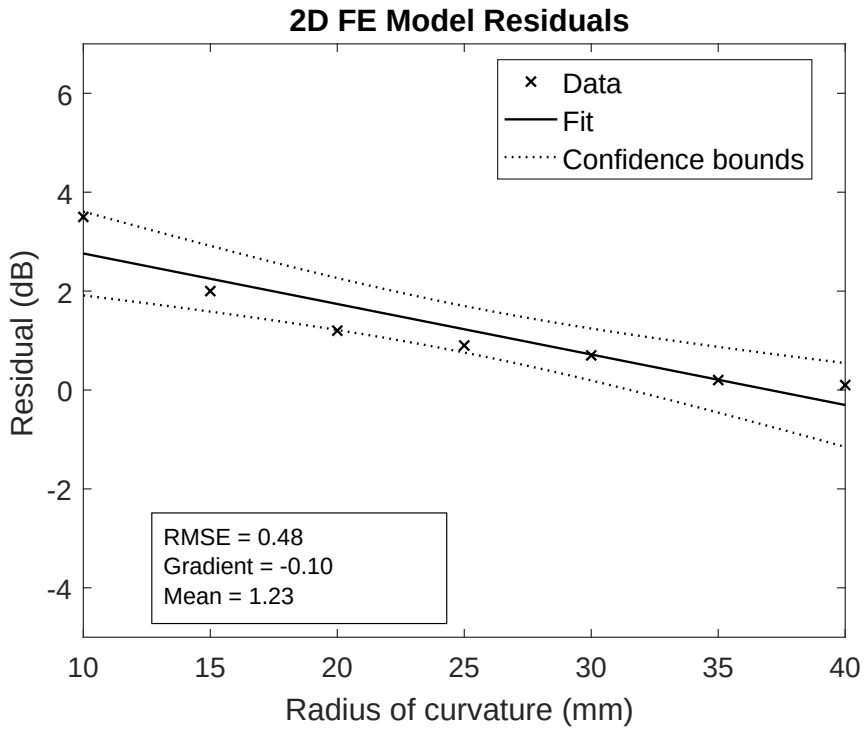

Figure 6.1.2: Residuals for 2D FE technique for convex curved SMP blocks.

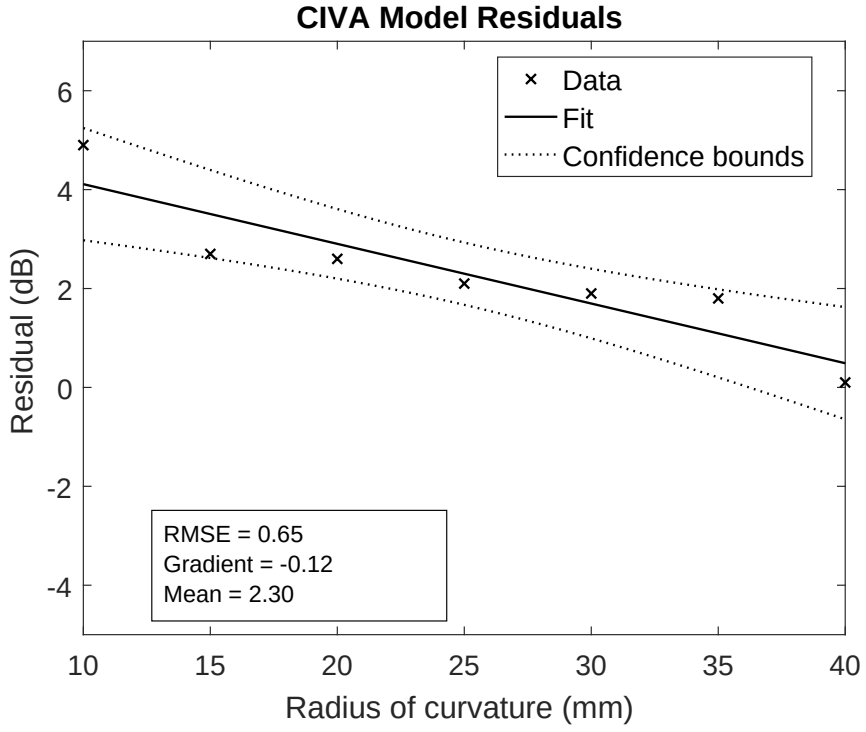

Figure 6.1.3: Residuals for CIVA technique for convex curved SMP blocks.

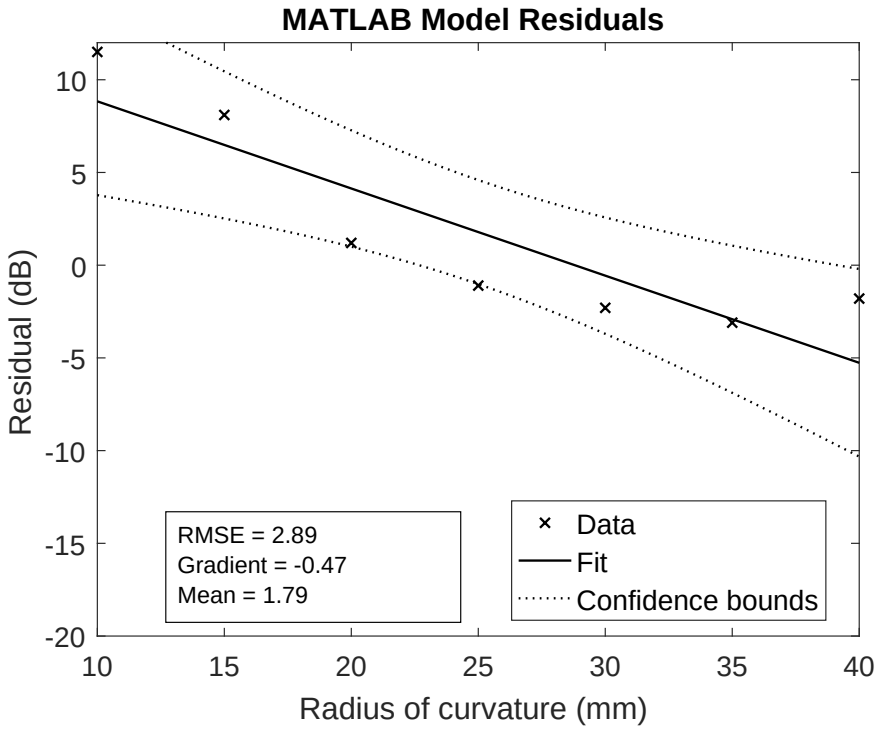

Figure 6.1.4: Residuals for ray-tracing technique for convex curved SMP blocks.

Results from the concave single metal path blocks are shown in Fig. 6.1.5. Residual plots are shown in Figs. 6.1.6 to 6.1.8.

Mean error and gradient is lowest for the 2D FE results, again giving the best performance in comparison to the experimental data. The spread of results is increased dramatically however compared to the convex case. The spread of results even in the best (2D FE) model is unlikely to be acceptable as a prediction for the inspection, as it can only guarantee the flaw magnitude to within 3 dB.

The CIVA model had the lowest spread, with 2.09 dB compared to 2.99 for the 2D FE technique; although with a large mean error. It was difficult to extract an accurate surface profile here, which could lead to this effect. Newer editions of CIVA have TFM surface detection and correction built in, which is likely to avoid this issue.

The mean residual for the ray-tracing model is lower than for the CIVA model, however some of the peak value results seem unrealistic. Most importantly, the ray-tracing model predicts an increase in the peak signal for the 10 mm radius compared to the 15 mm radius, disagreeing with the other predictions and observation. It is thought that this could be due to the MATLAB model incorrectly preferring a non-physical ray path that begins at the edge of the array and trav-

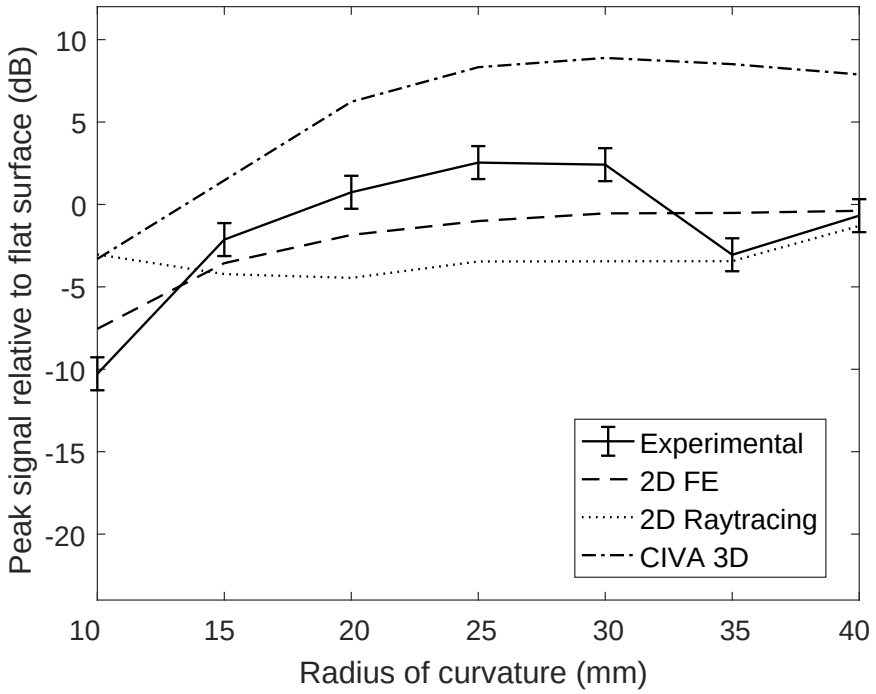

Figure 6.1.5: Relative peak signal values versus a flat interface for centrally-located FBHs imaged through different concave surfaces, with probe at 10 mm stand off.

els directly through the metal in the model. This is due to shortcomings in the geometrical boundary conditions of the model.

The difference amongst experimental results show an increase in the signal for radii between 15 mm to 30 mm compared to a flat interface. This shows that there is some sort of focusing effect for the concave block compared to the convex block for radii between 20 and 30 mm. Note that the dip in signal shown by the 35 mm experimental concave block may be partly due to a drill fragment that broke off into this FBH during manufacture.

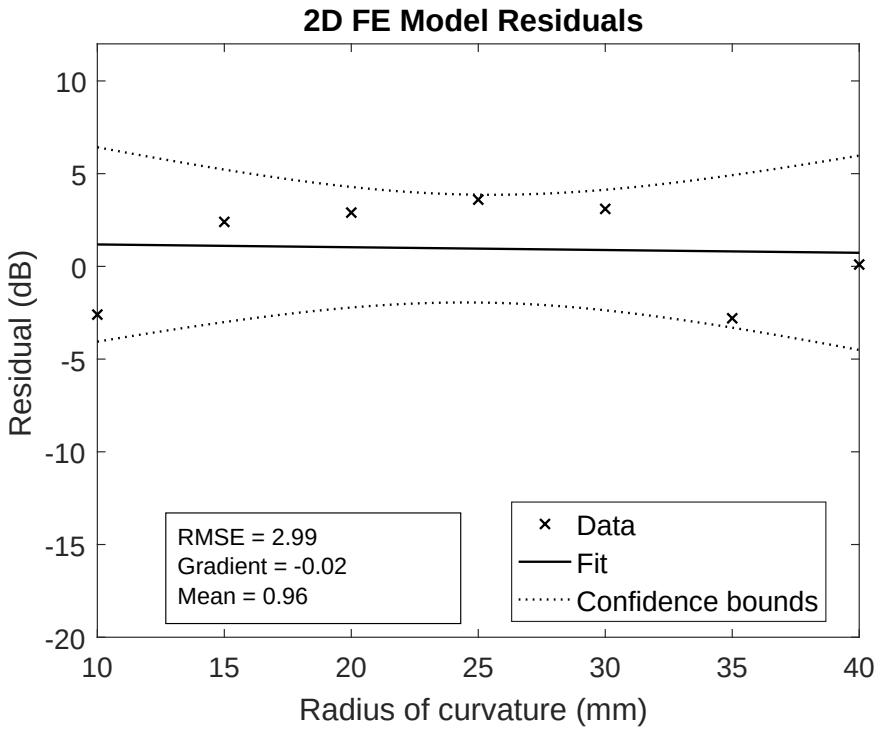

Figure 6.1.6: Residuals for 2D FE technique for concave curved SMP blocks.

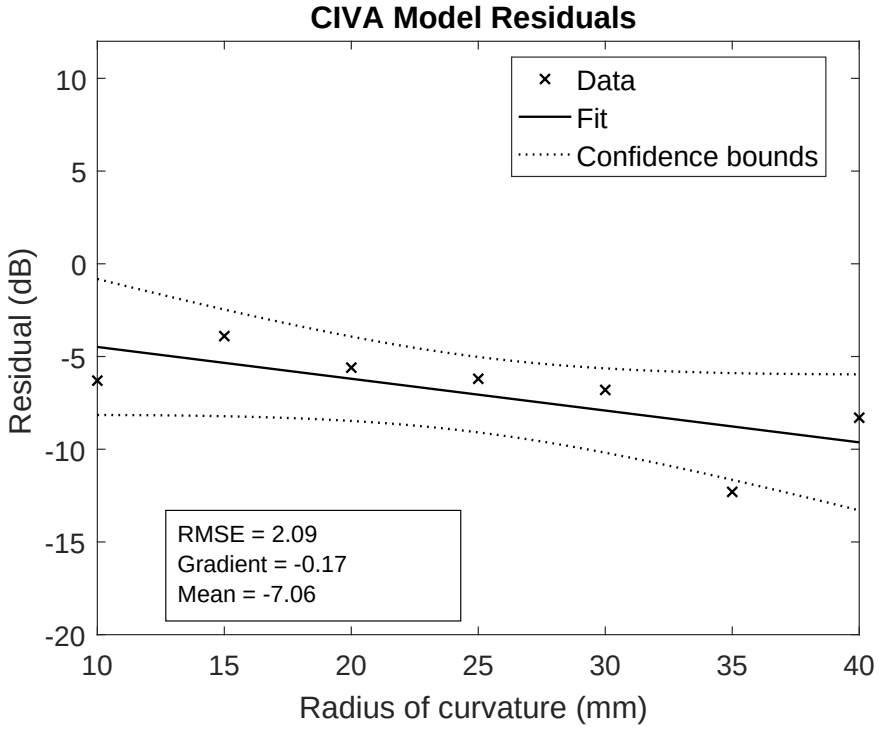

Figure 6.1.7: Residuals for CIVA technique for concave curved SMP blocks.

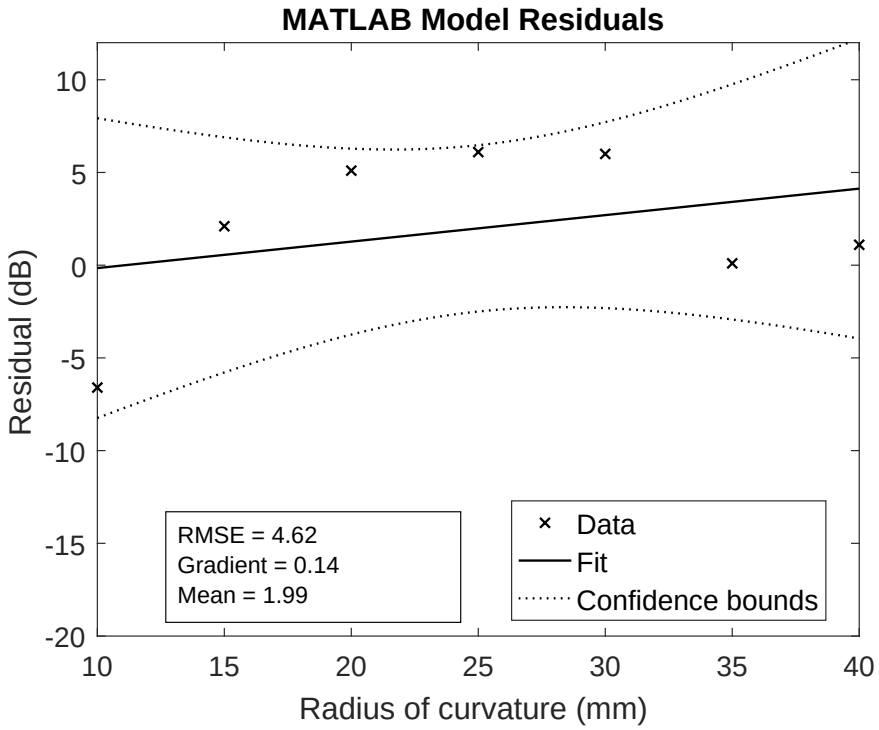

Figure 6.1.8: Residuals for ray-tracing technique for concave curved SMP blocks.

6.2 IMPACT ON SIZING FOR SMP BLOCKS

The amplitude error present in these predictions has consequences when it comes to flaw sizing. By using equation Eq. (6.3), the apparent sizing error for each method is shown in Figs. 6.2.1 and 6.2.2. In this case, A_{rel} is defined as the experimental amplitude, minus the model prediction.

This gives the size of flaw that would be inferred if the model results were used as a DAC curve, alongside the amplitudes obtained experimentally, to correct for the effects of curvature. Ideally, each model would predict the known flaw diameter of 0.635 mm, which is included in each plot for reference.

$$A_{\text{rel}} = 40 \log \frac{d_{\text{flaw}}}{d_{\text{FBH}}} \tag{6.3}$$

For the convex geometry, overestimation of the flaw size occurs consistently for the 2D FE model and the CIVA model, with a maximum diameter overestimation of 0.14 mm for the 2D FE model.

For the concave geometry, the 2D FE model shows a maximum error for the 25 mm radius where it oversizes the flaw by 0.15 mm. The result using CIVA

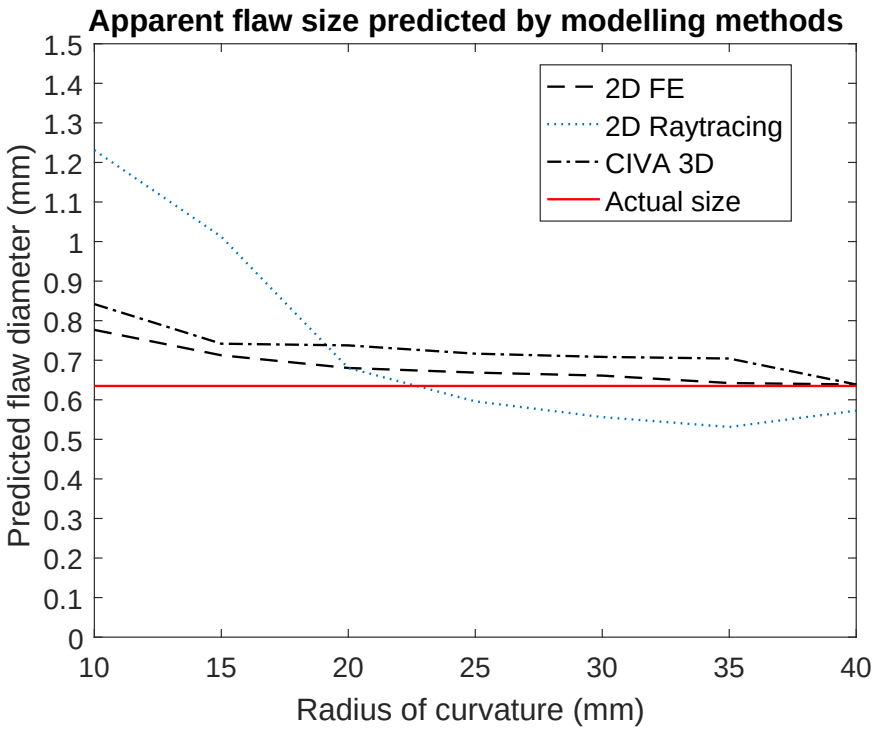

Figure 6.2.1: Flaw size predicted for each flaw using different modelling techniques, for the convex test blocks. The y-axis shows the size that would be inferred from the experimental amplitude found from each block, if the corresponding model prediction was used for sizing.

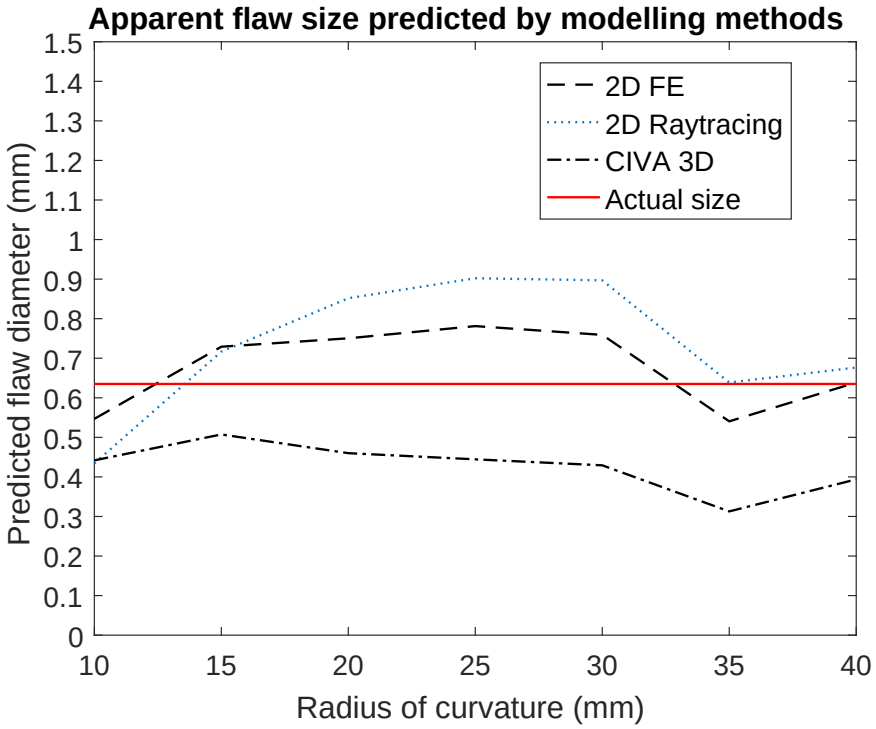

Figure 6.2.2: Flaw size predicted for each flaw using different modelling techniques, for the concave test blocks. The y-axis shows the size that would be inferred from the experimental amplitude found from each block, if the corresponding model prediction was used for sizing.

shows a consistent underestimation of the flaw size for each radius, due to the shortcomings of the model setup.

The implications for flaw sizing show that for the 2D FE model, the flaw size can be predicted with an accuracy of ±0.15 mm, or ± 24%.

6.3 SENSITIVITY MAP COMPARISON

Following consideration of results from the previous section, the MATLAB model was deemed to be too inaccurate to provide a useful sensitivity map (abbreviated to S-map in some titles and captions) representation of the flaw data. The 2D FE data, while providing the closest match to the experimental results, were not available for different flaw locations throughout the volume of interest, due to limited computing resources. Results from these two modelling methods were therefore not used to construct sensitivity maps.

The CIVA method was used to produce sensitivity maps built from TFM images of 0.635 mm FBHs throughout a 10 mm by 10 mm grid of locations for each test block (more details for this process are included in Section 4.3).

For each sensitivity map, the modelled results were corrected by using the difference found in Section 6.1 between experimental and CIVA model results for each block. The results in Section 6.1 match with experimental values when x equals zero and depth is 7.5 mm. Sensitivity maps were corrected using the difference for each block geometry; for example the concave 10 mm block sensitivity map was reduced by 6 dB, while the concave 15 mm block sensitivity map was reduced by 4 dB. This was carried out to bring the modelled results closer to experimental values for each sensitivity map.

For reference, the sensitivity map for a flat-surfaced block is shown in Fig. 6.3.1, with a reference value of 0 dB for the centrally-located position at 7.5 mm depth. All other results for the sensitivity maps are expressed in dB relative to this flaw position.

Sensitivity maps for convex curved surfaces are shown in Fig. 6.3.2 to Fig. 6.3.7.

Sensitivity maps for concave curved surfaces are shown in Fig. 6.3.8 to Fig. 6.3.13.

A number of effects can be observed from the sensitivity maps.

As radius increases, the distribution of peak signal strength is redistributed. For

radii of 10 mm concave, 10 mm convex and 20 mm convex (Figs. 6.3.2, 6.3.2 and 6.3.8), the maximum peak signal strength is obtained in a region towards the top of the sensitivity map, whereas for all other maps the peak signal eventually increases with depth over the range considered. This shows that for tighter curvatures, the depth where a strong signal can be obtained very quickly drops off compared to gentler curvatures.

In Table 6.1, the largest maximum signal is found for the 10 mm curvature, while the largest mean signal is found for the 20 mm. This suggests that there is a focusing effect for tighter radii, resulting in increased signal strength compared to flatter geometries.

For concave curvatures, the maximum and mean amplitudes in Table 6.2 reach their highest point for a radius of 25 mm, demonstrating that maximum and mean signal strength are also increased compared to flatter geometries.

Amplitudes of flaws offset from the central line drop off as distance from the centre increases. This effect is more pronounced in the concave maps, even at the gentlest curvature of 40 mm, which can be seen by comparing Figs. 6.3.7 and 6.3.13. A narrower band of high signal was found for concave sensitivity maps across the board compared to convex sensitivity maps.

There is an effect on the shape and apparent location of flaws for tighter curvatures. Comparing the 20 mm curved concave and convex results in Figs. 6.3.3 and 6.3.9 against the flat result in Fig. 6.3.1 demonstrates this. A convex surface draws flaws towards the centre of curvature, and smears them into crescent shapes. Conversely, a concave surface pushes the flaws away from the central location, and the flaws retain a rounder shape.

Movement of flaw centres is shown in Fig. 6.3.15. Convex flaws are drawn towards the centres for small radii (as shown for 10 mm and 25 mm radii in Fig. 6.3.15), but outwards for higher radii as shown in the convex 40 mm plot. Mean movement m_{mean} of the flaw centre decreases with increasing radius for convex curvatures, as detailed in Table 6.1.

Movement of flaw centres for concave curvatures is shown in Fig. 6.3.14. Flaws move out away from the centre line for all curvatures, and with a reduction in distance as radius increases. The mean distance decreases monotonically, and is quantified in Table 6.2.

Overall, the sensitivity mapping exercise shows that flaw peak amplitude distribu-

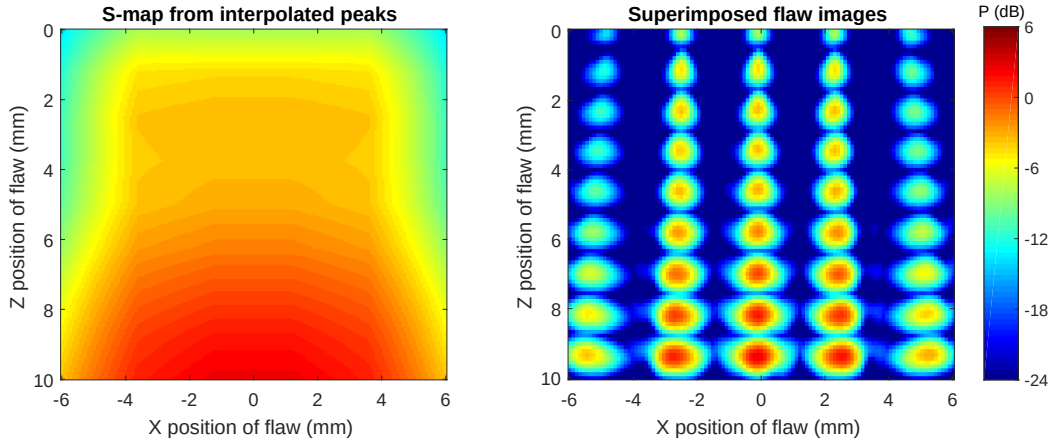

Figure 6.3.1: Sensitivity map for flat surface, produced from CIVA using interpolated peaks (left), and composite image of single TFM images (right) used to generate the sensitivity map.

tion and apparent centre position changes significantly according to the radially curved surface geometry, even after TFM correction has been performed. This must be taken into account for inspection planning. One example of how this approach can be used to help plan inspections is shown in Section 6.4, where the modelled distribution of peak flaw signal is used to predict the relationship between scan step and minimum signal for a robotic scan.

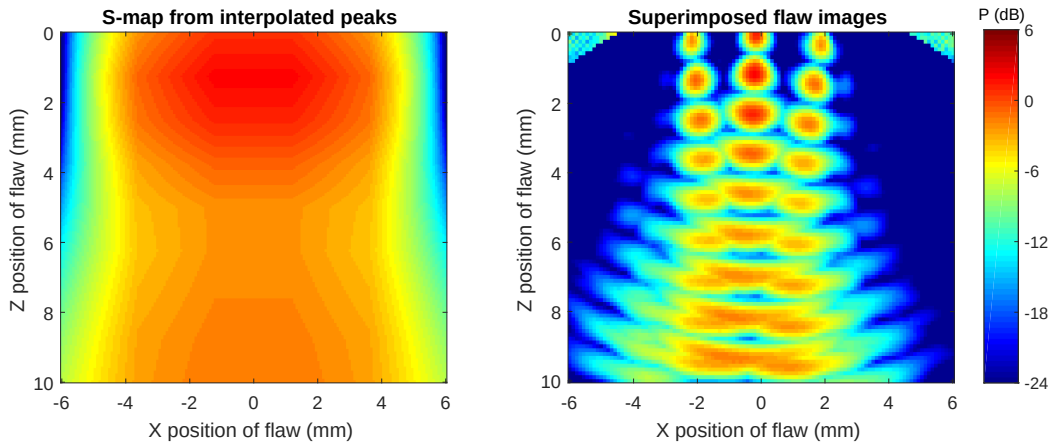

Figure 6.3.2: Sensitivity map for 10 mm convex surface curvature produced from CIVA model using interpolated peaks (left), and composite image of single TFM images (right) used to generate the sensitivity map.

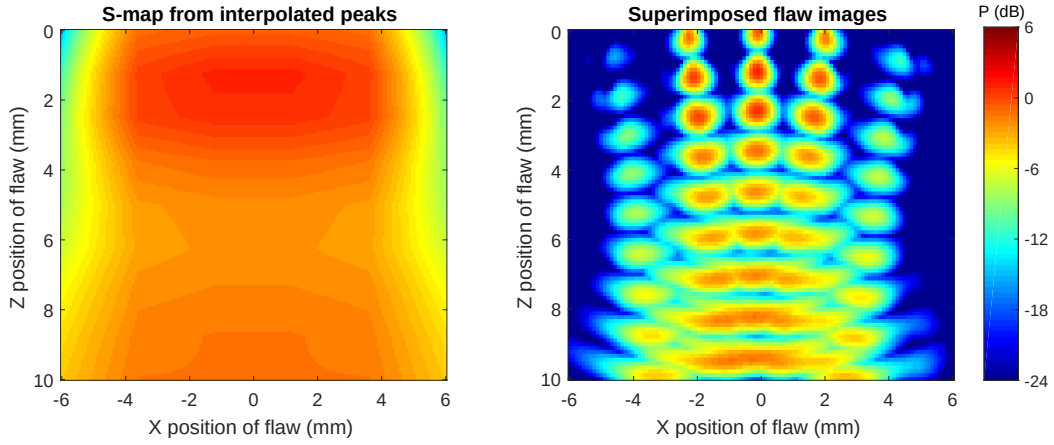

Figure 6.3.3: Sensitivity map for 20 mm convex surface curvature produced from CIVA model using interpolated peaks (left), and composite image of single TFM images (right) used to generate the sensitivity map.

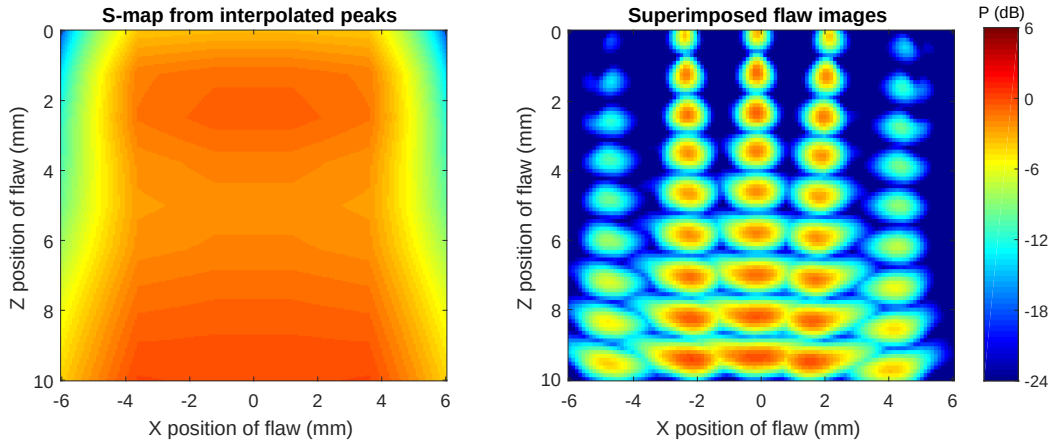

Figure 6.3.4: Sensitivity map for 25 mm convex surface curvature produced from CIVA model using interpolated peaks (left), and composite image of single TFM images (right) used to generate the sensitivity map.

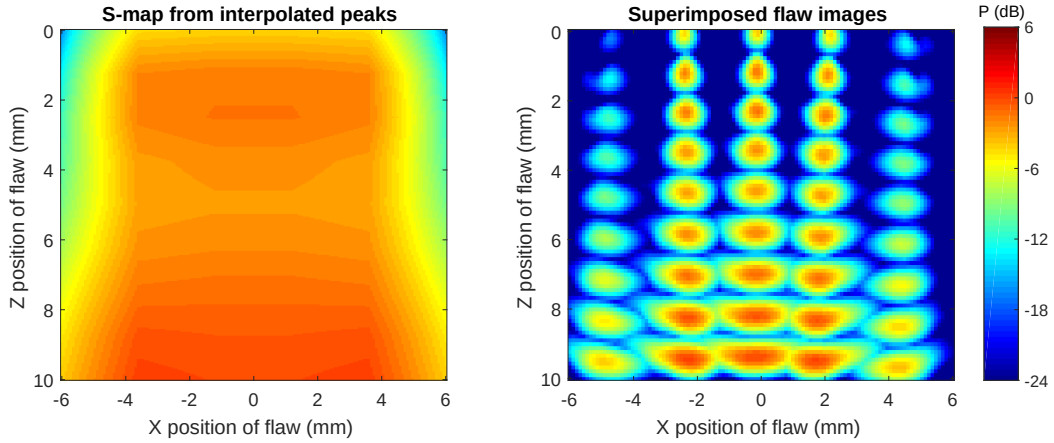

Figure 6.3.5: Sensitivity map for 30 mm convex surface curvature produced from CIVA model using interpolated peaks (left), and composite image of single TFM images (right) used to generate the sensitivity map.

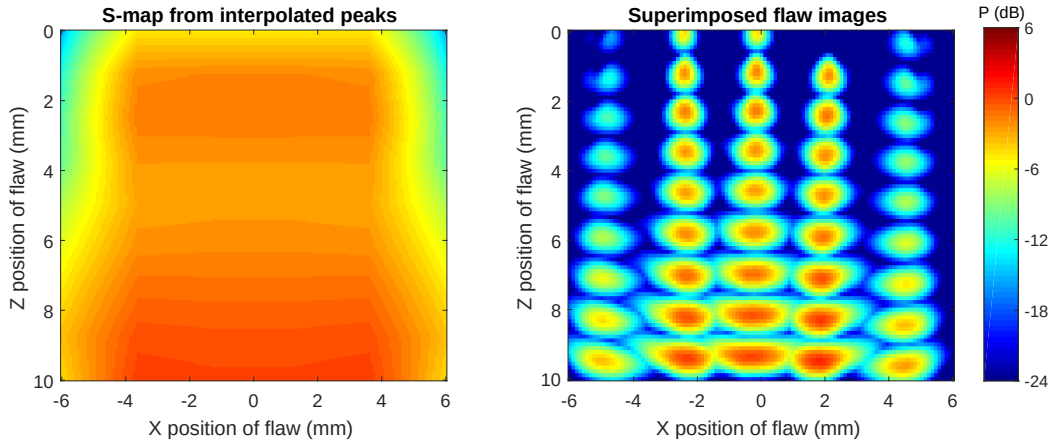

Figure 6.3.6: Sensitivity map for 35 mm convex surface curvature produced from CIVA model using interpolated peaks (left), and composite image of single TFM images (right) used to generate the sensitivity map.

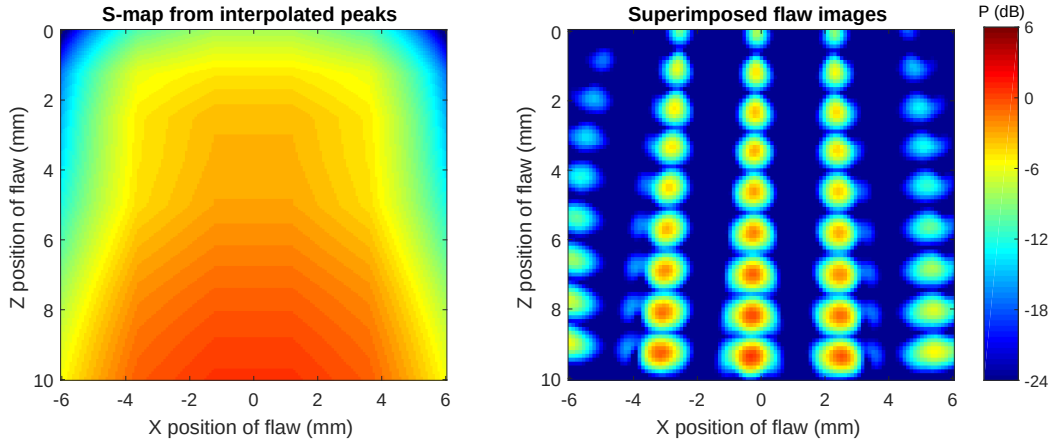

Figure 6.3.7: Sensitivity map for 40 mm convex surface curvature produced from CIVA model using interpolated peaks (left), and composite image of single TFM images (right) used to generate the sensitivity map.

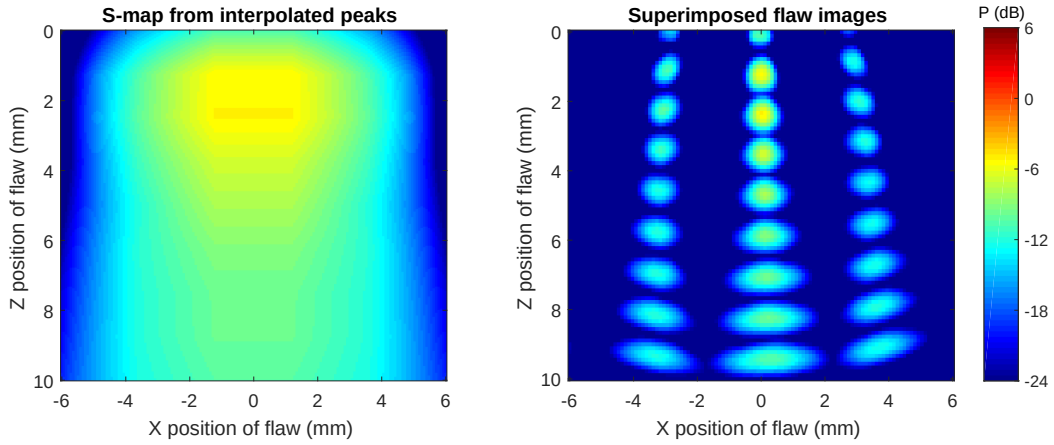

Figure 6.3.8: Sensitivity map for 10 mm concave surface curvature using interpolated peaks (left), and composite image of single TFM images (right) used to generate the sensitivity map.

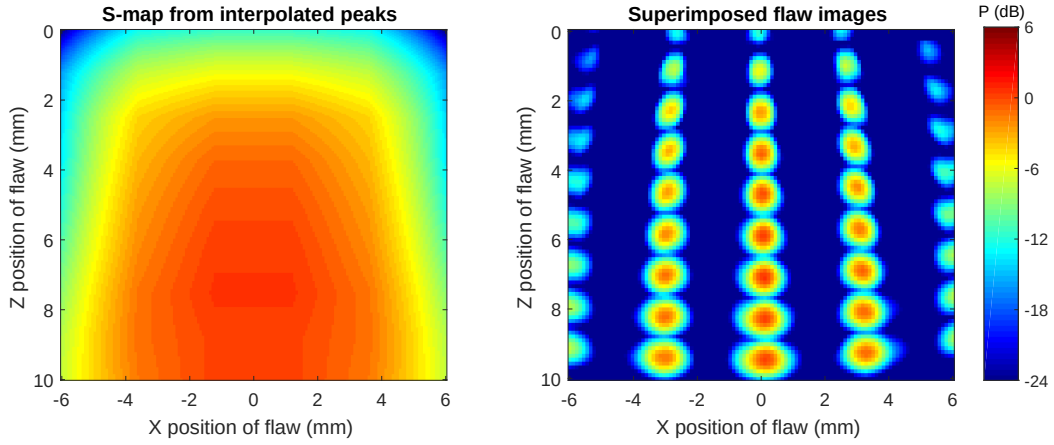

Figure 6.3.9: Sensitivity map for 20 mm concave surface curvature produced from CIVA model using interpolated peaks (left), and composite image of single TFM images (right) used to generate the sensitivity map.

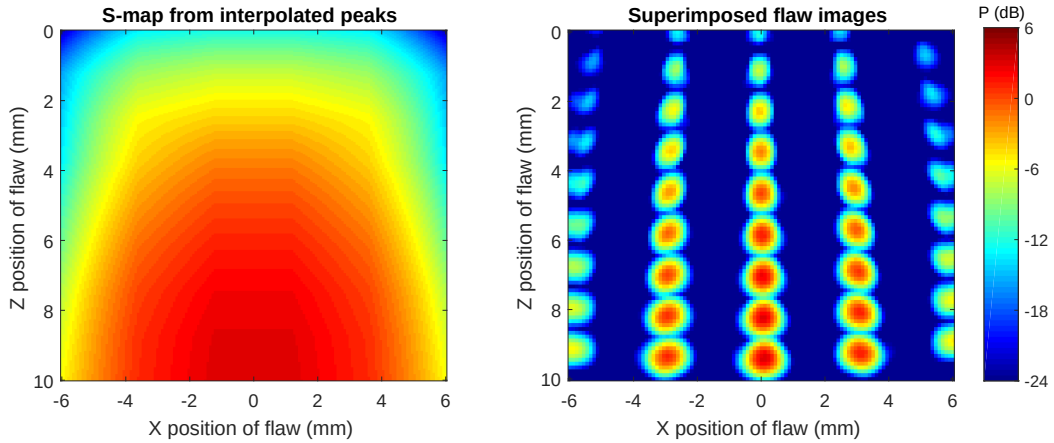

Figure 6.3.10: Sensitivity map for 25 mm concave surface curvature produced from CIVA model using interpolated peaks (left), and composite image of single TFM images (right) used to generate the sensitivity map.

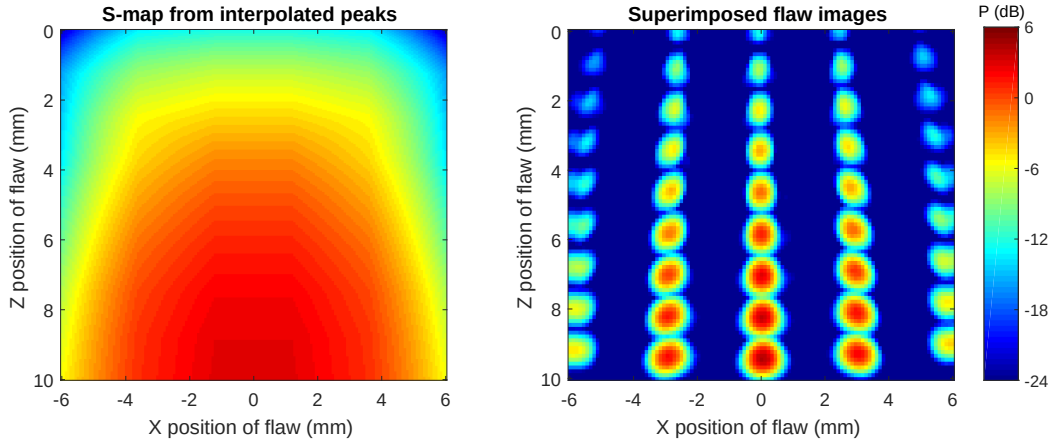

Figure 6.3.11: Sensitivity map for 30 mm concave surface curvature produced from CIVA model using interpolated peaks (left), and composite image of single TFM images (right) used to generate the sensitivity map.

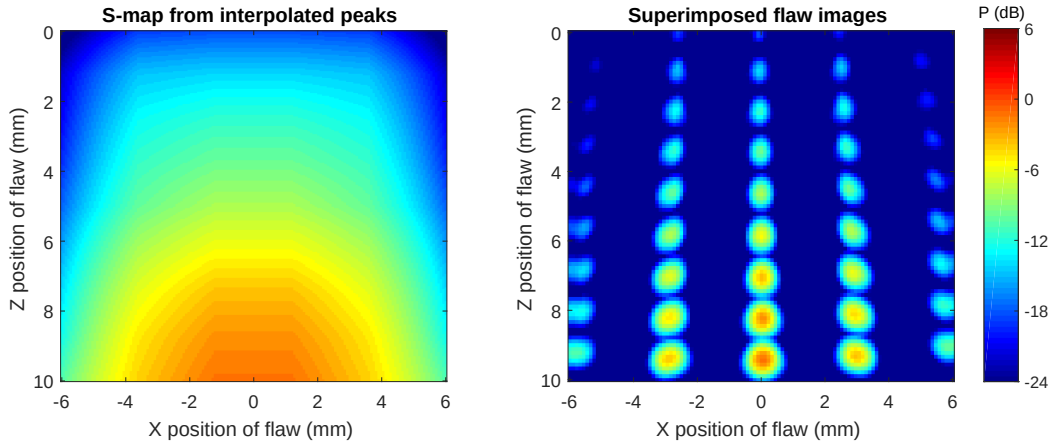

Figure 6.3.12: Sensitivity map for 35 mm concave surface curvature produced from CIVA model using interpolated peaks (left), and composite image of single TFM images (right) used to generate the sensitivity map. Note that there is a global amplitude reduction related to the correction to the measured value (which was reduced due to matter lodged in the FBH).

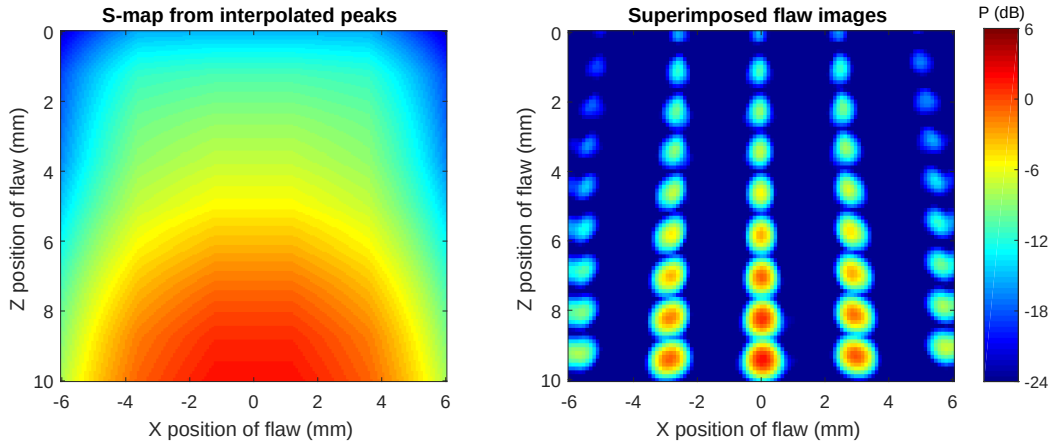

Figure 6.3.13: Sensitivity map for 40 mm concave surface curvature produced from CIVA model using interpolated peaks (left), and composite image of single TFM images (right) used to generate the sensitivity map.

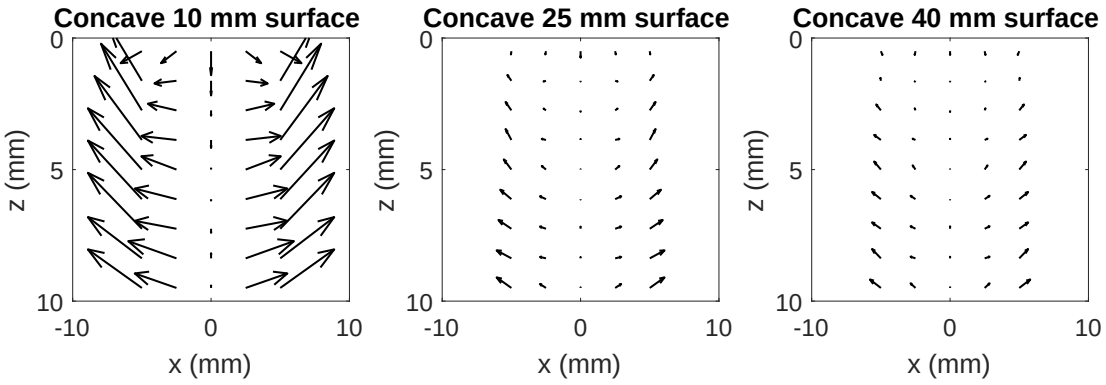

Figure 6.3.14: Relative position of flaw centres for selected concave surface curvatures. Arrows show relative magnitude and direction of shift from nominal flaw location to location detected in the TFM image.

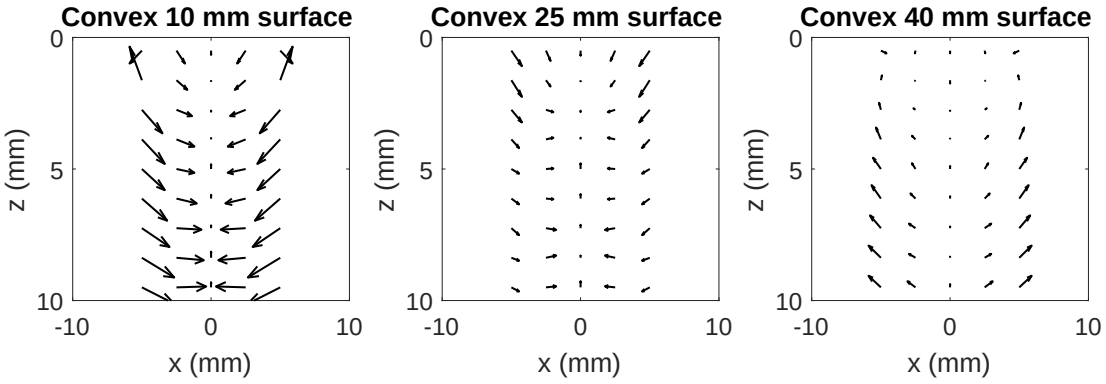

Figure 6.3.15: Relative position of flaw centres for selected convex surface curvatures. Arrows show relative magnitude and direction of shift from nominal flaw location to location detected in the TFM image.

Table 6.1: Flaw peak value statistics for convex curved surfaces using CIVA

R (mm)	$A_{\mathbf{min}}$**(dB)**	$A_{\mathbf{max}}$**(dB)**	$A_{\mathbf{mean}}$**(dB)**	$m_{\mathbf{min}}$	$m_{\mathbf{max}}$	$m_{\mathbf{mean}}$
10	-26.01	2.03	-6.66	0.16	2.45	1.20
20	-15.51	1.00	-3.54	0.06	2.30	1.08
25	-18.28	-0.03	-4.33	0.06	0.99	0.46
30	-16.55	0.17	-4.34	0.06	0.75	0.38
35	-15.58	0.23	-4.05	0.06	0.88	0.35
40	-27.60	0.56	-6.67	0.05	1.00	0.33

Table 6.2: Flaw peak value statistics for concave curved surfaces using CIVA model.

R (mm)	$A_{\mathbf{min}}$**(dB)**	$A_{\mathbf{max}}$**(dB)**	$A_{\mathbf{mean}}$**(dB)**	$m_{\mathbf{min}}$	$m_{\mathbf{max}}$	$m_{\mathbf{mean}}$
10	-59.14	-5.23	-16.48	0.07	4.53	0.84
20	-24.51	0.50	-6.31	0.06	1.17	0.50
25	-22.66	2.96	-5.76	0.06	1.14	0.42
30	-22.76	2.86	-5.86	0.05	1.09	0.36
35	-26.01	-1.37	-12.01	0.05	0.99	0.31
40	-22.10	1.69	-8.94	0.05	0.85	0.29

6.4 USING SENSITIVITY MAPS TO DETERMINE SCAN COVERAGE OF A CURVED SURFACE

In Section 6.3, sensitivity maps were developed to give a prediction for the peak signal strength distribution for FBHs throughout a volume below surfaces of different geometries. One potential use for these maps is to help determine the scanning step required to ensure a certain level of coverage through a surface. While single-element methods rely upon knowledge of the half-beam width at a certain depth, the profile of the sensitivity maps presented here is different to that of a traditional beam profile.

Consider a convex-curved surface with a radius of 10 mm, the sensitivity map for which is shown as the left plot in Fig. 6.4.1. A line showing a constant depth of 2.5 mm below the curved surface is shown, which has a variation in signal strength plotted on the right hand plot. For the right hand plot, the x-axis has been transformed to correspond to points along the surface of the part. This is referred to here as an echodynamic curve.

Note that the amplitudes shown in the sensitivity map here have not been corrected using the process described in the previous section. It is included for illustration of the technique using purely modelled results.

Once a curve like this is established, it can be used to determine the minimum signal expected for a scan, as shown in Fig. 6.4.2. This is only valid for the depth where the curve is drawn, in this case, for a depth of 2.5 mm. The technique creates a method by which it is possible to identify what the overlap between successive scans must be to achieve a certain level of minimum peak flaw signal at a given depth. This approach is the TFM curved surface equivalent of the scanning and echodynamic approach first introduced in Fig. 2.1.15.

By repeating this for a range of scan-step sizes, the relationship between scan step size and minimum signal is found. This method, together with the corrected results from the previous section, were used to generate the plots in Figs. 6.4.3 to 6.4.6.

This method could be used to help plan the scan step for robotic inspections, and enable efficient planning for shapes that are composed of different curvature values; using the data in the plots to select the required scan step for each radius

encountered by the planned scan path.

For all concave and convex geometries considered, the largest minimum amplitude was obtained for the deepest part of the scan. All of the blocks apart from the concave 25 mm block showed the trend that amplitude increased with depth. For the 25 mm block, a higher signal was predicted for a depth of 2.5 mm than for 5 mm. This is because the relevant sensitivity map Fig. 6.3.4 has higher amplitudes in the near surface region compared to the others.

For a fixed scan step size, these figures show that a better minimum amplitude would be obtained from the more tightly curved blocks. Perhaps more importantly, this implies that for a scan with a minimum required amplitude, slightly coarser scan steps could be made over the more tightly curved features to achieve the same amplitude. Note that this only applies to stepping over ideal, radially curved surfaces, and is unlikely to be a good strategy for more complex shapes. Nevertheless, the sensitivity bias found towards the near-surface in the sensitivity maps leads to this behaviour for radial curves.

Consider the problem introduced at the beginning of this thesis of designing a forging process, including a machining step. This thesis has provided evidence that TFM can be used to inspect through curved surfaces in a predictable manner, so the process is no longer constrained to inspect only flat sides.

The total number of FMC frames to capture, which affects speed (as discussed in Section 3.3.3), is partly determined by scan step size. The amount of machining required is determined by the minimum amplitude obtainable through the curvature. Additionally, the amount of machining after the inspection is based on the depth required to get a large enough coverage amplitude, which is quantified in these figures. These figures can therefore be used to optimise the intermediate rectilinear geometry cross-section (shown in green in Fig. 1.2.1). Additionally, the scan step size can be used with a robotic path planning technique similar to the one presented in Section 3.2.

This approach can therefore provide a way to optimise forging geometry, as well as robotic scan path, to obtain a desired level of sensitivity throughout a forging that has either rectilinear or radially curved surfaces.

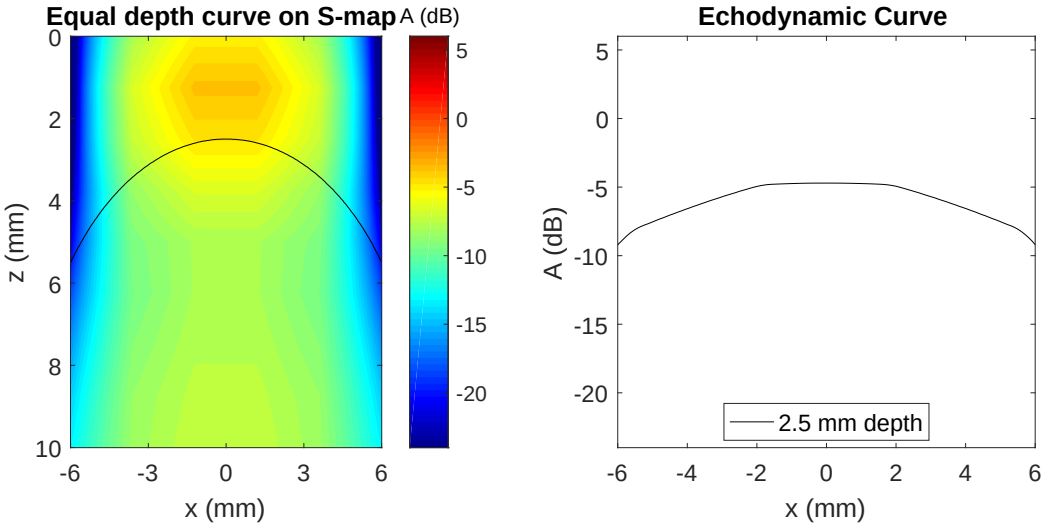

Figure 6.4.1: Echodynamic curves can be extracted from a depth below the surface - at a depth of 2.5 mm in this case. The signal strength variation along the line shown in the left hand plot is shown in the right hand plot. The x-axis of the left plot is the width of the block, whereas the x-axis on the right hand side is the distance along the surface of the block corresponding to the amplitude reading expected. The right hand x-axis is similar to a "flattening" of the curve shown in the left figure. Amplitude is normalised to the maximum flaw signal through a flat interface.

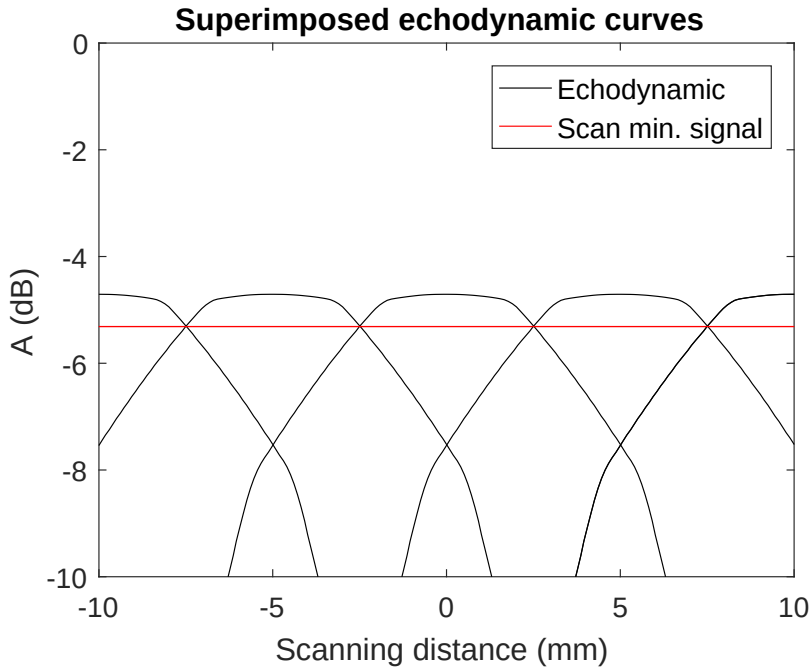

Figure 6.4.2: Echodynamic curves extracted and superimposed, translated across the scanning direction. The minimum signal expected for a given scan step can be extracted where the curves intersect, as shown by the red line.

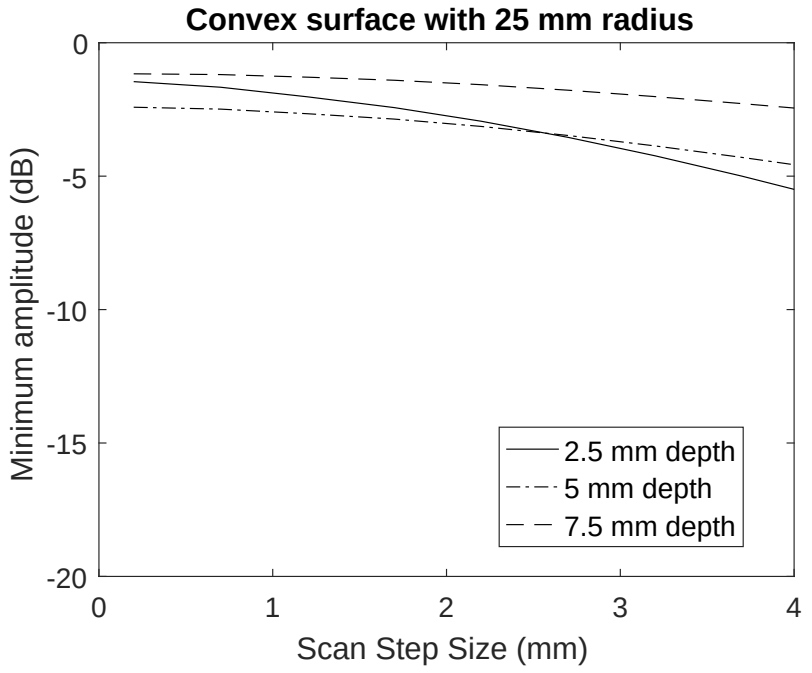

Figure 6.4.3: Minimum predicted signal for different scan steps, at different depths, using the echodynamic extraction technique.

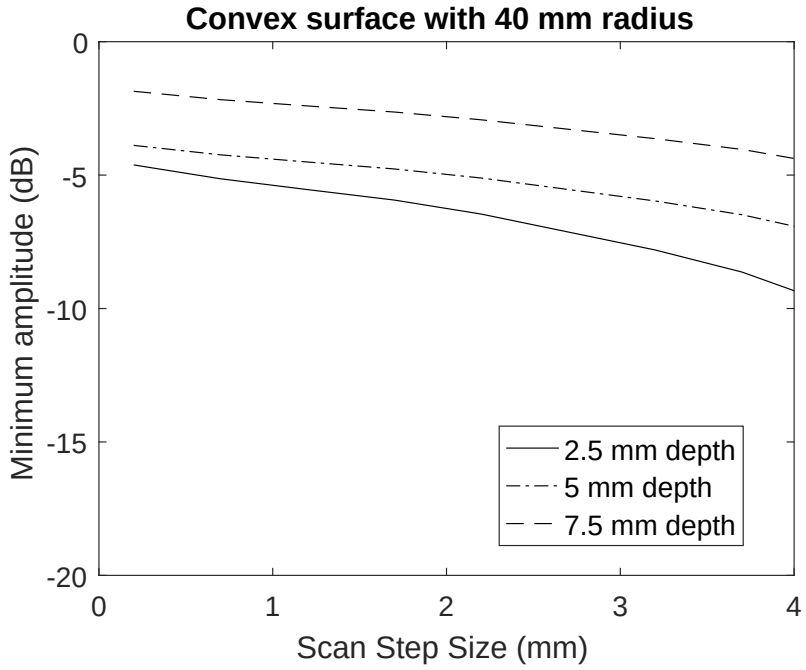

Figure 6.4.4: Minimum predicted signal for different scan steps, at different depths, using the echodynamic extraction technique.

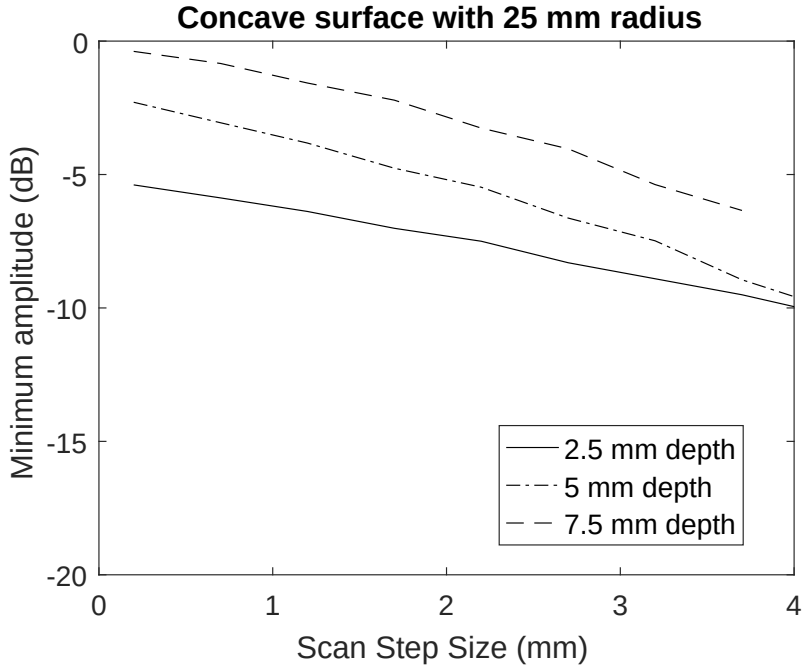

Figure 6.4.5: Minimum predicted signal for different scan steps, at different depths, using the echodynamic extraction technique.

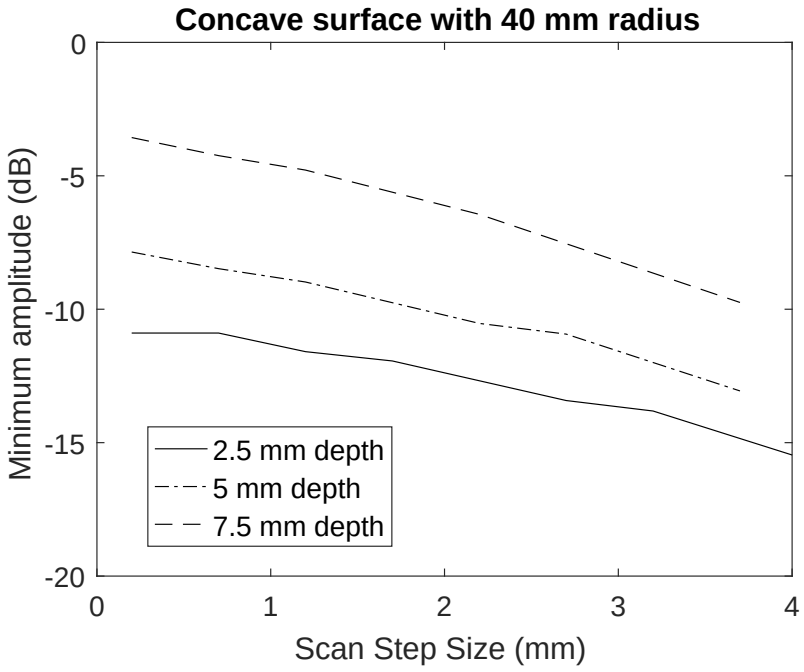

Figure 6.4.6: Minimum predicted signal for different scan steps, at different depths, using the echodynamic extraction technique.

6.5 MULTIPLE METAL PATH BLOCK RESULTS

The results in Section 6.1 provide experimental data at a constant depth. Work in Section 6.3 builds on this to show how modelled sensitivity maps can be linked to these experimental results to help create useful tools for inspection planning. The application does however require inspection to greater depths than those considered in the previous sections.

To investigate this, peak signal was measured from a set of multiple metal path blocks (described in Table 5.2), and is shown in Fig. 6.5.1. This plot shows all peak values, normalised to the maximum peak value found in the flat metal path block. This peak value was found at a metal path of 7.5 mm.

For the curved blocks, amplitude through depth was reduced more for smaller radii. The largest reduction in amplitude was seen with the 10 mm convex block. It was not found that amplitude was consistently higher for concave or convex blocks, rather, whether amplitude was higher through a concave or convex block was determined by the radius of curvature.

Note that the amplitude of all other blocks is significantly higher than that of the flat block for the 2.5 mm metal path. This was due to interference from the front surface echo, which entered the flaw gate; therefore the results from this region may not be accurate.

The results from Fig. 6.5.1 were replotted with each data series normalised to the value of the flat block at each depth, with results shown in Fig. 6.5.2. The convex and concave 20 mm blocks, as well as the convex 15 mm block, contained many indications that were stronger than the flat block at the same depth. This shows that it was not generally true to state that amplitude drops with increased curvature when applying surface corrected TFM.

In future, these results could be used together with the modelling and correction approach used in the previous three sections to produce effective sensitivity maps for deeper scan coverage. Time and resource limitations prevented the process being expanded to incorporate these results, however they are included for completeness.

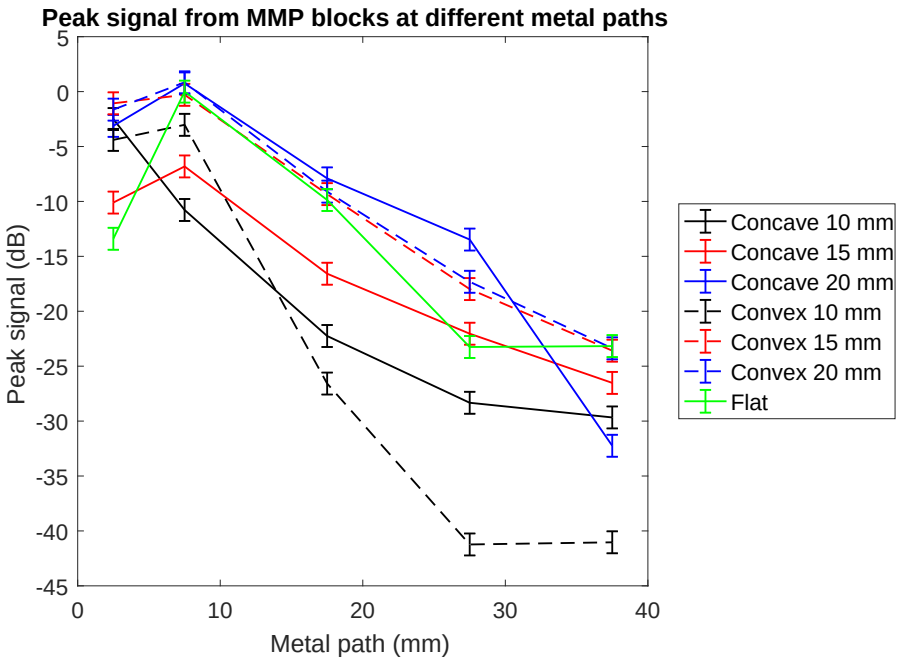

Figure 6.5.1: Peak amplitude comparison for FBHs at different depths measured from the convex MMP blocks.

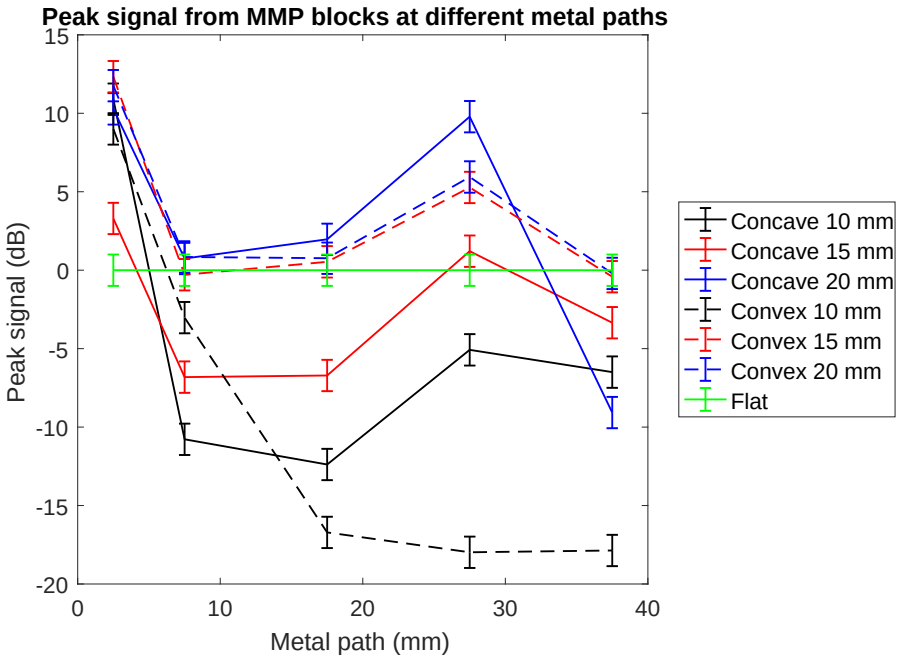

Figure 6.5.2: Peak amplitude comparison for FBHs at different depths measured from the concave MMP blocks, normalised to the flat block peak signal at each given depth.

6.6 KEY FINDINGS

From comparison of the three modelling techniques against experimental results in Section 6.1, it was found that the best method of modelling was 2D FE for predicting the ability of a surface-detection and correction TFM algorithm.

For convex cases, the 2D FE result had a mean error of 1.23 dB, while the CIVA method resulted in a mean error of 2.3 dB. Both of these methods exhibited a systematic effect whereby flaw amplitude was under predicted for tighter radii. Both have a small spread in results, with an RMSE of approximately 0.5 dB for each, however the strong gradient in each shows that there is a systematic error with either method.

The MATLAB model was found to have much larger errors, taking the form of over-prediction at large radii and under-prediction at lower radii. This was thought to mainly stem from the surface representation in the MATLAB model, which is a perfectly formed surface, known apriori. The relative peak value for the larger radii was therefore more pronounced, along with the effect of the tightening radial geometry.

For concave cases, 2D FE was the best method and had a mean residual of 0.96 dB, however it also had a much larger spread of 2.99 dB.

The most noticeable difference compared to the convex case was that the concave CIVA results exhibited a much worse mean residual value, with -7.06 dB compared to 2.3 dB. This was a consistent over-prediction of the observed results. It is thought that this occurred because of inaccurate reproduction of the surface detected in the CIVA data. This could potentially be improved by use of an edition of CIVA that incorporates the built-in surface reconstruction algorithm.

Overall, 2D FE had the best performance. Even though the curved geometry was a simple shape, the interactions at the top surface were not fully represented by either of the semi-analytical methods. This is likely because the FE method includes all mode-conversions, multiple reflections and diffraction present in the inspection. This provided a better representation of the reflection from each part of the surface, even at the widest angles of the array.

The ability of the model to simulate the surface curvature is doubly important to surface-corrected TFM. Firstly, the amplitude of the wavefront that is refracted through the top surface, scattered from the flaw, and refracted back through

is dependent on the modelled surface. Secondly, the reflected waves from the model determine the ability of the surface-detection TFM algorithm to suitably reconstruct the surface. Inaccuracies introduced by the model in either of these stages of the surface-correction algorithm affect the final flaw amplitude, and therefore the apparent size of the defect.

Overall, the key findings were:

- The 2D FE approach was the most accurate of those used in this study, estimating flaw size to within ± 24%.
- The CIVA method for sensitivity mapping can be combined with experimental results to create sensitivity maps.
- The maximum overall signal is found in the more tightly curved sensitivity maps for convex and concave surfaces.
- Peak signal drops more severely with depth for more tightly curved convex and concave surfaces.
- Flaw amplitude drops off when position is offset from the central axis, and more severely for concave surfaces.
- Tight concave curvatures pull the apparent flaw position towards the central axis, whereas concave curvatures have the opposite effect.
- Tighter curvatures move the apparent flaw centres more dramatically than gentler curvatures.
- Sensitivity maps can be used together with echodynamic curve extraction to predict the relationship between scan step size and minimum signal.

6.7 SUMMARY

This chapter has presented a range of results to help quantify the effect of curvature and metal path on peak flaw signal. The geometry of the test pieces was chosen to cover curvatures and metal paths of practical interest to Rolls-Royce. Broadly speaking, it has been shown that applying TFM through a curved surface does not guarantee the same peak value seen at the equivalent flaw depth through a flat surface.

Results showed that the relationship between curvature, metal path and flaw peak signal for TFM through a curved surface was not exactly the same as that through a flat surface. For design and calibration of a TFM inspection, this chapter underlined the importance of having test pieces with the relevant geometry, and the value of a reliable model.

Experimental results from the multiple metal path results could be used to control inspection of a part with radial curvatures within the range investigated here. Considering the large difference in amplitude amongst the traces for different curvatures, it is likely that any practical inspection would require either more blocks, or a reliable modelling approach to predict peak amplitude. Extension of the sensitivity mapping, plus echodynamic extraction technique could be used to develop a more complete method for predicting flaw strength through deeper components.

Together, these results show how modelling can be used to make an approximation of the reduction in peak amplitude expected for TFM inspection through curved surfaces. Modelling of sensitivity maps demonstrates a method for assessment of TFM coverage on curved parts, and for predicting the change in shape of a flaw indication. The metal path versus peak amplitude curves have been produced in a manner similar to that currently used for inspection through flat surface, using single element probes. Crucially, it shows that the effect on amplitude for radial surface curvatures between 10 mm to 40 mm can be quantified, allowing this technique to be considered for industrial applications, such as the inspection of disc forgings.

Chapter 7

CONCLUSIONS AND FUTURE WORK

This chapter summarises the work presented in this thesis. Firstly, the contents of chapters 3-6 are reviewed in comparison with the technical objectives set out at the end of chapter 2. Following this comparison, the key findings of this thesis are collated, and suggested future work is outlined. Personal reflection is included, to give more details on the parts of this project that do not fit neatly into the progression of work previously presented. The ultimate aim of this chapter is to provide enough information for research engineers such as those at Rolls-Royce to make informed decisions, including directions for future applied research and steps to integrate TFM methods into standard production.

7.1 REVIEW OF TECHNICAL OBJECTIVES

A literature review, combined with consultation with stakeholders within Rolls-Royce, was used to form the basis of technical objectives for this body of work. These were listed in Section 2.4.4, alongside a summary of the method undertaken to meet these objectives.

This section revisits each objective, evaluating the progress this thesis has made towards their completion.

7.1.1 OBJECTIVE 1. DEMONSTRATE A ROBOTIC FMC SCANNING SYSTEM ON A WAVY PLATE

This objective aimed to demonstrate that a robotic system using FMC could replace an existing, ultrasonic scan. Furthermore, the aim was to create a system that was open for integration with metrology systems, and kept overall cost low.

Firstly, a TFM C-scan was created of an area of roughly $0.5\,\mathrm{m}^2$, albeit using a manually driven probe. This was a proof-of-concept, carried out as a precursor to automation. Results showed that a TFM-based solution, together with a wheel probe, could be used to generate a C-scan of a flat component, with large flaws.

Secondly, the integration of a KUKA robot together with KUKA|prc and Grasshopper was found to be sufficient for planning arbitrary probe paths, which was a useful result. Compared to commercial path-planning software, the solution was more flexible, and much cheaper (only requiring a Rhinoceros CAD license as a dependency costing circa £1000, versus roughly £50000 for an off-the-shelf software package).

The open and adaptable nature of Grasshopper as an interface for automated NDE was demonstrated by projecting TFM data onto the CAD at relevant points. While this was not used for generation of a C-scan, individual B-scans slices were projected to help match the ultrasonic result with the geometry of the part. Another important aspect demonstrated by this data integration was the openness and flexibility of the approach. These aspects of the system are advantages over proprietary software.

This offline path-planning approach matched the ability of the purpose made surface-following 5-axis scanners employed by Rolls-Royce, while offering more flexibility, and the use of serial revolute joint manipulators. This alone would not improve the inspection quality however; key to this objective was the integration of FMC. The author, along with the robotics group at the Centre for Ultrasonic Engineering at Strathclyde, developed and tested integration with an FMC-enabled phased array controller. This ultimately allowed the capture of FMC data, encoded using the internal encoders of the robot. A complete robotic FMC scanning system was thus developed.

To complete this objective, a test piece with irregular geometry was obtained from Rolls-Royce. A raster scanning pattern was generated across this part, and FMC data captured. Using MATLAB, this data was reconstructed into a C-scan,

and flaw locations showed agreement with those in a production scan.

One major concern of Rolls-Royce was the scanning speed of a phased array system such as this. It was foreseen that a move to phased array could result in an increased rate of area coverage. To investigate this, some basic calculations were included in the results for chapter 3. These were based on the theoretical data rate for CuTFM, and the experimental time taken to calculate the TFM images. Results showed that several variables would affect speed, but confirmed that FMC capture could be performed at a rate up to 6 times faster than a current single element process. For this study, the robot scan path was only ever actuated at a significantly reduced speed. This was owing to data rate limitations on the hardware, which have since been improved.

Overall, this objective was met, providing an example of an automated TFM inspection applied to an existing Rolls-Royce component. Further development of the ease-of-use of the software, along with inspection trials at a higher execution speed, would be necessary before this could provide a useful platform at Rolls-Royce. This was outside the scope of this project however, and once the demonstration had been made, work shifted towards the next objectives.

7.1.2 OBJECTIVE 2. QUANTIFY EFFECT OF SURFACE CURVATURE ON TFM INSPECTION

The importance of this objective was highlighted by the end result of the robotic work. Much effort had been expended to create an integrated system that could capture and display TFM data. While this had been used on a part with an irregular surface, Rolls-Royce were more interested in the relationship between a well-defined curved surface, and the expected peak flaw signal for TFM.

This lead to a change in the project focus. Firstly, to ensure that results were relevant to Rolls-Royce, calibration blocks were designed to closely match those used for existing ultrasonic immersion processes. These used the same material, the same targets, and a similar range of depths. The only difference was a curved surface, either radial or convex, in the range of 10-40 mm.

To replicate the C-scan measurement of peak amplitude reflected from a target, a process was developed using a 3-axis scanning immersion tank at Rolls-Royce. This was adapted to drive a phased array probe, used to capture FMC information which was then time-encoded to create a C-scan. Different hardware and software

were used to suit the existing resources at the company. Scripts were developed in MATLAB, some of which called subroutines in Bristol University's BRAIN software, to generate C-scans from sets of FMC frames. The TFM "measure" mode was selected for all results in chapter 6; using an initial TFM image of the surface itself, rather than a profile known a priori.

Two sets of test blocks were used to quantify the effect of surface curvature. One set had a single metal path, and a range of curvatures from 10-40 mm. The other had a range of curvature from 10-20 mm, but also a range of metal paths. Experimental measurements were obtained for the peak signal value of targets under these different surfaces and metal paths. The relationships are shown in chapter 6.

Along with these results, three different approaches to modelling were considered. Selected results from these modelling techniques were shown alongside experimental measurements in chapter 6.

Together, the modelling and experimental results presented in chapter 6 show progress towards quantification of the effect of surface curvature when using TFM. These results are limited to the range of curvatures and metal paths explored, and also experimental results were limited to centrally-located flaws. Modelling techniques did not explore all possible options, as commercially available tools were favoured over creating a more sophisticated model.

7.1.3 OBJECTIVE 3. DEMONSTRATE APPLICATION TO NEW FORGING INSPECTION TECHNIQUE

Progress was made towards this objective, however it was the most ambitious objective of this thesis and was not completed. When setting the objective, it was imagined that an integrated solution involving the use of experimentally-backed models, optimization routines, and robotic delivery could be combined for arbitrarily shaped forgings. While this thesis progresses each of the constituent parts of such a proposed design, such an integrated solution was out of reach.

An example of work towards this objective was presented in Section 6.4. The ability to assess coverage level with scan step for different curvatures could be tied together with the robotic path planning work in chapter 3. This could be used to optimise the path, such that the maximum amount of coverage could be obtained, using the minimum number of FMC frames.

7.2 INDUSTRIAL BENEFIT OF THIS WORK

This work has had a positive industrial impact. The thesis itself provides justification for continued activities involving the use of phased arrays to inspect through curved surfaces. Care was taken by the author to ensure that all work in this thesis can be re-produced using equipment at Rolls-Royce.

The focus of this thesis has been on establishing a method equivalent to that of calibrating an existing immersion scanning inspection. One of the barriers to adoption in this instance is that the inspection would replace a very well tested and mature process. Towards this aim, this work acts as supporting evidence for larger and more comprehensive research and trials.

A much more immediate industrial benefit of this work has been the transfer of the methods presented here into investigative use at Rolls-Royce. Replacement of a large, established and routine post-manufacture inspection takes a long time to develop. Most inspections are not like this however, and many problems are presented at short notice, involving components with complex geometries.

During the course of conducting the work for this EngD, one such problem presented itself. Due to the capability introduced by this project, it was possible to follow the process of modelling a surface corrected TFM B-scan in CIVA, followed by performance of a C-scan. The part had a concave curvature of 40 mm, and a certain type of flaw that could be represented by a round-bottomed hole of 1 mm diameter.

Application of the methods developed in this thesis produced a result very quickly. This solved a challenging inspection problem through a curved surface, and was used as evidence that the department was capable of inspecting that type of defect in the component.

Further to this one example, for inspection of components using near-net shape manufacture, a method such as this may be the most practical approach. These will doubtlessly have curvature at the inspection stage, so this work helps prepare.

Finally, another common problem is the inspection of parts that have been worn-down in service to have an uneven surface profile. This approach is readily applicable, and could help when there is not time to develop a bespoke probe for an emergency inspection.

7.3 FUTURE WORK

There are many subject areas that the work in this thesis touches upon, but a common theme unites them. The overarching opportunity is that of closer integration between NDE processes and manufacture. Closer integration could bring an overall cost reduction, or improved product, even if it means an increase in cost and complexity of the NDE. This last point is hard to justify without further research. It is nevertheless the opinion of the author that improved automation and uptake of phased array techniques have much more to offer than faster scan rates and NDE process cost reductions.

A decision to invest in a new NDE process should be informed by two considerations other than the cost of the process itself. Firstly, the performance of the manufactured part. Investment in NDE should be considered where it would allow use of lighter components, or more complex geometries. The product is essentially worthless until it has been inspected, and its value increases with the quality of inspection.

Perhaps less immediately obvious is the link between NDE decisions and the cost of manufacture. It is easy to view the NDE as an isolated process. An aim to reduce its complexity would seem rational. However, when considered in isolation, an overly simplistic NDE process could result in complexities upstream in the manufacture process. Adding extra material to a forging to ease inspection is an example of this. Of course, this may be cheaper than developing and deploying a new NDE process - but how would we know?

For future work, these two considerations should act as industrial drivers. They can be summed up in two questions: "How could better NDE improve performance of this component?", and "How could better NDE save money in the overall manufacturing process?". Boiled down from the author's experience in industry, these questions help define the problem from the top down. To determine the tasks required to accomplish these from the bottom up is the next aim of the future work section.

The latter question, regarding manufacture, is more relevant to the work undertaken here. Ideas for future work are addressed in the form of an answer to that question, rather than exploring progress in each area of this thesis in a piecemeal fashion.

Work in this thesis utilized robotic manipulators, and development of software

to control them. Other research at the time of writing was under way to integrate external metrology systems to improve accuracy, and vastly improve speed of FMC-TFM processes. These are important avenues of improvement that can build upon the work presented here. A different stream of research, that the author is unaware of if being conducted, is a systems approach analysis of ultrasonic and cost modelling with automation.

Such a strand of research could build on the work in this thesis in the following ways.

A component and its associated manufacturing processes could be identified. Any addition of extra material could be noted, along with the cost incurred. Next, the NDE method could be designed with reference to all possible shapes of the part at the inspection stage. NDE techniques could be evaluated based on their ability to provide the appropriate coverage to candidate shapes, and the overall cost of manufacture plus inspection noted.

For this work flow, a comprehensive modelling ability would be required. Three different levels of inspection complexity and cost are given as an example. Level 1: a single element probe inspects flat surfaces of a forged component. Level 2: a linear phased array is used, using a TFM process to correct for curvatures between 20 mm and flat. Level 3: a 2D phased array, with partially fixed focus tailored to the part geometry, is scanned across a part with curvatures between 10 mm and flat. To select from these options, the modelling solution would have to be sufficient.

Modelling level 1 can be accomplished by use of commercially available packages. Modelling for level 2 could be accomplished by using some of the techniques presented in this thesis. Level 3 would require future work to extend the modelling approaches taken. One area of advancement then, would be to improve upon the accuracy obtained by the models presented in this thesis, and obtain a greater range of experimental flaw measurements with which to validate the modelling approach.

Once improved models could give an accurate sensitivity map for each NDE technique, coverage maps could be produced for each proposed inspection geometry. A cost-benefit analysis could then be conducted, and an appropriate technique chosen.

Robotic scanning could also factor into this analysis. The path, scan step, position of scans, multiple passes or tandem techniques would affect overall coverage. In

practise, this would act as an overlapping of sensitivity maps. Positional data could be used to implement data fusion, using overlapping regions to improve detectability [123], all of which could be modelled and incorporated into the analysis.

It is in the context of this vision that the technical, incremental future work should be considered.

Use of KUKA|prc and Grasshopper was found to be a functional solution. Any work on this particular implementation should focus on utilizing the option to code the internals of the graphical components using the integrated Python interface. The reason for this is to improve code maintainability, and speed of execution. One key improvement would be to use its ability to export co-ordinates to dispatch local surface geometry to an ultrasonic model.

Modelling in CIVA and PZFlex should be continued. Further work is required to understand the limitations of CIVA for predicting the relative signal through surface curvature. One improvement would be to develop a faster PZ flex model by adding it to a hybrid model. Further, an 3D FE model of a FBH could provide better agreement with experimental results.

Quantification of the abilities of TFM could be expanded to include experimental results from a larger range of test piece geometries and types of flaw. More of the many available TFM techniques could be benchmarked against these calibration blocks. Additively manufactured geometries and embedded defects present a good opportunity to explore more complex cases [124]. Further effort could be made to incorporate recent efforts to counter undesirable effects in TFM, such as backwall artefacts [125], beam distortion [126], near-surface effects [127],

Modelling techniques could be expanded to explore the affect of rough surfaces on TFM techniques, and investigate the interaction between surface curvature, roughness, and signal. Full imaging measurement models would give a more complete solution [1].

Most importantly, these activities could be combined to create a tool to optimize inspection planning, and design for inspection.

BIBLIOGRAPHY

[1] Lester W Schmerr Jr. *Fundamentals of ultrasonic phased arrays*, volume 215. Springer, 2014.

[2] J. Krautkrämer and H. Krautkrämer. *Ultrasonic testing of materials*. Springer-Verlag, 1977.

[3] C Huygens. *Treatise on Light by Christiaan Huygens*. Project Gutenberg, 1678.

[4] MESSINE: Eddy current modeling in CIVA. `https://www.ndt.net/article/wcndt00/papers/idn638/idn638.htm`. Accessed: 2018-08-14.

[5] Dominic Gates. O'hare engine explosion on boeing 767 poses puzzle for investigators. *Chicago Tribune*, November 2016.

[6] General requirements for qualification and PCN certification of NDT personnel. `https://www.bindt.org/downloads/pcngen.pdf`. Accessed: 2017-09-03.

[7] Mani Seethapathy et al. Method of determining wave propagation in a medium, November 4 2015. US Patent App. 14/932,531.

[8] L Le Jeune et al. Adaptive ultrasonic imaging with the total focusing method for inspection of complex components immersed in water. In *AIP Conference Proceedings*, volume 1650, pages 1037–1046. AIP, 2015.

[9] Ailidh McGilp, Jerzy Dziewierz, Timothy Lardner, Anthony Gachagan, John MacKersie, and Colin Bird. Inspection of complex components using 2D arrays and TFM. 2015.

[10] Carmelo Mineo, Stephen Gareth Pierce, Pascual Ian Nicholson, and Ian Cooper. Robotic path planning for non-destructive testing–a custom MATLAB toolbox approach. *Robotics and Computer-Integrated Manufacturing*, 37:1–12, 2016.

[11] Roy H Brown, S Gareth Pierce, Ian Collison, Ben Dutton, Jerzy Dziewierz, Joseph Jackson, Timothy Lardner, Charles MacLeod, and Maxim Morozov. Automated full matrix capture for industrial processes. In *AIP Conference Proceedings*, volume 1650, pages 1967–1976. AIP, 2015.

[12] Roy H Brown, Jeff Dobson, S Gareth Pierce, Ben Dutton, and Ian Collison. Quantifying performance of ultrasonic immersion inspection using phased arrays for curvilinear disc forgings. In *AIP Conference Proceedings*, volume 1806, page 040004. AIP Publishing, 2017.

[13] R. Halmshaw. *Non-destructive Testing*. Metallurgy and materials science. Edward Arnold, 1987.

[14] J Krautkrämer. Determination of the size of defects by the ultrasonic impulse echo method. *British Journal of Applied Physics*, 10(6):240, 1959.

[15] Mario Certo, G Nardoni, P Nardoni, M Feroldi, and D Nardoni. DGS curve evaluation applied to ultrasonic phased array testing. *Insight-Non-Destructive Testing and Condition Monitoring*, 52(4):192–194, 2010.

[16] IN Ermolov. The reflection of ultrasonic waves from targets of simple geometry. *Non-destructive testing*, 5(2):87–91, 1972.

[17] Rolls-Royce Plc. Ultrasonic immersion inspection procedure for rectilinear disc forgings. Technical report, Rolls-Royce Plc., Derby, 2010.

[18] Lester W Schmerr Jr and Alexander Sedov. The flat-bottom hole: an ultrasonic scattering model. *Research in Nondestructive Evaluation*, 1(3):181–196, 1989.

[19] Alexander Sedov, Lester W Schmerr Jr, and Sung Jin Song. Ultrasonic scattering by a flat-bottom hole in immersion testing: An analytical model. *The Journal of the Acoustical Society of America*, 92(1):478–486, 1992.

[20] Lester W Schmerr Jr, Sung-Jin Song, and Alexander Sedov. Ultrasonic flaw sizing inverse problems. *Inverse Problems*, 18(6):1775, 2002.

[21] Tim Gray, Mike Garton, and Paul Zombo. Distance amplitude correction factors for immersion ultrasonic measurements through curved surfaces. In *Review of Progress in Quantitative Nondestructive Evaluation*, pages 89–96. Springer, 1996.

[22] CR Bowen, LR Bradley, DP Almond, and PD Wilcox. Flexible piezoelectric transducer for ultrasonic inspection of non-planar components. *Ultrasonics*, 48(5):367–375, 2008.

[23] Hongjie Hu, Xuan Zhu, Chonghe Wang, Lin Zhang, Xiaoshi Li, Seunghyun Lee, Zhenlong Huang, Ruimin Chen, Zeyu Chen, Chunfeng Wang, et al. Stretchable ultrasonic transducer arrays for three-dimensional imaging on complex surfaces. *Science advances*, 4(3):eaar3979, 2018.

[24] D.C. Wright. Method of inspecting a component and an apparatus for inspecting a component, January 26 2010. US Patent 7,650,790.

[25] LS200 brochure. `http://scanmaster-irt.com/wp-content/uploads/2016/07/LS200_PA-Brochure.pdf`. Accessed: 2017-08-08.

[26] Esmeralda Cuevas, Miquel López, Monica García, and KUKA Robots Ibérica. Ultrasonic techniques and industrial robots: natural evolution of inspection systems. In *4th International Symposium on NDT in Aerospace, Berlin (Germany)*, 2012.

[27] Carmelo Mineo, Charles MacLeod, Maxim Morozov, S Gareth Pierce, Rahul Summan, Tony Rodden, Danial Kahani, Jonathan Powell, Paul McCubbin, Coreen McCubbin, et al. Flexible integration of robotics, ultrasonics and metrology for the inspection of aerospace components. In *AIP Conference Proceedings*, volume 1806, page 020026. AIP Publishing, 2017.

[28] Maxim Morozov, C Mineo, SG Pierce, Pascual Ian Nicholson, and Ian Cooper. Computer-aided tool path generation for robotic non-destructive inspection. 2013.

[29] M Morozov, J Riise, Rahul Summan, Stephen G Pierce, C Mineo, Charles N MacLeod, and RH Brown. Assessing the accuracy of industrial robots through metrology for the enhancement of automated non-destructive testing. In *Multisensor Fusion and Integration for Intelligent Systems (MFI), 2016 IEEE International Conference on*, pages 335–340. IEEE, 2016.

[30] Carmelo Mineo, Douglas Herbert, M Morozov, SG Pierce, PI Nicholson, and Ian Cooper. Robotic non-destructive inspection. In *51st Annual Conference of the British Institute of Non-Destructive Testing*, pages 345–352, 2012.

[31] C Mineo, SG Pierce, B Wright, I Cooper, and PI Nicholson. PAUT inspection of complex-shaped composite materials through six DOFs robotic

manipulators. *Insight-Non-Destructive Testing and Condition Monitoring*, 57(3):161–166, 2015.

[32] Carmelo Mineo, Momchil Vasilev, Charles N MacLeod, Riliang Su, and S Gareth Pierce. Enabling robotic adaptive behaviour capabilities for new industry 4.0 automated quality inspection paradigms. In *57th Annual British Conference on Non-Destructive Testing*, pages 1–12, 2018.

[33] Z Xiao, C Xu, D Xiao, F Liu, and M Yin. An optimized robotic scanning scheme for ultrasonic NDT of complex structures. *Experimental Techniques*, 41(4):389–398, 2017.

[34] F Bentouhami, B Campagne, E Cuevas, T Drake, M Dubois, T Fraslin, P Piñeiro, J Serrano, and H Voillaume. LUCIE-a flexible and powerful laser ultrasonic system for inspection of large CFRP components. In *2nd International Symposium on Laser Ultrasonics, Talence (France)*, 2010.

[35] Naresh Marturi, Alireza Rastegarpanah, Chie Takahashi, Maxime Adjigble, Rustam Stolkin, Sebastian Zurek, Marek Kopicki, Mohammed Talha, Jeffrey A Kuo, and Yasemin Bekiroglu. Towards advanced robotic manipulation for nuclear decommissioning: a pilot study on tele-operation and autonomy. In *Robotics and Automation for Humanitarian Applications (RAHA), 2016 International Conference on*, pages 1–8. IEEE, 2016.

[36] Ming-June Tsai and Chuan-Cheng Hung. Development of a high-precision surface metrology system using structured light projection. *Measurement*, 38(3):236–247, 2005.

[37] Charles N MacLeod, S Gareth Pierce, Maxim Morozov, Rahul Summan, Gordon Dobie, Paul McCubbin, Coreen McCubbin, Scott Dearie, and Gavin Munro. Automated metrology and NDE measurements for increased throughput in aerospace component manufacture. In *AIP Conference Proceedings*, volume 1650, pages 1958–1966. AIP, 2015.

[38] Zengxi Pan, Joseph Polden, Nathan Larkin, Stephen Van Duin, and John Norrish. Recent progress on programming methods for industrial robots. In *Robotics (ISR), 2010 41st International Symposium on and 2010 6th German Conference on Robotics (ROBOTIK)*, pages 1–8. VDE, 2010.

[39] Jonathan Riise, S Gareth Pierce, P Ian Nicholson, Ian Cooper, and Ben Wright. Deployment of ultrasonic through transmission inspection using twin cooperative industrial robots. 2016.

[40] Andrew Payne and Rajaa Issa. Grasshopper primer, 2009.

[41] Mostapha Sadeghipour Roudsari, Michelle Pak, Adrian Smith, et al. Ladybug: a parametric environmental plugin for grasshopper to help designers create an environmentally-conscious design. In *Proceedings of the 13th international IBPSA conference held in Lyon, France Aug*, 2013.

[42] Johannes Braumann and Sigrid Brell-Cokcan. Parametric robot control: integrated CAD/CAM for architectural design. 2011.

[43] Sigrid Brell-Cokcan and Johannes Braumann. A new parametric design tool for robot milling. In *Proceedings of the 30th Annual Conference of the Association for Computer Aided Design in Architecture*, pages 357–363, 2010.

[44] Olaf T Von Ramm and Stephen W Smith. Beam steering with linear arrays. *IEEE transactions on biomedical engineering*, (8):438–452, 1983.

[45] Douglas G Wildes, Richard Y Chiao, Chris MW Daft, KW Rigby, L Scott Smith, and Kai E Thomenius. Elevation performance of 1.25 D and 1.5 D transducer arrays. *IEEE Transactions on Ultrasonics, Ferroelectrics, and Frequency Control*, 44(5):1027–1037, 1997.

[46] Christopher JL Lane. The inspection of curved components using flexible ultrasonic arrays and shape sensing fibres. *Case Studies in Nondestructive Testing and Evaluation*, 1:13–18, 2014.

[47] J Russell, R Long, P Cawley, and N Habgood. Inspection of components with irregular surfaces using a conformable ultrasonic phased array. In *AIP Conference Proceedings*, volume 1096, pages 792–799. AIP, 2009.

[48] Theodosia Stratoudaki, Matt Clark, and Paul D Wilcox. Adapting the full matrix capture and the total focusing method to laser ultrasonics for remote non destructive testing. In *Ultrasonics Symposium (IUS), 2017 IEEE International*, pages 1–4. IEEE, 2017.

[49] H.D. Young, R.A. Freedman, A.L. Ford, F.W. Sears, and M.W. Zemansky. *Sears and Zemansky's University Physics: With Modern Physics*. Number v. 2 in Pearson custom library. Pearson Education, Limited, 2014.

[50] Bruce W Drinkwater and Paul D Wilcox. Ultrasonic arrays for non-destructive evaluation: A review. *NDT & E International*, 39(7):525–541, 2006.

[51] Shi-Chang Wooh and Yijun Shi. Optimum beam steering of linear phased arrays. *Wave motion*, 29(3):245–265, 1999.

[52] P Calmon, S Mahaut, S Chatillon, and R Raillon. CIVA: An expertise platform for simulation and processing ndt data. *Ultrasonics*, 44:e975–e979, 2006.

[53] SW Smith, DJ Phillips, OT Von Ramm, and FL Thurstone. Some advances in acoustic imaging through the skull. *Ultrasonic Tissue Characterization II*, 525:209–218, 1979.

[54] Bjørn AJ Angelsen, Hans Torp, Sverre Holm, Kjell Kristoffersen, and TA Whittingham. Which transducer array is best? *European Journal of Ultrasound*, 2(2):151–164, 1995.

[55] Najet Chakroun, Mathias A Fink, and François Wu. Time reversal processing in ultrasonic nondestructive testing. *IEEE Transactions on Ultrasonics, Ferroelectrics, and Frequency Control*, 42(6):1087–1098, 1995.

[56] Solomon R Ghorayeb, William Lord, and Satish S Udpa. Application of a beamforming technique to ultrasound imaging in nondestructive testing. *IEEE transactions on ultrasonics, ferroelectrics, and frequency control*, 41(2):199–208, 1994.

[57] B Beardsley, M Peterson, and JD Achenbach. A simple scheme for self-focusing of an array. *Journal of nondestructive evaluation*, 14(4):169–179, 1995.

[58] Steve Mahaut, Olivier Roy, Claude Beroni, and Bernhard Rotter. Development of phased array techniques to improve characterization of defect located in a component of complex geometry. *Ultrasonics*, 40(1):165–169, 2002.

[59] Jorge Camacho, Jorge F Cruza, Jose Brizuela, and Carlos Fritsch. Automatic dynamic depth focusing for NDT. *IEEE Transactions on Ultrasonics, Ferroelectrics, and Frequency Control*, 61(4):673–684, 2014.

[60] Foroohar Foroozan and Shahram ShahbazPanahi. MUSIC-based array imaging in multi-modal ultrasonic non-destructive testing. In *Sensor Array and Multichannel Signal Processing Workshop (SAM), 2012 IEEE 7th*, pages 529–532. IEEE, 2012.

[61] Chengguang Fan, Mihai Caleap, Mengchun Pan, and Bruce W Drinkwater. A comparison between ultrasonic array beamforming and super resolution imaging algorithms for non-destructive evaluation. *Ultrasonics*, 54(7):1842–1850, 2014.

[62] Caroline Holmes, Bruce W Drinkwater, and Paul D Wilcox. Post-processing of the full matrix of ultrasonic transmit–receive array data for non-destructive evaluation. *NDT & e International*, 38(8):701–711, 2005.

[63] J Russell, R Long, D Duxbury, and P Cawley. Development and implementation of a membrane-coupled conformable array transducer for use in the nuclear industry. *Insight-Non-Destructive Testing and Condition Monitoring*, 54(7):386–393, 2012.

[64] Jie Zhang, Bruce W Drinkwater, and Paul D Wilcox. Effects of array transducer inconsistencies on total focusing method imaging performance. *NDT & E International*, 44(4):361–368, 2011.

[65] David Duxbury, Jonathan Russell, and Michael Lowe. The effect of variation in phased array element performance for non-destructive evaluation (NDE). *Ultrasonics*, 53(6):1065–1078, 2013.

[66] M Ingram, A Gachagan, AJ Mulholland, A Nordon, J Dziewierz, M Hegarty, and E Becker. Calibration of ultrasonic phased arrays for industrial applications. *IEEE SENSORS 2017*, 2017.

[67] Nicolas Budyn, Rhodri Bevan, Anthony J Croxford, Jie Zhang, Paul D Wilcox, Artem Kashubin, and Peter Cawley. Sensitivity images for multi-view ultrasonic array inspection. In *AIP Conference Proceedings*, volume 1949, page 080001. AIP Publishing, 2018.

[68] Jie Zhang, Tom Barber, Andrew Nixon, and Paul Wilcox. Investigation into distinguishing between small volumetric and crack-like defects using multi-view total focusing method images. In *AIP Conference Proceedings*, volume 1806, page 040003. AIP Publishing, 2017.

[69] Brady J Engle, Lester W Schmerr, Jr, and Alexander Sedov. Quantitative ultrasonic phased array imaging. In *AIP Conference Proceedings*, volume 1581, pages 49–56. AIP, 2014.

[70] Li Lin, Huanqing Cao, and Zhongbing Luo. Total focusing method imaging of multidirectional CFRP laminate with model-based time delay correction. *NDT & E International*, 97:51–58, 2018.

[71] Anne Juengert, Sandra Dugan, Tobias Homann, Steffen Mitzscherling, Jens Prager, Sergey Pudovikov, and Thomas Schwender. Advanced ultrasonic techniques for nondestructive testing of austenitic and dissimilar welds in nuclear facilities. In *AIP Conference Proceedings*, volume 1949, page 110002. AIP Publishing, 2018.

[72] Ailidh McGilp, Jerzy Dziewierz, Tim Lardner, John Mackersie, Anthony Gachagan, Dale E Chimenti, Leonard J Bond, and Donald O Thompson. Inspection design using 2d phased array, TFM and cueMAP software. In *AIP Conference Proceedings*, volume 1581, pages 65–71. AIP, 2014.

[73] Jie Zhang, Bruce W Drinkwater, and Paul D Wilcox. Efficient immersion imaging of components with nonplanar surfaces. *IEEE transactions on ultrasonics, ferroelectrics, and frequency control*, 61(8):1284–1295, 2014.

[74] Jerzy Dziewierz and Anthony Gachagan. Correspondence: Computationally efficient solution of snell's law of refraction. *IEEE transactions on ultrasonics, ferroelectrics, and frequency control*, 60(6):1256–1259, 2013.

[75] W Kerr, SG Pierce, and P Rowe. Investigation of synthetic aperture methods in ultrasound surface imaging using elementary surface types. *Ultrasonics*, 72:165–176, 2016.

[76] Jerzy Dziewierz. *2D ultrasonic phased arrays for quantitative characterisation of complex defects*. PhD thesis, University of Strathclyde, 2015.

[77] John Nickolls and William J Dally. The GPU computing era. *IEEE micro*, 30(2), 2010.

[78] Jason Lambert, Antoine Pedron, Guillaume Gens, Franck Bimbard, Lionel Lacassagne, and Ekaterina Iakovleva. Performance evaluation of total focusing method on GPP and GPU. In *Design and Architectures for Signal and Image Processing (DASIP), 2012 Conference on*, pages 1–8. IEEE, 2012.

[79] Jerzy Dziewierz and Anthony Gachagan. Correspondence: Computationally efficient solution of Snell's law of refraction. *IEEE transactions on ultrasonics, ferroelectrics, and frequency control*, 60(6):1256–1259, 2013.

[80] Jerzy Dziewierz, Timothy Lardner, and Anthony Gachagan. A design methodology for 2D sparse NDE arrays using an efficient implementation of refracted-ray TFM. In *2013 IEEE International Ultrasonics Symposium (IUS)*, pages 136–138. IEEE, 2013.

[81] Marcin Lewandowski, Mateusz Walczak, Beata Witek, and Tomasz Steifer. A GPU-based ultrasound phased-array research system for non-destructive testing. In *Ultrasonics Symposium (IUS), 2016 IEEE International*, pages 1–4. IEEE, 2016.

[82] N Dominguez and G Ithurralde. Ultra-fast ultrasonic inspection for aeronautical composites using paintbrush acquisitions and data processing on gpu. In *European Conference on NDT, Moscow*, pages 53–58, 2010.

[83] David Romero-Laorden, Javier Villazón-Terrazas, Oscar Martinez-Graullera, Alberto Ibanez, Montserrat Parrilla, and M Santos Penas. Analysis of parallel computing strategies to accelerate ultrasound imaging processes. *IEEE Transactions on Parallel and Distributed Systems*, 27(12):3429–3440, 2016.

[84] Hongwei Hu, Jian Du, Na Xu, Hyunjo Jeong, and Xianghong Wang. Ultrasonic sparse-TFM imaging for a two-layer medium using genetic algorithm optimization and effective aperture correction. *NDT & E International*, 90:24–32, 2017.

[85] Mickael Njiki, Abdelhafid Elouardi, Samir Bouaziz, Olivier Casula, and Olivier Roy. A multi-FPGA architecture-based real-time TFM ultrasound imaging. *Journal of Real-Time Image Processing*, pages 1–17, 2016.

[86] BRAIN - ultrasonic array data acquisition and processing platform. `https://sourceforge.net/projects/bristol-brain/`. Accessed: 2017-08-14.

[87] Jie Zhang, Bruce W Drinkwater, and Paul D Wilcox. The use of ultrasonic arrays to characterize crack-like defects. *Journal of Nondestructive Evaluation*, 29(4):222–232, 2010.

[88] Jie Zhang, Bruce W Drinkwater, and Paul D Wilcox. Defect characterization using an ultrasonic array to measure the scattering coefficient matrix. *IEEE transactions on ultrasonics, ferroelectrics, and frequency control*, 55(10), 2008.

[89] M. Seethapathy, S.V. Tammineni, S. WISEALL, D. Wright, C. Chapman, and R. Pathmeswaran. Method of determining wave propagation in a medium, May 25 2016. EP Patent App. EP20,150,192,519.

[90] Ian Cooper, Ian Nicholson, Dawei Yan, Ben Wright, Dimos Liaptsis, and Carmelo Mineo. Development of a fast inspection system for aerospace

composite materials-the intacom project. In *5th International Symposium on NDT in Aerospace*, 2013.

[91] Diagnostic sonar ltd.: FIToolbox specifications. `http://diagnosticsonar.com/FIToolbox/architecture/FlawInspectaToolboxComponents.pdf`. Accessed: 2017-09-19.

[92] Zetec: Zetec dynaray specifications. `http://www.zetec.com/wp-content/uploads/2016/08/Zetec_Dynaray_Datasheet.pdf`. Accessed: 2017-09-19.

[93] Advanced OEM solutions: OEM-PA phased array ultrasonics specifications. `http://aos-ndt.com/product/advanced-fmc-tfm/`. Accessed: 2017-09-19.

[94] David IA Lines, J Wharrie, and J Hottenroth. Real-time full matrix capture+ total focusing and other novel imaging options using general purpose PC-based array instrumentation. *Insight-Non-Destructive Testing and Condition Monitoring*, 54(2):86–90, 2012.

[95] M2M: Gekko phased-array flaw detector specifications. `https://www.m2m-ndt.com/products/Spec%20Gekko.pdf`. Accessed: 2017-09-19.

[96] Xuefei Guan, Jingdan Zhang, El Mahjoub Rasselkorde, Waheed A Abbasi, and S Kevin Zhou. Material damage diagnosis and characterization for turbine rotors using three-dimensional adaptive ultrasonic NDE data reconstruction techniques. *Ultrasonics*, 54(2):516–525, 2014.

[97] Kyle Hoegh and Lev Khazanovich. Extended synthetic aperture focusing technique for ultrasonic imaging of concrete. *NDT & E International*, 74:33–42, 2015.

[98] Dayong Guo, Guojun Jiang, Yue Wu, and Jiayi Cheng. Automatic ultrasonic testing for components with complex surfaces. *DEStech Transactions on Engineering and Technology Research*, (mime), 2016.

[99] FARO ARM: Bronze, silver and gold FARO arm specification sheet. `https://knowledge.faro.com/Hardware/FaroArm_and_ScanArm/FaroArm_Gold-Silver-Bronze/Technical_Specification_Sheet_for_the_Gold-Silver_and_Bronze_Arms`. Accessed: 2017-10-03.

[100] A. Stevenson. *Oxford Dictionary of English*. Oxford Dictionary of English. OUP Oxford, 2010.

[101] Lung-Wen Tsai. *Robot analysis: the mechanics of serial and parallel manipulators*. John Wiley & Sons, 1999.

[102] Harry Colestock. *Industrial robotics: selection, design, and maintenance*. TAB/Electronics, 2005.

[103] Jonathan Riise, Lance Farr, Martin Lindop, Gareth Pierce, P Ian Nicholson, and Ian Cooper. Methods for improving the accuracy of automated NDE systems. In *12th European Conference on Non-Destructive Testing*, pages 1–9, 2018.

[104] YH Chen and CY Liu. Robust segmentation of CMM data based on NURBS. *The International Journal of Advanced Manufacturing Technology*, 13(8):530–534, 1997.

[105] Peng Zhang. Chapter 13 - humanÃćâĆňâĂIJmachine interfaces. In Peng Zhang, editor, *Advanced Industrial Control Technology*, pages 527 – 555. William Andrew Publishing, Oxford, 2010.

[106] Human ui for grasshopper project page. `http://designplaygrounds.com/blog/creating-interfaces-for-data-visualization-with-human-ui-for-grassho` Accessed: 2019-04-07.

[107] Julio Isla and Frederic Cegla. Coded excitation for low SNR pulse-echo systems: Enabling quasi-real-time low-power EMATs. In *Ultrasonics Symposium (IUS), 2016 IEEE International*, pages 1–4. IEEE, 2016.

[108] S Bannouf, S Robert, O Casula, and C Prada. Data set reduction for ultrasonic TFM imaging using the effective aperture approach and virtual sources. In *Journal of Physics: Conference Series*, volume 457, page 012007. IOP Publishing, 2013.

[109] Ge krautkramer hydrastar information sheet. `https://www.industrial.ai/inspection-technologies/automated-ut-systems/composite-inspection/krautkramer-hydrastar`. Accessed: 2019-03-24.

[110] G Harvey, A Tweedie, C Carpentier, and P Reynolds. Finite element analysis of ultrasonic phased array inspections on anisotropic welds. In *AIP Conference Proceedings*, volume 1335, pages 827–834. AIP, 2011.

[111] Jeff Dobson, Andrew Tweedie, Gerald Harvey, Richard OâĂŹLeary, Anthony Mulholland, Katherine Tant, and Anthony Gachagan. Finite ele-

ment analysis simulations for ultrasonic array NDE inspections. In *AIP Conference Proceedings*, volume 1706, page 040005. AIP Publishing, 2016.

[112] Steffen Marburg and Bodo Nolte. *Computational acoustics of noise propagation in fluids: finite and boundary element methods*, volume 578. Springer, 2008.

[113] Python (version 2.7), python software foundation. `https://www.python.org/`. Downloaded: 2015-03-01.

[114] CIVA (version 11), EXTENDE. `http://www.extende.com/available-civa-version`. Accessed: 2017-11-04.

[115] Georges A Deschamps. Ray techniques in electromagnetics. *Proceedings of the IEEE*, 60(9):1022–1035, 1972.

[116] S Robert, P Calmon, M Calvo, L Le Jeune, and E Iakovleva. Surface estimation methods with phased-arrays for adaptive ultrasonic imaging in complex components. In *AIP Conference proceedings*, volume 1650, pages 1657–1666. AIP, 2015.

[117] Lester Schmerr and Jung-Sin Song. *Ultrasonic nondestructive evaluation systems*. Springer, 2007.

[118] JMM Pinkerton. A pulse method for the measurement of ultrasonic absorption in liquids: results for water. *Nature*, 160(4056):128–129, 1947.

[119] Nicolas Forcadel, Carole Le Guyader, and Christian Gout. Generalized fast marching method: applications to image segmentation. *Numerical Algorithms*, 48(1-3):189–211, 2008.

[120] Wenshuo Gao, Xiaoguang Zhang, Lei Yang, and Huizhong Liu. An improved sobel edge detection. In *Computer Science and Information Technology (ICCSIT), 2010 3rd IEEE International Conference on*, volume 5, pages 67–71. IEEE, 2010.

[121] Vaughan Pratt. Direct least-squares fitting of algebraic surfaces. In *ACM SIGGRAPH computer graphics*, volume 21, pages 145–152. ACM, 1987.

[122] Ronald L Klueh and Donald R Harries. *High-chromium ferritic and martensitic steels for nuclear applications*, volume 3. ASTM International, 2001.

[123] N Brierley, T Tippetts, and P Cawley. Data fusion for automated nondestructive inspection. *Proc. R. Soc. A*, 470(2167):20140167, 2014.

[124] Lucas Koester, Ronald A Roberts, DJ Barnard, Sunil Chakrapani, Surendra Singh, Robert Hogan, and LJ Bond. NDE of additively manufactured components with embedded defects (reference standards) using conventional and advanced ultrasonic methods. In *AIP Conference Proceedings*, volume 1806, page 140006. AIP Publishing, 2017.

[125] Frederic Dupont-Marillia, Mohammad Jahazi, and Pierre Belanger. Phased array inspection of large size forged steel parts. In *AIP Conference Proceedings*, volume 1949, page 080004. AIP Publishing, 2018.

[126] Ricardo Baiotto, Benjamin Knight-Gregson, Channa Nageswaran, and Thomas Clarke. Coherence weighting applied to FMC/TFM data from austenitic CRA clad lined pipes. *Journal of Nondestructive Evaluation*, 37(3):49, 2018.

[127] JN Potter, PD Wilcox, and AJ Croxford. Diffuse field full matrix capture for near surface ultrasonic imaging. *Ultrasonics*, 82:44–48, 2018.

Appendix A

HARDWARE AND SOFTWARE INFORMATION

A.1 EXPERIMENTAL EQUIPMENT USED

Table A.1: Specification for calipers used in experiments

Type	Vernier calipers
Resolution	0.01 mm
Power	1.5 V button cell
Measuring Speed	1.5 m/s
Working temperature	0 to 40 degrees C
Relative humidity	$< 80\%$
Storage temperature	-10 to 60 degrees C

Table A.2: Array probe A used in experiments

Manufacturer	Vermon
Type	Linear 1D array
Centre Frequency	10 MHz
Number of Elements	128
Pitch	0.5 mm
Elevation	7 mm
Matching	Water

Table A.3: Array probe B used in experiments

Manufacturer	Imasonic
Type	Linear 1D array
Centre Frequency	10 MHz
Number of Elements	32
Pitch	0.3 mm
Elevation	5 mm
Matching	Water

Table A.4: Example single element probe C used for comparison

Manufacturer	GE
Type	Single element unfocused
Centre Frequency	10 MHz
Diameter	19.1 mm
Min. recommended focal length in water	40 mm
Max. recommended focal length in water	200 mm

Table A.5: Laptop used for experiments and simulation.

Manufacturer	Lenovo
Model Number	Y70 Touch
CPU	2.5 GHz Intel Core i7-4710HQ (quad-core, 6 MB cache)
Graphics	Nvidia GeForce GTX 860M (4 GB GDDR5 RAM)
RAM	16 GB DDR3L
Storage	Hybrid 1 TB (5400 RPM) plus 8 GB SSD

A.2 THIRD-PARTY SOFTWARE INFORMATION

Rhinoceros 3D This is a 3D CAD package, generally used by architects more often than engineers. In this thesis, it was used for its add-ons, and its compatibility with many different file formats.

Grasshopper 3D An add-on to Rhinoceros 3D. This is a graphical programming language that enables parametric geometry generation. It was used in this work to produce smooth surfaces and raster scan patterns across test pieces. It also provided user interface elements, such as sliders and dials, that could be used to update the automated inspection plan.

KUKA PRC An add-on to Grasshopper 3D. Developed by Robotics in Architecture, this tool allows simulation of the kinematics of KUKA robots, as well as generation of the necessary KRL 2 code for programming a path. It was used to ensure that the robot scan path for the inspection was feasible, and to generate code for the experiment in Chapter 3.

MATLAB A programming platform for engineers. This was used extensively for work in this thesis. Most important was its use for capturing, processing and organizing ultrasonic TFM data.

cueART An array research tool developed by Strathclyde University. Implemented in MATLAB, this allows fast capture and processing of FMC data. It was used in this thesis for the experiments in Chapter 3.

BRAIN An array research tool developed by The University of Bristol. Implemented in MATLAB, this allows fast capture and processing of FMC data. It was used in this thesis for the experiments in Chapter 5.

PZ Flex Finite element analysis software, specialised for piezoelectric material modelling. This was used for simulating full-matrix capture through curved surfaces in chapter 4.

Python General purpose programming language. This was used to develop a batch-controller for automatically generating and executing PZFlex models.

Table A.6: Versions of software used

Name	**Latest version used**	**Release Date**
Rhinoceros 3D	Version 5 SR14 32-bit (5.14.522.8390)	October 2012
Grasshopper 3D	Version 0.9.0076	August 2014
KUKA PRC	Version 1	February 2012
MATLAB	2014b	October 2014
cueART	0.1	Unreleased at time of use
BRAIN	1.71	February 2015
PZ Flex	2015	April 2015
Python	2.7.4	April 2013